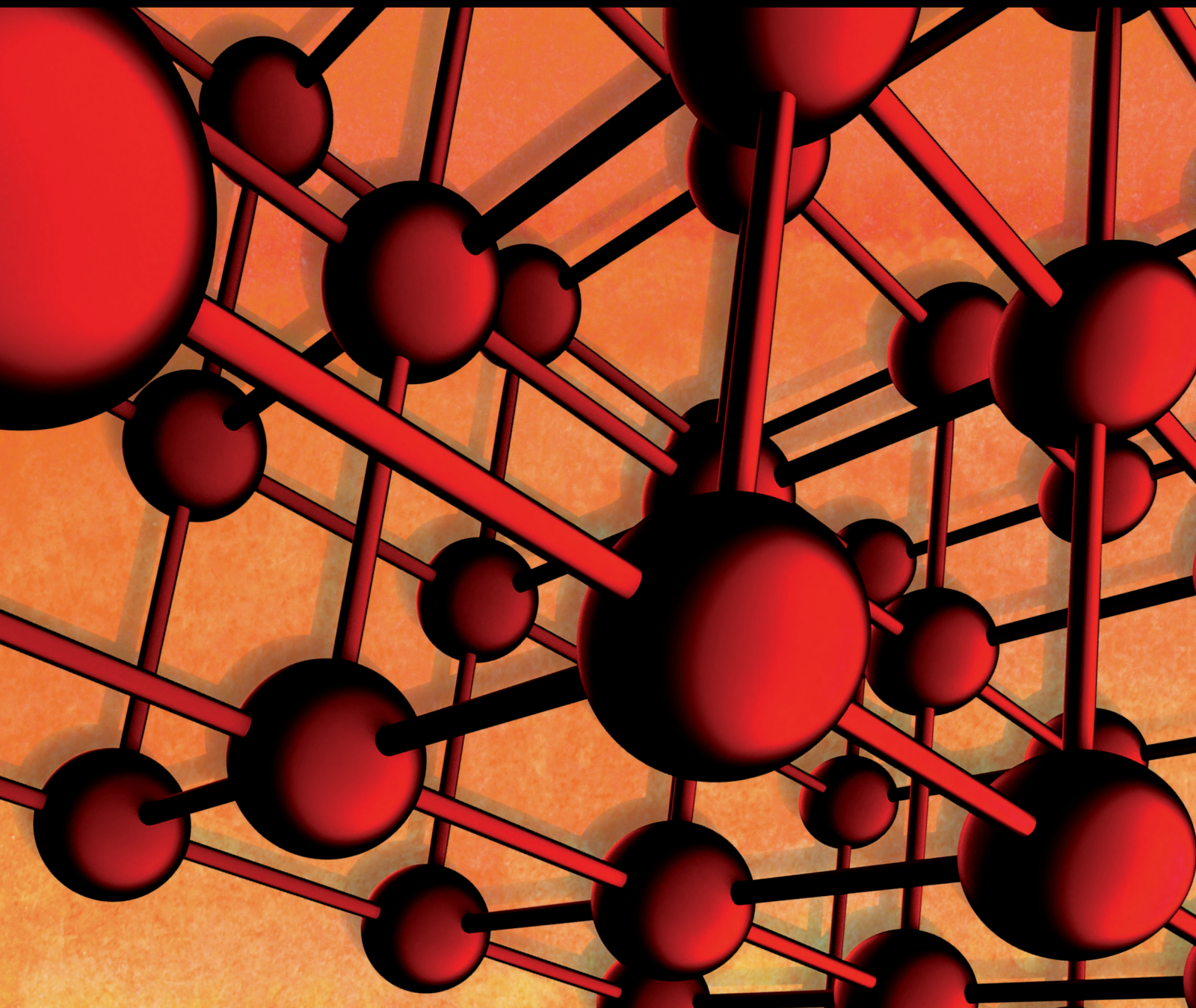


Advances in Materials Science and Engineering

# Design, Synthesis, and Characterization of Hybrid Materials

Guest Editors: Kwang Ho Kim, Mihai Barboiu, Simo-Pekka Hannula, and Doo-In Kim





---

# **Design, Synthesis, and Characterization of Hybrid Materials**

Advances in Materials Science and Engineering

---

# **Design, Synthesis, and Characterization of Hybrid Materials**

Guest Editors: Kwang Ho Kim, Mihai Barboiu,  
Simo-Pekka Hannula, and Doo-In Kim



---

Copyright © 2015 Hindawi Publishing Corporation. All rights reserved.

This is a special issue published in “Advances in Materials Science and Engineering.” All articles are open access articles distributed under the Creative Commons Attribution License, which permits unrestricted use, distribution, and reproduction in any medium, provided the original work is properly cited.

## Editorial Board

Dimitrios G. Aggelis, Belgium  
Jarir Aktaa, Germany  
K. G. Anthymidis, Greece  
Amit Bandyopadhyay, USA  
Arun Bansil, USA  
Massimiliano Barletta, Italy  
Jozef Bednarcik, Germany  
Avi Bendavid, Australia  
Jamal Berakdar, Germany  
Giovanni Berselli, Italy  
Alessandra Bianco, Italy  
Susmita Bose, USA  
Heinz-Günter Brokmeier, Germany  
Steve Bull, UK  
Peter Chang, Canada  
Daolun Chen, Canada  
Gabriel Cuello, France  
Narendra B. Dahotre, USA  
João P. Davim, Portugal  
Francesco Delogu, Italy  
Seshu B. Desu, USA  
Yong Ding, USA  
Aziz Dinia, France  
Kaveh Edalati, Japan  
Gilbert Fantozzi, France  
Massimo Fresta, Italy  
Eric Freysz, France  
Sergi Gallego, Spain  
Santiago Garcia-Granda, Spain  
Filippo Giannazzo, Italy  
Daniel Guay, Canada  
Hiroki Habazaki, Japan  
Joke Hadermann, Belgium  
Satoshi Horikoshi, Japan  
Rui Huang, USA  
Jacques Huot, Canada

Michele Iafisco, Italy  
Katsuyuki Kida, Japan  
Jae-Ho Kim, Korea  
Akihiko Kimura, Japan  
Takayuki Kitamura, Japan  
Hongchao Kou, China  
Prashant Kumta, USA  
Luciano Lamberti, Italy  
Heinrich Lang, Germany  
Pavel Lejcek, Czech Republic  
Cristina Leonelli, Italy  
Markku Leskela, Finland  
Ying Li, USA  
Wei Liu, France  
Yunqi Liu, China  
Meilin Liu, Georgia  
Ying Liu, USA  
Jun Liu, China  
Fernando Lusquios, Spain  
Peter Majewski, Australia  
Philippe Miele, France  
Hossein Moayed, Malaysia  
Paul Munroe, Australia  
Rufino M. Navarro, Spain  
Luigi Nicolais, Italy  
Hiroshi Noguchi, Japan  
Chérif Nouar, France  
José L. Ocaña, Spain  
Tsutomu Ohzuku, Japan  
Olanrewaju Ojo, Canada  
Xiaoqing Pan, USA  
Anna Paradowska, Australia  
Gianluca Percoco, Italy  
Jean-Francois Pierson, France  
Simon C. Potter, Canada  
Manijeh Razeghi, USA

Anna Richelli, Italy  
Antonio Riveiro, Spain  
Pascal Roussel, France  
Timo Sajavaara, Finland  
Antti Salminen, Finland  
Fawzy Samuel, Canada  
Carlo Santulli, Italy  
Franz-Josef Schmitt, Germany  
Jainagesh A. Sekhar, USA  
Fridon Shubitidze, USA  
Charles C. Sorrell, Australia  
Costas M. Soukoulis, USA  
Sam-Shajing Sun, USA  
Kohji Tashiro, Japan  
Somchai Thongtem, Thailand  
Achim Trampert, Germany  
Filip Tuomisto, Finland  
Stuart Turner, Belgium  
Krystyn Van Vliet, USA  
Rui Vilar, Portugal  
Holger von Wenckstern, Germany  
Rui Wang, China  
Qiang Wang, China  
Rong Wang, USA  
Lu Wei, China  
Jörg M. K. Wiezorek, USA  
Wei Wu, USA  
Hemmige S. Yathirajan, India  
Wenbin Yi, China  
Belal F. Yousif, Australia  
Jinghuai Zhang, China  
Li Zhang, China  
Ming-Xing Zhang, Australia  
Wei Zhou, China

## Contents

**Design, Synthesis, and Characterization of Hybrid Materials**, Young-Keun Jeong, Mihai Barboiu, Simo-Pekka Hannula, and Kwang Ho Kim  
Volume 2015, Article ID 867913, 2 pages

**The Polymerization of MMA and ST to Prepare Material with Gradient Refractive Index in Electric Field**, Yao Huang, Daming Wu, Dongyun Ren, Qingyun Meng, and Xiaojun Di  
Volume 2015, Article ID 401897, 6 pages

**Optimization and Static Stress Analysis of Hybrid Fiber Reinforced Composite Leaf Spring**, Luay Muhammed Ali Ismaeel  
Volume 2015, Article ID 374609, 13 pages

**Conductivity and Dielectric Studies of Lithium Trifluoromethanesulfonate Doped Polyethylene Oxide-Graphene Oxide Blend Based Electrolytes**, A. A. Azli, N. S. A. Manan, and M. F. Z. Kadir  
Volume 2015, Article ID 145735, 10 pages

**Influence of Tensile Speeds on the Failure Loads of the DP590 Spot Weld under Various Combined Loading Conditions**, Jung Han Song and Hoon Huh  
Volume 2015, Article ID 297915, 9 pages

**Characteristics of Nanophase WC and WC-3 wt% (Ni, Co, and Fe) Alloys Using a Rapid Sintering Process for the Application of Friction Stir Processing Tools**, Daeup Kim, Young Choi, Yongil Kim, and Seungboo Jung  
Volume 2015, Article ID 343619, 9 pages

**Fabrication of a Microtubular  $\text{La}_{0.6}\text{Sr}_{0.4}\text{Ti}_{0.2}\text{Fe}_{0.8}\text{O}_{3-\delta}$  Membrane by Electrophoretic Deposition for Hydrogen Production**, Kyoung-Jin Lee, Yeong-Ju Choe, Jun-Sung Lee, and Hae-Jin Hwang  
Volume 2015, Article ID 505989, 6 pages

**Improvement of Surface Properties of Inconel718 by HVOF Coating with WC-Metal Powder and by Laser Heat Treatment of the Coating**, Hui Gon Chun, Tong Yul Cho, Jae Hong Yoon, and Gun Hwan Lee  
Volume 2015, Article ID 468120, 7 pages

**Kinetic Studies of Atom Transfer Radical Polymerisations of Styrene and Chloromethylstyrene with Poly(3-hexyl thiophene) Macroinitiator**, Nattawoot Rattanathamwat, Jatuphorn Wootthikanokkhan, Nonsee Nimitsiriwat, Chanchana Thanachayanont, and Udom Asawapirom  
Volume 2015, Article ID 973632, 13 pages

**Preparation and Properties of OMMT/PU Composites**, Chen Yufei, Han Yang, Dai Qiwan, Zhang Xiwang, and Qingyu Zhang  
Volume 2015, Article ID 715879, 9 pages

**Feasibility Studies on Underwater Laser Surface Hardening Process**, Biao Jin, Min Li, TaeWoo Hwang, and YoungHoon Moon  
Volume 2015, Article ID 845273, 6 pages

## Editorial

# Design, Synthesis, and Characterization of Hybrid Materials

**Young-Keun Jeong,<sup>1</sup> Mihai Barboiu,<sup>2</sup> Simo-Pekka Hannula,<sup>3</sup> and Kwang Ho Kim<sup>4</sup>**

<sup>1</sup>Graduate School of Convergence Science, Pusan National University, Busan 609-735, Republic of Korea

<sup>2</sup>Institut Européen des Membranes, 34095 Montpellier, France

<sup>3</sup>Department of Materials Science and Engineering, Aalto University School of Chemical Technology, 02150 Espoo, Finland

<sup>4</sup>Materials Science and Engineering, Pusan National University, Busan 609-735, Republic of Korea

Correspondence should be addressed to Kwang Ho Kim; [hymap@hanmail.net](mailto:hymap@hanmail.net)

Received 25 April 2015; Accepted 25 April 2015

Copyright © 2015 Young-Keun Jeong et al. This is an open access article distributed under the Creative Commons Attribution License, which permits unrestricted use, distribution, and reproduction in any medium, provided the original work is properly cited.

For last decade, the nanoparadigm has dominated materials science and technology. Nanotechnology has ushered in a paradigm shift in science, industry, and our daily lives. However, high-tech industries continuously need to be fed innovations in materials and components. New materials and components required in pioneering 21st century industries can be revealed through “hybrid” technology. Many researchers believe that this new “hybrid” paradigm will create great opportunities and changes in science, industry, and our daily lives, as the nanoparadigm greatly plays a role in the materials innovation and developments. This interest resulted in an agreement to organize a new International Symposium on Hybrid Materials and Processing (HyMaP) in 2008. And The 3rd International Symposium on Hybrid Materials and Processing (HyMaP 2014) was held at the Haeundae Grand Hotel in Busan, Korea, from November 10, 2014.

The papers in this special issue were selected among the papers submitted at HyMaP 2014. This special issue provides a wide spectrum of new information on hybrid materials and processing. The topics focused on the hybrid function, that is, functionally hybridized materials where new specific characteristics are simultaneously realized, along with the typical function of those materials.

The special issue contains numerous papers focused on the functional hybrid materials. More specifically, topics of hybrid materials for electronic devices, membrane for hydrogen production, laser surface treatment on hybrid

materials, and mechanical properties of hybrid materials are discussed in this special issue.

In the paper entitled “Conductivity and Dielectric Studies of Lithium Trifluoromethanesulfonate Doped Polyethylene Oxide-Graphene Oxide Blend Based Electrolytes,” A. A. Azli et al. study the conductivity and dielectric properties of polymer/graphene oxide hybrid materials for electrolytes. In plasticized system, the conductivity has been enhanced as compared to the conductivity in salted system.

In a paper entitled “Influence of Tensile Speeds on the Failure Loads of the DP590 Spot Weld under Various Combined Loading Conditions,” J. H. Song and H. Huh investigate the evaluation of the dynamic failure load of the spot weld under combined axial and shear loading conditions. They show that the failure contour is expanded with increasing loading speeds and failure loads show similar dynamic sensitivity with respect to the loading angles.

In a paper entitled “Characteristics of Nanophase WC and WC-3 wt% (Ni, Co, and Fe) Alloys Using a Rapid Sintering Process for the Application of Friction Stir Processing Tools,” D. Kim et al. introduce microstructures and mechanical characteristics of tungsten carbide (WC) based alloys fabricated using a spark plasma sintering (SPS) method for the application of friction stir processing tools. The density of the sintering bodies was about 99% and the average grain size was in the range from 0.26 to 0.41  $\mu\text{m}$ . The sintered bodies were obtained without almost grain growth during sintering.

In a paper entitled "Optimization and Static Stress Analysis of Hybrid Fiber Reinforced Composite Leaf Spring," L. M. A. Ismaeel investigates a monofiber reinforced composite leaf spring, which is proposed as an alternative to the typical steel one as it is characterized by high strength to weight ratio. Fibers are the most predominant and controlling element on the bending stiffness of the structure. And E-glass fiber in the hybrid composites does not exhibit a regular behavior making it difficult to accurately predict hybrid composite spring performance, response, and stresses, while boron is the opposite; thus it is advisable to adopt it in such applications with various matrices.

In a paper entitled "The Polymerization of MMA and ST to Prepare Material with Gradient Refractive Index in Electric Field," Y. Huang et al. consider light scattering material with gradient refractive index was prepared under the electrical field by taking methyl methacrylate (MMA) monomer as the matrix with the addition of a little preheated styrene (ST) and peroxidation benzoin formyl (BPO). They conclude that electrical field has a significant effect on polymerization.

In a paper entitled "Improvement of Surface Properties of Inconel718 by HVOF Coating with WC-Metal Powder and by Laser Heat Treatment of the Coating," H. G. Chun et al. investigate when high-velocity oxygen-fuel (HVOF) thermal-spray coating with WC-metal powder was carried out by using optimal coating process on an Inconel718 surface. For the improvement of surface properties and durability of materials, HVOF coating of WC-metal powder on the surface and faster heat-treated coating were strongly recommended.

In a paper entitled "Fabrication of a Microtubular  $\text{La}_{0.6}\text{Sr}_{0.4}\text{Ti}_{0.2}\text{Fe}_{0.8}\text{O}_{3-\delta}$  Membrane by Electrophoretic Deposition for Hydrogen Production," K.-J. Lee et al. prepare microtubular type  $\text{La}_{0.6}\text{Sr}_{0.4}\text{Ti}_{0.2}\text{Fe}_{0.8}\text{O}_{3-\delta}$  (LSTF) by electrophoretic deposition (EPD). The oxygen permeation and hydrogen production behavior of the membranes were investigated under various conditions. They suggest that hydrogen production via water splitting using these tubular LSTF membranes is possible.

In a paper entitled "Preparation and Properties of OMMT/PU Composites," C. Yufei et al. introduce prepolymer of polyurethane (PU) by toluene diisocyanate (TDI) and polyether diol through polymerization, organically modified montmorillonite (OMMT) gained by montmorillonite (MMT) that was modified by octadecyl trimethyl ammonium chloride (OTAC), and the OMMT was used as intercalator; alcohol-based OMMT/PU adhesive was synthesized. The morphology of OMMT filler was clear and OMMT dispersed uniformly in OMMT/PU adhesive, and the size of OMMT was nanoscale. The uniform mixing of OMMT layer and PU matrix could achieve on nanoscale, so mechanical properties of OMMT/PU were improved, and water absorption quantity decreased.

The paper entitled "Feasibility Studies on Underwater Laser Surface Hardening Process" by B. Jin et al. experimentally characterizes laser surface hardening of tool steel in both water and air. As the hardened depth depends on the thermal conductivity of the material, the surface temperature and the penetration depth have been varied by underwater laser processing. On the view point of hardness, harder layer

has been obtained at underwater hardening that is supposed to be caused by faster cooling rate due to accelerated heat dissipation along water layer.

In a paper entitled "Kinetic Studies of Atom Transfer Radical Polymerisations of Styrene and Chloromethylstyrene with Poly(3-hexyl thiophene) Macroinitiator," N. Rattanathamwat et al. investigate the kinetics of ATRP as a function of monomers to the macroinitiator molar ratio. They found that all of the three types of ATRP systems led to first-order kinetics with respect to monomers.

## Acknowledgments

We would like to thank the authors for their excellent contributions and patience in assisting us. Finally, the fundamental work of all the reviewers of these papers is also very warmly acknowledged.

*Young-Keun Jeong  
Mihai Barboiu  
Simo-Pekka Hannula  
Kwang Ho Kim*

## Research Article

# The Polymerization of MMA and ST to Prepare Material with Gradient Refractive Index in Electric Field

Yao Huang,<sup>1</sup> Daming Wu,<sup>2</sup> Dongyun Ren,<sup>1</sup> Qingyun Meng,<sup>3</sup> and Xiaojun Di<sup>4</sup>

<sup>1</sup>Engineering Research Center for Polymer Processing Equipment, Ministry of Education, Beijing 100029, China

<sup>2</sup>State Key Laboratory of Organic-Inorganic Composites, Beijing 100029, China

<sup>3</sup>The Key Laboratory of Preparation and Processing of Novel Polymer of Beijing City, Beijing University of Chemical Technology, Beijing 100029, China

<sup>4</sup>Department of Chemical Engineering, Texas Tech University, Lubbock, TX 79409, USA

Correspondence should be addressed to Qingyun Meng; mqybuct@163.com and Xiaojun Di; xiaojun.di@ttu.edu

Received 16 September 2014; Revised 18 December 2014; Accepted 19 December 2014

Academic Editor: Kwangho Kim

Copyright © 2015 Yao Huang et al. This is an open access article distributed under the Creative Commons Attribution License, which permits unrestricted use, distribution, and reproduction in any medium, provided the original work is properly cited.

Light scattering material with gradient refractive index was prepared under the electrical field by taking methyl methacrylate (MMA) monomer as the matrix with the addition of a little preheated styrene (ST) and peroxidation benzoin formyl (BPO). The material obtained under electrical field presented different transmittance and molecular weight at different parts of the cylindrical sample along the axis of the direction of electric field which led to the layering phenomenon and gradient refractive index. The disparity of molecular weight between different layers can be as much as 230 thousand. There were several peaks in the figure of GPC test of the sample under electric field. This proved that there were polymers with different molecular weights in the sample. Therefore, it can be concluded that electrical field has a significant effect on polymerization.

## 1. Introduction

There are at least two kinds of substance in light scattering material [1]. One is body material, the other is scattering material. The body material normally presents good light transmittance which guides light and forms the skeleton of light scattering material. In order to scatter light, the molecular polarity of the added scattering material should be different from that of the body material [2]. The content of the scattering material is much smaller than that of the body material. For example, polymethylmethacrylate/polystyrene (PMMA/PS) composite light scattering material is a kind of new light scattering material that has high transmittance and haze, which is widely used in polymer scattering elements and back light for liquid crystal display [3–7].

There are two methods to prepare light scattering material [8]. The first method is to copolymerize the monomers of two transparent polymers whose refractive indexes are different. This method often leads to phase separation due to poor compatibility. A more common operation is first to polymerize the scattering particle monomers and then swell

the scattering polymer in the body polymer's monomers, before finally polymerizing them together. The second method is to mechanically mix the transparent polymer body material with the scattering particle together. In comparison, the haze of the sample obtained from the first method could not be very large, while the transmittance of the sample obtained from second method is difficult to control.

Due to its excellent mechanical and optical properties, PMMA was always chosen to be a body material. PS was chosen to be scattering material because the refractive index of both PMMA/PS and MMA/ST had a gap. But when MMA and ST were mixed together to polymerize, copolymerization reaction [9] would occur, which may result in the decrease of haze. On the other hand, if we mechanically mixed PMMA and PS like the second method, the transmittance [10] could decrease to 20–30%. Furthermore, the mechanical properties of the sample would decrease due to the phase separation of PMMA/PS caused by mismatch of the polarity. For example, the impact strength could decrease to 1000 J/m<sup>2</sup>, which was much lower than the pure PMMA sample. Therefore, the elimination of the phase interface was the key to prepare

the PMMA/PS light scattering material. In this work, we tried the first method which could prepare the light scattering material in polymerization method. In order to achieve the same scattering strength in all directions, the particle size and the refractive index of the light scattering material should be in gradient distribution.

The structure of the light scattering material was designed accordingly to meet the above requirements. It was shown in the studies that the size of scattering particle affected the optical property of the light scattering material [11–13]. The size of the scattering particle depended on the molecular weight of polymer. The higher the molecular weight, the bigger the particle size. So the size of scattering particle could be obtained by controlling the scattering monomer's polymerization degree. In the experiment, we first polymerized ST to get the prepolymer in different degrees of polymerization so that the molecular weight of the prepolymer ST was different and the polydispersity of the prepolymer was larger. Then we polymerized MMA and prepolymer ST to get the scattering particle PS and P(ST-MMA) in different molecular weights. So the degree of polymerization of the scattering particle PS and P(ST-MMA) was also in wide polydispersity, which may result in the various refractive index and polarizability. As the particles of different polarizabilities exerted different electric field forces in the gradient electric field, the particles in different molecular weights could be separated in gradient field to obtain the light scattering material with gradient refractive index.

This experiment took PS as scattering materials and PMMA as body materials [14] by using in situ copolymerization method [15]. The influence of the electrical field on eliminating the phase interface was studied during the preparation of the sample. We also did preliminary research on the property of the sample prepared in electrical field.

## 2. Equipment

American Waters company GPC apparatus: 515 HPLC Pump (precision 0.1% RSD), 717 Autosample, 2410 Refractive Index Detector, 996 Photodiode Array Detector, Millennium32, Styragel (HT3\_HT5\_HT6E). Situation: flow phase: furfuran (THF), velocity of flow: 1 mL/min, temperature: 30°C, standard sample: PS, molecular weight range: 500–3,000,000.

FESEM X-ray energy dispersive spectrum (EDX) XL30 S-EFG (Philips Company).

## 3. Experiment

### 3.1. Reagents and Purification

**3.1.1. Reagents.** The main reagents used in the experiment were MMA (analytical purity); BPO (analytical purity); ferrocene (98%); phosphoric acid (85%); anhydrous sodium carbonate (chemical purity); sodium borohydride (96%); anhydrous alcohol (analytical purity); petroleum ether (60°C–90°C), analytical purity; anhydrous ether (analytical purity).

**3.1.2. Purification.** Purification of MMA: firstly MMA was washed three times with 10% NaOH to remove inhibitor and

then washed another three times with deionized water. MMA was predried with anhydrous  $\text{CaCl}_2$  and dried with  $\text{CaH}_2$ . Then the MMA was distilled under reduced pressure with the existence of  $\text{CaH}_2$ , and the middle distillation products were collected. Distilled monomer should first be vacuumed before being put in  $\text{N}_2$  for protection and then kept in refrigerator for use at last.

Purification of ST: the same procedure and reagents as MMA are used.

Purification of BPO: firstly acetone was dehydrated with anhydrous  $\text{K}_2\text{CO}_3$  before being distilled and collected between 55°C and 56°C. BPO was dissolved in the distilled acetone until saturation. Then the saturated filtrate solution was vacuumed till crystal appeared. The crystal was kept in refrigerator for 3 to 6 hours, and solvent was removed to dry the crystal. Finally crystal was protected with  $\text{N}_2$  and kept in the refrigerator for use.

**3.2. Sample Preparation.** BPO (volume ratio is 0.5%) was put in the purified ST and polymerized in 60°C for 15 minutes in natural environment. The prepolymer ST was added to the mixture of MMA and BPO (volume ratio is 0.5%), and we kept the volume ratio of the prepolymer ST to be 0.2%.

The above polymerized system was kept about 20 to 25 minutes at 60°C. The prepolymer ST was under electric field (the electric field intensity is 5000 V/5 cm) [16]. The polymerization temperature was room temperature (approximately 27–31°C). The light scattering material with gradient refractive index was obtained until the polymerization system solidified [17].

## 4. Result and Discussion

During polymerization of MMA and prepolymer ST, the distribution of the BPO monomer (namely, the strength of BPO in different parts of the system) and prepolymer ST in the polymerization system were the primary factors that influenced the distribution of the final homopolymer and copolymer in the system. In PMMA body material, the refractive index of PS was different with the P(ST-MMA) copolymers and PMMA. When the light transmits in the material and encounters the PS scattering particle, the scattering happens. If the transmittance of the material was lower than 75%, the material could be produced as light scattering material [18].

**4.1. Sample Figure and Colour.** The sample figure of P(ST-MMA)/PS/PMMA prepared in natural environment (shown in Figure 1(a)) was compared with the sample prepared under electrical field (Figure 1(b)). The shape of the sample was cylinder with diameter of 15 mm and height of 40 mm. The vertical direction in Figure 1 was the cylindrical axial.

From Figure 1(b), it can be seen that the sample presented several layers along the cylindrical axial, which was consistent with the prediction in the introduction. Because every layer had different transmittance, the layering phenomenon occurred. The transmittance of the PMMA body material was very good; however in this material the layering phenomenon

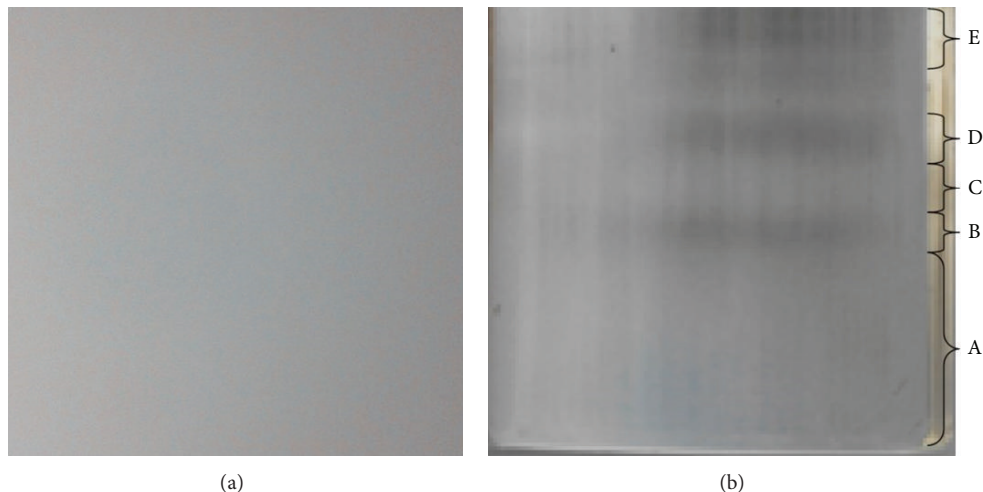


FIGURE 1: Layering phenomenon of the sample in natural environment and electrical field. (a) In natural environment. (b) In electrical field.

took place. The main reason was distribution of small amount of PS and P(ST-MMA) in the PMMA body material. PS and P(ST-MMA) were different from PMMA in refractive index and transmittance. As the content of the PS and P(ST-MMA) copolymer in different layers was different, the transmittance at different layers was different, which could result in the layering phenomenon. The ST and BPO monomers distribution varied in the polymerization system under the high strength electric field, which influenced the polymerizing process and the physical properties of the material, for example, transmittance.

**4.2. Result of the GPC Test.** From Figure 2, each layer of the sample contained three obvious peaks. One was big and the other two were small. It showed that there were polymers with different molecular weights in each layer, the big peak indicated polymer of high content and the small peaks indicated polymer of low content like PS. So we inferred that each layer had PS and P(ST-MMA) copolymer. Also the areas of the peak in each layer were different suggesting the different content of PS and P(ST-MMA) copolymer.

The transmittance of the layers depended on the content and compatibility of the polymers of different molecular weights in each layer. The results of the molecular weight test in different layers were shown in Table 1.

Based on Table 1, it can be concluded that the molecular weight and content of the PS and P(ST-MMA) in different layers were different. But the margin of the difference was just 0.1–1%. It indicated that the monomer ST and MMA were under different electric force in external electric field. When the polymerization was incomplete, the electric dipole moment of molecules in the solution was different which could cause the different displacement of the molecules under the gradient field. The electric dipole moment of the molecules could be arranged in the direction of the external electric field. As a result, the layering and the orientation phenomenon would occur in the sample. So the transmittance of the samples was different in the direction of cylinder axis.

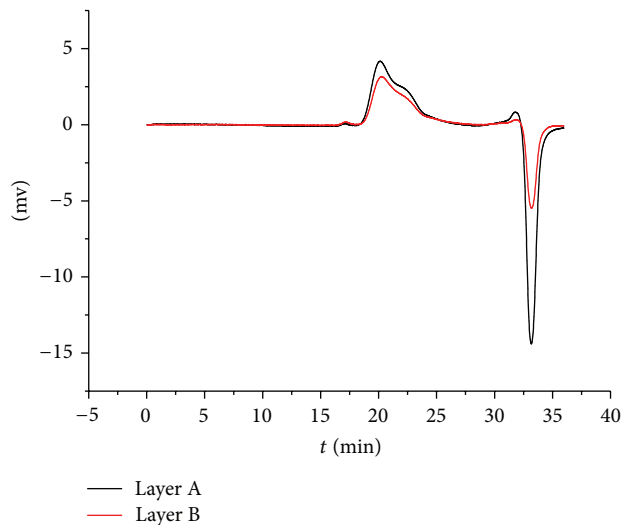


FIGURE 2: The GPC test result of layer A and layer B produced in electrical field.

The transmittance of layer A was smaller than other layers. It was because that the ST monomer had already prepolymerized for certain time, with PS already formed. However, due to the poor compatibility of the PS and PMMA and the huge refractive index disparity between two phases, the intertwined chain segment of the PS and PMMA led to huge interface area between two phases, which resulted in the small transmittance of the whole layers.

As layer B, from the test result of the GPC, the content of PS and P(ST-MMA) copolymer was more than that of layer A, but layer B's transmittance was higher than the layer A. The reason of this phenomenon was that the content of P(ST-MMA) copolymer was more than PS. The P(ST-MMA) copolymer was easily compatible with PMMA body material than PS, so the transmittance of layer B was better.

The rest of the layers also had different transmittance. The reason was the same with the mechanism studied above.

TABLE 1: PS and P(ST-MMA)'s molecular weight.

Layers of the light scattering (from bottom to up)	The bid peak's MP	The bid peak's Mn	The ratio of the small peak's area (%)	Haze (%)	Light transmittance (%)
Layer A	972237	787555	1.80	82.5	58.2
Layer B	1020879	678337	1.69	66.1	79.3
Layer C	1016391	665288	2.02	86.3	52.4
Layer D	1083097	888294	1.04	60.4	73.8
Layer E	1032240	677765	0.92	69.2	78.0

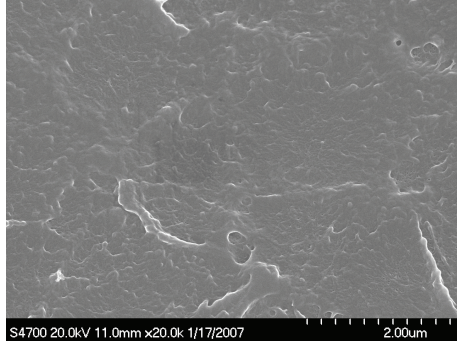


FIGURE 3: SEM microstructure of the pure PMMA sample.

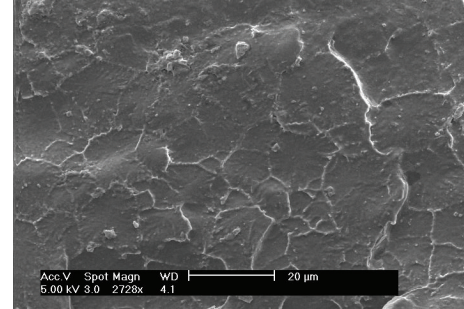


FIGURE 4: SEM microstructure of the section of layer A produced in electrical field.

The variety of the transmittance in different layers depended on the content of the two phases and the refractive index disparity between the two phases related to the two phases' compatibility. The compatibility of PS and PMMA body material was not good. But the compatibility of P(ST-MMA) copolymer and PMMA body material was much better. The copolymer forming factors were the content of the BPO and ST monomers. By controlling the electric field strength and the ST monomer polymerization time and distribution, the ST content could be changed in the system.

**4.3. Information in the SEM Photograph.** From Figure 3, no obvious structural characteristics could be seen. We could only see the unordered surface.

From Figure 4, the transmittance of layer A was little and the haze of this layer was high. The polymer chain section of the layer was small, while the configuration and appearance seem complex. The chain section distributed out-of-order and at long intervals there were some small particles. It showed that the PS content in layer A was higher. And the compatibility of PS and PMMA was not good. It resulted in the refractive index disparity between the two phases and the decrease of the transmittance.

Figure 5 showed microscopic configuration of layer B containing several small regions arranged disorderly. With improved degree of order in this layer, the chain section's integrity also increased. Clearly, less small particles are observed because P(ST-MMA) copolymer in layer B was more than that in other layers, and the compatibility between copolymer and PMMA was good. It leads to less disparity

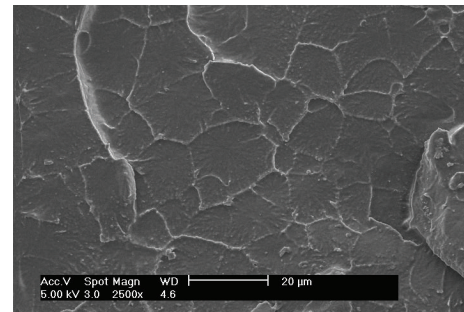


FIGURE 5: SEM microstructure of the section of layer B produced in electrical field.

of refractive index between two phases and higher transmittance.

Figure 6 was a 40000x photograph of small particles in Figure 4. It could be seen that the small particles were a node of the chain segment whose size was in range of micron meter and dispersed light intensively. It was the main matter which caused the light scattering.

The distribution of several scattering particles in PMMA body material could be seen in Figure 7. This distribution made scattering intensity uniform and let the material get good body scattering.

The SEM photograph showed the disparity of molecular structure of different layers which had different transmittances. The content of the PS or P(ST-MMA) copolymer dominated the layers' transmittance.

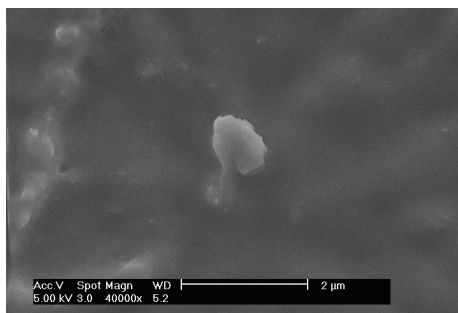


FIGURE 6: The configuration of the scattering substance.

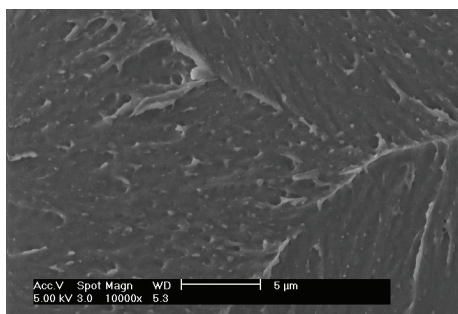


FIGURE 7: The distribution of several scattering material.

## 5. Conclusion

PMMA/PS light scattering material with gradient refractive index was prepared under electric field by in situ polymerization method. The material obtained under electrical field had different transmittance at different parts of the cylindrical sample along the direction of electric field which caused the layering phenomenon. The disparity of molecular weight between different layers could be as much as 230 thousand.

From the results of GPC and SEM, the difference between the samples obtained under electric field and natural environment was observed: the GPC test of the sample in natural environment had one peak; however the sample obtained under electric field had two peaks. The SEM results of the sample in natural environment indicated that chain section was out-of-order and the low-weight molecules were little. The SEM results of the sample obtained under electric field showed that chain section tended to be more regular with more low-weight molecules.

## Conflict of Interests

The authors declare that there is no conflict of interests regarding the publication of this paper.

## Acknowledgments

This work was supported by National Natural Science Foundation of China (no. 51173015). This work was supported by the Fundamental Research Funds for the Central Universities (no. JD1412).

## References

- [1] Z. Chen, P. Hu, Q. Meng, and X. Dong, "Novel optical fiber dynamic light scattering measurement system for nanometer particle size," *Advances in Materials Science and Engineering*, vol. 2013, Article ID 250121, 4 pages, 2013.
- [2] J. Arbaoui, Y. Schmitt, J. Pierrot, and F. Royer, "Comparison study and mechanical characterisation of a several sandwich composites structures," *Advances in Materials Science and Engineering*. In press.
- [3] M. Ishiharada, I. Tanuma, and K. Naito, "Light scattering material," U.S. Patent, 5,744,534, 1998.
- [4] H. Zhu, Y. Wang, X. Zhang, Y. Sub, and X. Donga, "Influence of molecular architecture and melt rheological characteristic on the optical properties of LDPE blown films," *Polymer*, vol. 48, no. 17, pp. 5098–5106, 2007.
- [5] J. Wu, G. Huang, X. Wang, X. He, and B. Xu, "Changes in the viscoelastic mechanisms of polyisobutylene by plasticization," *Macromolecules*, vol. 45, no. 19, pp. 8051–8057, 2012.
- [6] Y. Yang, "brief introduction of liquid crystal display technology," *New Chemical Materials*, vol. 8, pp. 33–35, 1996.
- [7] B. Xu, X. Di, and G. B. McKenna, "Swelling behavior of cross-linked rubber: explanation of the elusive peak in the swelling activity parameter (dilatational modulus)," *Macromolecules*, vol. 45, no. 5, pp. 2402–2410, 2012.
- [8] F. Gao, X. Cao, and Z. Tong, "Preparation of high scattering light conducting PMMA and optical scattering properties," *Plastics Industry*, vol. 69, no. 4, pp. 69–71, 1997.
- [9] B. Alhamad, J. A. Romagnoli, and V. G. Gomes, "Advanced modelling and optimal operating strategy in emulsion copolymerization: application to styrene/MMA system," *Chemical Engineering Science*, vol. 60, no. 10, pp. 2795–2813, 2005.
- [10] B. Li, H. Yuan, and Y. Zhang, "transparent PMMA-based nanocomposite using electrospun graphene-incorporated PA-6 nanofibers as the reinforcement," *Composites Science and Technology*, vol. 89, pp. 134–141, 2013.
- [11] Q. Qin, "Research and development status of new light scattering material," *New Chemical Materials*, vol. 28, pp. 20–22, 2000.
- [12] N. P. Balsara and L. J. Fetters, "Reevaluation of light scattering from living polymer solutions," *Macromolecules*, vol. 32, no. 15, pp. 5147–5148, 1999.
- [13] A. Somwangthanaroj, E. C. Lee, and M. J. Solomon, "Early stage quiescent and flow-induced crystallization of intercalated polypropylene nanocomposites by time-resolved light scattering," *Macromolecules*, vol. 36, no. 7, pp. 2333–2342, 2003.
- [14] A. F. Mansour, "Photostability and optical parameters of copolymer styrene/MMA as a matrix for the dyes used in fluorescent solar collectors," *Polymer Testing*, vol. 23, no. 3, pp. 247–252, 2004.
- [15] B. A. Bhanvase, D. V. Pinjari, P. R. Gogate, S. H. Sonawane, and A. B. Pandit, "Synthesis of exfoliated poly(styrene-co-methyl methacrylate)/montmorillonite nanocomposite using ultrasound assisted in situ emulsion copolymerization," *Chemical Engineering Journal*, vol. 181–182, pp. 770–778, 2012.
- [16] D. Wu, Y. Huang, and Q. Meng, "Artificial environment and the structure of gradient soft matter," *Chemical Physics Letters*, vol. 588, pp. 114–118, 2013.
- [17] W. Hao, Y. Zhang, Q. Suo, L. Jian, and W. He, "Preparation and determination of optimum experiment plan of methyl

methacrylate styrene copolymer," *Journal of Baotou College*, vol. 21, no. 1, pp. 46–49, 2002.

- [18] Q. Meng and Y. Si, "Study on the preparation of gradient materials of PMMA in the non natural environment," *Chemical Industry and Engineering Progress*, vol. 23, no. 7, pp. 736–739, 2004.

## Research Article

# Optimization and Static Stress Analysis of Hybrid Fiber Reinforced Composite Leaf Spring

**Luay Muhammed Ali Ismaeel**

*Machineries and Equipments Technologies Department, Najaf Technical Institute, Iraq*

Correspondence should be addressed to Luay Muhammed Ali Ismaeel; [luay.m.63@gmail.com](mailto:luay.m.63@gmail.com)

Received 7 July 2014; Revised 19 October 2014; Accepted 22 October 2014

Academic Editor: Kwangho Kim

Copyright © 2015 Luay Muhammed Ali Ismaeel. This is an open access article distributed under the Creative Commons Attribution License, which permits unrestricted use, distribution, and reproduction in any medium, provided the original work is properly cited.

A monofiber reinforced composite leaf spring is proposed as an alternative to the typical steel one as it is characterized by high strength-to-weight ratio. Different reinforcing schemes are suggested to fabricate the leaf spring. The composite and the typical steel leaf springs are subjected to the same working conditions. A weight saving of about more than 60% can be achieved while maintaining the strength for the structures under consideration. The objective of the present study was to replace material for leaf spring. This study suggests various materials of hybrid fiber reinforced plastics (HFRP). Also the effects of shear moduli of the fibers, matrices, and the composites on the composites performance and responses are discussed. The results and behaviors of each are compared with each other and verified by comparison with analytical solution; a good convergence is found between them. The elastic properties of the hybrid composites are calculated using rules of mixtures and Halpin-Tsi equation through the software of MATLAB v-7. The problem is also analyzed by the technique of finite element analysis (FEA) through the software of ANSYS v-14. An element modeling was done for every leaf with eight-node 3D brick element (SOLID185 3D 8-Node Structural Solid).

## 1. Introduction

Leaf springs are special kind of springs used in automobile suspension systems. The advantage of leaf spring over helical spring is that the ends of the spring may be guided along a definite path as it deflects to act as a structural member in addition to energy absorbing device [1]. In order to conserve natural resources and economize energy, weight reduction has been the main focus of automobile manufacturers in the present scenario. Weight reduction can be achieved primarily by the introduction of better material, design optimization, and better manufacturing processes [2]. The suspension leaf spring is one of the potential items for weight reduction in automobile as it accounts for ten to twenty percent of the unsprung weight. This helps in achieving the vehicle with improved riding qualities. It is well known that springs are designed to absorb and store energy and then release it. Hence, the strain energy of the material becomes a major factor in designing the springs. The relationship of the specific strain energy can be expressed as [2]

$$U = \frac{\sigma^2}{2\rho E}, \quad (1)$$

where  $\sigma$  is the strength,  $\rho$  the density, and  $E$  the Young modulus of the spring material. It can be easily observed that material having lower modulus and density will have a greater specific strain energy capacity. The introduction of composite materials has made reducing the weight of the leaf spring possible without any reduction on load carrying capacity and stiffness. Since the composite materials have more elastic strain energy storage capacity and high strength-to-weight ratio as compared to those of steel, they are proposed for such a task [3]. In addition, composite and hybrid composite materials have good corrosion resistance and tailorable properties [4]. In this work, an analysis of a hybrid composite monoleaf spring is made with many different composite materials constructed from four fibers each with three composite matrices (a composite matrix is that one composed of short fibers and a certain matrix material), with various volume fractions in order to get vast range of collections of different

hybrid composites. The design constraints are the bending and Von Mises stresses and deflections. The leaf spring should absorb vertical vibrations and impacts due to road irregularities by means of vibrations in the spring deflection so that the potential energy is stored in spring as strain energy and then released slowly [5]. Other advantages of using fiber-reinforced polymers instead of steel are (a) the possibility of reducing noise, vibrations, and ride harshness due to their high damping factors; (b) the absence of corrosion problems, which means lower maintenance costs; and (c) lower tooling costs, which has favorable impact on the manufacturing costs [4]. Advanced composite materials seem ideally suited for suspension (leaf spring) applications. Their elastic properties can be adjusted to increase the strength and reduce the stresses induced during application [6]. This paper is mainly focused on the implementation of composite materials by replacing steel in conventional leaf springs of a suspension system. This is the reason why leaf springs are still used widely in a variety of automobiles to carry axial loads, lateral loads, and brake-torque in the suspension system. Therefore analysis of composite material leaf springs has become essential in showing the comparative results with conventional leaf springs.

## 2. Literature Survey

A lot of studies and researches were carried out on the applications of the composite materials in monoleaf springs. Kumar and Vijayarangan [7] studied and tested monoleaf spring fabricated from a traditional E-glass/epoxy composite material for the static load conditions; fatigue life prediction was also done by these authors so as to ensure a reliable number of life cycles of that spring. Cyclic creep and cyclic deformation were also studied by Yang and Wang [8]. Fuentes et al. [9], Clarke and Borowski [10], and Mayer et al. [11] studied the premature failure in leaf springs so as to suggest remedies on application of composite leaf springs. Patunkar and Dolas discussed modelling and analysis of composite leaf spring under the static load condition by using FEA, but they did not mention much about hybrid composite materials; it is again E-glass/epoxy material adopted for their work [12]. Some of the recent works turned to discuss the geometric shape of the leaf spring made from traditional metallic alloys; Kumar and Aggarwal considered the parabolic leaf spring and studied its effect on the performance and behavior of the leaf spring used by a light commercial automotive vehicle. The researchers used a CAD modeling of parabolic leaf spring which has been done in CATIA V5 and the analysis of the model is imported and performed in ANSYS-11 workbench [13]. This paper focuses on introducing hybrid fiber-reinforced composite materials of various reinforcing schemes in order to get more detailed scene about the effect of different factors on the response of and stresses induced in the leaf spring. These factors include effects of matrix material variation, fiber type variation, and fiber volume fraction. The leaf spring adopted in this paper is of elliptic geometry and only a half of it is considered here (Figure 3), due to the symmetry about the center U-bolt (Figure 4) [14]. Elliptic leaf springs are the most common types of suspension and

springing used in automobiles due to their larger radius of curvature than parabolic counterparts [15].

*2.1. Fabrication of Hybrid Composite Leaf Spring.* The pattern is made up of wood. The pattern dimensions are calculated by the dimensions of designed leaf spring, as shown in Figure 4(a). This process requires developing a mold or a pattern as described below.

*2.2. Development of Pattern.* For fabrication of composite spring, the composition of fibers and matrix should be used. For this paper E-glass fiber and epoxy (as well as other types of fibers and matrices) as a composite matrix are used. The constant cross-section is selected for design due to its capability of mass production and accommodating continuous reinforcement of fibers and also it is quite suitable for hand lay-up technique. Some methods of fabrication are as follows [16]:

- (1) pultrusion;
- (2) resin transfer molding (RTM);
- (3) vacuum assisted resin transfer molding (VARTM);
- (4) hand lay-up-open molding process;
- (5) compression molding;
- (6) filament winding.

The leaf spring is going to be fabricated by hand lay-up method [16–18]. Hand lay-up method is adopted for fabrication due to its advantages over the others. Tooling cost is low, no skilled worker is required, large items can be fabricated, it is an easy method compared to others, and so forth.

*Hand Lay-Up Method.* See the following.

*(1) Cutting of Fibers.* For this project the fiber material, for example, E-glass, is taken. This fiber is available in sheet format. This fiber sheet is cut by composite scissor.

*(2) Preparation of Composite Matrix (Epoxy/Short Fibers).* In preparation of matrix we used two solutions named resin and hardener. After preparation of epoxy matrix, the composite matrix is fabricated constituting one type of short fibers selected in the paper. The composite matrix composed of short fibers and a polymeric matrix can be prepared after the completion of the epoxy matrix by the method of “fiberglass spray lay-up process”: fiberglass spray lay-up process is very different from the hand lay-up process. The difference comes from the application of the fibre and resin material to the mold. Spray-up is an open-molding composites fabrication process where resin and reinforcements are sprayed onto a reusable mold. The resin and glass may be applied separately or simultaneously “chopped” in a combined stream from a chopper gun. Workers roll out the spray-up to compact the laminate. The part is then cured, cooled, and removed from the mold.

**2.3. Fabrication.** First take the wood pattern (Figure 4(a)), on which keep plastic bagging first as per the dimensions available. On the bagging keep peel ply of the same dimension. The bagging is required to leak proof fabrication or the resin should not be in contact with the pattern. Resin is sticky in nature and hence the contact with pattern should be avoided. Peel ply is required for the finishing of the required component. Now, keep the first sheet of fiber and apply the composite matrix over the first fiber sheet. Apply composite matrix such that all air should be removed. Now, keep the second lamina over the applied matrix and again apply matrix as discussed above. Continue this process till the last fiber sheet. The produced leaf spring is as shown in Figure 4(b).

### 3. Theory and Mathematical Formulation of Leaf Spring

A spring is defined as an elastic body, whose function is to distort when loaded and to recover its original shape when the load is removed (Figure 2). Leaf springs absorb vehicle vibrations, shocks, and bump loads (induced due to road irregularities) by means of spring deflections, so that the potential energy is stored in the leaf spring and then relieved slowly [1]. Ability to store and absorb more amount of strain energy ensures the comfortable suspension system. Semielliptic leaf springs are almost universally used for suspension in light and heavy commercial vehicles. For cars also, these are widely used in rear suspension. The spring consists of a number of leaves called blades. The blades are varying in length. The blades are usually given an initial curvature or cambered so that they will tend to straighten under the load (Figure 1). The leaf spring is based upon the theory of a beam of uniform strength. The lengthiest blade has eyes on its ends. This blade is called main or master leaf; the remaining blades are called graduated leaves. All the blades are bound together by means of steel straps (Figure 4). The spring is mounted on the axle of the vehicle. The entire vehicle load rests on the leaf spring. The front end of the spring is connected to the frame with a simple pin joint, while the rear end of the spring is connected with a shackle. Shackle is the flexible link which connects leaf spring rear eye and frame. When the vehicle comes across a projection on the road surface, the wheel moves up, leading to deflection of the spring. This changes the length between the spring eyes. If both the ends are fixed, the spring will not be able to accommodate this change of length. So, to accommodate this change in length, shackle is provided at one end, which gives a flexible connection. The front eye of the leaf spring is constrained in all the directions, whereas rear eye is not constrained in  $x$ -direction. This rear eye is connected to the shackle. During loading the spring deflects and moves in the direction perpendicular to the load applied. When the leaf spring deflects, the upper side of each leaf tip slides or rubs against the lower side of the leaf above it. This produces some damping reducing spring vibrations, but this type of damping may change with time, so it is preferred not to be depended on. Moreover, it produces squeaking sound. Further if moisture is also present, such interleaf friction will

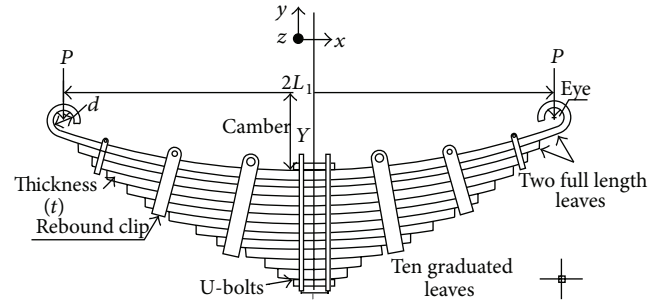


FIGURE 1: Typical leaf spring structure showing symmetry about central U-bolt.

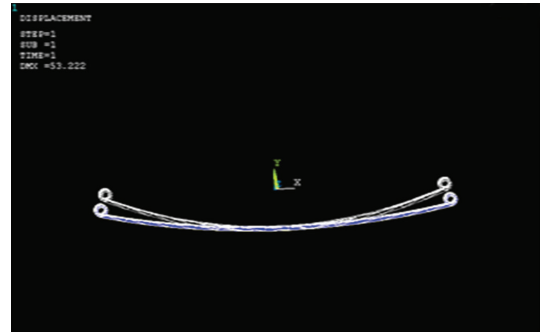


FIGURE 2: Geometry of leaf spring in ANSYS before and after deflection.

cause fretting corrosion which decreases the fatigue strength of the spring; phosphate paint may reduce this problem fairly. The elements of leaf spring are shown in Figure 1, where  $t$  is the thickness of the plate,  $b$  is the width of the plate, and  $2L$  is the length of plate or distance of the load  $W$  from the cantilever end. A single leaf spring blade can be treated as a cantilever beam with a concentrated load at its free end [1, 4, 14]. A half of it is considered for the purpose of analysis and computation (Figures 3 through 5) [14, 19].

Let  $t$  be thickness of plate (spring leaf),  $b$  width of plate, and  $L$  length of plate or distance of the load  $W$  from the cantilever end.

It is known that the maximum deflection for a cantilever with concentrated load at free end is given by

$$\delta_{\max} = \frac{W \cdot L^3}{3 \cdot E \cdot I}, \quad (2)$$

and the maximum bending stress induced in terms of modulus of elasticity and maximum deflection can be found as [1, 2, 19]

$$\sigma_{\text{bending}} = \frac{3 \cdot E \cdot \delta_{\max} \cdot t}{2L^2}, \quad (3)$$

where  $\delta_{\max}$  is maximum deflection in (m).  $W$  is applied load on the cantilever end in (N).  $L$  is distance from the cantilever end to the central bolt (in meters).  $E$  is modulus of elasticity ( $\text{N/m}^2$ ).  $t$  is leaf spring plate thickness (m).

For composite materials, the modulus of elasticity ( $E$ ) mentioned in (2) and (3) is taken as the longitudinal modulus

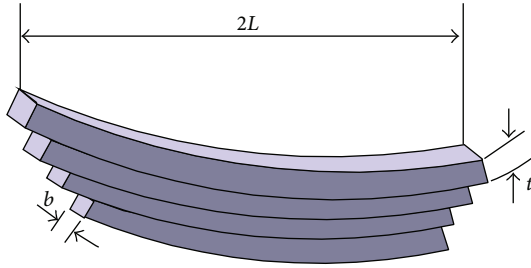


FIGURE 3: Elements of leaf spring.



(a)



(b)

FIGURE 4: (a) Configuration of the pattern. (b) A monocomposite leaf spring.

of elasticity, which is the one being in the direction of fibers. The model of this paper is constructed such that its matrix is made up from short fibers and a pure matrix to form a composite matrix. Long fibers are then used to reinforce the composite matrix constituting a hybrid composite material. Thus (3) can be rewritten as follows to match with composite materials considerations:

$$\delta_{\max} = \frac{W \cdot L^3}{3 \cdot E_1 \cdot I}, \quad (4)$$

$$\sigma_x = \frac{3 \cdot E_1 \cdot \delta_{\max} \cdot t}{2L^2}.$$

The bending stress is in the  $x$ -direction because the reinforcing longitudinal fibers are laid along the longitudinal direction of spring plate. The model of interest is drawn and built in AutoCAD Mechanical v-2010 and then analyzed in ANSYS-14, as shown in Figures 2 and 5, with the following dimensions which are either exactly or approximately commonly adopted for such an application [20].

- (1) Plate width = 200 mm.
- (2) Plate thickness = 40 mm.

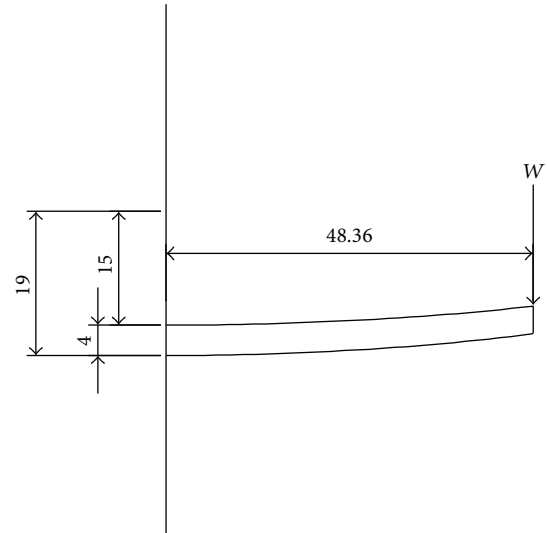


FIGURE 5: A half of an elliptic monoleaf spring.

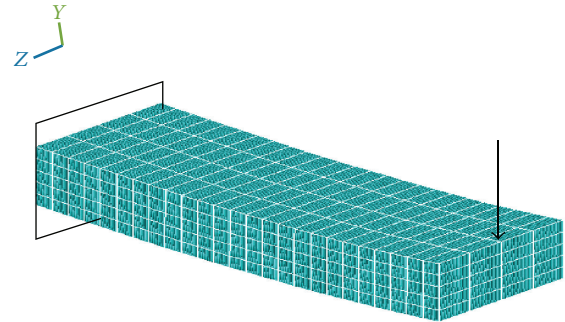


FIGURE 6: Meshing and boundary conditions of the ANSYS model.

- (3) Total length of leaf spring = 0.966 m.
- (4) Camber = 150 mm.

The applied load on the leaf spring of interest equals the automobile total weight which is about 3000 Kgs with 5 passengers of about 100 Kgs each; therefore

$$W_{\text{total}} = 3000 + 5 * 100 * 9.81 = 34335 \text{ N let it be } 35000 \text{ N.} \quad (5)$$

Each tire shares a load of  $35000/4 = 8750 \text{ N}$ . Thus a load of this magnitude will be considered for the leaf spring as the applied load (Figure 5). The single leaf is first modeled in AutoCAD Mechanical 2010 as two concentric ellipses as shown in Figure 5. Afterwards, the configuration is moved to ANSYS-14 by generating key points extracted from the AutoCAD file and then mapped-meshed according to the element type of eight-node 3D brick element (SOLID-185 3D 8-Node Structural Solid). Boundary conditions are then imposed for an applied bending load at the free end of 8750 N with locking all degrees of freedom of the cutting plane zone at the middle of leaf spring due to its symmetry (Figures 5 and 6).

Equations (2) and (4) will be considered for the analytical calculations of deflection and bending stresses for the purpose of results verification and comparison with numerical findings obtained from the software ANSYS.

#### 4. Assumptions

The following assumptions are adopted for both of the fibers and matrix while a static bending analysis of a hybrid fiber-reinforced composite leaf spring is made assuming the following [21].

- (1) The longitudinal stress in the fiber varies linearly across its width while the transverse stress is uniform across the fiber.
- (2) Perfect bonding between fibers and matrix is assumed to exist.
- (3) Fibers and matrix are assumed to be isotropic, homogeneous, and linearly elastic.
- (4) No voids, inclusions, impurities, or manufacturing defects and deficiencies are assumed to be involved in spring material.
- (5) The composite material is considered homogeneous on macroscopic level.
- (6) The loads are assumed to be applied at the infinity (for the sake of the problem of contact stresses and the Saint Venant principle to be turned away).
- (7) Initially stress-free
- (8) The composite material is transversely isotropic [21].
- (9) The short fibers are randomly and homogeneously distributed throughout matrix material constituting the composite matrix such that it exhibits isotropic behavior [22].

### 5. Mathematical Formulation of Hybrid Composite Material

#### 5.1. Composite Lamina Composed of Composite Matrix and Reinforcement Continuous Fiber

5.1.1. *Composite Matrix (Combination of Resin and Discontinuous Fiber)*. For unidirectional fiber-reinforced matrix shown in Figure 7, the following Halpin-Tsai relations are used to determine the elastic properties [22, 23]:

$$E_{1m} = \frac{1 + 2 \cdot a_f \cdot \eta_l \cdot \nabla_{sfm}}{1 - \eta_l \cdot \nabla_{sfm}} \cdot E_m, \quad (6)$$

$$E_{2m} = \frac{1 + 2 \cdot \eta_T \cdot \nabla_{sfm}}{1 - \eta_T \cdot \nabla_{sfm}} \cdot E_m, \quad (7)$$

$$G_{12m} = \frac{1 + \eta_G \cdot \nabla_{sfm}}{1 - \eta_G \cdot \nabla_{sfm}} \cdot G_m, \quad (8)$$

$$\nu_{12m} = \nu_{sf} \cdot \nabla_{sfm} + \nu_m \cdot \nabla_{mm}, \quad (9)$$

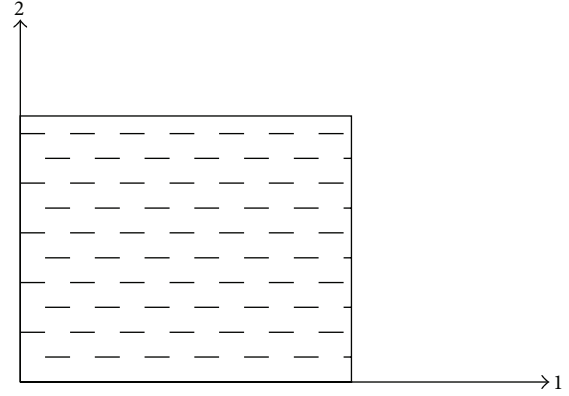


FIGURE 7: Unidirectional discontinuous fiber matrix.

where

$$\eta_l = \frac{E_{sf}/E_m - 1}{E_{sf}/E_m + 2 \cdot a_f}, \quad (10)$$

$$\eta_T = \frac{E_{sf}/E_m - 1}{E_{sf}/E_m + 2}, \quad (11)$$

$$\eta_G = \frac{G_{sf}/G_m - 1}{G_{sf}/G_m + 1}. \quad (12)$$

Let  $E_{1m}$  and  $E_{2m}$  be the longitudinal and transverse moduli defined by (6) and (7) for unidirectional fiber  $0^\circ$  composite matrix of the same fiber aspect ratio and fiber volume fraction as the randomly oriented discontinuous fiber matrix shown in Figure 8. Since the fiber is randomly oriented, the matrix exhibits isotropic behavior. The Young and shear moduli of such a composite matrix are given by [22]

$$E_{cm} = \frac{3}{8} \cdot E_{1m} + \frac{5}{8} \cdot E_{2m}, \quad (13)$$

$$G_{cm} = \frac{1}{8} \cdot E_{1m} + \frac{1}{4} \cdot E_{2m}. \quad (14)$$

Or they can be rewritten as

$$G_{cm} = \frac{E_{cm}}{2(1 + \nu_{cm})} \quad (15)$$

or

$$\nu_{cm} = \left( \frac{E_{cm}}{2 \cdot G_{cm}} - 1 \right). \quad (16)$$

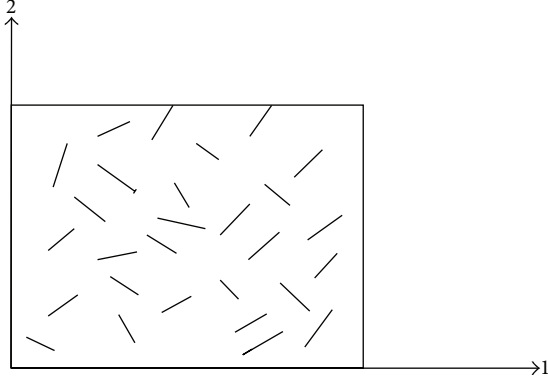


FIGURE 8: Randomly oriented discontinuous fiber-reinforced matrix.

The fractions  $\forall_{sfm}$  and  $\forall_{mm}$  are considered to be matrix; then

$$\forall_{sfm} + \forall_{mm} = 1, \quad (17)$$

$$\forall_{sfm} + \forall_{mp} + \forall_f = 1, \quad (18)$$

$$\forall_m + \forall_f = 1, \quad \text{for } \forall_{sfp} + \forall_{mp} = \forall_m, \quad (19)$$

$$\forall_{sfm} = \frac{(\forall_{sfp})}{(\forall_{sfp} + \forall_{mp})} = \frac{(\forall_{sfp})}{(\forall_m)}, \quad (20)$$

$$\forall_{mm} = \frac{\forall_{mp}}{\forall_{sfp} + \forall_{mp}} = \frac{\forall_{mp}}{\forall_m}. \quad (21)$$

Then, using (21) in (6) through (10) results in

$$E_{1m} = \frac{1 + 2 \cdot a_f \cdot \eta_l \cdot (\forall_{sfm}/\forall_m)}{1 - \eta_l \cdot (\forall_{sfm}/\forall_m)} \cdot E_m, \quad (22)$$

$$E_{2m} = \frac{1 + 2 \cdot \eta_T \cdot (\forall_{sfp}/\forall_m)}{1 - \eta_T \cdot (\forall_{sfp}/\forall_m)} \cdot E_m, \quad (23)$$

$$G_{12m} = \frac{1 + \eta_G \cdot (\forall_{sfp}/\forall_m)}{1 - \eta_G \cdot (\forall_{sfp}/\forall_m)} \cdot G_m, \quad (24)$$

$$\nu_{12m} = \nu_{sf} \cdot \frac{\forall_{sfp}}{\forall_m} + \nu_m \frac{\forall_{mp}}{\forall_m}, \quad (25)$$

where  $\eta_l$ ,  $\eta_T$ , and  $\eta_G$  are as defined in (10) through (12).

Then, by substitution of (22) and (23) into (13), (14), and (16), one gets

$$\begin{aligned} E_{cm} &= \left[ \left( \frac{3 \cdot (1 - \forall_f) + 6 \cdot a_f \cdot \eta_l \cdot \forall_{sfp}}{(1 - \forall_f) - \eta_l \cdot \forall_{sfp}} \right) \right. \\ &\quad \left. + \left( \frac{5 \cdot (1 - \forall_f) + 10 \cdot \eta_T \cdot \forall_{sfp}}{(1 - \forall_f) - \eta_T \cdot \forall_{sfp}} \right) \right] \cdot \frac{E_m}{8}, \\ G_{cm} &= \left[ \left( \frac{(1 - \forall_f) + 2 \cdot a_f \cdot \eta_l \cdot \forall_{sfp}}{(1 - \forall_f) - \eta_l \cdot \forall_{sfp}} \right) \right. \\ &\quad \left. + \left( \frac{2 \cdot (1 - \forall_f) + 4 \cdot \eta_T \cdot \forall_{sfp}}{(1 - \forall_f) - \eta_T \cdot \forall_{sfp}} \right) \right] \cdot \frac{E_m}{8}, \\ \nu_{cm} &= \left( \frac{E_{cm}}{2 \cdot G_{cm}} - 1 \right), \end{aligned} \quad (26)$$

where  $E_{cm}$  and  $G_{cm}$  are as defined above.

There are in all quantities  $E_{cm}$ ,  $G_{cm}$ , and  $\nu_{cm}$  to describe the elastic behavior of the composite matrix combination of discontinuous randomly oriented fibers and resin bonding material.

**5.2. Hybrid Composite Lamina (Discontinuous Random Short Fiber, Resin, and Continuous Fiber).** Figure 8 shows a simple schematic model of a composite lamina consisting of discontinuous random fiber, resin, and continuous fiber. The fibers are assumed to be uniformly distributed throughout the composite matrix, composed of discontinuous random short fiber and resin material. A perfect bonding is assumed to be free of any voids. The fibers and the matrix are both assumed to be linear and elastic. The elastic analysis of such a lamina will be as follows [21]:

$$\varepsilon_f = \mathcal{E}_{cm} + \mathcal{E}_c, \quad (27)$$

$$\sigma_f = E_f \cdot \mathcal{E}_f = E_f \cdot \mathcal{E}_c, \quad (28)$$

$$\sigma_m = E_{cm} \cdot \mathcal{E}_{cm} = E_{cm} \cdot \mathcal{E}_c, \quad (29)$$

$$P = P_f + P_{cm}, \quad (30)$$

$$\sigma_c A_c = \sigma_f \cdot A_f + \sigma_m \cdot A_m, \quad (31)$$

$$\sigma_c = \frac{1}{A_c} (\sigma_f \cdot A_f + \sigma_m \cdot A_m) = \sigma_f \cdot \forall_f + \sigma_m \cdot \forall_m, \quad (32)$$

$$\forall_f = \frac{A_f}{A_c}, \quad \forall_m = \forall_{sfp} + \forall_{mp} = (1 - \forall_f) = \frac{A_m}{A_c}. \quad (33)$$

Then, the longitudinal modulus of the lamina is given by

$$E_1 = \frac{\sigma_c}{\mathcal{E}_c} = E_f \cdot \forall_f + E_{cm} \cdot (1 - \forall_f). \quad (34)$$

By using (21) in (27) one gets

$$E_1 = E_f \cdot \forall_f + (1 - \forall_f) \left[ \frac{3}{8} E_{1m} + \frac{5}{8} E_{2m} \right] \quad (35)$$

or

$$E_1 = E_f \cdot V_f + (1 - V_f) \cdot E_m \times \left[ \left( \frac{3 \cdot (1 - V_f) + 6 \cdot a_f \cdot \eta_l \cdot V_{sfp}}{8(1 - V_f) - 8\eta_l \cdot V_{sfp}} \right) + \left( \frac{5 \cdot (1 - V_f) + 10 \cdot \eta_T \cdot V_{sfp}}{8(1 - V_f) - 8\eta_T \cdot V_{sfp}} \right) \right]. \quad (36)$$

The corresponding major Poisson ratio is

$$v_{12} = v_f \cdot V_f + v_{cm} (1 - V_f). \quad (37)$$

Using (26) and (13) in (37) results in

$$v_{12} = v_f \cdot V_f + \left( \frac{E_{cm}}{2 \cdot G_{cm}} - 1 \right) (1 - V_f). \quad (38)$$

The transverse modulus and minor Poisson's ratio for the loading transverse to the continuous fiber direction as shown in Figures 9(a) and 9(b) are

$$E_2 = \frac{E_f \cdot E_{cm}}{E_f (1 - V_f) + E_{cm} \cdot V_f} \quad \text{or}$$

$$E_2 = E_f \cdot E_{cm} \left[ \left( \frac{3 \cdot (1 - V_f) + 6 \cdot a_f \cdot \eta_l \cdot V_{sfp}}{8(1 - V_f) - 8\eta_l \cdot V_{sfp}} \right) + \left( \frac{5 \cdot (1 - V_f) + 10 \cdot \eta_T \cdot V_{sfp}}{8(1 - V_f) - 8\eta_T \cdot V_{sfp}} \right) \right] \times \left( E_f (1 - V_f) + E_{cm} \cdot V_f \right) \times \left[ \left( \frac{3 \cdot (1 - V_f) + 6 \cdot a_f \cdot \eta_l \cdot V_{sfp}}{8(1 - V_f) - 8\eta_l \cdot V_{sfp}} \right) + \left( \frac{5 \cdot (1 - V_f) + 10 \cdot \eta_T \cdot V_{sfp}}{8(1 - V_f) - 8\eta_T \cdot V_{sfp}} \right) \right]^{-1}, \quad (39)$$

$$v_{21} = \frac{E_2}{E_1} v_{12}, \quad (40)$$

where  $E_1$ ,  $E_2$ , and  $v_{12}$  are as in (36), (38), and (39).

For a shear force loading as shown in Figures 9(a) and 9(b),

$$G_{12} = \frac{G_f \cdot G_{cm}}{G_f \cdot V_m + G_{cm} \cdot V_f} = \frac{G_f \cdot G_{cm}}{G_f (1 - V_f) + G_{cm} \cdot V_f}. \quad (41)$$

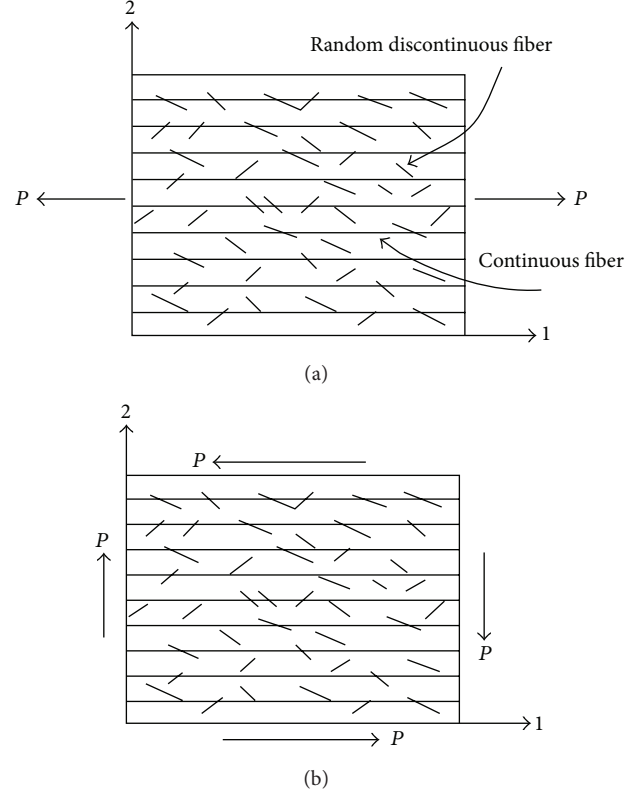


FIGURE 9: Unidirectional continuous fiber ( $0^\circ$ ) lamina.

Substitution of (26) into (41) leads to

$$G_{12} = G_f \cdot E_m \cdot \left[ \left( \frac{(1 - V_f) + 2 \cdot a_f \cdot \eta_l \cdot V_{sfp}}{(1 - V_f) - \eta_l \cdot V_{sfp}} \right) + \left( \frac{2 \cdot (1 - V_f) + 4 \cdot \eta_T \cdot V_{sfp}}{(1 - V_f) - \eta_T \cdot V_{sfp}} \right) \right] \times \left( 8 \cdot G_f \cdot (1 - V_f) + E_m \cdot V_f \left[ \left( \frac{(1 - V_f) + 2 \cdot a_f \cdot \eta_l \cdot V_{sfp}}{(1 - V_f) - \eta_l \cdot V_{sfp}} \right) + \left( \frac{2 \cdot (1 - V_f) + 4 \cdot \eta_T \cdot V_{sfp}}{(1 - V_f) - \eta_T \cdot V_{sfp}} \right) \right] \right)^{-1}. \quad (42)$$

There are in all quantities  $E_1$ ,  $E_2$ ,  $G_{12}$ , and  $v_{12}$  to describe the elastic behavior of a hybrid lamina composed of composite matrix and continuous reinforcement fibers.

Some of the effective elastic properties of the hybrid composite materials considered in this work based on the analysis above are tabulated in Table 1.

TABLE 1: Some of the elastic properties of some hybrid composites considered.

Number	Hybrid composite	$E_1$ (N/m <sup>2</sup> )	$E_2 = E_3$ (N/m <sup>2</sup> )	$\nu_{21} = \nu_{31}$	$\nu_{23} = \nu_{32}$	$G_{12} = G_{13}$ (N/m <sup>2</sup> )	$G_{23} = G_{32}$ (N/m <sup>2</sup> )
1	K49-epoxy1	5.37E + 10	9.89E + 09	7.20E - 02	5.95E - 01	2.41E + 09	3.10E + 09
2	K49-epoxy2	5.64E + 10	1.69E + 10	1.21E - 01	5.95E - 01	3.39E + 09	5.31E + 09
3	K49-epoxy3	5.94E + 10	2.40E + 10	1.65E - 01	5.78E - 01	4.07E + 09	7.60E + 09
4	K49-epoxy4	6.24E + 10	3.11E + 10	2.05E - 01	5.57E - 01	4.59E + 09	9.98E + 09
5	Boron-epoxy1	1.59E + 11	1.98E + 10	5.15E - 02	6.65E - 01	6.79E + 09	5.96E + 09
6	Boron-epoxy2	1.66E + 11	3.74E + 10	9.53E - 02	6.60E - 01	1.28E + 10	1.13E + 10
7	Boron-epoxy3	1.73E + 11	5.56E + 10	1.37E - 01	6.39E - 01	1.90E + 10	1.70E + 10
8	Boron-epoxy4	1.81E + 11	7.45E + 10	1.76E - 01	6.14E - 01	2.55E + 10	2.31E + 10
9	E-glass-epoxy1	3.54E + 10	7.68E + 09	7.12E - 02	4.54E - 01	2.71E + 09	2.64E + 09
10	E-glass-epoxy2	3.74E + 10	1.25E + 10	1.14E - 01	4.60E - 01	4.37E + 09	4.29E + 09
11	E-glass-epoxy3	3.94E + 10	1.73E + 10	1.53E - 01	4.52E - 01	6.04E + 09	5.97E + 09
12	E-glass-epoxy4	4.15E + 10	2.22E + 10	1.88E - 01	4.40E - 01	7.74E + 09	7.71E + 09

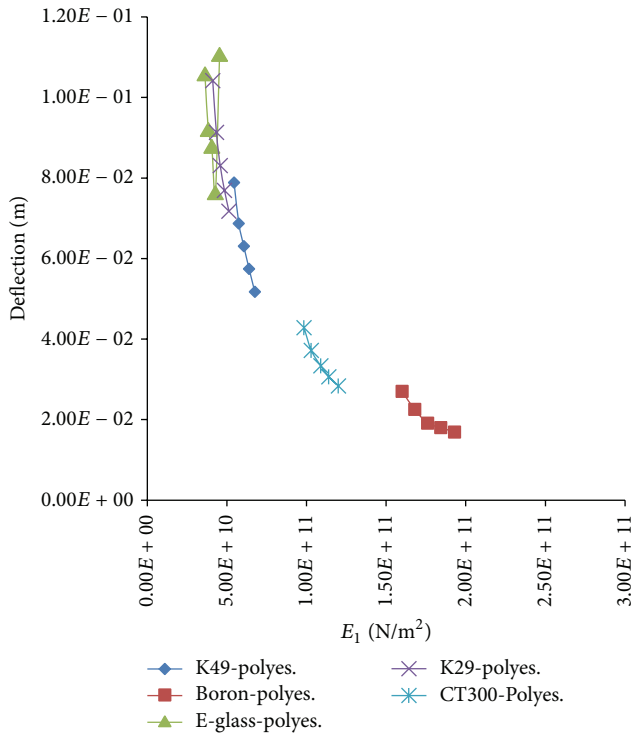


FIGURE 10: Effect of longitudinal modulus of elasticity on leaf spring deflection of various composite leaf springs based on matrix type.

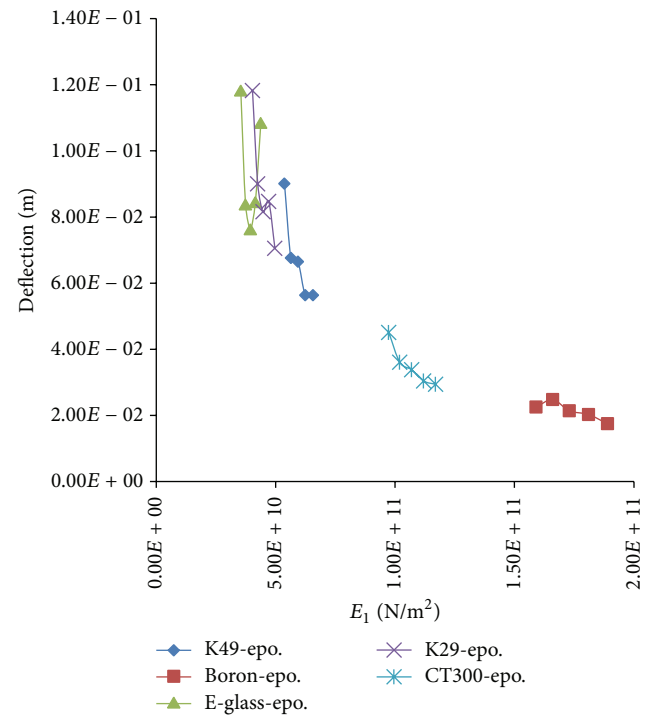


FIGURE 11: Effect of longitudinal modulus of elasticity on leaf spring deflection of various composite leaf springs based on matrix type.

## 6. Results and Discussion

As it is seen from (4), both maximum deflection and maximum bending stress depend on the longitudinal modulus of elasticity ( $E_1$ ) which itself is affected by the constituents' mixing schemes and their volume fractions. Plotted figures clearly explain the effects of fibers only, matrices only, and fiber volume fractions, each of which on the leaf spring responses. For the deflection, it is more highly affected by fibers type than matrix type. Figures 10 through 12 show the effect of matrix variation with the same group of fibers; they all exhibit the same behavior against load application

except that for E-glass group as it irregularly behaves for all of its collections with different matrices; therefore it may be suggested to make use of the other four types of fibers in case of selecting them as constituents in hybrid fiber-reinforced composite leaf springs. It can also be clearly seen that the more the higher longitudinal modulus of elasticity of a fiber is, the more the lower deflection of a spring is.

A more accurate indication can be obtained when Figures 13, 14, 15, 16, and 17 are examined to explore the predominant effect of fibers on leaf springs performance such that the irregular behavior of E-glass appears more clearly in Figure 14 with two matrices (epoxy and polyester) except

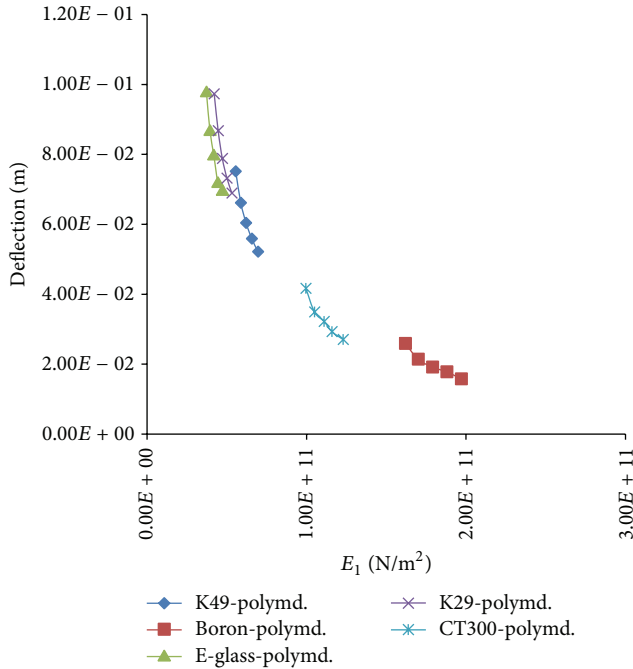


FIGURE 12: Effect of longitudinal modulus of elasticity on leaf spring deflection of various composite leaf springs based on matrix type.

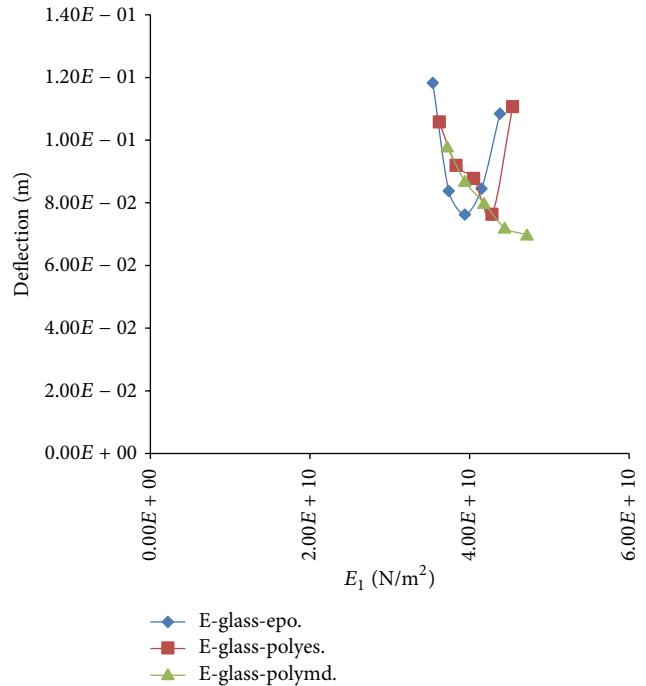


FIGURE 14: Effect of longitudinal modulus of elasticity on leaf spring deflection of various composite leaf springs based on fiber type.

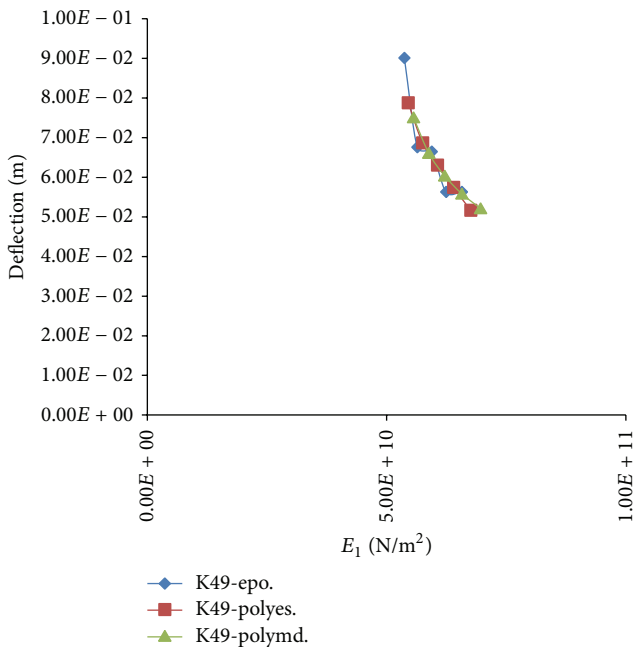


FIGURE 13: Effect of longitudinal modulus of elasticity on leaf spring deflection of various composite leaf springs based on fiber type.

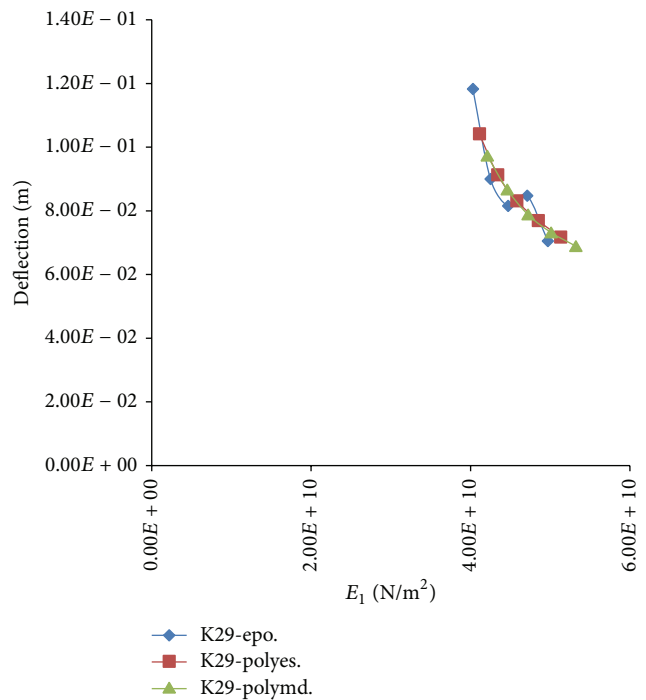


FIGURE 15: Effect of longitudinal modulus of elasticity on leaf spring deflection of various composite leaf springs based on fiber type.

with polyamide, but this is not the case when E-glass is introduced in simple traditional fiber-reinforced composite materials [24, 25]; this may be due to hybridization effect with respect to E-glass particularly, consolidating what has already been mentioned in Figures 10 and 11. Other fibers maintain uniform behavior analytically and numerically

with all matrices. The predominance of fibers effect can be attributed to mainly their high modulus of elasticity affecting the macroscopic flexural and bending stiffness of the hybrid composite structure as a whole. Bending stresses are investigated under the same conditions as of the deflections. Figures 18 and 19 show the variation of bending stresses induced in

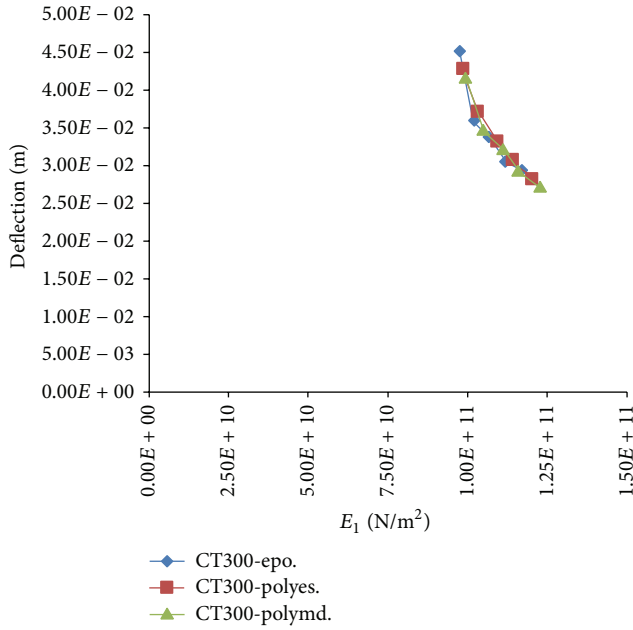


FIGURE 16: Effect of longitudinal modulus of elasticity on leaf spring deflection of various composite leaf springs based on fiber type.

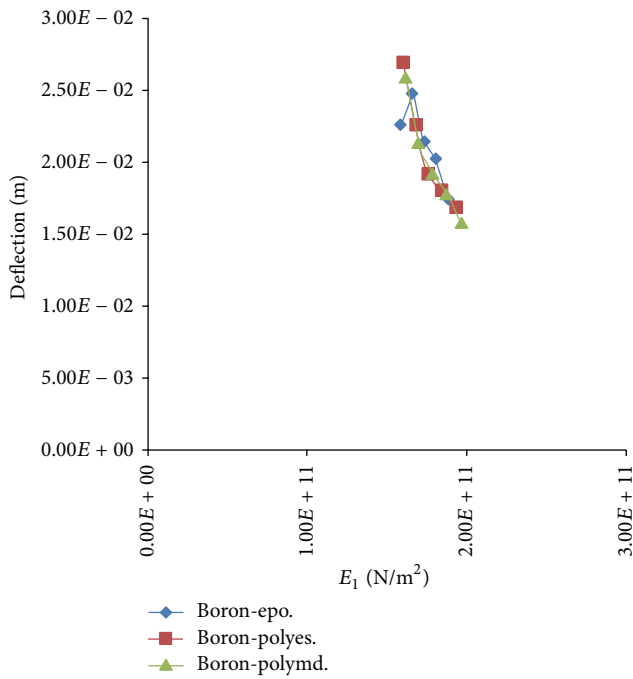


FIGURE 17: Effect of longitudinal modulus of elasticity on leaf spring deflection of various composite leaf springs based on fiber type.

the structure according to fiber variation with the same matrix. An inverse proportionality is displayed between the increase of longitudinal modulus of elasticity of the hybrid composite structure (which is highly affected by the fiber type) and the magnitude of the bending stresses induced, since the bending stiffness of the structure ( $E_1I$ ) increases with increase of  $E_1$ , expressing the maximization of

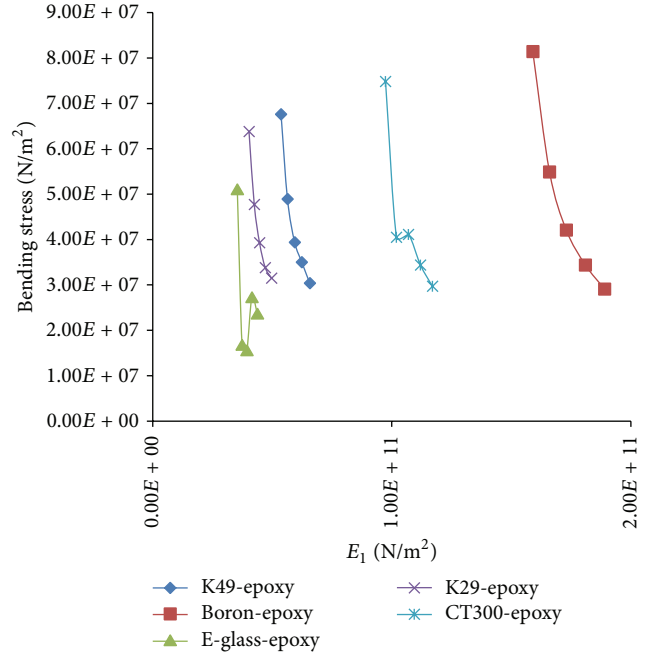


FIGURE 18: Effect of longitudinal modulus of elasticity on bending stresses of various composite leaf springs based on matrix type.

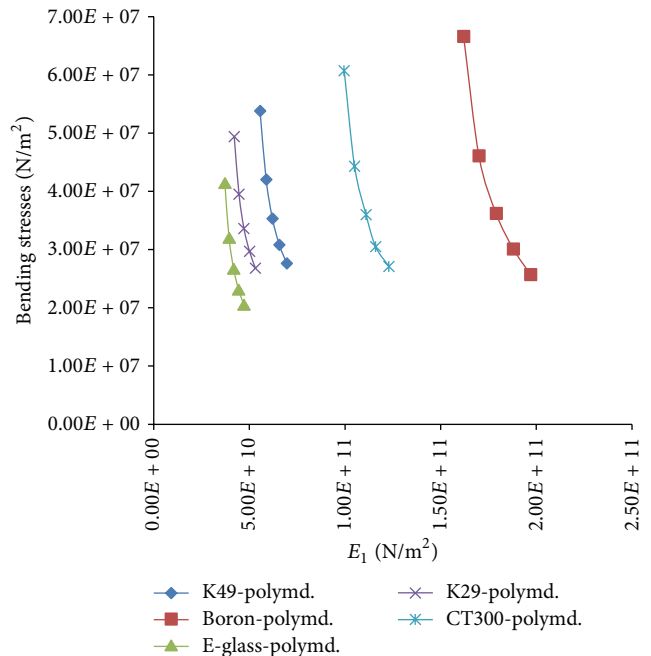


FIGURE 19: Effect of longitudinal modulus of elasticity on bending stresses of various composite leaf springs based on matrix type.

the bending strength of the structure. All of the hybrid composites collections reveal the same overall behavior numerically and analytically for both deflections and bending stresses values. As the fiber volume fraction increases the conformity between the results increases up to 94% as it is clearly noticed through Figures 20 and 21, referring to the validity of the results.

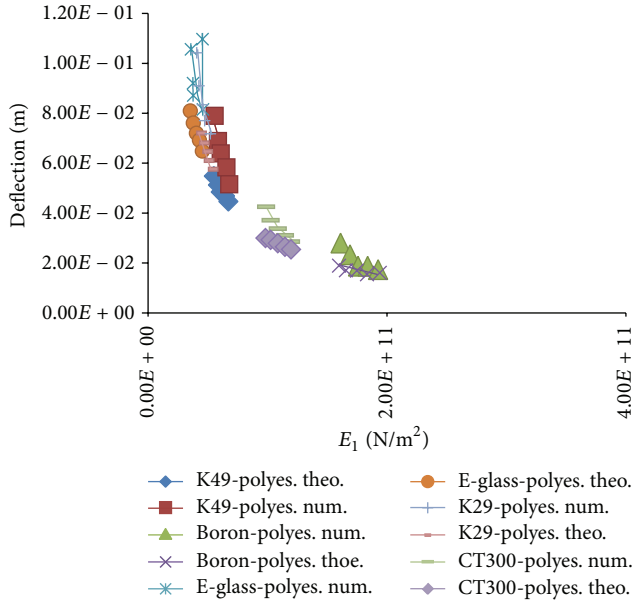


FIGURE 20: Comparison of numerical and theoretical results of effect of  $E_1$  on spring deflection based on fibers variation with polyester.

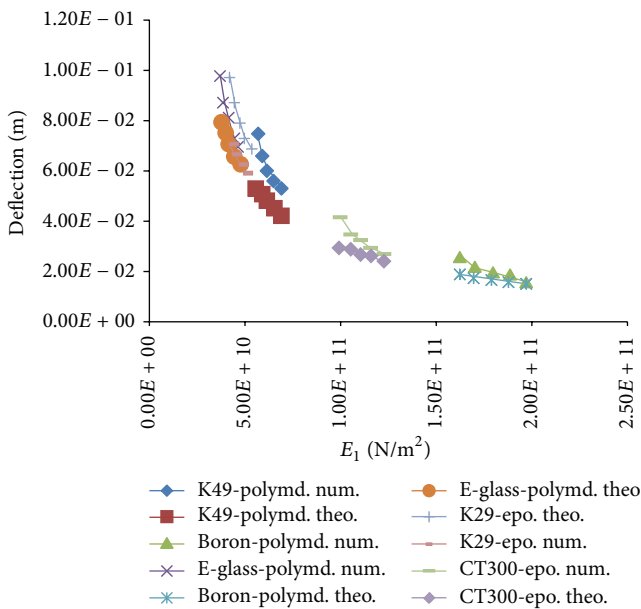


FIGURE 21: Comparison of numerical and theoretical results of effect of  $E_1$  on spring deflection based on fibers variation with polyamide.

### 7. Verification of the Results

A comparison has been made among the numerical results obtained from the FEA made by the ANSYS software and their corresponding theoretical counterparts as a means of proving the validity and authenticity of the manipulation and solution of the problem. Referring to (4), there is an inverse proportionality between  $E_1$  and the deflection of the hybrid leaf spring and it is seen from Figures 20 and 21 that the nature of variation of deflection is identical and

the ratio of conformity is ranging from 63% at low fiber volume fraction of 6% of short fibers constituting the composite matrix of K49/epoxy up to 99% at a fiber volume fraction of 18% of short fibers constituting the composite matrix of E-glass/epoxy. But as a general case a ratio of more than 80% is obtained between both results. Figures 20 and 21 graphically show in detail the convergence of various comparisons for various hybrid composites.

### 8. Conclusions

From the above discussion, the following conclusions can be made.

- (1) Fibers are the most predominant and controlling element on the bending stiffness of the structure.
- (2) For heavier trucks, hybrid composite springs of higher longitudinal moduli of elasticity fibers should be adopted instead of using multilayer softer ones for the sake of
  - (a) total weight reduction of a truck;
  - (b) easiness and quickness of fabrication, manufacturing, and maintenance;
  - (c) economy of maintenance.
- (3) E-glass fiber in the hybrid composites does not exhibit a regular behavior making it difficult to accurately predict hybrid composite spring performance, response, and stresses, while boron is the opposite; thus it is advisable to adopt it in such applications with various matrices.

### Nomenclature

- $E_{1m}$ : Longitudinal moduli for a unidirectional discontinuous fiber  $0^\circ$  composite matrix, composed of resin and discontinuous fiber
- $E_{2m}$ : Transverse moduli for a unidirectional discontinuous fiber  $0^\circ$  composite matrix, composed of resin and discontinuous fiber
- $E_{cm}$ : Moduli of isotropic composite matrix, composed of resin and random discontinuous fiber
- $E_1$ : Longitudinal modulus for unidirectional continuous fiber  $0^\circ$  composite lamina, composed of composite matrix and continuous fiber
- $E_2$ : Transverse modulus for unidirectional continuous fiber  $0^\circ$  composite lamina, composed of composite matrix and continuous fiber
- $E_{sf}$ : Moduli of discontinuous fiber material
- $E_f$ : Moduli of continuous fiber material
- $E_m$ : Moduli of resin material
- $G_{12m}$ : Shear modulus for a unidirectional discontinuous fiber  $0^\circ$  composite matrix

$G_{cm}$ : Shear modulus of isotropic composite matrix  
 $G_{12}$ : Shear modulus for a unidirectional continuous fiber  $0^\circ$  composite lamina  
 $G_{sf}$ : Shear modulus of discontinuous fiber material  
 $G_f$ : Shear modulus of continuous fiber material  
 $G_m$ : Shear of resin material  
 $\nu_{12m}$ : The major Poisson ratio for a unidirectional discontinuous fiber  $0^\circ$  composite matrix  
 $\nu_{cm}$ : Poisson's ratio of isotropic composite matrix  
 $\nu_{12}$ : The major Poisson ratio for a unidirectional continuous fiber  $0^\circ$  composite lamina  
 $\nu_{sf}$ : Poisson's ratio for discontinuous fiber material  
 $\nu_f$ : Poisson's ratio for continuous fiber  
 $\nu_m$ : Poisson's ratio for resin material  
 $V_{sfp}$ : Volume fraction of discontinuous fiber, ratio of the volume of discontinuous fiber to the volume of composite lamina  
 $V_{mm}$ : Volume fraction of resin matrix, ratio of the volume of resin to the volume of composite matrix  
 $V_{mp}$ : Volume fraction of resin matrix, ratio of the volume of resin to the volume of composite lamina  
 $V_f$ : Volume fraction of continuous fiber, ratio of the volume of continuous fiber to the volume of composite lamina  
 $V_m$ : Volume fraction of matrix, ratio of the volume of composite matrix to the volume of composite lamina  
 $a_f$ : The ratio of average fiber length to fiber diameter =  $l_f/d_f$ , which is taken to be 500 for the purpose of elastic properties calculations of hybrid composite matrix and material [26]  
 $d_f$ : Fiber diameter  
 $l_f$ : Average fiber length.

### Conflict of Interests

The author declares that there is no conflict of interests regarding the publication of this paper.

### References

- [1] G. H. Gowd and E. V. Goud, "Static analysis of leaf spring," *International Journal of Engineering Science and Technology*, vol. 4, no. 8, 2012.
- [2] D. Ashok, M. V. Mallikarjun, and V. R. Mamilla, "Design and structural analysis of composite multi leaf spring," *International Journal of Emerging trends in Engineering and Development*, vol. 5, no. 2, 2012, [http://www.rpublication.com/ijeted/ijeted\\_index.htm](http://www.rpublication.com/ijeted/ijeted_index.htm).
- [3] I. Rajendran and S. Vijayarangan, "Optimal design of a composite leaf spring using genetic algorithms," *Computers and Structures*, vol. 79, no. 11, pp. 1121–1129, 2001.
- [4] K. K. Jadhao and R. S. Dalu, "Experimental investigation & numerical analysis of composite leaf spring," *International Journal of Engineering Science and Technology*, vol. 3, no. 6, pp. 4759–4764, 2011.
- [5] M. Raghavedra, S. A. Hussain, V. Pandurangadu, and K. PalaniKumar, "Modeling and analysis of laminated composite leaf spring under the static load condition by using FEA," *International Journal of Modern Engineering Research (IJMER)*, vol. 2, no. 4, pp. 1875–1879, 2012.
- [6] Y. N. V. Santhosh Kumar and M. Vimal Teja, "Design and analysis of composite leaf spring in light vehicle," *International Journal of Mechanical and Industrial Engineering*, vol. 2, no. 1, pp. 213–218, 2012.
- [7] S. Kumar and S. Vijayarangan, "Analytical and experimental studies on fatigue life prediction of steel and composite multi-leaf spring for light passenger vehicles using life data analysis," *Material Science*, vol. 13, no. 2, pp. 141–146, 2007.
- [8] Z. Yang and Z. Wang, "Cyclic creep and cyclic deformation of high-strength spring steels and the evaluation of the sag effect: part I: cyclic plastic deformation behavior," *Metallurgical and Materials Transactions A*, vol. 32, no. 7, pp. 1687–1698, 2001.
- [9] J. J. Fuentes, H. J. Aguilar, J. A. Rodríguez, and E. J. Herrera, "Premature fracture in automobile leaf springs," *Engineering Failure Analysis*, vol. 16, no. 2, pp. 648–655, 2009.
- [10] C. K. Clarke and G. E. Borowski, "Evaluation of a leaf spring failure," *ASM International, Journal of Failure Analysis and Prevention*, vol. 5, no. 6, pp. 54–63, 2005.
- [11] R. M. Mayer, J. P. Hou, J. Y. Cherruault, I. Nairne, and G. Jeronimidis, "Evolution of the eye-end design of a composite leaf spring for heavy axle loads," *Composite Structures*, vol. 64, pp. 351–358, 2007.
- [12] M. M. Patunkar and D. R. Dolas, "Modelling and analysis of composite leaf spring under the static load condition by using FEA," *International Journal of Mechanical & Industrial Engineering*, vol. 1, no. 1, 2011.
- [13] K. Kumar and M. L. Aggarwal, "Computer aided FEA simulation of EN45A parabolic leaf spring," *International Journal of Industrial Engineering Computations*, vol. 4, no. 2, pp. 297–304, 2013.
- [14] G. S. Shiva Shankar and S. Vijayarangan, "Mono composite leaf spring for light weight vehicle—design, end joint analysis and testing," *Materials Science*, vol. 12, no. 3, pp. 220–225, 2006.
- [15] A. C. Baviskar, V. G. Bhamre, and S. S. Sarode, "Design and Analysis of a Leaf Spring for automobile suspension system: a review," *International Journal of Emerging Technology and Advanced Engineering*, vol. 3, no. 6, pp. 407–410, 2013.
- [16] A. A. Satpute and S. S. Chavan, "Mono composite leaf spring—design and testing," *Indian Journal of Applied Research*, vol. 3, no. 7, 2013.
- [17] G. H. Staab, *Laminar Composites*, Butterworth-Heinemann, Woburn, Mass, USA, 1999.
- [18] B. B. Deshmukh and S. B. Jaju, "Design and analysis of glass fiber reinforced polymer (GFRP) leaf spring," in *Proceedings of the 4th International Conference on Emerging Trends in Engineering and Technology (ICETET '11)*, pp. 82–87, November 2011.
- [19] R. B. Charde and D. V. Bhoje, "Investigation of stresses in master leaf of leaf spring by FEM and its experimental verification," *International Journal of Engineering Science and Technology*, vol. 4, no. 2, 2012.

- [20] V. Jadhav Mahesh, B. Zoman Digambar, Y. R. Kharde, and R. R. Kharde, "Performance analysis of two mono leaf spring used for maruti 800 vehicle," *International Journal of Innovative Technology and Exploring Engineering*, vol. 2, no. 1, pp. 65–67, 2012.
- [21] R. M. Jones, *Mechanics of Composite Materials*, Scripta Book, Washington, DC, USA, 1999.
- [22] J. S. Rao, *Dynamic of Plate*, Narosa Publishing House, 1999.
- [23] A. B. Londhe, "FEA and analytical analysis of natural fibers composite leaf spring," *International Journal of Mechanical Engineering and Research*, vol. 3, no. 4, pp. 355–360, 2013.
- [24] M. M. Shokrieh and D. Rezaei, "Analysis and optimization of a composite leaf spring," *Composite Structures*, vol. 60, no. 3, pp. 317–325, 2003.
- [25] U. S. Ramakanth and K. Sowjanya, "Design and analysis of automotive multi-leaf springs using composite materials," *International Journal of Mechanical, Production Engineering Research and Development*, vol. 3, no. 1, pp. 155–162, 2013.
- [26] M. Nanko, "Definitions and categories of hybrid materials," *The AZo Journal of Materials Online*, vol. 6, 2009.

## Research Article

# Conductivity and Dielectric Studies of Lithium Trifluoromethanesulfonate Doped Polyethylene Oxide-Graphene Oxide Blend Based Electrolytes

A. A. Azli,<sup>1</sup> N. S. A. Manan,<sup>2</sup> and M. F. Z. Kadir<sup>3</sup>

<sup>1</sup>Institute of Graduate Studies, University of Malaya, 50603 Kuala Lumpur, Malaysia

<sup>2</sup>Chemistry Department, Faculty of Science, University of Malaya, 50603 Kuala Lumpur, Malaysia

<sup>3</sup>Centre for Foundation Studies in Science, University of Malaya, 50603 Kuala Lumpur, Malaysia

Correspondence should be addressed to M. F. Z. Kadir; [mfzkadir@um.edu.my](mailto:mfzkadir@um.edu.my)

Received 13 November 2014; Accepted 19 December 2014

Academic Editor: Kwangho Kim

Copyright © 2015 A. A. Azli et al. This is an open access article distributed under the Creative Commons Attribution License, which permits unrestricted use, distribution, and reproduction in any medium, provided the original work is properly cited.

Series of polymer blend consisting of polyethylene oxide (PEO) and graphene oxide (GO) as co-host polymer were prepared using solution cast method. The most amorphous PEO-GO blend was obtained using 90 wt.% of PEO and 10 wt.% of GO as recorded by X-ray diffraction (XRD). Fourier transform infrared spectroscopy (FTIR) analysis proved the interaction between PEO, GO, lithium trifluoromethanesulfonate ( $\text{LiCF}_3\text{SO}_3$ ), and ethylene sulfite (ES). Incorporation of 25 wt.%  $\text{LiCF}_3\text{SO}_3$  into the PEO-GO blend increases the conductivity to  $(3.84 \pm 0.83) \times 10^{-6} \text{ S cm}^{-1}$ . The conductivity starts to decrease when more than 25 wt.% salt is doped into the polymer blend. The addition of 1 wt.% ES into the polymer electrolyte has increased the conductivity to  $(1.73 \pm 0.05) \times 10^{-5} \text{ S cm}^{-1}$ . Dielectric studies show that all the electrolytes obey non-Debye behavior.

## 1. Introduction

Polymer electrolytes are an important component of many electrochemical devices such as lithium batteries, capacitors, fuel cells, and solar cells. Armand et al. [1] first proposed the use of polyethylene oxide (PEO) and alkali salts system as solid polymer electrolytes (SPE) for lithium batteries, which immediately spurred an enormous amount of research worldwide. Application of SPE especially in electrochemical devices offers advantages in terms of ease of fabrication as thin-film materials, high reliability without leakage problem of liquid electrolytes, and higher temperatures of operation and miniaturization to ensure high energy density [2]. Despite its advantages, the low ionic conductivity of SPE at room temperature often limits their applications [3].

PEO is a widely used film-forming polymer with high tensile strength and flexibility [4, 5]. PEO also exhibits many other useful properties such as chemical stability, ease of electrolyte fabrication, and excellent complexation with many ionic salts [6, 7]. However, most PEO based polymer

electrolytes have low conductivity due to its semicrystalline polymer nature in which, below the melting temperature of PEO at 330 K, the polymer may consist of both lamellar crystals and amorphous regions, as well as intermediate regions at the crystal/amorphous interphase [8]. Crystalline polymer electrolytes have long been considered as insulators while ionic conductivity is confined exclusively to the amorphous state [9]. The ion migration in SPE is believed to occur predominantly in the amorphous rich phase; thus reducing crystallinity of PEO by blending PEO with other materials as a co-host polymer increases the conductivity of PEO based SPE.

Blend polymer of PEO with carbon materials can be considered as new perspective for electrochemical applications, especially for the storage of energy because the existence of different carbon allotropes (graphite, diamond, and fullerenes/nanotubes), various microtextures (more or less ordered) owing to the degree of graphitization, and a rich variety of dimensionality from 0 to 3D and ability for existence under different forms (from powders to fibres, foams, fabrics, and composites) indicate that carbon is

a very attractive material to explore [10]. Graphene oxide (GO) is a highly oxygenated, hydrophilic layered material derived from graphite oxide resulting from oxidation of graphite by strong oxidising agents. Under the application of external energy, such as from ultrasonic vibration or thermal shock, three-dimensional graphite oxide can be exfoliated into two-dimensional graphite oxide nanosheets of single layer graphite oxide [11, 12]. Graphite oxide nanosheets can be as thin as a one carbon layer and can then be described as GO nanosheets [13]. Reinforcement of nanometer sized materials may enhance most properties of polymer blend if they are well dispersed in the matrix polymer [14]. Other interesting features of GO are that it can be chemically functionalized and modified for the preparation of polymer-based composite materials and it is also precursor materials for preparing graphene nanosheets in large quantity for many other functional applications such as secondary batteries, ionic conductors, and supercapacitors [15, 16].

Incorporating appropriate salts into the PEO-GO host polymer matrix provides charge carriers to the polymer matrix in order to increase the ionic conductivity of the system. High molecular weight PEO based polymer electrolytes containing lithium salts are of particular interest because of their easy formation of complexes with lithium salts and high mobility of charge carriers particularly lithium trifluoromethanesulfonate ( $\text{LiCF}_3\text{SO}_3$ ) because the ionic conduction of  $\text{LiCF}_3\text{SO}_3$  salt is ambipolar, which has lower Columbic potential and possesses higher segmental mobility of polymer chains [6, 17, 18]. Many studies on PEO-lithium salt system have reported that doping salt into the system has increased conductivity significantly [6, 18, 19]. The major drawback of these PEO-Li electrolyte systems for SPE is that they tend to crystallize at room temperatures resulting in low ionic conductivity [20, 21]. Plasticization is one of the common ways of reducing crystallinity and also increasing the amorphous phase content of polymer electrolytes. Previous work has reported that the use of ethylene sulfite (ES) as plasticizer increased the room temperature conductivity to the order of  $\sim 10^{-4} \text{ s cm}^{-1}$  on PEO-chitosan blend polymer system [22]. ES has dielectric constant,  $\epsilon$  of 39.6, which is higher than other common plasticizers, that is, dimethylacetamide ( $\epsilon = 37.8$ ) and diethyl carbonate ( $\epsilon = 2.82$ ). Increase in electrolytes conductivity has been reported with incorporation of plasticizer with higher dielectric constant [5]. Besides, ES also has low melting point ( $-17^\circ\text{C}$ ) which can ensure the plasticizer molecules will not solidify at room temperature which may limit the ion mobility [23]. The feasibility of ES in improving conductivity of the PEO based SPE can be investigated further and small loadings of ES contents minimize deterioration of the mechanical properties and the potential stability of the polymer films with the addition of plasticizers [24].

In this work, we prepare salted and plasticized SPE systems based on PEO-GO polymer blend doped with  $\text{LiCF}_3\text{SO}_3$  as doping salt; meanwhile ES is reinforced as plasticizer in order to enhance the conductivity. The conductivity and dielectric properties of the electrolytes will be discussed.

## 2. Materials and Methods

**2.1. Preparation of the Graphene Oxide (GO).** GO nanosheets were prepared by a modified Hummers method [25]. Any extra acids and salts were removed through washing process using distilled water (DI). Mild sonication was applied to the suspension for about 10 min to exfoliate graphite oxide that still remains in the GO suspension. Finally, GO suspension was put into the oven for 48 hours at  $60^\circ\text{C}$  to discard water present, thus obtaining dark brown GO nanosheets.

**2.2. Preparation and Characterization of Various PEO-GO Blend Films.** Different weight percentages ( $x$  wt.%) of GO nanosheets were mixed in 50 mL DI and homogenized using ultrasonicator XO-650D (Nanjing Xianou Instruments Co. Ltd.) for about 15 min at 50% crusher capacity. After the solutions cooled at room temperature,  $(100 - x)$  wt.% of PEO ( $M_v \sim 300,000$  containing 200–500 ppm butylated hydroxytoluene as inhibitor, Aldrich Chemistry) was then added to the GO solutions. The mixtures were stirred until homogeneous solutions were obtained. All solutions were cast onto different plastic Petri dishes and left to dry at room temperature and then kept in a desiccator filled with silica gel desiccants for further drying.

X-ray diffraction (XRD) measurements of the polymer blend films were carried out using a Siemens D5000 X-ray diffractometer where X-rays of  $1.54 \text{ \AA}$  wavelengths were generated by a Cu  $K\alpha$  source. The  $2\theta$  angle was varied from  $5^\circ$  to  $80^\circ$ .

**2.3. Preparation of Electrolytes.** The polymer blend electrolyte system was prepared by homogenizing 10 wt.% of GO nanosheets in 50 mL DI from total of 0.5 g polymer blend. After the solution was cooled to room temperature, 90 wt.% of PEO was added and stirred until homogenous solution was obtained. Prior to the preparation of the salted electrolytes,  $\text{LiCF}_3\text{SO}_3$  (Aldrich Chemistry) was dried at  $100^\circ\text{C}$  for 1 hour to eliminate trace amounts of water in the material. Different amounts of  $\text{LiCF}_3\text{SO}_3$  were added to the PEO-GO solutions and stirred until complete dissolution. For the preparation of plasticized system, different amounts of ES (Aldrich Chemistry) were added to the highest conducting salted electrolyte solutions and stirred until complete dissolution. All homogenous solutions were cast onto plastic Petri dishes and left to dry at room temperature for 2-3 days to form film. The dry films were then kept in desiccators filled with silica gel desiccants for several hours before being characterized to avoid any trace of moisture.

**2.4. Characterization of Electrolytes.** Impedance measurements were conducted using HIOKI 3532-50 LCR HiTESTER from room temperature to 373 K in the frequency range of 50 Hz to 5 MHz. The electrolyte films were sandwiched between two stainless steel electrodes of a conductivity holder with diameter of 1.9 cm. The value of bulk resistance ( $R_b$ ) was determined from the Cole-Cole plots. Conductivity ( $\sigma$ ) was calculated using the following equation:

$$\sigma = \frac{d}{R_b A}, \quad (1)$$

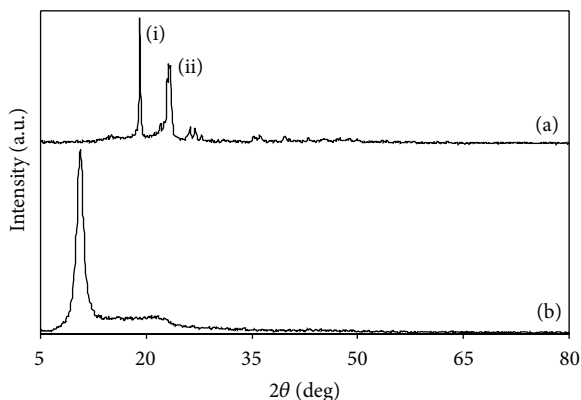


FIGURE 1: XRD pattern for (a) pure PEO and (b) pure GO.

where  $d$  is the thickness of the electrolyte samples and  $A$  is the electrode-electrolyte contact area. A digital thickness gauge (Mitutoyo Corp.) was employed to measure the thickness of the electrolytes.

The Fourier transform infrared spectroscopy (FTIR) studies were performed using attenuated total reflection infrared spectroscopy (ATR-IR) Perkin Elmer Spectrum 400 GladiATR in the wavenumber range of 400–4000  $\text{cm}^{-1}$ . The objective of FTIR was to confirm complexation between polymer and salt.

### 3. Results and Discussion

**3.1. XRD of PEO-GO Blends.** The choice of a proper ratio of polymer blend is crucial to its ability to serve as a polymer host in electrolytes because suitable ratio of polymer blend controls the reduction in crystallinity of the polymer blend. Qualitative identification of crystallinity structure can be made by comparing the position of XRD peaks and intensity of the peaks for polymer blends with standard patterns of pure material. Figure 1 shows XRD pattern for (a) pure PEO and (b) pure GO films. The maximum intensity peaks of pure PEO film were observed at (i)  $2\theta = 19.1^\circ$  and at (ii)  $2\theta = 23^\circ$ . These two peaks of PEO also have been reported by Kumar et al. [26] at  $2\theta = 19.36^\circ$  and at  $2\theta = 23.72^\circ$  and other authors [27, 28]. Several less intense peaks are exhibited around  $2\theta = 26.3^\circ, 27.0^\circ, 35.6^\circ, 36.4^\circ, 39.9^\circ,$  and  $43.1^\circ$ . The sharp peaks indicate the crystalline phase of PEO, which originates from the ordering of polyether side chains because there is strong intermolecular interaction between PEO chains through the hydrogen bonding [26]. Meanwhile, a very intense and sharp peak of pure GO film was found to be at  $2\theta = 10.7^\circ$  on Figure 1. According to Mural et al. [29], XRD peak of graphite, that is, starting material of GO occurring at  $2\theta = 26.46^\circ$ , has shifted to lower angle at  $2\theta = 9.5^\circ$  due to oxidative functionalization of graphitic structures.

Figure 2 shows the XRD pattern for different ratio (wt.%) of PEO-GO films in comparison to the pure PEO film (100 wt.% PEO) and pure GO film (100 wt.% GO). Changes in peak position or peak shape can be seen consequently in Figure 2. The very sharp peak of 100 wt.% GO shifts in

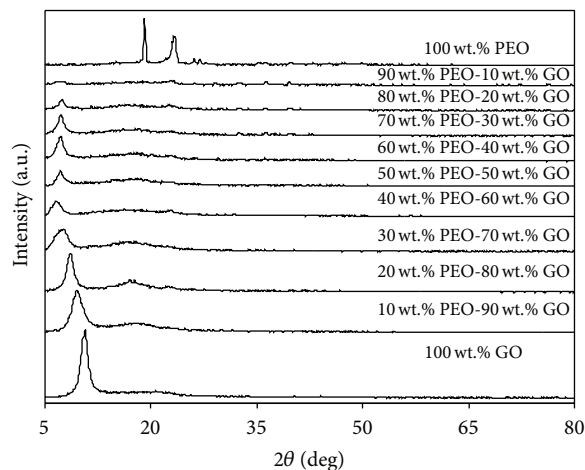


FIGURE 2: XRD pattern for pure PEO (100 wt.% PEO), pure GO (100 wt.% GO), and different ratio (wt.%) of PEO-GO blends.

the lower angle  $2\theta = 9.8^\circ$  with the presence of 10 wt.% of PEO in the blend and the trend is similar for 20 wt.% of PEO ( $2\theta = 8.7^\circ$ ), 30 wt.% PEO ( $2\theta = 7.8^\circ$ ), and 40 wt.% of PEO ( $2\theta = 6.8^\circ$ ). At 50 wt.% PEO-50 wt.% GO blend, GO peak has already shifted to slightly higher angle of  $2\theta = 7.4^\circ$  and the trend of GO peak follows for up to 80 wt.% PEO-20 wt.% GO blend. The shift in high or lower angle for every different ratio proved that PEO and GO have been blended together. It was observed that, at 90 wt.% PEO-10 wt.% GO blend, the peak shape of GO has become broad compared to others indicating that high intensity of GO peak has been lowered at this particular ratio. Throughout Figure 2, the peaks of PEO are not visible because those peaks have been superimposed by the maximum intensity of the GO peak. Since the relative intensities of 90 wt.% PEO-10 wt.% GO crystalline peaks are decreased, it is chosen in this work as polymer host because less crystallinity or amorphous phase observed signifies disruption of the rigid bonding of the material which enables ion migration for ionic conductivity [9].

**3.2. FTIR Analysis.** The complexation between the materials was studied using FTIR technique. Figure 3 shows two regions of FTIR spectra in which Figure 3(a) represents O-H band for pure GO while Figure 3(b) represents C-H stretching for pure PEO. These two main characteristics for each material were compared to the 90 wt.% PEO-10 wt.% GO blend which is selected based on XRD results. The FTIR spectra of the graphene oxide nanosheets show a broad absorption band at  $3190 \text{ cm}^{-1}$  due to the typical carbonyl and carboxyl groups present in the GO structure. Wang et al. [13] and Cao et al. [30] also have reported the presence of O-H band in GO nanosheets near  $3300 \text{ cm}^{-1}$  and  $3390 \text{ cm}^{-1}$ . Upon addition of 90 wt.% PEO through polymer blending, the O-H band has shifted to  $3223 \text{ cm}^{-1}$ ; meanwhile Figure 3(b) depicts the C-H stretching mode for pure PEO at  $2871 \text{ cm}^{-1}$  also has shifted to  $2877 \text{ cm}^{-1}$  when 10 wt.% GO was added to the polymer host. Alteration in wavenumber of O-H band and

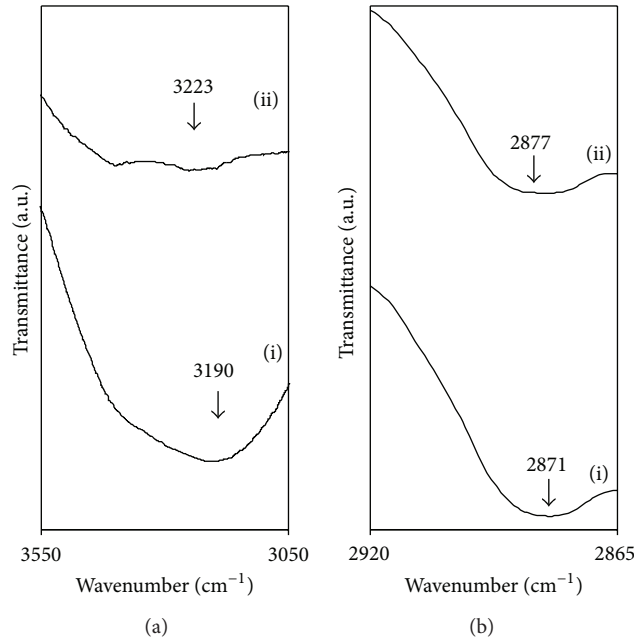


FIGURE 3: (a) FTIR spectra for (i) pure GO and (ii) 90 wt.% PEO-10 wt.% GO blend in the region of 3050–3550  $\text{cm}^{-1}$ . (b) FTIR spectra for (i) pure PEO and (ii) 90 wt.% PEO-10 wt.% GO blend in the region of 2865–2920  $\text{cm}^{-1}$ .

C-H stretching indicates that interaction in PEO-GO blend has occurred as reported by Mural et al. in [29].

Figure 4(a) shows the FTIR spectra of salted system of selected sample in the two main regions of O-H band 3050–3650  $\text{cm}^{-1}$  and also in the lower region around 630–650  $\text{cm}^{-1}$  as presented in Figure 4(b). According to Starkey and Frech [31], band at 764  $\text{cm}^{-1}$  is assigned to the  $\delta_s(\text{CF}_3)$  mode of the triflate ion ( $\text{CF}_3^-$ ). The appearance of a peak at 638  $\text{cm}^{-1}$  for 5 wt.%  $\text{LiCF}_3\text{SO}_3$  could be attributed to triflate ion in the pure  $\text{LiCF}_3\text{SO}_3$  salt as shown in Figure 4(b)(ii) because it is understood that the vibrational spectrum of triflate ion is very sensitive to its state of coordination, producing a series of different FTIR active bands as its environment changes [32]. It can be seen that, with increasing of the  $\text{LiCF}_3\text{SO}_3$  content, intensities of the region around 635  $\text{cm}^{-1}$  have become higher compared to the intensity of the peak for 5 wt.%  $\text{LiCF}_3\text{SO}_3$ . For O-H band, the wavenumber has shifted to the higher wavenumber values as depicted in Figure 4(a). Addition of 10 wt.%  $\text{LiCF}_3\text{SO}_3$  to the 90 wt.% PEO-10 wt.% GO blend has shifted the value number from 3223  $\text{cm}^{-1}$  to 3434  $\text{cm}^{-1}$ . Upon addition of 40 wt.% salt, the O-H band shifts to lower wavenumber of 3468  $\text{cm}^{-1}$  indicating a decrease in conductivity of the electrolyte. This result indicates that more salt aggregates have been formed which limit the conduction of ions. The increased wavenumber suggested that interaction in polymer blend with doping salt has occurred. Previous work by Karan et al. [33] proposed the coordination of the Li ions to the oxygen atoms of polymer backbone of PEO due to an increase in the glass transition temperature of the PEO- $\text{LiCF}_3\text{SO}_3$  electrolytes with increasing Li salt content. Another work by Yadav et al. [34] on graphene oxide/carboxymethylcellulose/alginate

(GO/CMC/Alg) composite blends stated that there are hydrogen bonding-type interactions due to the occurrence of such shifting in the FTIR spectra. The hydrophilic oxygenated functional groups on the surface or at the edge of the GO sheets played a critical role in improving the compatibility between GO and the polymer matrix.

Figure 5 represents the FTIR spectra of selected sample from PEO-GO- $\text{LiCF}_3\text{SO}_3$ -ES system in the region of O-H band at 3400–3550  $\text{cm}^{-1}$ . From salted system, the O-H band appearing at 3456  $\text{cm}^{-1}$  has shifted to 3461  $\text{cm}^{-1}$  with incorporation of 0.2 wt.% ES. The increase in wavenumber for each ES loading suggested that complexation of ES into the PEO-GO- $\text{LiCF}_3\text{SO}_3$  electrolyte system occurred. From Figure 5(b), the C=O band appearing at 1645  $\text{cm}^{-1}$  shifts to lower wavenumber of 1641  $\text{cm}^{-1}$  with incorporation of 0.2 wt.% ES and the same peak can be observed for addition of 0.4 wt.% ES–1.4 wt.% ES in the polymer blend. The peak shape also has become broad and less intense compared to the peak without addition of ES. Bhatt and O'Dwyer [35] used computational studies to predict theoretical FTIR spectra on ES as additives in propylene carbonate-based Li-ion battery electrolyte in which wavenumber of C=O of propylene carbonate increases as a result of a significant change in the bond length due to the interaction of ES on C=O frequency. This demonstrates that changes in wavenumber could be possibly due to interaction between ES and PEO-GO- $\text{LiCF}_3\text{SO}_3$  system that alter the bond length of C=O of the polymer host.

3.3. *Conductivity Analysis.* The effect of  $\text{LiCF}_3\text{SO}_3$  concentration on room temperature conductivity is represented in Figure 6(a). The conductivity of pure PEO-GO film at

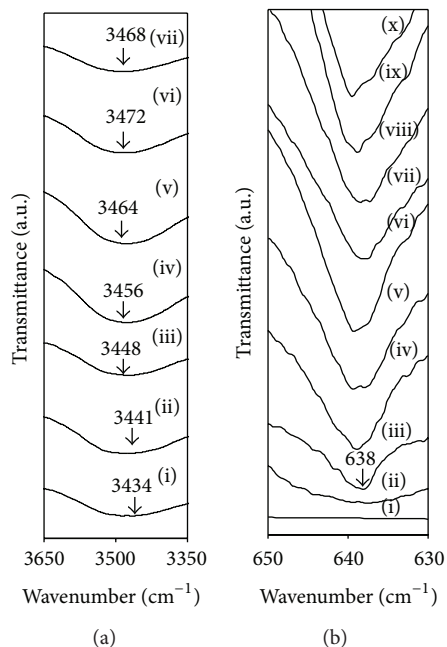


FIGURE 4: (a) FTIR spectra for 90 wt.% PEO-10 wt.% GO film with (i) 10 wt.%  $\text{LiCF}_3\text{SO}_3$ , (ii) 15 wt.%  $\text{LiCF}_3\text{SO}_3$ , (iii) 20 wt.%  $\text{LiCF}_3\text{SO}_3$ , (iv) 25 wt.%  $\text{LiCF}_3\text{SO}_3$ , (v) 30 wt.%  $\text{LiCF}_3\text{SO}_3$ , (vi) 35 wt.%  $\text{LiCF}_3\text{SO}_3$ , and (vii) 40 wt.%  $\text{LiCF}_3\text{SO}_3$  in the region of  $3350\text{--}3650\text{ cm}^{-1}$ . (b) FTIR spectra for (i) 90 wt.% PEO-10 wt.% GO film, (ii) pure  $\text{LiCF}_3\text{SO}_3$  and PEO-GO blend with (iii) 5 wt.%  $\text{LiCF}_3\text{SO}_3$ , (iv) 10 wt.%  $\text{LiCF}_3\text{SO}_3$ , (v) 15 wt.%  $\text{LiCF}_3\text{SO}_3$ , (vi) 20 wt.%  $\text{LiCF}_3\text{SO}_3$ , (vii) 25 wt.%  $\text{LiCF}_3\text{SO}_3$ , (viii) 30 wt.%  $\text{LiCF}_3\text{SO}_3$ , (ix) 35 wt.%  $\text{LiCF}_3\text{SO}_3$ , and (x) 40 wt.%  $\text{LiCF}_3\text{SO}_3$  in the region of  $630\text{--}650\text{ cm}^{-1}$ .

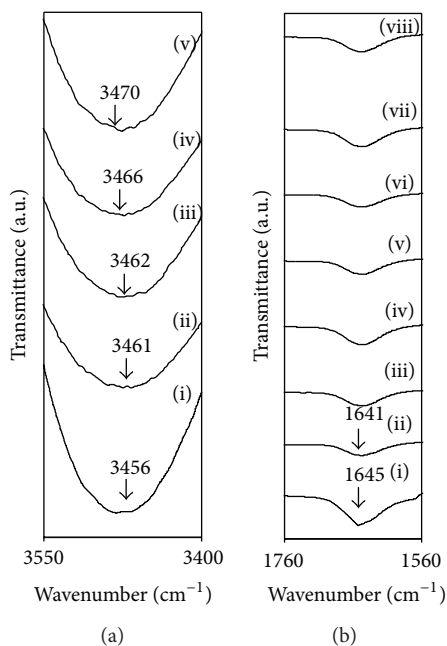


FIGURE 5: (a) FTIR spectra of (i) 90 wt.% PEO-10 wt.% GO-25 wt.%  $\text{LiCF}_3\text{SO}_3$  film with (ii) 0.2 wt.% ES, (iii) 0.4 wt.% ES, (iv) 1.0 wt.% ES, and (v) 1.2 wt.% ES in the region of  $3400\text{--}3550\text{ cm}^{-1}$ . (b) FTIR spectra of (i) 90 wt.% PEO-10 wt.% GO-25 wt.%  $\text{LiCF}_3\text{SO}_3$  film with (ii) 0.2 wt.% ES, (iii) 0.4 wt.% ES, (iv) 0.6 wt.% ES, (v) 0.8 wt.% ES, (vi) 1.0 wt.% ES, (vii) 1.2 wt.% ES, and (viii) 1.4 wt.% ES in the region  $1560\text{--}1760\text{ cm}^{-1}$ .

room temperature is  $(7.45 \pm 1.51) \times 10^{-11}\text{ S cm}^{-1}$ , which is relatively low since no mobile ions are provided within the film. On addition of 5 wt.%  $\text{LiCF}_3\text{SO}_3$ , the conductivity increases to  $(4.07 \pm 1.41) \times 10^{-9}\text{ S cm}^{-1}$ . The conductivity

further increases to  $(3.84 \pm 0.83) \times 10^{-6}\text{ S cm}^{-1}$  on addition of 25 wt.%  $\text{LiCF}_3\text{SO}_3$ . The conductivity of PEO- $\text{LiCF}_3\text{SO}_3$  electrolyte is reported to be in the order of  $\sim 10^{-6}\text{ S cm}^{-1}$  [6, 27, 36]. The conductivity decreases to  $(6.25 \pm 1.03) \times 10^{-7}\text{ S cm}^{-1}$

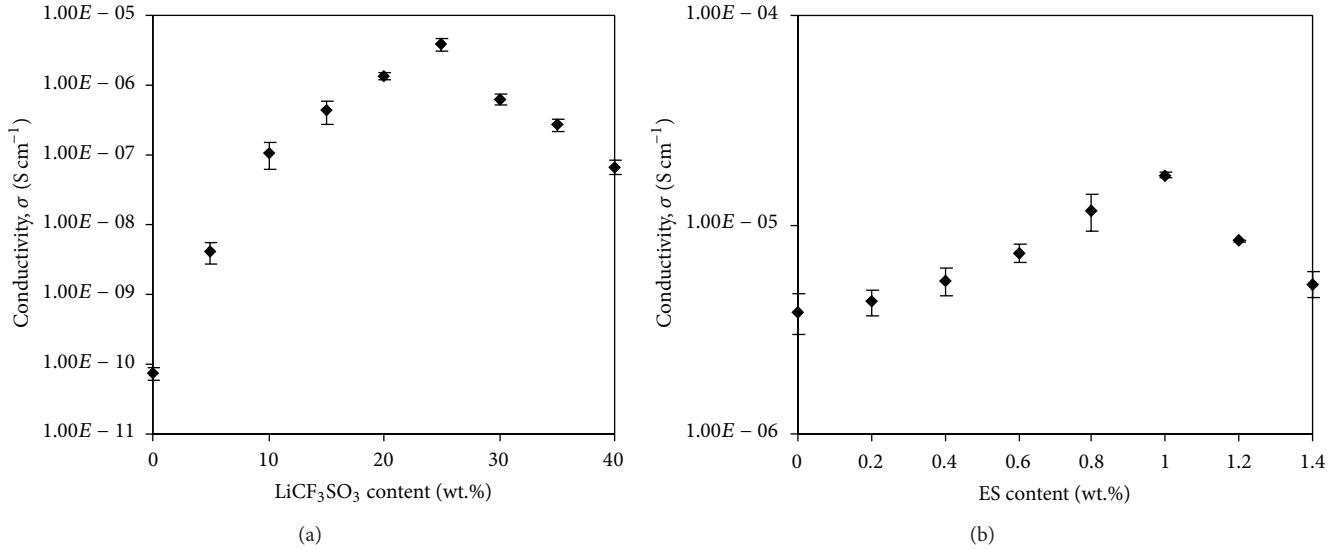


FIGURE 6: Room temperature conductivity as a function of (a) LiCF<sub>3</sub>SO<sub>3</sub> content and (b) ES content.

with the addition of 30 wt.% LiCF<sub>3</sub>SO<sub>3</sub>. The conductivity further decreases as salt concentration increases to 40 wt.%. This phenomenon can be attributed to the influence of the ion pairs and higher ion aggregations, reducing the overall mobility and degree of freedom, hence decreasing the conductivity [37].

Apart from polymer blending, plasticization can also assist the conductivity enhancement by weakening the Coulombic force between anions and cations of salt to promote salt dissociation. Since the 25 wt.% LiCF<sub>3</sub>SO<sub>3</sub> added electrolyte obtained the highest conductivity in salted system, the electrolyte was incorporated with different amounts of ES to enhance the conductivity. From Figure 6(b), the conductivity increases to  $(1.73 \pm 0.51) \times 10^{-5} \text{ S cm}^{-1}$  upon addition of 1 wt.% ES. The incorporation of ES to the electrolyte assists the production of free mobile ions and lowered the viscosity of the electrolyte [38]. More free mobile ions are produced with addition of ES because the presence of plasticizer further weakens the Coulombic force between cations and anions of the LiCF<sub>3</sub>SO<sub>3</sub> salt, hence promoting more salts dissociation [22, 38, 39]. The use of ES in PEO-KOH films has been reported to increase the number density of mobile ions indicating that ES has dissociated more salts into ions and thus elevated the conductivity of SPE system [40]. The presence of plasticizer also creates alternative pathways for ions conduction which lead to conductivity enhancement [41]. This is because ES creates network formation through oxygen atoms in its molecules and thus increases the conductivity of the electrolyte system at room temperature.

**3.4. Dielectric Studies.** Dielectric study is useful in revealing the conductivity behavior of polymer electrolyte. This study gives an important insight into the polarization effect at the electrode/electrolyte interface and further understanding in conductivity trend [42]. The conductivity trend of the salted system and plasticized system of PEO-GO polymer host can be further verified by dielectric studies. Dielectric constant  $\epsilon_r$  is representative of stored charge in a material while dielectric

loss  $\epsilon_i$  is a measure of energy losses to move ions when the polarity of electric field reverses rapidly [43, 44]. The frequency dependence of  $\epsilon_r$  and  $\epsilon_i$  at room temperature for salted system (PEO-GO-LiCF<sub>3</sub>SO<sub>3</sub>) and plasticized system (PEO-GO-LiCF<sub>3</sub>SO<sub>3</sub>-ES) is shown in Figures 7(a) and 7(b) and Figures 8(a) and 8(b), respectively. The equations for the dielectric constant  $\epsilon_r$  and dielectric loss  $\epsilon_i$  are as follows:

$$\begin{aligned} \epsilon_r &= \frac{Z_i}{\omega C_0 (Z_r^2 + Z_i^2)} \\ \epsilon_i &= \frac{Z_r}{\omega C_0 (Z_r^2 + Z_i^2)}, \end{aligned} \quad (2)$$

where  $Z_r$  and  $Z_i$  are the real and imaginary parts of the impedance,  $\omega$  is angular frequency, and  $C_0$  is the vacuum capacitance. Based on the frequency dependence of real and imaginary parts of the  $\epsilon_r$  for both salted and plasticized system, there are no appreciable relaxation peaks observed in the frequency range use in this study. No relaxation peaks are observed signifying that the increase in conductivity is mainly due to the increase in number density of mobile ions [45]. The  $\epsilon_r$  rises sharply towards low frequencies for salted system and selected sample of plasticized system (Figure 7). This is due probably to the electrode polarization effects [46]. At high frequencies, the periodic reversal of the electric field occurs so fast that there is no excess ion diffusion in the direction of the field. The polarization due to the charge accumulation decreased, leading to the observed decrease in the value of  $\epsilon_r$  at high frequencies as reported by Ramesh et al. on PEO-LiCF<sub>3</sub>SO<sub>3</sub> system [6]. Based on Figure 8(a) of salted system, the higher value of dielectric loss  $\epsilon_i$  at low frequency is due to the free charge motion within material and also addition on the plasticizer  $\epsilon_i$  increases in the lower frequency region which reflects the enhancement of mobility charge carrier [47]. From Figure 8(b),  $\epsilon_i$  first decreases with rise in frequency in low frequency region followed by a peak in the loss spectra. The appearance of peak is attributed to the relaxation phenomena of polymer (motion of salt free

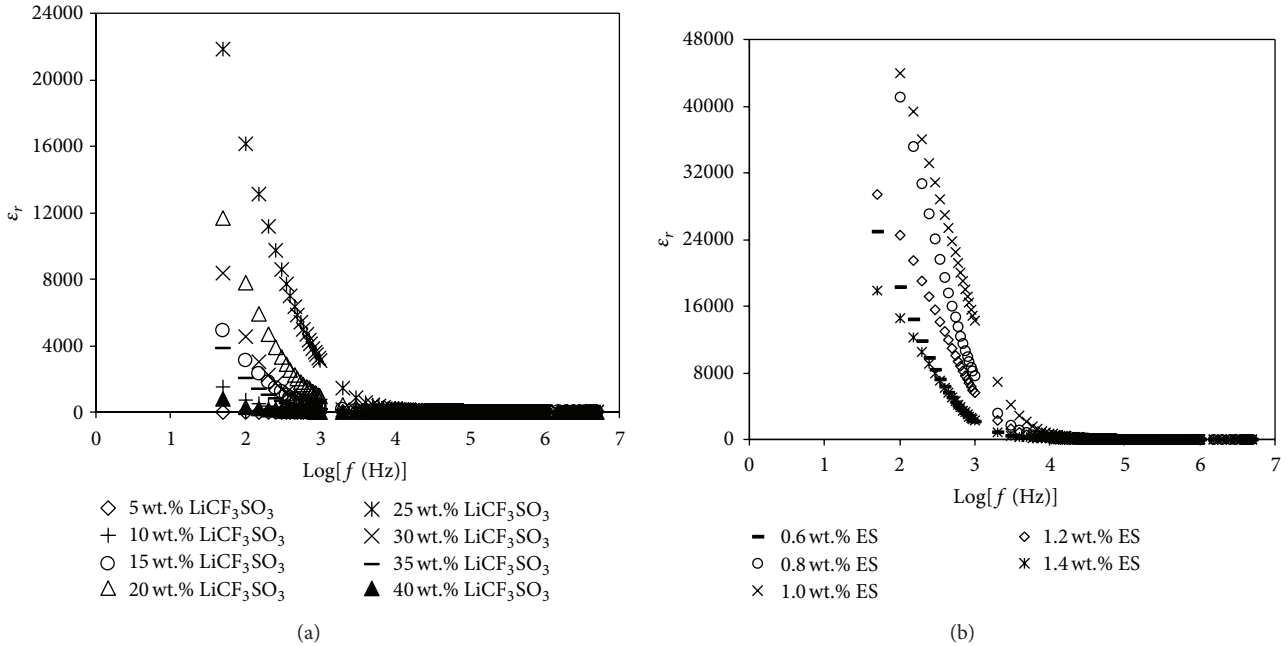


FIGURE 7: The frequency dependence of dielectric constant,  $\epsilon_r$ , at room temperature: (a) salted system and (b) plasticized system for selected sample.

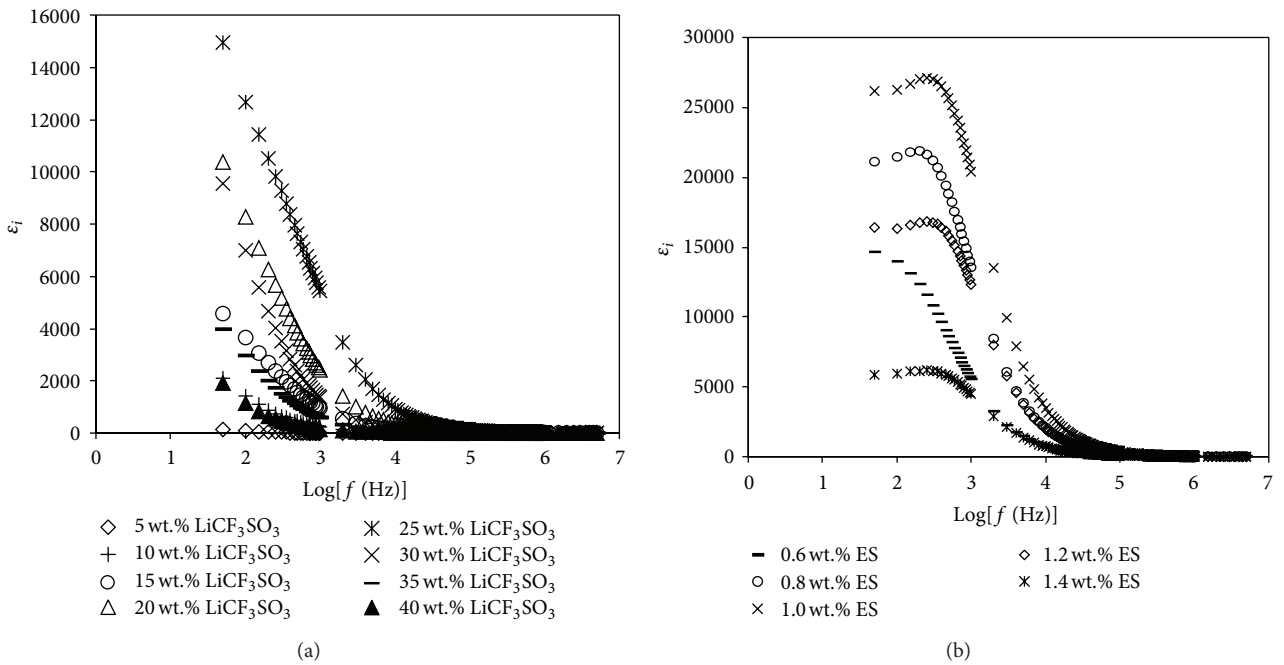


FIGURE 8: The frequency dependence of dielectric loss,  $\epsilon_i$ , at room temperature: (a) salted system and (b) plasticized system for selected sample.

chain segment) [47]. Similar types of observations have been reported in the literature [45].

The plot of loss tangent ( $\tan \delta$ ) as a function of frequency can obtain the information of the relaxation phenomena. The value of  $\tan \delta$  was calculated using

$$\tan \delta = \frac{\epsilon_i}{\epsilon_r} \quad (3)$$

The frequency dependence of  $\tan \delta$  for selected electrolyte samples in salted and plasticized systems at room temperature is shown in Figures 9(a) and 9(b), respectively. The maximum of  $\tan \delta$  ( $\tan \delta_{\max}$ ), which represents the relaxation peak, is located at higher frequency for higher conducting electrolyte. The relaxation time ( $t_r$ ) for each electrolyte was obtained from the relation

$$t_r \omega_{\text{peak}} = 1, \quad (4)$$

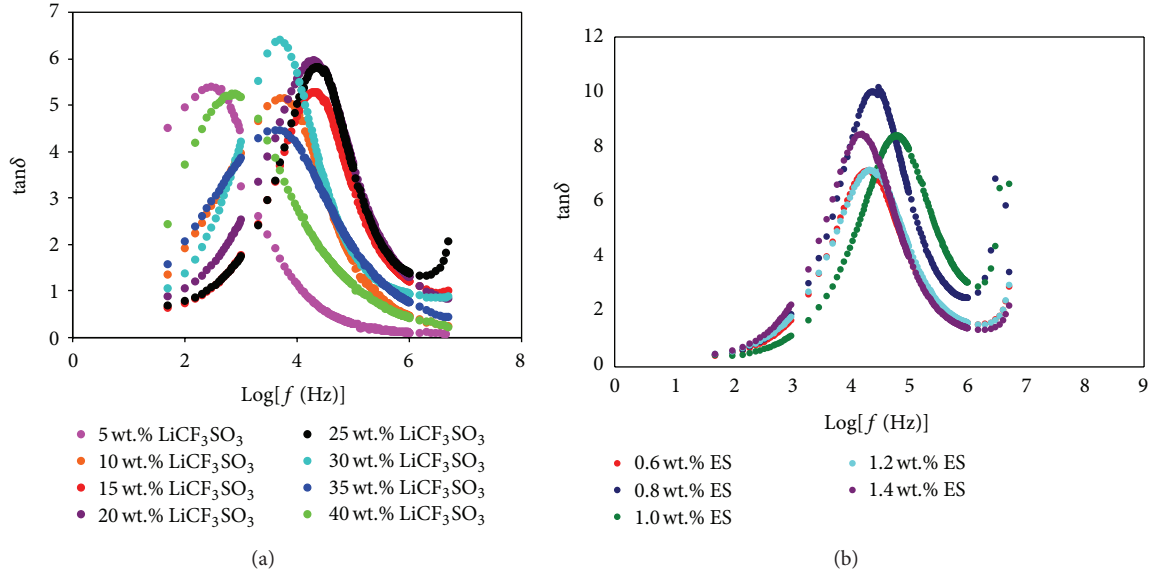


FIGURE 9: The frequency dependence of  $\tan \delta$  at room temperature: (a) salted system and (b) plasticized system for selected sample.

TABLE 1: Relaxation time ( $t_r$ ) for PEO-GO-LiCF<sub>3</sub>SO<sub>3</sub> system.

LiCF <sub>3</sub> SO <sub>3</sub> (wt.%)	$t_r$ (s)
5	$4.55 \times 10^{-4}$
10	$3.18 \times 10^{-5}$
15	$7.95 \times 10^{-6}$
20	$8.37 \times 10^{-6}$
25	$7.23 \times 10^{-6}$
30	$3.18 \times 10^{-5}$
35	$3.98 \times 10^{-5}$
40	$1.98 \times 10^{-4}$

TABLE 2: Relaxation time ( $t_r$ ) for PEO-GO-LiCF<sub>3</sub>SO<sub>3</sub>-ES system.

ES (wt.%)	$t_r$ (s)
0.6	$7.23 \times 10^{-6}$
0.8	$5.13 \times 10^{-6}$
1	$2.41 \times 10^{-6}$
1.2	$7.57 \times 10^{-6}$
1.4	$9.94 \times 10^{-6}$

where  $\omega_{\text{peak}}$  is the angular frequency of the relaxation peak. The occurrence of relaxation time is the result of the efforts carried out by ionic charge carriers to obey the change in the direction of the applied field [48]. The values of  $t_r$  for the salted system and selected samples of plasticized systems are shown in Tables 1 and 2, respectively. From Table 1, the highest conducting electrolyte with incorporation of 25 wt.% LiCF<sub>3</sub>SO<sub>3</sub> possesses the lowest  $t_r$  value of  $7.23 \times 10^{-6}$  s. In plasticized system,  $t_r$  value is observed to decrease to  $2.41 \times 10^{-6}$  s as ES content increases to 1 wt.% as shown in Table 2. Other reports also show that the higher conducting electrolytes have the lower values of  $t_r$  [48, 49].

#### 4. Conclusion

Electrolyte systems based on PEO-GO blend doped with LiCF<sub>3</sub>SO<sub>3</sub> have been successfully prepared via solution cast technique. Based on the XRD results, the less crystallinity was obtained using 90 wt.% of PEO and 10 wt.% of GO as polymer host. In salted system, highest conductivity of the PEO-GO blend polymer was achieved utilizing 25 wt.% LiCF<sub>3</sub>SO<sub>3</sub> with

the value of  $(3.84 \pm 0.83) \times 10^{-6}$  S cm<sup>-1</sup> at room temperature. In plasticized system, the addition of 1.0 wt.% ES has further enhanced the conductivity to  $(1.73 \pm 0.51) \times 10^{-5}$  S cm<sup>-1</sup>. The relaxation time of the electrolytes is found to decrease with increasing conductivity at room temperature for both salted and plasticized system. From FTIR analysis, the complexation between the electrolyte components is proven by the shifting of O-H band at 3000–3700 cm<sup>-1</sup>, C-H stretch at 2800–2900 cm<sup>-1</sup>, CF<sub>3</sub> vibration at 600–700 cm<sup>-1</sup>, and C=O band at 1500–1700 cm<sup>-1</sup>.

#### Conflict of Interests

The authors declare that there is no conflict of interests regarding the publication of this paper.

#### Acknowledgment

The authors thank the University of Malaya for the financial support (UMRG: RP010B-13AFR).

#### References

- [1] M. B. Armand, J. M. Chabagno, and M. Duclot, "Poly-ethers as solid electrolytes," in *Fast Ion Transport in Solids*, P. Vashisha, J.

- N. Mundy, and G. K. Shenoy, Eds., p. 131, North Holland, New York, NY, USA, 1979.
- [2] S. A. Hashmi, R. J. Latham, R. G. Linford, and W. S. Schlindwein, "Studies on all solid state electric double layer capacitors using proton and lithium ion conducting polymer electrolytes," *Journal of the Chemical Society, Faraday Transactions*, vol. 93, no. 23, pp. 4177–4182, 1997.
- [3] G. S. MacGlashan, Y. G. Andreev, and P. G. Bruce, "Structure of the polymer electrolyte poly(ethylene oxide)<sub>6</sub>:LiAsF<sub>6</sub>," *Nature*, vol. 398, no. 6730, pp. 792–794, 1999.
- [4] C. H. Manaratne, R. M. G. Rajapakse, and M. A. K. L. Dissanayake, "Ionic conductivity of poly(ethylene oxide) (PEO)-montmorillonite (MMT) nanocomposites prepared by intercalation from aqueous medium," *International Journal of Electrochemical Science*, vol. 1, no. 1, pp. 32–46, 2006.
- [5] M. Kumar and S. S. Sekhon, "Role of plasticizer's dielectric constant on conductivity modification of PEO-NH<sub>4</sub>F polymer electrolytes," *European Polymer Journal*, vol. 38, no. 7, pp. 1297–1304, 2002.
- [6] S. Ramesh, T. F. Yuen, and C. J. Shen, "Conductivity and FTIR studies on PEO-LiX X : CF<sub>3</sub>SO<sub>3</sub><sup>-</sup>, SO<sub>2</sub><sup>-4</sup> polymer electrolytes," *Spectrochimica Acta Part A: Molecular and Biomolecular Spectroscopy*, vol. 69, no. 2, pp. 670–675, 2008.
- [7] K. Kesavan, C. M. Mathew, S. Rajendran, and M. Ulaganathan, "Preparation and characterization of novel solid polymer blend electrolytes based on poly (vinyl pyrrolidone) with various concentrations of lithium perchlorate," *Materials Science and Engineering B: Solid-State Materials for Advanced Technology*, vol. 184, no. 1, pp. 26–33, 2014.
- [8] B. K. Money, K. Hariharan, and J. Swenson, "Relation between structural and conductivity relaxation in PEO and PEO based electrolytes," *Solid State Ionics*, vol. 262, pp. 785–789, 2014.
- [9] E. Staunton, Y. G. Andreev, and P. G. Bruce, "Factors influencing the conductivity of crystalline polymer electrolytes," *Faraday Discussions*, vol. 134, pp. 143–156, 2007.
- [10] E. Frackowiak and F. Béguin, "Carbon materials for the electrochemical storage of energy in capacitors," *Carbon*, vol. 39, no. 6, pp. 937–950, 2001.
- [11] X. Li, X. Wang, L. Zhang, S. Lee, and H. Dai, "Chemically derived, ultrasmooth graphene nanoribbon semiconductors," *Science*, vol. 319, no. 5867, pp. 1229–1232, 2008.
- [12] L. M. Viculis, J. J. Mack, O. M. Mayer, H. T. Hahn, and R. B. Kaner, "Intercalation and exfoliation routes to graphite nanoplatelets," *Journal of Materials Chemistry*, vol. 15, no. 9, pp. 974–978, 2005.
- [13] G. Wang, B. Wang, J. Park, J. Yang, X. Shen, and J. Yao, "Synthesis of enhanced hydrophilic and hydrophobic graphene oxide nanosheets by a solvothermal method," *Carbon*, vol. 47, no. 1, pp. 68–72, 2009.
- [14] W. E. Mahmoud, "Morphology and physical properties of poly(ethylene oxide) loaded graphene nanocomposites prepared by two different techniques," *European Polymer Journal*, vol. 47, no. 8, pp. 1534–1540, 2011.
- [15] M. Cano, U. Khan, T. Sainsbury et al., "Improving the mechanical properties of graphene oxide based materials by covalent attachment of polymer chains," *Carbon*, vol. 52, pp. 363–371, 2013.
- [16] A. K. Geim and K. S. Novoselov, "The rise of graphene," *Nature Materials*, vol. 6, no. 3, pp. 183–191, 2007.
- [17] F. Croce, S. Sacchetti, and B. Scrosati, "Advanced, lithium batteries based on high-performance composite polymer electrolytes," *Journal of Power Sources*, vol. 162, no. 1, pp. 685–689, 2006.
- [18] K. Vignarooban, M. A. K. L. Dissanayake, I. Albinsson, and B.-E. Mellander, "Effect of TiO<sub>2</sub> nano-filler and EC plasticizer on electrical and thermal properties of poly(ethylene oxide) (PEO) based solid polymer electrolytes," *Solid State Ionics*, vol. 266, pp. 25–28, 2014.
- [19] M. R. Johan, O. H. Shy, S. Ibrahim, S. M. M. Yassin, and T. Y. Hui, "Effects of Al<sub>2</sub>O<sub>3</sub> nanofiller and EC plasticizer on the ionic conductivity enhancement of solid PEO-LiCF<sub>3</sub>SO<sub>3</sub> solid polymer electrolyte," *Solid State Ionics*, vol. 196, no. 1, pp. 41–47, 2011.
- [20] H. M. J. C. Pitawala, M. A. K. L. Dissanayake, and V. A. Seneviratne, "Combined effect of Al<sub>2</sub>O<sub>3</sub> nano-fillers and EC plasticizer on ionic conductivity enhancement in the solid polymer electrolyte (PEO)<sub>9</sub>LiTf," *Solid State Ionics*, vol. 178, no. 13–14, pp. 885–888, 2007.
- [21] J. Szydek, M. Armand, M. Marcinek, A. Zalewska, G. Zukowska, and W. Wiczeorek, "Detailed studies on the fillers modification and their influence on composite, poly(oxyethylene)-based polymeric electrolytes," *Electrochimica Acta*, vol. 55, no. 4, pp. 1314–1322, 2010.
- [22] M. F. Z. A. Kadir, M. F. Z. Abdul, L. P. Teo, S. R. Majid, and A. K. Arof, "Conductivity studies on plasticised PEO/chitosan proton conducting polymer electrolyte," *Materials Research Innovations*, vol. 13, no. 3, pp. 259–262, 2009.
- [23] M. Ue, Y. Sasaki, Y. Tanaka, and M. Morita, "Nonaqueous electrolytes with advances in solvents," in *Electrolytes for Lithium and Lithium-Ion Batteries*, T. R. Jow, K. Xu, O. Borodin, and M. Ue, Eds., p. 148, Springer, New York, NY, USA, 2014.
- [24] C. W. Lin, C. L. Hung, M. Venkateswarlu, and B. J. Hwang, "Influence of TiO<sub>2</sub> nano-particles on the transport properties of composite polymer electrolyte for lithium-ion batteries," *Journal of Power Sources*, vol. 146, no. 1–2, pp. 397–401, 2005.
- [25] W. S. Hummers Jr. and R. E. Offeman, "Preparation of graphitic oxide," *Journal of the American Chemical Society*, vol. 80, no. 6, p. 1339, 1958.
- [26] K. K. Kumar, M. Ravi, Y. Pavani, S. Bhavani, A. K. Sharma, and V. V. R. Rao, "Investigations on PEO/PVP/NaBr complexed polymer blend electrolytes for electrochemical cell applications," *Journal of Membrane Science*, vol. 454, pp. 200–211, 2014.
- [27] A. Asghar, Y. A. Samad, and R. Hashaikeh, "Cellulose/PEO blends with enhanced water absorption and retention functionality," *Journal of Applied Polymer Science*, vol. 125, no. 3, pp. 2121–2127, 2012.
- [28] N. Reddeppa, T. J. R. Reddy, V. B. S. Achari, V. V. R. N. Rao, and A. K. Sharma, "Electrical and optical characterization of (PEO+PVAc) polyblend films," *Ionics*, vol. 15, no. 2, pp. 255–259, 2009.
- [29] P. K. S. Mural, A. Banerjee, M. S. Rana et al., "Polyolefin based antibacterial membranes derived from PE/PEO blends compatibilized with amine terminated graphene oxide and maleated PE," *Journal of Materials Chemistry A*, vol. 2, no. 41, pp. 17635–17648, 2014.
- [30] Y.-C. Cao, C. Xu, X. Wu, X. Wang, L. Xing, and K. Scott, "A poly (ethylene oxide)/graphene oxide electrolyte membrane for low temperature polymer fuel cells," *Journal of Power Sources*, vol. 196, no. 20, pp. 8377–8382, 2011.

- [31] S. R. Starkey and R. Frech, "Plasticizer interactions with polymer and salt in propylene carbonate-poly(acrylonitrile)-lithium triflate," *Electrochimica Acta*, vol. 42, no. 3, pp. 471–474, 1997.
- [32] S. S. Sekhon, K. V. Pradeep, and S. A. Agnihotry, *Solid State Ionics: Science and Technology*, Edited by: B. V. R. Chowdari, K. Lal, S. A. Agnihotry, N. Khare, S. S. Sekhon, P. C. Srivastava, S. Chandra, World Scientific, Singapore, 1998.
- [33] N. K. Karan, O. K. Pradhan, R. Thomas, B. Natesan, and R. S. Katiyar, "Solid polymer electrolytes based on polyethylene oxide and lithium trifluoro-methane sulfonate (PEO-LiCF<sub>3</sub>SO<sub>3</sub>): ionic conductivity and dielectric relaxation," *Solid State Ionics*, vol. 179, no. 19–20, pp. 689–696, 2008.
- [34] M. Yadav, K. Y. Rhee, and S. J. Park, "Synthesis and characterization of graphene oxide/carboxymethylcellulose/alginate composite blend films," *Carbohydrate Polymers*, vol. 110, pp. 18–25, 2014.
- [35] M. D. Bhatt and C. O'Dwyer, "The role of carbonate and sulfite additives in propylene carbonate-based electrolytes on the formation of SEI layers at graphitic Li-ion battery anodes," *Journal of the Electrochemical Society*, vol. 161, no. 9, pp. A1415–A1421, 2014.
- [36] H. M. J. C. Pitawala, M. A. K. L. Dissanayake, V. A. Seneviratne, B.-E. Mellander, and I. Albinson, "Effect of plasticizers (EC or PC) on the ionic conductivity and thermal properties of the (PEO)<sub>9</sub>LiTf: Al<sub>2</sub>O<sub>3</sub> nanocomposite polymer electrolyte system," *Journal of Solid State Electrochemistry*, vol. 12, no. 7–8, pp. 783–789, 2008.
- [37] K. W. Chew and K. W. Tan, "The effects of ceramic fillers on PMMA-based polymer electrolyte salted with lithium triflate, LiCF<sub>3</sub>SO<sub>3</sub>," *International Journal of Electrochemical Science*, vol. 6, no. 11, pp. 5792–5801, 2011.
- [38] M. F. Z. Kadir, S. R. Majid, and A. K. Arof, "Plasticized chitosan-PVA blend polymer electrolyte based proton battery," *Electrochimica Acta*, vol. 55, no. 4, pp. 1475–1482, 2010.
- [39] M. F. Shukur, R. Ithnin, H. A. Ilias, and M. F. Z. Kadir, "Proton conducting polymer electrolyte based on plasticized chitosan-PEO blend and application in electrochemical devices," *Optical Materials*, vol. 35, no. 10, pp. 1834–1841, 2013.
- [40] M. F. Hassan, N. H. Idris, S. R. Majid, T. Winie, A. S. A. Khair, and A. K. Arof, "Effect of ethylene sulphite on the conductivity and morphology of PEO-KOH films," *Materials Science Forum*, vol. 517, pp. 89–92, 2006.
- [41] A. Pawlicka, A. C. Sabadini, E. Raphael, and D. C. Dragunski, "Ionic thermogravimetry measurements of starch-based polymeric electrolytes," *Molecular Crystal and Liquid Crystals*, vol. 485, no. 1, pp. 804–816, 2008.
- [42] M. C. Wintersgill, J. J. Fontanella, Y. S. Pak, S. G. Greenbaum, A. Al-Mudaris, and A. V. Chadwick, "Electrical conductivity, differential scanning calorimetry and nuclear magnetic resonance studies of amorphous poly(ethylene oxide) complexed with sodium salts," *Polymer*, vol. 30, no. 6, pp. 1123–1126, 1989.
- [43] M. H. Buraidah, L. P. Teo, S. R. Majid, and A. K. Arof, "Ionic conductivity by correlated barrier hopping in NH<sub>4</sub>I doped chitosan solid electrolyte," *Physica B: Condensed Matter*, vol. 404, no. 8–11, pp. 1373–1379, 2009.
- [44] H. J. Woo, S. R. Majid, and A. K. Arof, "Dielectric properties and morphology of polymer electrolyte based on poly( $\epsilon$ -caprolactone) and ammonium thiocyanate," *Materials Chemistry and Physics*, vol. 134, no. 2–3, pp. 755–761, 2012.
- [45] M. Marzantowicz, J. R. Dygas, F. Krok, Z. Florjańczyk, and E. Zygadlo-Monikowska, "Influence of crystallization on dielectric properties of PEO:LiTFSI polymer electrolyte," *Journal of Non-Crystalline Solids*, vol. 352, no. 42, pp. 5216–5223, 2006.
- [46] R. Mishra and K. J. Rao, "Electrical conductivity studies of poly(ethyleneoxide)-poly(vinylalcohol) blends," *Solid State Ionics*, vol. 106, no. 1–2, pp. 113–127, 1998.
- [47] D. K. Pradhan, R. N. P. Choudhary, and B. K. Samantaray, "Studies of dielectric relaxation and AC conductivity behavior of plasticized polymer nanocomposite electrolytes," *International Journal of Electrochemical Science*, vol. 3, no. 5, pp. 597–608, 2008.
- [48] K. Ramly, M. I. N. Isa, and A. S. A. Khair, "Conductivity and dielectric behaviour studies of starch/PEO+x wt-%NH<sub>4</sub>NO<sub>3</sub> polymer electrolyte," *Materials Research Innovations*, vol. 15, no. 2, pp. S82–S85, 2011.
- [49] N. H. Idris, H. B. Senin, and A. K. Arof, "Dielectric spectra of LiTFSI-doped chitosan/PEO blends," *Ionics*, vol. 13, no. 4, pp. 213–217, 2007.

## Research Article

# Influence of Tensile Speeds on the Failure Loads of the DP590 Spot Weld under Various Combined Loading Conditions

Jung Han Song<sup>1</sup> and Hoon Huh<sup>2</sup>

<sup>1</sup>*Metal Forming R&BD Group, Korea Institute of Industrial Technology, 156 Gaetbeol-ro, Yeosu-gu, Incheon 406-840, Republic of Korea*

<sup>2</sup>*School of Mechanical, Aerospace and Systems Engineering, Korea Advanced Institute of Science and Technology, Daeduk Science Town, Daejeon 305-701, Republic of Korea*

Correspondence should be addressed to Jung Han Song; [jhsong@kitech.re.kr](mailto:jhsong@kitech.re.kr)

Received 13 November 2014; Accepted 10 December 2014

Academic Editor: Doo-In Kim

Copyright © 2015 J. H. Song and H. Huh. This is an open access article distributed under the Creative Commons Attribution License, which permits unrestricted use, distribution, and reproduction in any medium, provided the original work is properly cited.

This paper is concerned with the evaluation of the dynamic failure load of the spot weld under combined axial and shear loading conditions. The testing fixture is designed to impose the combined axial and shear load on the spot weld. Using the proposed testing fixtures and specimens, quasi-static and dynamic failure tests of the spot weld are conducted with seven different combined loading conditions. The failure load and failure behavior of the spot weld are investigated with different loading conditions. Effect of tensile speeds on the failure load of the spot weld, which is critical for structural crashworthiness, is also examined based on the experimental data. The failure loads measured from the experiment are decomposed into the two components along the axial and shear directions and failure contours are plotted with different loading speeds. Dynamic sensitivities of failure loads with various combined loading conditions were also analyzed. Experimental results indicate that the failure contour is expanded with increasing loading speeds and failure loads show similar dynamic sensitivity with respect to the loading angles.

## 1. Introduction

Increasing concern of environmental safety and reduction of fuel consumption motivates car manufacturers to use lightweight materials having a higher tensile strength coupled with better ductility. By reducing the weight of a car less fuel consumption along with less CO<sub>2</sub> emission can be achieved. Considering the safety standards required in the automobile industry, dual phase (DP) steel has gained its popularity as this steel has a higher tensile strength in conjunction with higher elongation compared to the steel grades of similar yield strength [1]. The resistance spot welding process has become indispensable in the joining of sheet metals in the automobile industry since the 1950s. Because a modern vehicle typically contains several thousand spot welds, it is extremely important to understand the strength of the spot weld under quasi-static, fatigue, and impact loading conditions in order to evaluate durability and crashworthiness of an auto-body [2]. Failure of a spot weld is likely to occur

prior to failure of the base metal when a large load is applied to the structure since extremely high stress is concentrated at the interface between the nugget and the base metal [3]. It is necessary to estimate the strength of spot welds of DP steel sheets in order to provide a failure criterion of a spot weld in the structural analysis or crashworthiness assessment of auto-body members. For that purpose, lap-shear tests, coach-peel tests, and cross-tension tests have been elaborately performed to estimate the failure loads of the spot weld [4–6]. It is, however, insufficient to perform simple lap-shear tests and cross-tension tests to construct the failure criteria that describe the behavior of spot welds under combined loading conditions because spot welds in automotive components are subjected to complicated loading conditions when they undergo deformation.

With advances in computer simulation technology, automotive companies attempt to implement accurate spot weld models into finite element analysis so as to predict the failure of spot-welded components in the crash analysis of

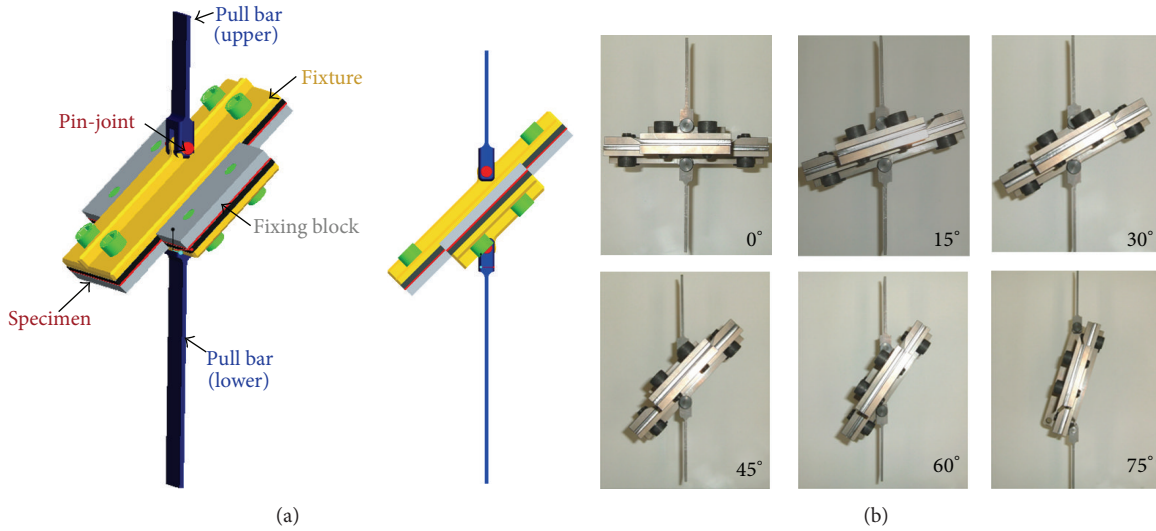


FIGURE 1: Fixture set with pin-joints for failure tests of a spot weld under combined loading conditions: (a) schematic diagram of a fixture; (b) fabricated testing fixtures at various loading angles.

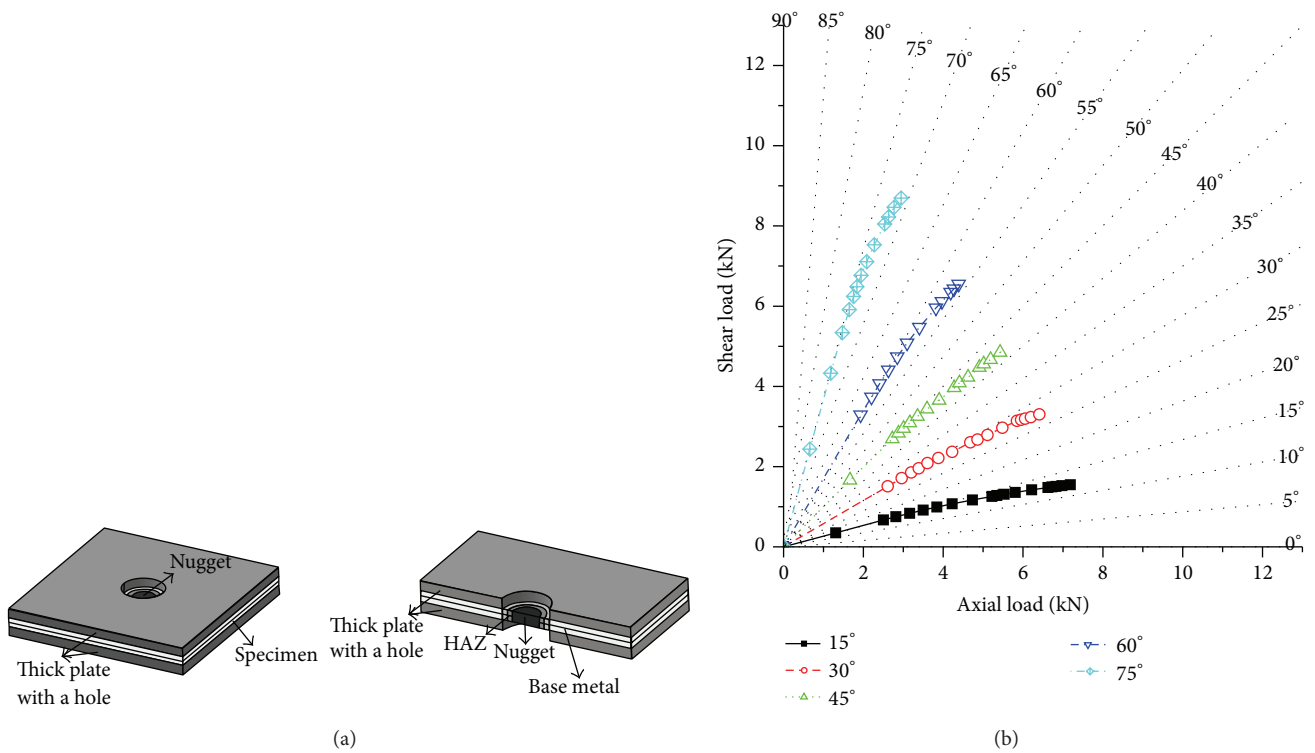


FIGURE 2: Design of specimen to impose the constant ratio of axial and shear loads on the spot weld during tests: schematic description of a specimen with a guide plate; (b) loading path acting on the spot weld at various loading angles (FEM results).

an auto-body. In order to describe the failure of a spot weld in the crash analysis, it is necessary to evaluate the failure characteristics of a spot weld under impact loading condition. Birch and Alves [7] conducted dynamic lap-shear tests of spot-welded mild steels using a servohydraulic testing machine. Schneider and Jones [8] performed dynamic coach-peel tests at a crosshead speed of 0.8 m/s. Bayraktar et al. [9]

investigated dynamic failure loads of spot-welded lap-shear specimens using a Charpy impact test. Their experimental results revealed that the dynamic failure load of spot welds increases relative to the quasi-static failure load. Sun and Khaleel [10] also observed the strain-rate dependent failure load of spot welds in dynamic cross-tension tests. Khan et al. conducted drop weight test using lab-shear specimen to

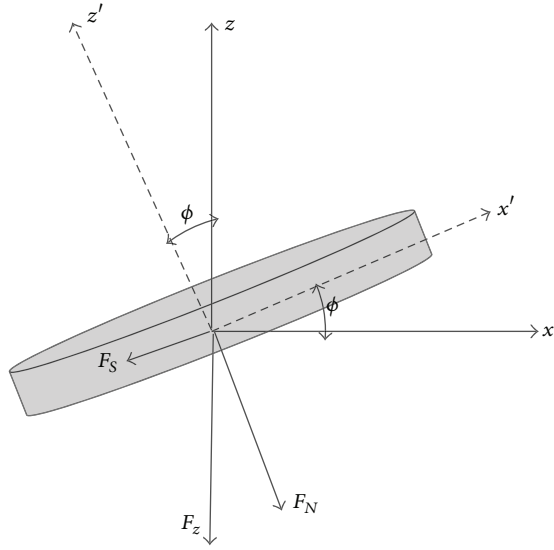


FIGURE 3: Decomposition of the applied load on a spot weld into the axial and the shear component at the loading angle of  $\phi$ .

investigate the impact performance of spot welds in advanced high strength steels [11]. It is, however, not feasible to perform dynamic lap-shear, cross-tension, and coach-peel tests for constructing a strain-rate dependent failure criterion that describes the behavior of spot welds under impact loading conditions because spot welds in automotive components are subjected to complicated dynamic loading conditions when they undergo crashed deformation [12].

In this paper, the failure behavior of the DP590 spot weld under combined loading conditions is investigated under quasi-static and impact loading condition. Dynamic failure tests of the spot weld are conducted with seven different combined loading conditions at various tensile speeds from quasi-static to 1.2 m/s. Dynamic effects on the failure load of the spot weld, which is critical for structural crashworthiness, are examined based on the experimental data.

## 2. Dynamic Failure Tests of a Spot Weld under Combined Loading Conditions

**2.1. Testing Fixtures to Impose Combined Loading Conditions on the Spot Weld.** In order to impose the combined axial and shear loads on a spot weld, specially designed testing fixtures and specimens were adopted in this paper [13]. The testing fixture shown in Figure 1 contains the pin-joints that eliminate the horizontal force and bending moment. The specimen shown in Figure 2(a) involves guide plates that prevent unfavorable rotation of the nugget due to bending deformation. The testing fixture and specimen ensure a combined loading condition with a constant ratio of the shear load to the axial load during the test, as shown in Figure 2(b) [13]. Therefore, as explained in Figure 3, the applied load  $F_z$  can be decomposed into the axial load  $F_N$  and the shear

load  $F_S$  at the nugget region using the simple trigonometric functions:

$$\begin{aligned} F_N &= F_z \cos \phi \\ F_S &= F_z \sin \phi. \end{aligned} \quad (1)$$

Here,  $F_N$ ,  $F_S$ , and  $\phi$  denote the axial load, the shear load, and the initial inclined angle with respect to the pulling direction, respectively. The inclined angle  $\phi$  is equal to the loading angle, which represents the angle between the load application line and the centerline of the specimen.

**2.2. Testing Material and Preparation of Specimen.** The spot weld of DP590 with the thickness of 1.0 mm is considered in this paper. The chemical compositions are listed in Table 1. Prior to spot welding of a specimen, the specimen surface was wiped with a weak acetone solution using a cloth in order to remove grease and dirt from its surface. Spot welding was then performed using a static spot/projection welding machine. The welding schedules shown in Table 2 were determined after several trials with the aid of industry standards to guarantee a button-type failure.

The specimen used in the tests is shown in Figure 4(a). To restrict the bending of the region outside the spot weld, two guide plates made of SPFC590 steel with the thickness of 3.2 mm were attached onto the outsides of the specimen in the following procedure.

- (1) Two guide plates with a hole at the center are prepared. Thickness and hole diameter of the guide plate are 3.2 mm and 10 mm, respectively.
- (2) A guide plate was joined with a steel sheet on one side using six points of spot welding around the hole at the center of the guide plate.
- (3) Two pairs of the joined guide plate and the steel sheet were spot welded to each other through the holes at the center of guide plates.

As the diameter of the hole in the guide plate was 10 mm, the six spot weld points that joined the guide plate and the steel sheet only serve to prevent excessive bending of the spot-welded region; they have little influence on the strength of the spot-welded region in the specimen. Additionally, a pure shear test was also performed in order to obtain the failure load at a loading angle of  $90^\circ$ . Three sheets are joined with a spot weld so that only the shear load is applied on the spot weld as shown in Figure 4(b). Cross-sectional shape and hardness profile of the specimen are also depicted in Figure 5.

**2.3. Testing Equipment and Conditions.** In the present experiment, the servohydraulic high speed material testing machine [14] shown in Figure 6 was utilized in order to obtain the dynamic failure loads of the spot weld at intermediate strain rates. The machine has a maximum stroke velocity of 7800 mm/s, a maximum load of 30 kN, and a maximum displacement of 300 mm. For the dynamic failure test, the instrument that measures the load and the displacement must have good response in the dynamic motion since failure tests

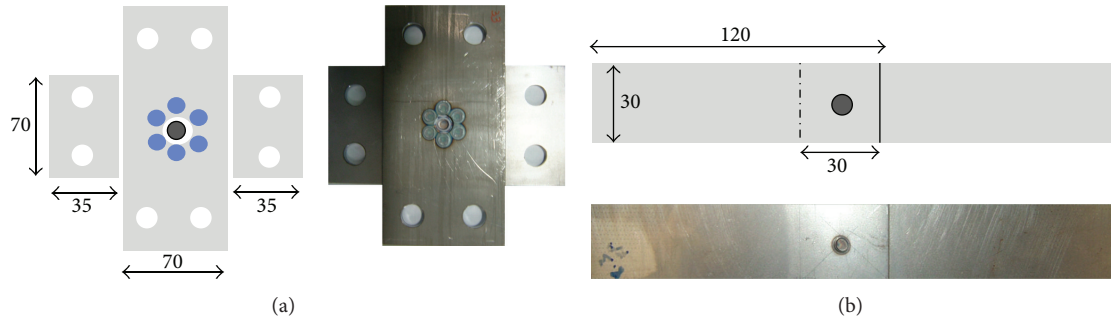


FIGURE 4: Specimens used in the failure test: (a) combined loading tests at loading angles of 0°, 15°, 30°, 45°, 60°, and 75°; (b) pure shear tests at loading angle of 90°.

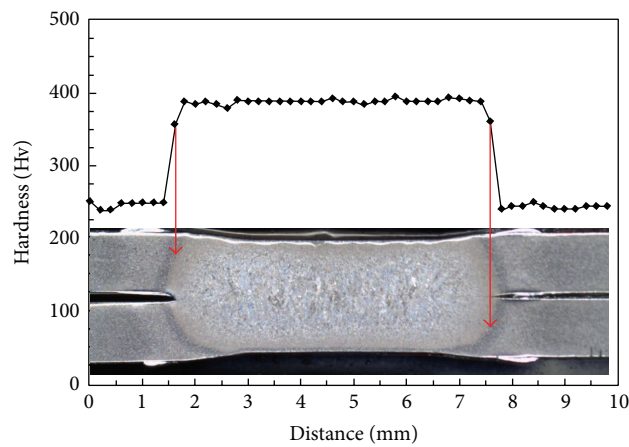


FIGURE 5: Cross-sectional shape and hardness profile of the specimen.



FIGURE 6: High speed material testing machine.

TABLE 1: Chemical composition of steel sheets tested.

Material	Chemical composition [wt%]						
	C	Si	Mn	P	S	Al	Fe
DP590 (thickness: 1.0 mm)	0.073	0.034	1.75	0.075	0.005	0.038	Bal.

TABLE 2: Welding schedule and associated nugget diameter of DP590.

Material	Squeeze time (cycles)	Weld time (cycles)	Hold time (cycles)	Weld current (kA)	Weld force (kN)	Nugget diameter (mm)
DP590 (thickness: 1.0 mm)	20	15	20	7.8	3.5	6.32

TABLE 3: Dynamic failure loads of a spot weld for DP590 at various loading angles.

Loading angle (°)	Failure Load of a spot weld for DP590 1.0t (kN)											
	Quasi-static						Dynamic					
	1 × 10 <sup>-5</sup> m/s			0.01 m/s			0.1 m/s			1.2 m/s		
	1st	2nd	3rd	1st	2nd	3rd	1st	2nd	3rd	1st	2nd	3rd
0°	9.20	9.08	9.29	9.72	9.80	9.63	10.02	9.94	10.08	10.36	10.29	10.21
15°	8.47	8.38	8.61	8.81	8.08	8.94	9.23	9.16	9.35	9.43	9.58	9.69
30°	8.10	8.22	8.34	8.89	8.77	8.73	8.85	9.06	8.98	9.29	9.23	9.36
45°	8.57	8.55	8.73	9.13	9.18	9.26	9.39	9.48	9.43	9.68	9.79	9.56
60°	10.09	9.88	10.13	10.48	10.76	10.63	10.74	10.86	10.92	11.12	11.38	11.23
75°	12.66	12.42	12.47	13.16	13.08	13.23	13.59	13.47	13.76	14.18	13.92	14.03
90°	16.88	17.15	16.92	17.91	18.02	17.68	18.28	18.62	18.45	19.01	18.74	18.89

at intermediate strain rates last only for several milliseconds. The machine equipment is set up with a piezoelectric load cell of Kistler 9051A. The displacement is acquired by a linear displacement transducer (LDT) from Sentech Company. The testing fixtures were mounted in the high speed material testing machine as shown in Figure 6. Dynamic failure tests at the different tensile speeds of  $1 \times 10^{-5}$  m/s, 0.01 m/s, 0.1 m/s, and 1.2 m/s were conducted under seven different loading conditions until the spot weld failed and the specimen separated into two components. The load and displacement were measured simultaneously during each test. The load was measured using the load cell in the testing machine and the displacement was calculated from the relative movement of the two pull bars.

### 3. Evaluation of Dynamic Effect on the Failure Load of a Spot Weld

**3.1. Failure Loads with Various Loading Angles and Loading Speeds.** With the testing conditions described in Section 2.3, dynamic failure tests were carried out at seven different loading angles to evaluate the dynamic impact failure load of the spot-welded specimen. Figure 7 shows load-displacement curves for spot-welded DP590 specimens at various loading angles with different tensile speeds of  $1 \times 10^{-5}$  m/s, 0.01 m/s, 0.1 m/s, and 1.2 m/s. The figure shows that the maximum load decreases as the loading angle increases when the loading angle is less than 30°, whereas the maximum load increases as the loading angle increases at the interval from 45° to 90°. Figure 8 shows the typical load-displacement curves for spot-welded DP590 specimens at the loading angles of 0°, 45°, and 90° with different loading speeds. The figure shows that the maximum load for spot welds in DP590 steels increases when the imposed strain rate increases. When the tensile speeds change from  $1 \times 10^{-5}$  m/s, which is almost

quasi-static states, to 1.2 m/s, the maximum load for spot-welded DP590 increases by approximately 13%. Failure loads obtained from tests for spot-welded DP590 specimens at various loading angles and strain rates were listed in Table 3. Figure 9 represents the deformed shapes of the specimens made of DP590 at the onset of failure at various loading angles with the tensile speed of 1.2 m/s. Shear failure mode was observed around the circumferential boundary of the nugget as shown in Figure 9, when the pure axial load acts on the spot weld at the loading angle of 0°. For combined axial and shear loading conditions, failure is initiated with the localized necking in the interface between the HAZ and the base metal. A similar failure mechanism was also observed in the quasi-static experimental results [13, 15].

**3.2. Dynamic Sensitivity of the Failure Load and Failure Contours.** Failure contours of a spot weld at different tensile speeds were also constructed by decomposing the failure loads measured in the experiment into two components along the axial and shear directions. These were plotted in the force domain as shown in Figure 10, which shows that the failure contour expands as the tensile speed increases. In order to examine the effect of the tensile speeds on the failure load of spot welds, the axial and shear failure loads were plotted in a logarithmic scale of the tensile speeds as shown in Figure 11. The figure shows that the axial and shear failure load increase as the tensile speeds increase. Moreover, the dynamic sensitivity can be interpolated in terms of the quasi-static failure load and the logarithm of the tensile speeds. Dynamic sensitivity of the failure loads at various loading angles was also investigated. The dynamic failure loads at various loading angles were normalized by the quasi-static loads as  $\bar{F}(v) = F(v)/F_0(v_0)$ , where  $F_0(v_0)$  denotes the quasi-static failure load at a given loading angle. The normalized failure loads of spot-welded DP590 specimens were plotted in

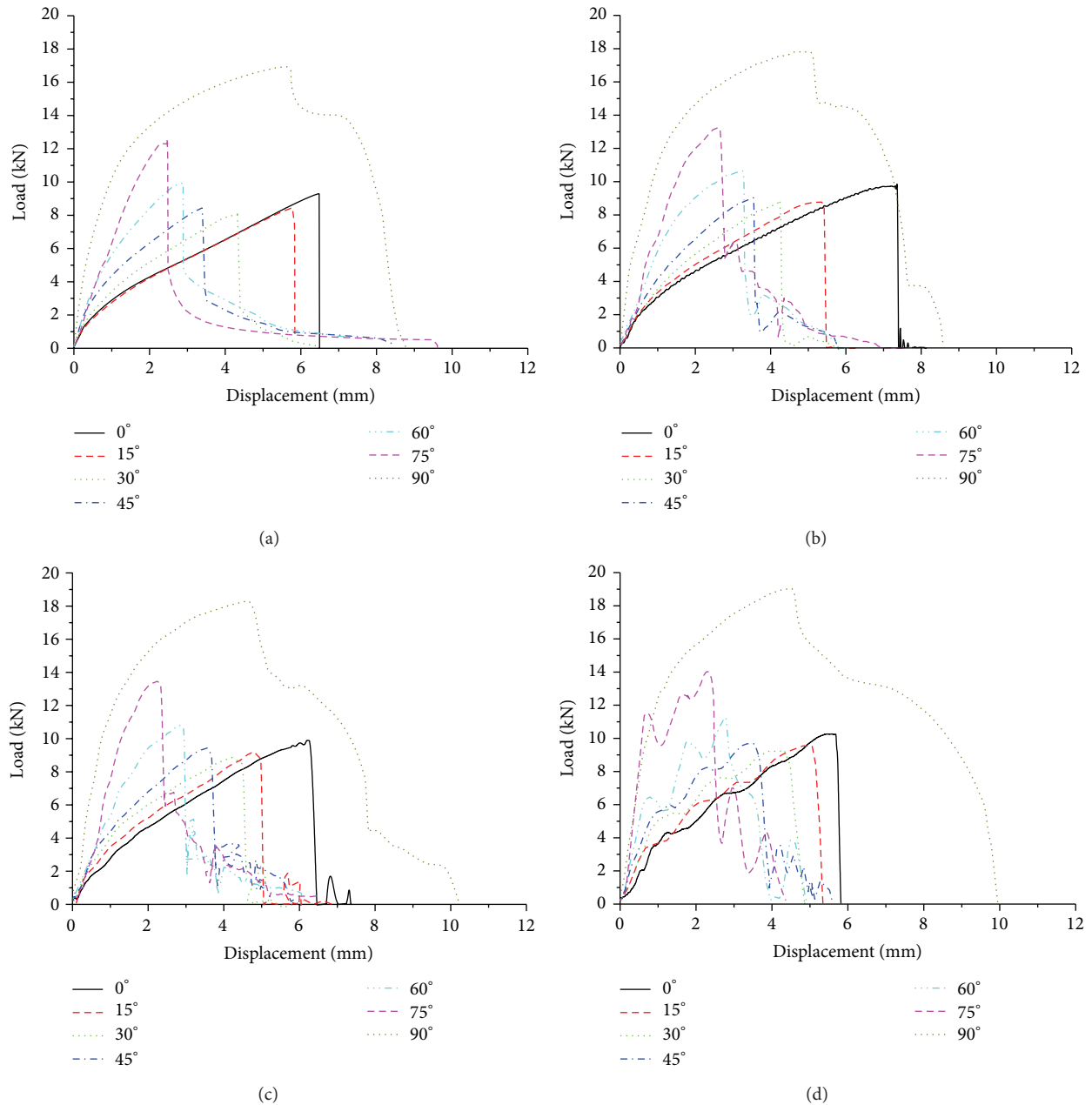


FIGURE 7: Load-displacement curves of spot-welded specimens for DP590 at various loading speeds: (a) quasi-static ( $1 \times 10^{-5}$  m/s); (b) dynamic (0.01 m/s); (c) dynamic (0.1 m/s); (d) dynamic (1.2 m/s).

Figure 12 at various loading angles. The figure shows that the tensile speeds have effects on the normalized failure loads for a given tensile loading angle while the normalized failure loads at a given tensile speed are insensitive to the loading angles, which implies that the failure loads show similar dynamic sensitivity with respect to the loading angles.

#### 4. Conclusion

In this paper, effects of tensile speeds on the failure load of a DP590 spot weld are evaluated under combined axial and shear loading conditions. Dynamic failure tests of spot welds were conducted at seven different combined loading conditions in order to obtain the dynamic failure loads of spot welds at the tensile speed from quasi-static to 1.2 m/s. The experimental results indicated that the failure load decreases as the loading angle increases when the loading angle is less than  $30^\circ$ , whereas the failure load increases as the loading

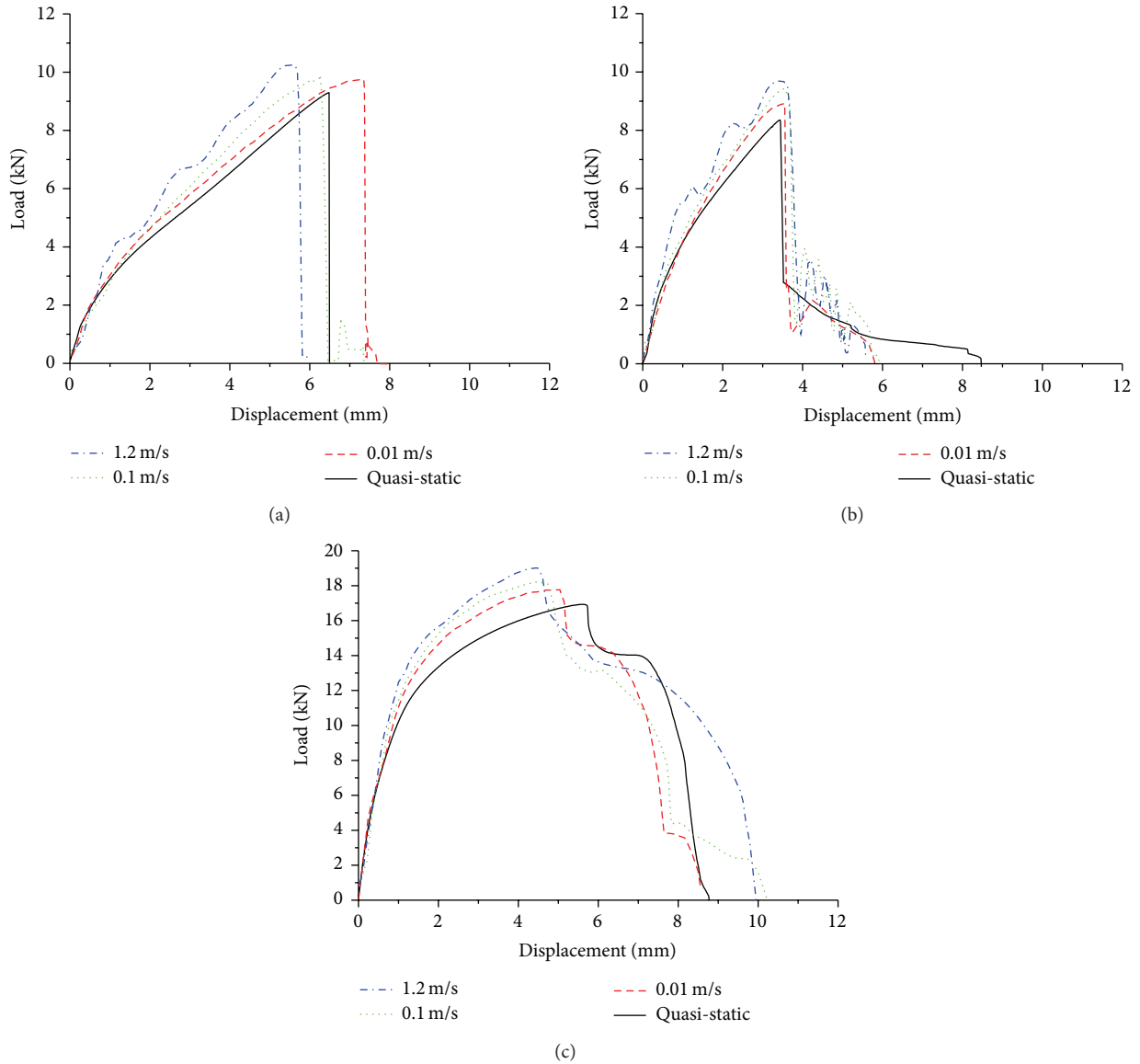


FIGURE 8: Load-displacement curves of spot-welded specimens for DP590 at various loading angles: (a) 0°; (b) 45°; (c) 90°.

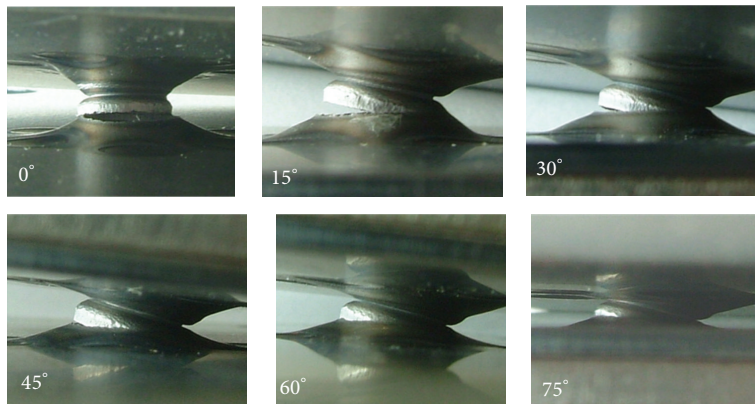


FIGURE 9: Deformed shape of the specimen made of DP590 spot welds at various loading angles with the tensile speed of 1.2 m/s.

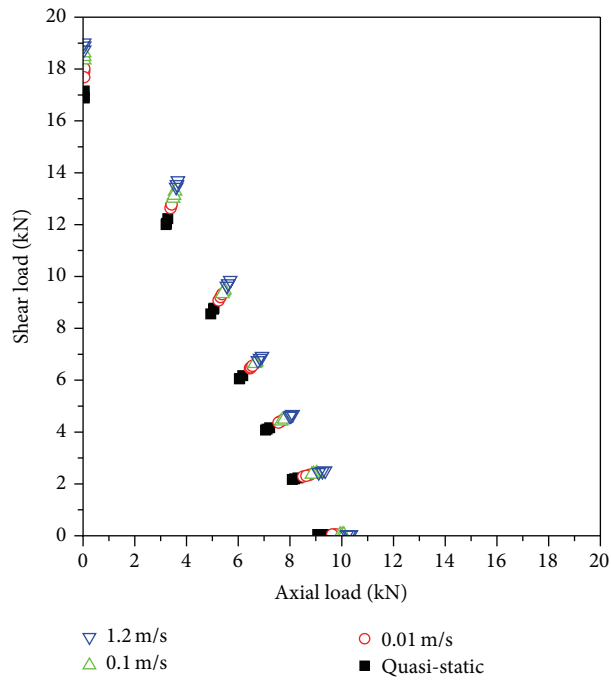


FIGURE 10: Dynamic failure contour of the DP590 spot weld with various tensile speeds.

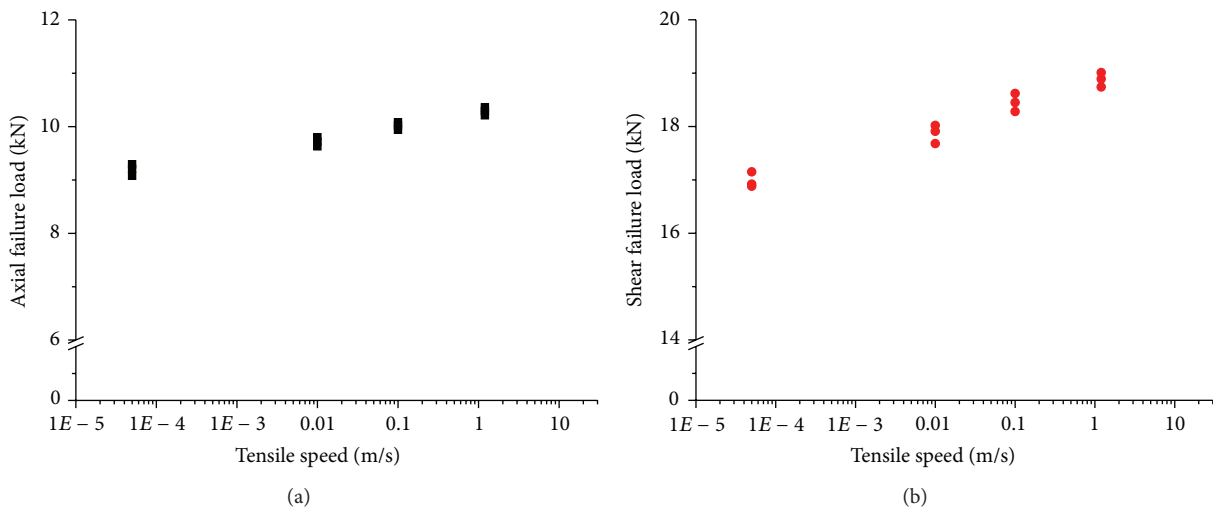


FIGURE 11: Dynamic sensitivity of failure loads of DP590 spot weld: (a) axial failure load; (b) shear failure load.

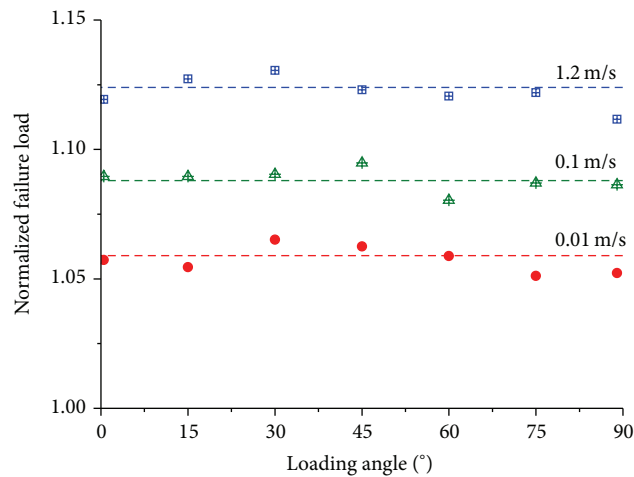


FIGURE 12: Normalized failure loads of a DP590 spot weld at various loading angles.

angle increases at the interval from 45° to 90°. Failure contours of a spot weld at different tensile speeds were also constructed by decomposing the failure loads measured in the experiment into two components along the axial and shear directions. The constructed failure contours indicate that failure contour expands as the tensile speed increases. The results also revealed that dynamic sensitivity can be interpolated in terms of the quasi-static failure load and the logarithm of the tensile speeds. Moreover, the failure loads show similar dynamic sensitivity with respect to the loading angles.

### Conflict of Interests

The authors declare that there is no conflict of interests regarding the publication of this paper.

### References

- [1] N. Farabi, D. L. Chen, J. Li, Y. Zhou, and S. J. Dong, "Microstructure and mechanical properties of laser welded DP600 steel joints," *Materials Science and Engineering A*, vol. 527, no. 4-5, pp. 1215–1222, 2010.
- [2] N. Farabi, D. L. Chen, and Y. Zhou, "Microstructure and mechanical properties of laser welded dissimilar DP600/DP980 dual-phase steel joints," *Journal of Alloys and Compounds*, vol. 509, no. 3, pp. 982–989, 2011.
- [3] S. Zhang, "Fracture mechanics solutions to spot welds," *International Journal of Fracture*, vol. 112, no. 3, pp. 247–274, 2001.
- [4] S. Zuniga and S. D. Sheppard, "Resistance spot weld failure loads and modes in overload conditions," in *Fatigue and Fracture Mechanics*, ASTM STP 1296, pp. 469–489, American Society for Testing and Materials, West Conshohocken, Pa, USA, 1997.
- [5] M. Marya, K. Wang, L. G. Hector Jr., and X. Gayden, "Tensile-shear forces and fracture modes in single and multiple weld specimens in dual-phase steels," *Transactions of the ASME Journal of Manufacturing Science and Engineering*, vol. 128, no. 1, pp. 287–298, 2006.
- [6] Y. J. Chao, "Ultimate strength and failure mechanism of resistance spot weld subjected to tensile, shear, or combined tensile/shear loads," *Journal of Engineering Materials and Technology*, vol. 125, no. 2, pp. 125–132, 2003.
- [7] R. S. Birch and M. Alves, "Dynamic failure of structural joint systems," *Thin-Walled Structures*, vol. 36, no. 2, pp. 137–154, 2000.
- [8] F. Schneider and N. Jones, "Influence of spot-weld failure on crushing of thin-walled structural sections," *International Journal of Mechanical Sciences*, vol. 45, no. 12, pp. 2061–2081, 2003.
- [9] E. Bayraktar, D. Kaplan, C. Buirette, and M. Grumbach, "Application of impact tensile testing to welded thin sheets," *Journal of Materials Processing Technology*, vol. 145, no. 1, pp. 27–39, 2004.
- [10] X. Sun and M. A. Khaleel, "Dynamic strength evaluations for self-piercing rivets and resistance spot welds joining similar and dissimilar metals," *International Journal of Impact Engineering*, vol. 34, no. 10, pp. 1668–1682, 2007.
- [11] M. I. Khan, M. L. Kuntz, and Y. Zhou, "Effects of weld microstructure on static and impact performance of resistance spot welded joints in advanced high strength steels," *Science and Technology of Welding and Joining*, vol. 13, no. 3, pp. 294–304, 2008.
- [12] N. Khandoker and M. Takla, "Tensile strength and failure simulation of simplified spot weld models," *Materials and Design*, vol. 54, pp. 323–330, 2014.
- [13] J. H. Song and H. Huh, "Failure characterization of spot welds under combined axial/shear loading conditions," *International Journal of Mechanical Sciences*, vol. 53, no. 7, pp. 513–525, 2011.
- [14] H. Huh, S.-B. Kim, J.-H. Song, and J.-H. Lim, "Dynamic tensile characteristics of TRIP-type and DP-type steel sheets for an auto-body," *International Journal of Mechanical Sciences*, vol. 50, no. 5, pp. 918–931, 2008.
- [15] S.-H. Lin, J. Pan, T. Tyan, and P. Prasad, "A general failure criterion for spot welds under combined loading conditions," *International Journal of Solids and Structures*, vol. 40, no. 21, pp. 5539–5564, 2003.

## Research Article

# Characteristics of Nanophase WC and WC-3 wt% (Ni, Co, and Fe) Alloys Using a Rapid Sintering Process for the Application of Friction Stir Processing Tools

Daeup Kim,<sup>1</sup> Young Choi,<sup>1</sup> Yongil Kim,<sup>2</sup> and Seungboo Jung<sup>2</sup>

<sup>1</sup>Korea Institute of Industrial Technology (KITECH), 838-11 Palbok-dong 2-ga, Deokjin-gu, Jeonju, Jeollabuk-do 531-202, Republic of Korea

<sup>2</sup>SKKU Advanced Institute of Nanotechnology (SAINT), Sungkyunkwan University, 300 Cheoncheon-dong, Jangan-gu, Suwon, Gyeonggi-do 440-746, Republic of Korea

Correspondence should be addressed to Daeup Kim; [dukim@kitech.re.kr](mailto:dukim@kitech.re.kr)

Received 28 November 2014; Accepted 26 December 2014

Academic Editor: Kwangho Kim

Copyright © 2015 Daeup Kim et al. This is an open access article distributed under the Creative Commons Attribution License, which permits unrestricted use, distribution, and reproduction in any medium, provided the original work is properly cited.

Microstructures and mechanical characteristics of tungsten carbide- (WC-) based alloys, that is, WC, WC-3 wt% Ni, WC-3 wt% Co, and WC-3 wt% Fe, fabricated using a spark plasma sintering (SPS) method for the application of friction stir processing tools were evaluated. The sintered bodies with a diameter of 66 mm showed relative densities of up to 99% with an average particle size of 0.26~0.41  $\mu\text{m}$  under a pressure condition of 60 MPa with an electric current for 35 min without noticeable grain growth during sintering. Even though no phase changes were observed after the ball milling process the phases of  $\text{W}_2\text{C}$  and  $\text{WC}_{1-x}$  appeared in all sintered samples after sintering. The Vickers hardness and fracture toughness of the WC, WC-3 wt% Ni, WC-3 wt% Co, and WC-3 wt% Fe samples ranged from 2,240  $\text{kg mm}^{-2}$  to 2,730  $\text{kg mm}^{-2}$  and from 6.3  $\text{MPa}\cdot\text{m}^{1/2}$  to 9.1  $\text{MPa}\cdot\text{m}^{1/2}$ , respectively.

## 1. Introduction

The trend of energy savings and the enhanced environmental regulations have promoted the substitutional usage of lighter parts in industries recently. However, bonding two dissimilar materials has been a bottleneck to overcome in manufacturing process. Friction stir welding (FSW) that is well known for a joining process of dissimilar materials, especially aluminum-based alloys and other soft alloys, has been applied widely [1–5].

The FSW tool typically consists of a rotating round shoulder and a threaded cylindrical pin and heats up the workpiece mostly by mechanical friction and displaces the softened workpiece around it, eventually to form the bonding joint. Since FSW process does not involve the melting of bulk workpiece, the common problems of fusion welding such as the solidification and liquidation cracking, the porosity formation, and the loss of volatile alloying elements can be avoided. Compared to conventional other joining processes, FSW process sustains excellent mechanical properties of

bonded joint and rarely deforms the workpiece after joining process, since process involves heating the workpiece minimally below the melting temperature and relatively localized joining area. However, the FSW tool itself can be subjected to severe stress and high temperatures, particularly for the cases of welding of hard alloys, such as steels and titanium alloys. Therefore, the commercial application of FSW to these alloys has been limited by the high cost and short life of FSW tools [6, 7]. Although significant efforts [8, 9] have been made in order to develop cost-effective and reusable tools, most of the efforts have not been successful for the commercial applications and further work is needed for an improvement of tool to utilize the practice of FSW for joining of hard materials.

In general, WC has been widely used as processing tools because of an excellent mechanical strength with high melting point and wear resistance and therefore is considered to be a suitable candidate for a long life FSW tool with improved toughness by an addition of metal binders, such as cobalt and nickel. In order to make a WC tool, it is also

critical to control the grain size because grain growth usually occurs during conventional sintering process of WC powder [10]. It was reported that an initial grain size increased more than five times during conventional sintering, hot pressing (HP), or hot isostatic pressing (HIP) processes [11]. Jeong et al. also reported that the particle size increased up to about 300 nm from 100 nm even with an addition of particle growth inhibitor [12].

Recently, the enhanced rapid sintering process called spark plasma sintering (SPS) has been developed for the dramatically reduced sintering time by employing high-frequency induction heating and pressure simultaneously, which reveals superior sintering properties [13, 14].

In the current study, the SPS process is employed to sinter WC powder with binders (Fe, Ni, and Co) for 35 min and the sintered bodies of a diameter of 66 mm were fabricated to form FSW tools. Effects of binder kind and composition on the microstructures and mechanical properties of sintered bodies were investigated and compared to the results of the previous research.

## 2. Experimental Procedure

In this study, 99.95% pure tungsten carbide ( $0.5 \mu\text{m}$ ), 99.5% pure ferrum ( $10 \mu\text{m}$ ), 99.5% pure nickel ( $10 \mu\text{m}$ ), and 99.5% pure cobalt ( $10 \mu\text{m}$ ) were used as powder materials. Horizontal ball milling was carried out at 250 rpm for 48 h under the conditions that tungsten carbide and binders (Fe, Ni, and Co) were mixed with a weight ratio of 97:3 and the weight ratio of the powder to balls was 2:1. The particle sizes of initial powders and the ball milled powders were measured using a particle size analyzer.

After the mixed powders were placed in a graphite die (outside diameter, 140 mm; inside diameter, 66 mm; height, 160 mm), it was sealed top and bottom by graphite punches. Then, it was placed into a system and spark plasma sintered as shown in Figure 1. A pressure of 60 MPa was applied in vacuum and a 30,000 A current was imposed through punches during sintering process. Heating was carried out gradually as in Figure 2. When there is no more shrinkage displacement of the sintered body, the current was turned off and the sintered body was cooled in the chamber. The sintered bodies for FSW tool application were fabricated.

Apparent density was measured with the fabricated sintered bodies. Microstructure of the sintered bodies was observed after being etched using Murakami reagent (5 g  $\text{K}_3\text{Fe}(\text{CN})_6$ , 5 g NaOH, and 50 mL distilled water) for 4 minutes at room temperature. Qualitative and quantitative analysis were carried out for the phases through field-emission scanning electron microscopy (FE-SEM) and energy dispersive spectrometer (EDS). Also, phase analysis and grain size were measured using X-ray diffractometer. The mechanical properties of the sintered bodies were evaluated by hardness and fracture toughness. Hardness was taken using a Vickers hardness tester by performing indentation tests at a load of 30 kgf and a dwell time of 15 s. Fracture toughness was calculated with indentations produced via hardness measurement.

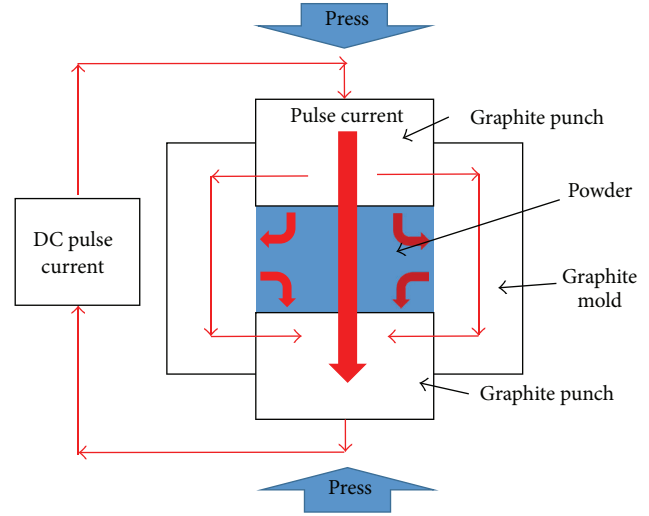


FIGURE 1: Schematic diagram of the apparatus for spark plasma sintering.

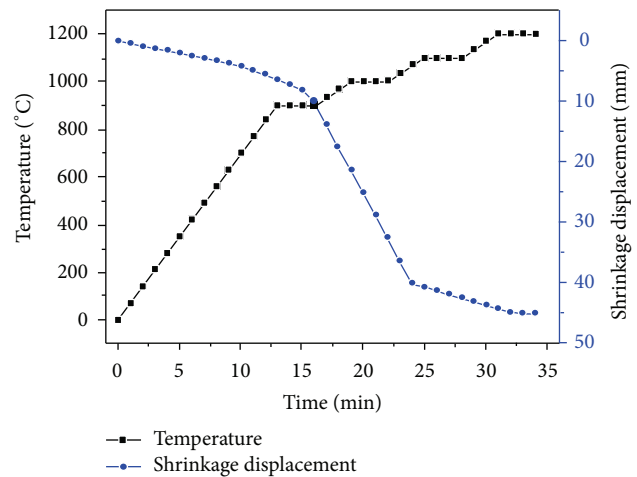


FIGURE 2: Variations of temperature and shrinkage as a function of heating time during spark plasma sintering of WC-3 wt% Co powder.

## 3. Results and Discussion

Figure 3 shows the FE-SEM images of WC and WC-3 wt% Ni, WC-3 wt% Co, and WC-3 wt% Fe powders after ball milling process. The initial powder size of  $10 \mu\text{m}$  was decreased in the size of  $0.1\text{--}0.3 \mu\text{m}$  in all powders after ball milling and also its values were similar to the result of particle size analyzer. All powders had sphere and polygonal shapes and were shown as the aggregation of the powder particles slightly. It seems that the initial powders with sphere and cylinder shapes were mixed enough during ball milling process because of pulverization between hard metal ball and the powder. The relative densities of WC, WC-3 wt% Fe, WC-3 wt% Ni, and WC-3 wt% Co sintered bodies were measured after SPS process. They were shown to be 99.5%, 98.8%, 99.6%, and 98.9%, relatively.

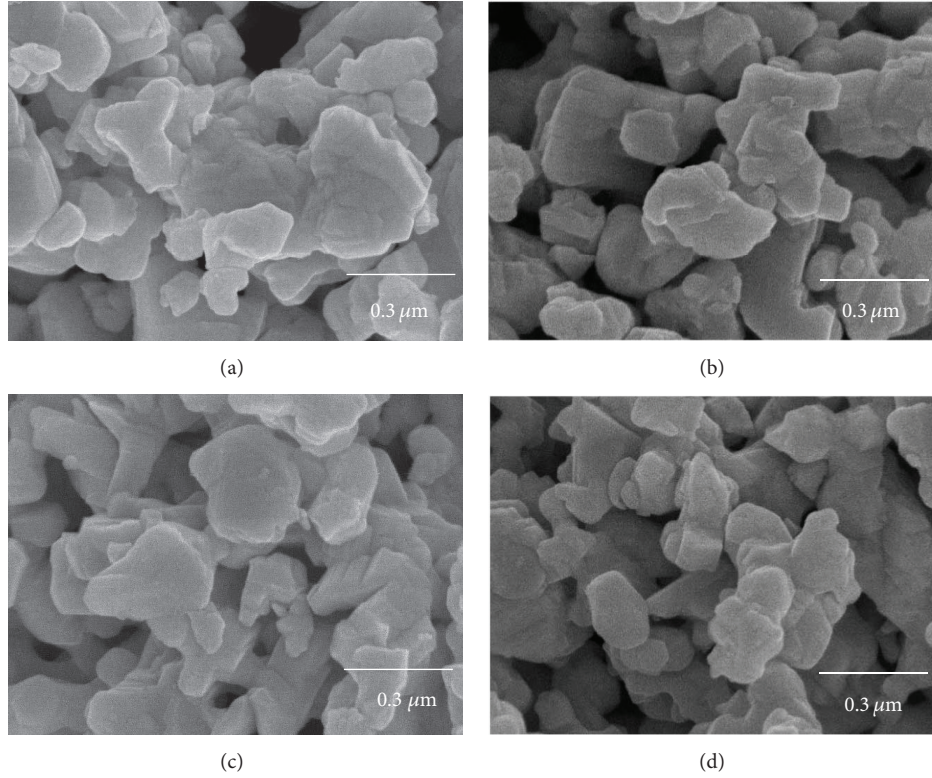


FIGURE 3: FE-SEM images of powders after ball milling: (a) WC, (b) WC-3 wt% Fe, (c) WC-3 wt% Ni and (d) WC-3 wt% Co.

Figure 4 shows the microstructure of each sintered body. Fine grains and dense structure were formed in the sintered bodies. Fine grains formed dense structure at all sintered bodies overall. The WC, WC-3 wt% Fe, and WC-3 wt% Ni sintered bodies had polygonal grains structure and WC-3 wt% Co sintered body was observed to have the round shaped grains. In addition, WC was surrounded by Fe, Ni, and Co binders in the sintered bodies. Meanwhile, the grain size of each sintered body was measured by a linear analysis method. The average grain size of WC sintered body was about  $0.45 \mu\text{m}$  and it was slightly larger than that of WC-3 wt%  $X$  ( $X = \text{Fe, Ni, Co}$ ) sintered bodies. In addition to the XRD analysis, the grain size was calculated using the Suryanarayana and Grant Norton's formula [15]:

$$\text{Br} (B_{\text{crystalline}} + B_{\text{strain}}) \cos \theta = \frac{k\lambda}{L} + \eta \sin \theta, \quad (1)$$

where Br is the sum of  $B_{\text{crystalline}}$  and  $B_{\text{strain}}$ , meaning the increases in full width at half maximum (FWHM) by refinement and by strain, respectively.  $k$  is the Boltzmann constant (with a value of 0.9),  $\lambda$  is the wavelength of X-ray radiation,  $L$  is the grain size,  $\eta$  is the strain, and  $\theta$  is the Bragg angle. The average grain sizes of WC, WC-3 wt% Fe, WC-3 wt% Ni, and WC-3 wt% Co sintered bodies were shown to be  $0.41 \mu\text{m}$ ,  $0.26 \mu\text{m}$ ,  $0.30 \mu\text{m}$ , and  $0.27 \mu\text{m}$ , respectively, and they were not significantly different in microstructure analysis. Grain growth did not occur in sintered bodies and also its size was almost the same as initial powder size; it seems that SPS process is processed with short time and single process. Kim et al. reported that the more the content of a binder increases,

the more the sintering proceeds at low temperature. Thus, the grain size became smaller. As the content of a binder decreases, WC particles have chance to contact each other, which means easy particle growth. In this study, the grain size of WC sintered body was larger than the sintered bodies with binders due to the effect of added binders. Also, the grain size had no difference according to the composition of a binder and binder material does not have effect on the grain size.

On the basis of the microstructure observation as shown in Figure 4, mapping analysis was carried out by EDS to observe phases for each sintered body. Figure 5 shows the mapping result of WC-3 wt% Ni sintered body. The W and C were distributed generally but Ni was distributed mainly around grain boundaries. Also, Fe and Co contents were distributed around the grain boundaries of WC in WC-3 wt% Fe and WC-3 wt% Co sintered bodies. From these results, it was observed that Fe, Ni, and Co particles as binders smeared into gaps between WC particles during sintering and they surrounded the WC particles through liquid phase sintering. The result of qualitative and quantitative analysis in the midsection of WC-3 wt% Co sintered body is shown in Figure 6. There was no element except W, C, and Co in EDS analysis. The sintered body of the other compositions could obtain in the same result.

For each sintered body, XRD analysis was carried out to get detailed phase analysis before and after sintering. Figure 7 shows the analysis results after sintering, ball milling, and the initial powder of WC and WC-3 wt% Fe sintered body. The phase of WC and Fe existed in all initial powders and the ball milled powders. However the phases of  $\text{W}_2\text{C}$  and  $\text{WC}_{1-x}$  in

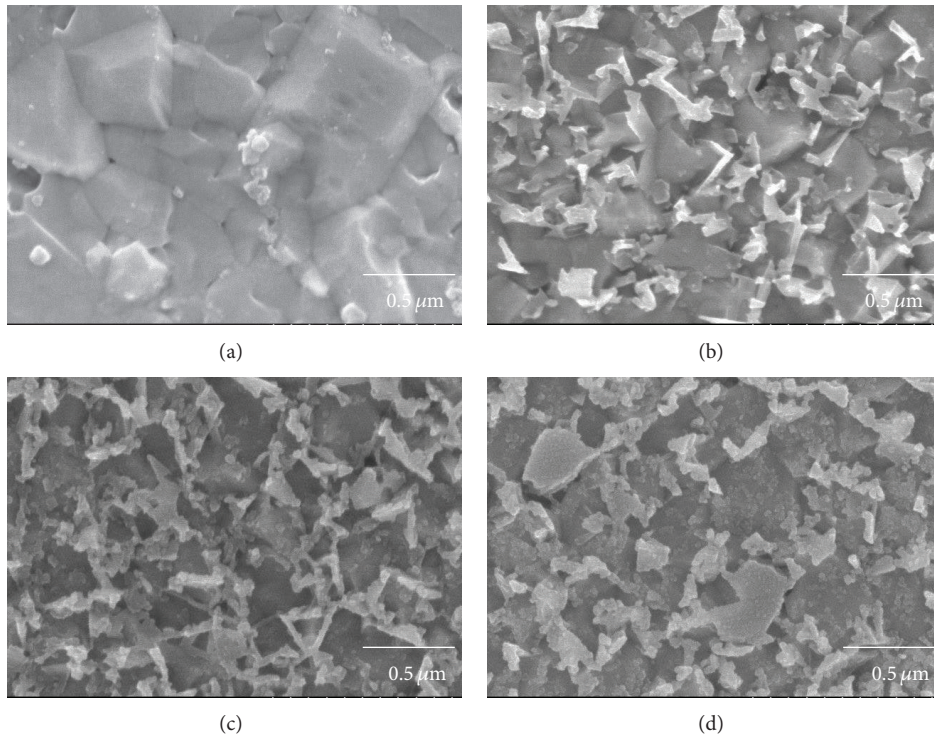


FIGURE 4: Microstructures of sintered hard materials: (a) WC, (b) WC-3 wt% Fe, (c) WC-3 wt% Ni, and (d) WC-3 wt% Co.

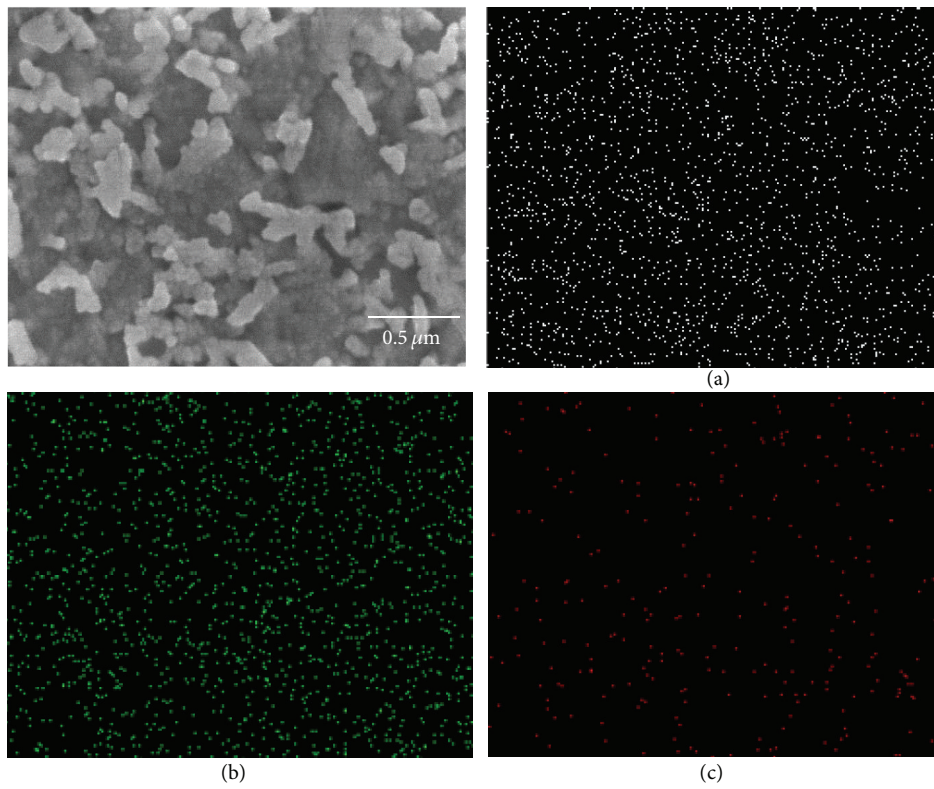


FIGURE 5: EDS mapping result of WC-3 wt% Ni sintered body.

TABLE 1: Mechanical properties of sintered hard materials.

Sintered material (wt%)	Relative density (%)	Vickers hardness ( $Hv$ )	Fracture toughness ( $\text{MPa}\cdot\text{m}^{1/2}$ )	Grain size ( $\mu\text{m}$ )	Reference
WC	99.5	2,730	6.3	0.41	
WC-3 Fe	98.8	2,242	6.8	0.26	<b>This study</b>
WC-3 Ni	99.6	2,240	9.1	0.30	
WC-3 Co	98.9	2,269	7.4	0.27	
WC	99	2,660	7.2	0.1	
WC-2.9 Co	98.3	2,014	6.5	0.94	[19]
WC-6 Co	100	1,816	15.1	0.3	[20]
WC-10 Co	98.9	1,333	13.5	1.9	[21]
WC-10 Co	99.5	1,756	11.6	0.38	[22]
WC-10 Fe	99.7	1,814	10.4	0.45	[23]
WC-9.6 Ni-0.4 Co	99.5	1,180	12.5	1.8	[24]

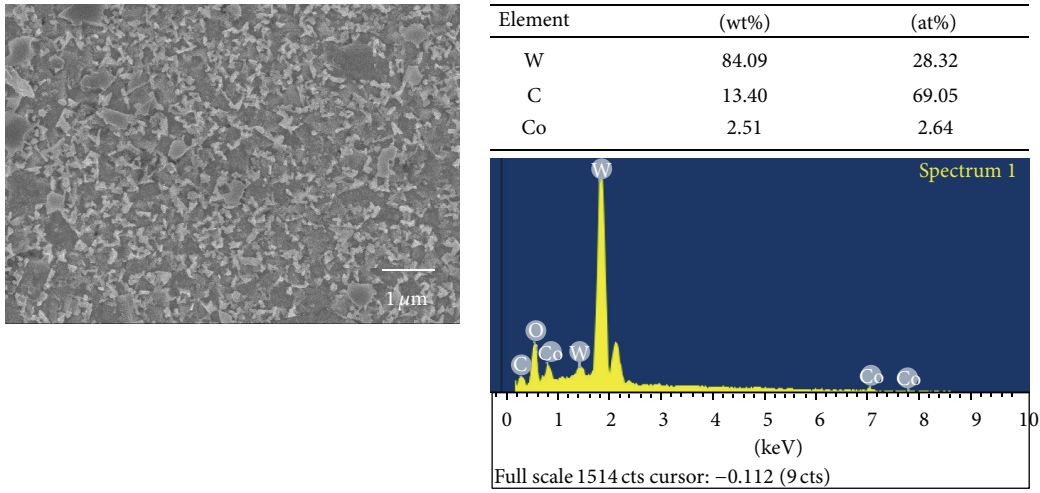


FIGURE 6: EDX analysis result of WC-3 wt% Co sintered body.

all sintered bodies were observed after sintering. Kang et al. reported that only WC peaks were observed in WC sintered body after high-frequency induction heated sintering [14]. Also Youn et al. reported that phase change did not occur in WC-Mo<sub>2</sub>C-Co sintered body which is sintered by SPS process [16]. On the other hand, the W<sub>2</sub>C peaks were observed in the WC sintered body which is sintered by SPS at 1750°C [13]. When the liquid state of Co transformed the solid state during sintering in WC-10 wt% Co using SPS process, Co with HCP crystalline structure transformed stabilized FCC structure after sintering [4]. In this study, the reason that W<sub>2</sub>C and WC<sub>1-x</sub> phases appeared after sintering was that the oxide layer existed on surface of the initial powder reacted with carbon partially and then the content of carbon was decreased. To eliminate W<sub>2</sub>C phases, carbon of 0.5 wt% was added and the result showed no formation of the W<sub>2</sub>C phase [13].

In order to evaluate the mechanical properties of the sintered bodies, hardness and fracture toughness were evaluated using Vickers hardness tester. Table 1 shows the results of Vickers hardness measurement by performing indentation tests. Hardness of WC sintered body was about 2,730 kg mm<sup>2</sup> and those of WC-3 wt% Fe, WC-3 wt% Ni, and WC-3 wt%

Co sintered bodies were in the range from 2,240 kg mm<sup>2</sup> to 2,269 kg mm<sup>2</sup>.

The cracks occurred from the indentation corner as shown in Figure 8. Fracture toughness was calculated by Niihara's formula with crack length:

$$K_{IC} = 0.203 \left( \frac{c}{a} \right)^{-3/2} \cdot Hv \cdot a^{1/2}, \quad (2)$$

where  $c$  is the trace length of the crack that was measured from the center of the indentation,  $a$  is the half of diagonal length of indentation, and  $Hv$  is the Vickers hardness value. Table 1 shows the fracture toughness, the relative density, Vickers hardness value, and grain size from the sintered bodies synthetically and it was compared to other references. In this study, the fracture toughness value of WC-3 wt% Ni sintered body was about 9.1 MPa·m<sup>1/2</sup>, the highest among the four types. The fracture toughness of WC-3 wt% Fe and WC-3 wt% Co was 6.8 MPa·m<sup>1/2</sup> and 7.4 MPa·m<sup>1/2</sup>, respectively. Commonly, hardness and fracture toughness are significant factors to evaluate the mechanical properties in hard metals and they are affected by density, particle size, and content of a binder. The more the content of a binder increases, the more

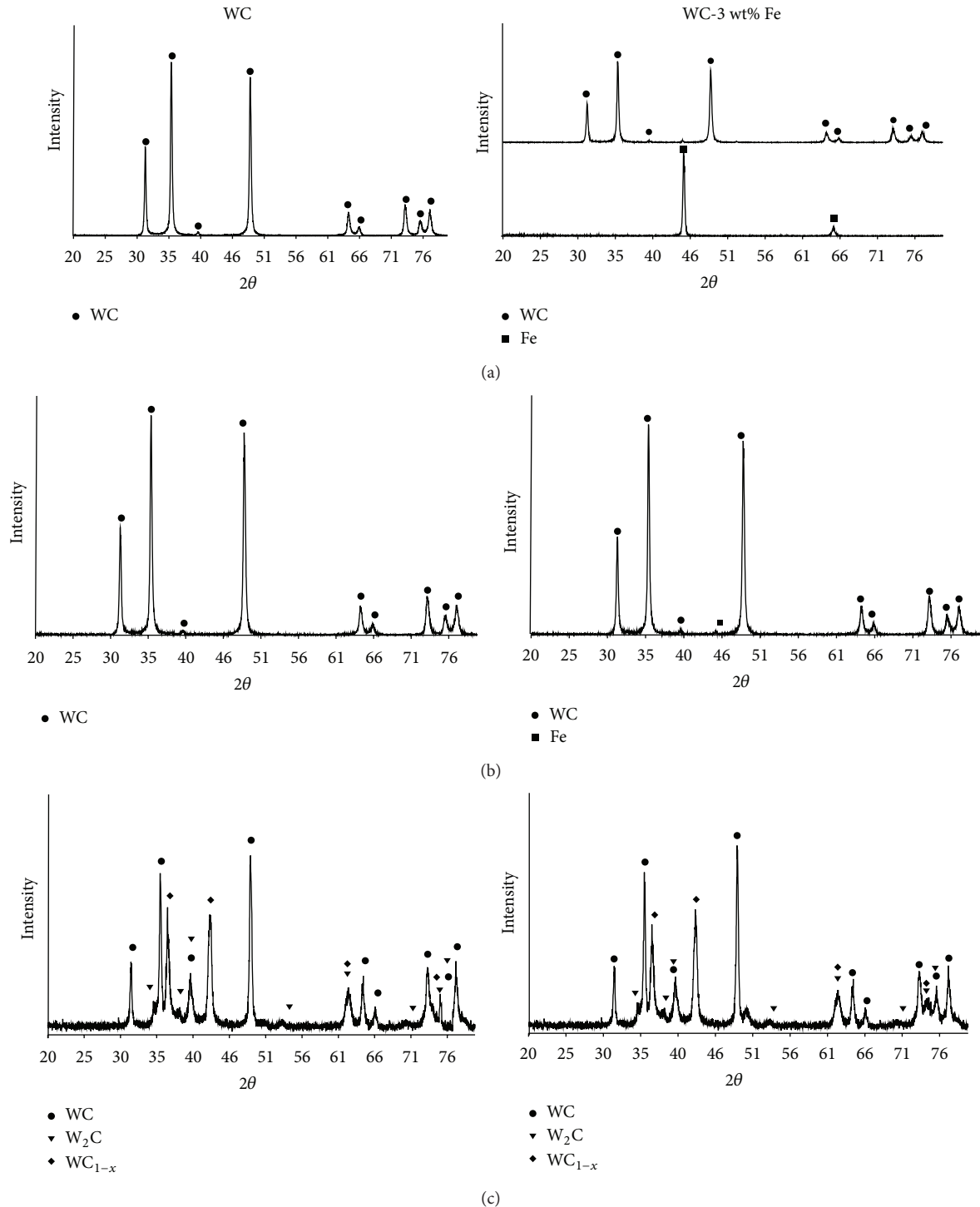


FIGURE 7: XRD patterns of raw powder (a), ball milled (b) and after sintering (c).

the thickness of a binder increases inside of particles; thus hardness increases and fracture toughness decreases [17]. According to the relation of Hall Petch, as the particle size of WC was smaller, hardness increases [18]. As mentioned above, the fracture toughness of sintered body added Ni as a binder indicates that it is higher than that of sintered body added Fe and Co. It is considered that the Fe and Co with

BCC crystalline structure have 4 slip systems while 12 slip systems of Ni with FCC crystalline structure contribute to improving of the fracture of sintered body. Compared to the result of the other research, hardness was little high but fracture toughness did not decrease in the same content of binders. In this study,  $W_2C$ ,  $WC_{1-x}$  phases appeared after sintering but the grain growth did not occur because SPS

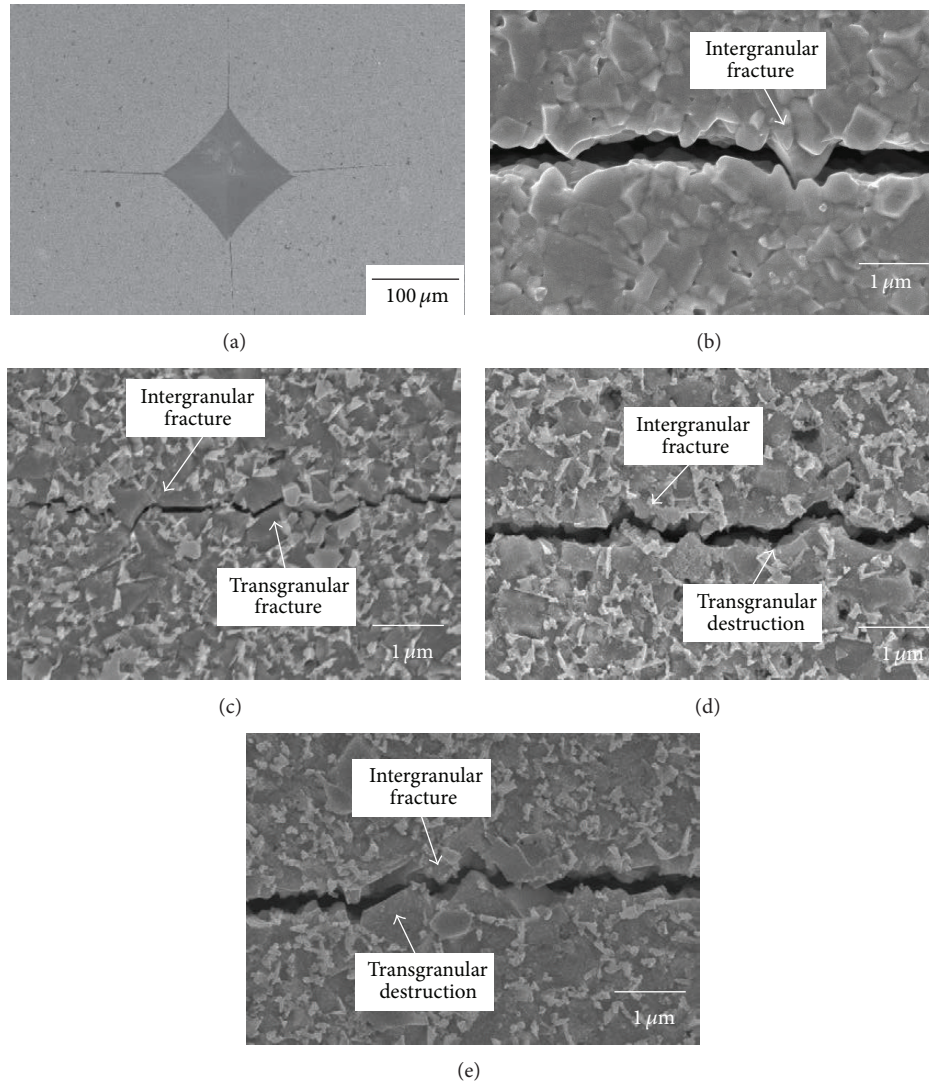


FIGURE 8: Vickers hardness indentation (a) and median crack propagation of sintered hard materials: (b) WC, (c) WC-3 wt% Fe, (d) WC-3 wt% Ni, and (e) WC-3 wt% Co.

process conducted in short amounts of time in comparison with HIP sintering. The relative densities of sintered bodies were about 99% and the dense sintered bodies without pores were made on surface and the center part. Considering the diameter of sintered body was about 66 mm which was bigger than other research results, sintered bodies in this study had excellent mechanical properties.

Figure 8 shows microstructures of propagated cracks from the indentation corner. Generally, most intergranular fractures are known to be caused by grain refinement and the hampered crack growth because cracks usually propagate along intergranular path rather than transgranular one; thus fracture toughness was increased [20]. Intergranular fracture was observed in the WC sintered body (b). Both transgranular and intergranular fractures were observed in the sintered bodies (c~e) that Fe, Ni, and Co binders added. Also it was observed that fracture mode was shifted according to WC particles morphology. It was reported that the intergranular fracture occurred and fracture toughness was improved

in nanosized metals [4]. In this study, most intergranular fractures and minor transgranular fractures were observed and high hardness was obtained and fall of toughness was not observed. The following is the reason of obtaining high strength sintered bodies. Localized high temperature heating and rapid atomic diffusion occurred by a direct current in relatively low sintering temperature within a short time. The superior sintered bodies is characterized by the applied pressure of sintering which serves as a driving force and thereby increases sintering density. Also, Fe, Ni, and Co binders made the stable sintered bodies that liquid phase changed into solid phase on the interface of WC particle. The FSW tool requiring high hardness was considered to have suitable characterization.

#### 4. Conclusion

Tungsten carbide- (WC-) based alloys, that is, WC, WC-3 wt% Ni, WC-3 wt% Co, and WC-3 wt% Fe powders, were

mixed by ball milling and fabricated using a spark plasma sintering method. The microstructures and mechanical characteristics were evaluated. The following is the conclusion.

- (1) The density of the sintered bodies was about 99% and the average grain size was in the range from 0.26 to 0.41  $\mu\text{m}$ . The sintered bodies were obtained without almost grain growth during sintering.
- (2) WC, WC-3 wt% Fe, and WC-3 wt% Ni sintered bodies had polygonal grains and WC-3 wt% Co had slightly round shape grains. Fine and dense microstructure was observed.
- (3) By EDS analysis, the contents of W and C were distributed generally while Fe, Ni, and Co content as a binder mainly surrounded the grain boundary of WC.
- (4) Only initial phase existed in initial powers and the ball milled powders but the phases of  $\text{W}_2\text{C}$  and  $\text{WC}_{1-x}$  in all sintered bodies were observed after sintering.
- (5) Hardness and fracture toughness of sintered WC were 2,730  $\text{kg mm}^{-2}$ , 6.3  $\text{MPa}\cdot\text{m}^{1/2}$ , and those of WC-3 wt% Fe, WC-3 wt% Ni, and WC-3 wt% Co sintered body were 2,240  $\text{kg mm}^{-2}$  ~2,269  $\text{kg mm}^{-2}$  and 6.8~9.1  $\text{MPa}\cdot\text{m}^{1/2}$ , relatively. The fracture toughness of WC-3 wt% Ni showed the highest value among four types.
- (6) WC-3 wt% X (X = Fe, Ni, Co) sintered bodies showed good mechanical property for FSW tool due to its high density and small grain size.

## Conflict of Interests

The authors declare that there is no conflict of interests regarding the publication of this paper.

## References

- [1] P. B. Srinivasan, W. Dietzel, R. Zettler, J. F. dos Santos, and V. Sivan, "Stress corrosion cracking susceptibility of friction stir welded AA7075-AA6056 dissimilar joint," *Materials Science and Engineering A*, vol. 392, no. 1-2, pp. 292-300, 2005.
- [2] K.-S. Bang, K.-J. Lee, and H.-S. Bang, "Interfacial microstructure and mechanical properties of dissimilar friction stir welds between 6061-T6 aluminum and Ti-6%Al-4% V alloys," *Materials Transactions*, vol. 52, no. 5, pp. 974-978, 2011.
- [3] Y. S. Sato, Y. Kurihara, S. H. C. Park, H. Kokawa, and N. Tsuji, "Friction stir welding of ultrafine grained Al alloy 1100 produced by accumulative roll-bonding," *Scripta Materialia*, vol. 50, no. 1, pp. 57-60, 2004.
- [4] H.-K. Park, H.-J. Youn, J.-H. Ryu et al., "Fabrication and mechanical properties of WC-10 wt.% Co hard materials for a friction stir welding tool application by a spark plasma sintering process," *Journal of Ceramic Processing Research*, vol. 13, no. 6, pp. 705-712, 2012.
- [5] K. Nakata, Y. G. Kim, H. Fujii, T. Tsumura, and T. Komazaki, "Improvement of mechanical properties of aluminum die casting alloy by multi-pass friction stir processing," *Materials Science and Engineering A*, vol. 437, no. 2, pp. 274-280, 2006.
- [6] Y. S. Sato, H. Yamanoi, H. Kokawa, and T. Furuhashi, "Microstructural evolution of ultrahigh carbon steel during friction stir welding," *Scripta Materialia*, vol. 57, no. 6, pp. 557-560, 2007.
- [7] K. Lee and K. Bang, "Interfacial microstructure of dissimilar friction stir welds between Al and Ti alloy sheet," *Journal of Korean Welding and Joining Society*, vol. 28, pp. 5-19, 2010 (Korean).
- [8] K. Lee, S. Kim, H. Park, and I. Oh, "Development of the tool for friction stir welding of high temperature materials," *Journal of Korean Welding and Joining Society*, vol. 29, no. 5, pp. 54-57, 2011 (Korean).
- [9] T. Miyazawa, Y. Iwamoto, T. Maruki, and H. Fujii, "Development of Ir based tool for friction stir welding of high temperature materials," *Proceedings of the Japan Welding Society*, vol. 86, article 43, 2010 (Japanese).
- [10] A. Couret, G. Molénat, J. Galy, and M. Thomas, "Microstructures and mechanical properties of TiAl alloys consolidated by spark plasma sintering," *Intermetallics*, vol. 16, no. 9, pp. 1134-1141, 2008.
- [11] K. Jia, T. E. Fischer, and B. Gallois, "Microstructure, hardness and toughness of nanostructured and conventional WC-Co composites," *Nanostructured Materials*, vol. 10, no. 5, pp. 875-891, 1998.
- [12] I. K. Jeong, J. H. Park, J. M. Doh et al., "Mechanical properties and consolidation of ultra-fine WC-10Co and Wc-10Fe hard materials by rapid sintering process," *Journal of the Korean Institute of Metals and Materials*, vol. 46, no. 4, pp. 223-226, 2008.
- [13] J. Zhao, T. Holland, C. Unuvar, and Z. A. Munir, "Spark plasma sintering of nanometric tungsten carbide," *International Journal of Refractory Metals and Hard Materials*, vol. 27, no. 1, pp. 130-139, 2009.
- [14] H.-S. Kang, J.-M. Doh, K.-T. Hong, I.-Y. Ko, and I.-J. Shon, "Rapid sintering of nanostructured tungsten carbide by high-frequency induction heating and its mechanical properties," *Journal of Korean Institute of Metals and Materials*, vol. 48, no. 11, pp. 1009-1013, 2010.
- [15] C. Suryanarayana and M. G. Norton, *X-Ray Diffraction: A Practical Approach*, Plenum Press, New York, NY, USA, 1998.
- [16] H. Youn, H. Bang, I. Oh, and H. Park, "Fabrication and mechanical properties of WC-Mo<sub>2</sub>C-Co hard materials by the pulsed current activated sintering method," *Journal of Korean Institute of Metals and Materials*, vol. 50, no. 12, pp. 921-929, 2012.
- [17] K. Niihara, R. Morena, and D. P. H. Hasselman, "Evaluation of  $K_{Ic}$  of brittle solids by the indentation method with low crack-to-indent ratios," *Journal of Materials Science Letters*, vol. 1, no. 1, pp. 13-16, 1982.
- [18] Y. V. Milman, S. Chugunova, V. Goncharuck, S. Luyckx, and I. T. Northrop, "Low and high temperature hardness of WC-6 wt%Co alloys," *International Journal of Refractory Metals and Hard Materials*, vol. 15, no. 1-3, pp. 97-101, 1997.
- [19] C.-D. Park, H.-C. Kim, I.-J. Shon, and Z. A. Munir, "One-step synthesis of dense tungsten carbide-cobalt hard materials," *Journal of the American Ceramic Society*, vol. 85, no. 11, pp. 2670-2677, 2002.
- [20] H.-K. Park, S.-M. Lee, H.-J. Youn, K.-S. Bang, and I.-H. Oh, "Fabrication and mechanical properties of ultra fine WC-6wt.%co by spark plasma sintering process," *Journal of Korean Institute of Metals and Materials*, vol. 49, no. 1, pp. 40-45, 2011.

- [21] G. R. Anstis, P. Chantikul, B. R. Lawn, and D. B. Marshall, "A critical evaluation of indentation techniques for measuring fracture toughness: I, direct crack measurements," *Journal of the American Ceramic Society*, vol. 64, no. 9, pp. 533–538, 1981.
- [22] L. S. Sigl and H. F. Fischmeister, "On the fracture toughness of cemented carbides," *Acta Metallurgica*, vol. 36, no. 4, pp. 887–897, 1988.
- [23] J.-H. Han and D.-Y. Kim, "Determination of three-dimensional grain size distribution by linear intercept measurement," *Acta Materialia*, vol. 46, no. 6, pp. 2021–2028, 1998.
- [24] H.-C. Kim, H.-K. Park, I.-K. Jeong, I.-Y. Ko, and I.-J. Shon, "Sintering of binderless WC-Mo<sub>2</sub>C hard materials by rapid sintering process," *Ceramics International*, vol. 34, no. 6, pp. 1419–1423, 2008.

## Research Article

# Fabrication of a Microtubular $\text{La}_{0.6}\text{Sr}_{0.4}\text{Ti}_{0.2}\text{Fe}_{0.8}\text{O}_{3-\delta}$ Membrane by Electrophoretic Deposition for Hydrogen Production

Kyoung-Jin Lee, Yeong-Ju Choe, Jun-Sung Lee, and Hae-Jin Hwang

*Department of Materials Science and Engineering, Inha University, 253 Yonghyun-dong, Nam-gu, Incheon 402-751, Republic of Korea*

Correspondence should be addressed to Hae-Jin Hwang; [hjhwang@inha.ac.kr](mailto:hjhwang@inha.ac.kr)

Received 30 November 2014; Revised 25 March 2015; Accepted 6 April 2015

Academic Editor: Simo-Pekka Hannula

Copyright © 2015 Kyoung-Jin Lee et al. This is an open access article distributed under the Creative Commons Attribution License, which permits unrestricted use, distribution, and reproduction in any medium, provided the original work is properly cited.

Microtubular type  $\text{La}_{0.6}\text{Sr}_{0.4}\text{Ti}_{0.2}\text{Fe}_{0.8}\text{O}_{3-\delta}$  (LSTF) membranes were prepared by electrophoretic deposition (EPD). The oxygen permeation and hydrogen production behavior of the membranes were investigated under various conditions. LSTF green layer was successfully coated onto a carbon rod and, after heat treatment at  $1400^\circ\text{C}$  in air, a dense LSTF tubular membrane with a thickness of 250  $\mu\text{m}$  can be obtained. The oxygen permeation and hydrogen production rate were enhanced by  $\text{CH}_4$  in the permeate side, and the hydrogen production rate by water splitting was  $0.22 \text{ mL}/\text{min}\cdot\text{cm}^2$  at  $1000^\circ\text{C}$ . It is believed that hydrogen production via water splitting using these tubular LSTF membranes is possible.

## 1. Introduction

Hydrogen is considered to be a next generation clean and efficient fuel that can be used in electrochemical devices, such as fuel cells or internal combustion engines, to power vehicles or generate electricity. Hydrogen is normally produced by methane steam reforming ( $\text{CH}_4 + 2\text{H}_2\text{O} = 3\text{H}_2 + \text{CO}$ ) or the electrolysis of water because pure hydrogen does not occur naturally on Earth in large quantities. However, the methane steam reforming releases carbon dioxide into the atmosphere and does not help to decrease greenhouse gases. In addition, the electrolysis of water requires large amounts of electricity to decompose water and produce hydrogen.

Hydrogen production by high temperature water splitting ( $\text{H}_2\text{O} \rightleftharpoons \text{H}_2 + 1/2\text{O}_2$ ) is one of the most important long-term goals in hydrogen fuel production [1, 2]. Since the equilibrium constant of the water splitting reaction is very small, it generates very low concentrations of hydrogen and oxygen, even at high temperatures (0.1% hydrogen and 0.042% oxygen at  $1600^\circ\text{C}$ ). This limitation of water dissociation can be overcome by controlling the thermodynamic equilibrium. If the produced oxygen or hydrogen can be removed from the reactor, the equilibrium is shifted towards the dissociation of water, thereby increasing the hydrogen production rate up to a realistic level.

Putting this in mind, water splitting via an oxygen transport membrane (OTM) is one of the most promising routes for sustainable hydrogen production without releasing carbon dioxide. Dissociated oxygen can be selectively transported outside the reactor through the OTM, and the hydrogen production rate depends on the rate at which oxygen is removed from the reactor. Therefore, an OTM with high oxygen permeability (i.e., excellent mixed ionic and electronic conductivity and good oxygen surface exchange kinetics [3, 4]) is required.

Perovskite-type oxides have been widely used as oxygen transport membrane materials because of their high oxygen permeability and good durability at high temperatures (both in oxidized and reduced atmospheres). Strontium and cobalt codoped barium ferrite (BSCF) are the most common materials for OTMs. Although BSCF shows excellent oxygen ionic and electronic transport properties, it suffers from a large thermal expansion coefficient and long-term structural and electrochemical instability, especially in atmospheres containing carbon dioxide.

Alternatively, lanthanum and iron codoped strontium titanate ( $\text{La}_{1-x}\text{Sr}_x\text{Ti}_{1-y}\text{Fe}_y\text{O}_{3-\delta}$  (LSTF)) has been developed as an OTM material by some researchers. Unlike cobalt, which exists at the B site of the perovskite  $\text{ABO}_3$ , titanium is less likely to undergo valence changes and provides a more

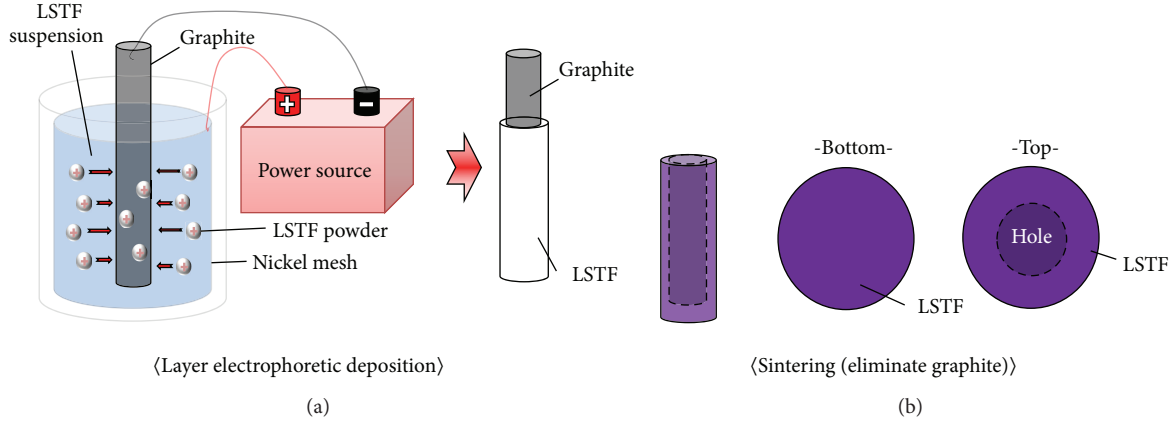


FIGURE 1: Schematic diagram of the (a) EPD process and (b) sintering process.

stable crystal structure in a reducing atmosphere. The substitution of Fe by Ti is expected to improve durability and to lower the cost of materials. In addition, titanium-doped perovskite materials have been reported to catalyze the methane reforming reaction [5]. In this study, a dense microtubular  $\text{La}_{0.6}\text{Sr}_{0.4}\text{Ti}_{0.2}\text{Fe}_{0.8}\text{O}_{3-\delta}$  (LSTF) membrane was fabricated by electrophoretic deposition (EPD). The microstructure and oxygen permeation behavior of this material were investigated.

## 2. Experimental Procedure

**2.1. Preparation of a Microtubular Membrane by EPD.** LSTF powders were synthesized from  $\text{La}_2\text{O}_3$  (99.9%, YAKURI, Japan),  $\text{SrCO}_3$  (99.9%, Sigma Aldrich, USA),  $\text{TiO}_2$  (99.9%, High Purity Chemicals, Japan), and  $\text{Fe}_2\text{O}_3$  (99.9%, High Purity Chemicals, Japan) by a solid state reaction technique. The starting materials were mixed using a planetary ball mill and then calcined at  $1000^\circ\text{C}$  for 5 h.

Microtubular LSTF membranes were fabricated using a sealless tube design by electrophoretic deposition (EPD), as shown in Figure 1(a). EPD is a colloidal deposition technique that has been proven to be simple and inexpensive for the production of many advanced ceramics bodies. EPD is recognized for its great potential to economically fabricate thin, dense, and gas-tight electrolytes, as well as porous electrodes for solid oxide fuel cell applications [6].

First, the LSTF powder was dispersed in acetyl acetone. After 15 min of ultrasonication, a stable slurry can be obtained. The LSTF slurry was stable for at least for 24 h. A graphite rod (10 mm in diameter and 50 mm in length), which was used as the substrate, was immersed in the LSTF slurry and 100 V of DC voltage was applied between the graphite rod and the nickel counter electrode for 10 min. The distance between the graphite rod and counter electrode was 13 mm. After the EPD process, a thin LSCF green layer was homogeneously formed on the graphite rod. The dip-coating process was conducted using the same LSTF slurry to improve the strength of the membrane. The graphite tube, coated by the LSTF green layer, was finally fired at  $1400^\circ\text{C}$

for 2 h in air to remove the graphite substrate and sinter the LSCF green body. The active surface area of the microtubular membrane was  $1.85\text{ cm}^2$ .

**2.2. Characterization.** The crystal structure of the microtubular LSTF membranes was analyzed by X-ray diffraction (XRD, RU-200B, Rigaku Co., Ltd., Japan) with Ni-filtered  $\text{CuK}\alpha$  radiation. The microstructure was examined by field emission scanning electron microscopy (FE-SEM, JSM-6700F, JEOL, Japan).

The oxygen permeability and hydrogen production rate were measured as a function of temperature by micro gas chromatography (micro-GC, Varian). The membranes were sealed and blocked using Pyrex glass rings on both sides of the alumina tube, as shown in Figure 2. Air or 50%  $\text{H}_2\text{O}/\text{Ar}$  was supplied as a feed gas on the upper side of the alumina tube. Also, Ar or 1%  $\text{CH}_4/\text{Ar}$  was supplied as a sweep gas on the bottom side of the alumina. The gas flow rate was 100 mL/min. The oxygen permeability was calculated using (1) and (2), from the oxygen concentration measured by GC in the sweep gas.

In the case of the air || Ar/1%  $\text{CH}_4$  system, the oxygen concentration was calculated with (3), using the  $\text{CH}_4$  concentration. The overall oxygen permeation rate was also calculated with (1) and (2). The hydrogen production rate was calculated with (4) using the oxygen permeation rate

$$\begin{aligned} \text{O}_2 \text{ flow rate} &= \frac{\text{Ar flow rate} \times \text{O}_2 \text{ concentration}}{\text{Ar concentration}} \\ &= \frac{\text{Ar flow rate} \times \text{O}_2 \text{ concentration}}{1 - \text{O}_2 \text{ concentration}} \end{aligned} \quad (1)$$

$$\text{O}_2 \text{ permeability} = \frac{\text{O}_2 \text{ flow rate}}{\text{Membrane area}} \quad (2)$$

$$\begin{aligned} \text{O}_2 \text{ concentration} &= (\text{Inlet } \text{CH}_4 \text{ concentration} \\ &\quad - \text{Outlet } \text{CH}_4 \text{ concentration}) \times 2 \end{aligned} \quad (3)$$

$$\text{H}_2 \text{ production rate} = \text{O}_2 \text{ permeability} \times 2. \quad (4)$$

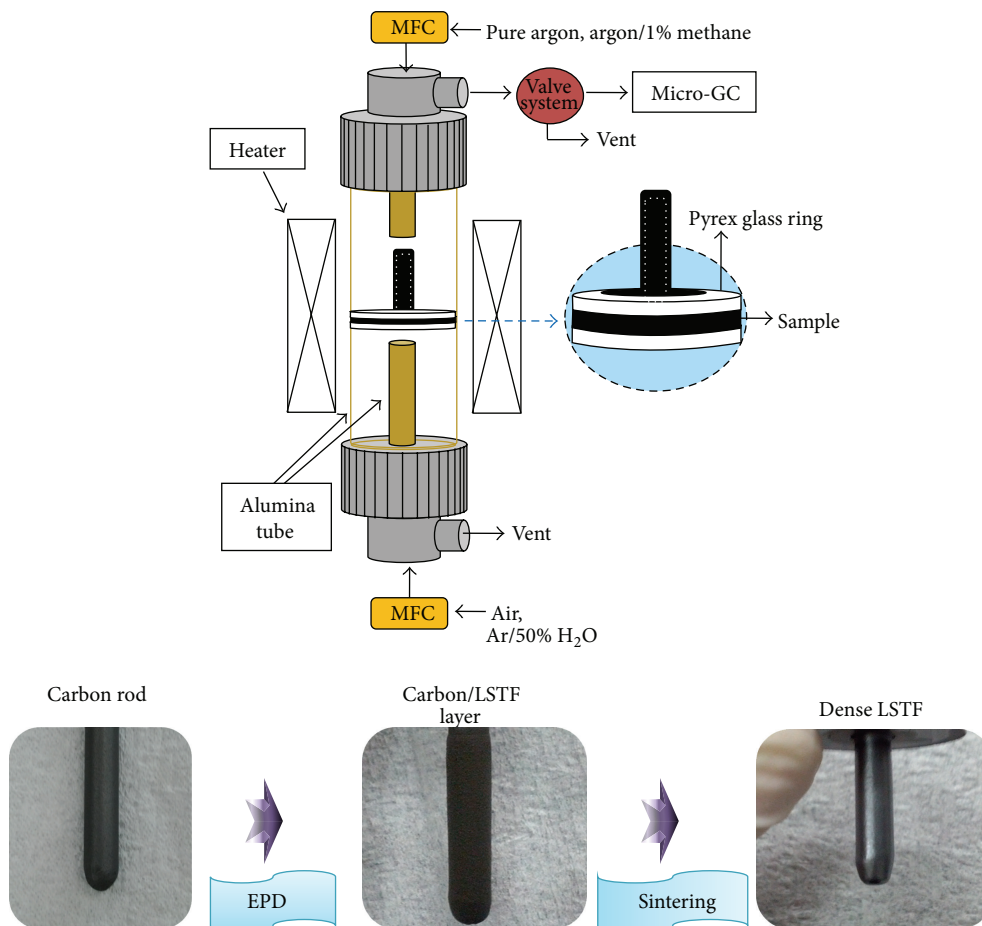


FIGURE 2: Characterization set-up for the oxygen permeability measurement and photo images of the microtubular membrane.

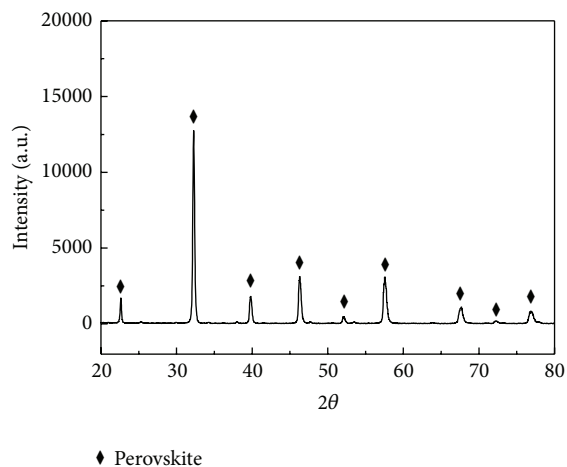


FIGURE 3: XRD pattern of the LSTF powder sample heat-treated at 1000°C.

### 3. Results and Discussion

XRD patterns for the powder sample heat-treated at 1000°C are shown in Figure 3. It was confirmed that the powder sample is  $\text{La}_{0.6}\text{Sr}_{0.4}\text{Ti}_{0.2}\text{Fe}_{0.8}\text{O}_{3-\delta}$  and has a single phase of

cubic perovskite with a lattice parameter of 0.3950 nm, cubic lattice symmetry, and a space group of Pm3m [5, 7].

Cross-sectional images of the microtubular LSTF membrane are shown in Figure 4. These show that a uniform and dense LSTF microtubular membrane was successfully

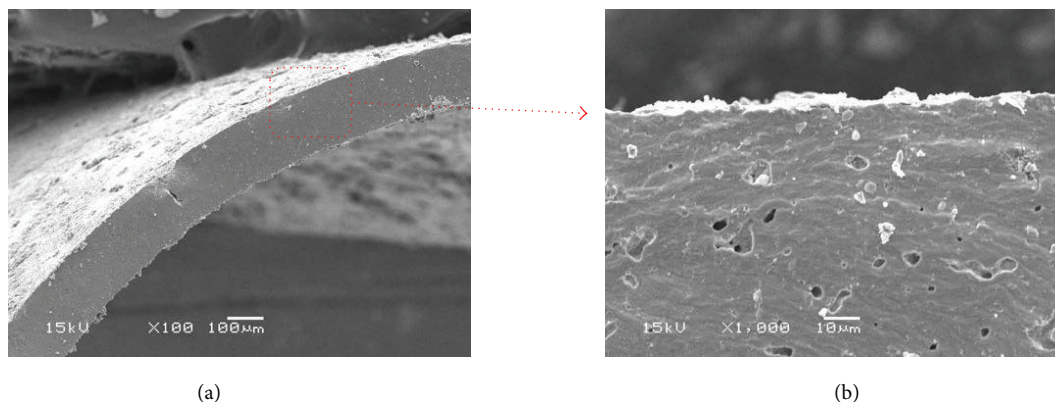


FIGURE 4: Cross-sectional SEM images of the microtubular LSTF membrane.

fabricated; the thickness of the tube is estimated to be approximately  $250\ \mu\text{m}$ . Although some closed pores are observed in the membrane tube, it seems that these do not affect the gas tightness of the tube. In addition, LSTF particles, which were coated by dip-coating, were uniformly distributed on the tube surface.

Figure 5 shows the oxygen permeability of the LSTF membrane as a function of temperature. It was found that the oxygen permeation rate gradually increased as the operating temperature increased. This result is associated with the increase in the oxygen ion mobility at higher temperatures [8]. The oxygen permeability was higher in the Ar/1% CH<sub>4</sub> || air system than in the Ar || air system. This can be explained by the difference in the oxygen partial pressure between the feed and permeated (sweep) sides. The oxygen partial pressure was much higher in Ar/1% CH<sub>4</sub> than in Ar [9, 10]. However, the oxygen permeability was lowest in the Ar/1% CH<sub>4</sub> || Ar/50% H<sub>2</sub>O system ( $0.11\ \text{mL}/\text{min}\cdot\text{cm}^2$  at  $1000^\circ\text{C}$ ). This suggests that hydrogen production should be possible because the permeated oxygen must be originating from the dissociation of water in the feed side.

Figure 6(a) shows the hydrogen production rate of the microtubular LSTF membrane and Figure 6(b) shows the methane conversion and hydrogen selectivity as a function of temperature in the permeated side (sweep) gas of Ar/1% CH<sub>4</sub>. In this study, hydrogen is produced in two ways: by splitting water in the feed side and by the partial oxidation of methane in the sweep side. Methane, which is supplied in the sweep side, is oxidized by oxygen permeating from the feed side and produces either hydrogen/carbon monoxide (partial oxidation) or water vapor/carbon dioxide mixtures (oxidation).

The open and closed circles indicate the hydrogen production rate, which is derived from water splitting and methane partial oxidation, respectively. The hydrogen production rate by water splitting is  $0.22\ \text{mL}/\text{min}\cdot\text{cm}^2$  at  $1000^\circ\text{C}$ . Although hydrogen production by water splitting is modest and lower than the values previously reported in the literature, this observed phenomenon indicates that the catalytic thermal dissociation of water vapor can occur in the microtubular LSTF membrane and that the hydrogen

production rate is proportional to the oxygen permeability of the membrane. An interesting feature observed in Figure 6(a) is that the hydrogen production rate by water splitting is much higher than that by methane partial oxidation ( $0.05\ \text{mL}/\text{min}\cdot\text{cm}^2$  at  $1000^\circ\text{C}$ ). It appears that low hydrogen selectivity is responsible for this phenomenon.

The methane conversion and hydrogen selectivity were both low: 4.3% and 22.8% at  $1000^\circ\text{C}$ , respectively. However, it appears that these results are somewhat reasonable because the oxygen permeation was small in the Ar/1% CH<sub>4</sub> || Ar/50% H<sub>2</sub>O system. The relatively low hydrogen selectivity might be associated with the poor catalytic activity for partial oxidation at low temperatures. The increase in the hydrogen selectivity at higher temperatures might be caused by the enhanced catalytic activity for partial oxidation at high temperatures.

#### 4. Conclusions

Dense and crack-free microtubular type La<sub>0.6</sub>Sr<sub>0.4</sub>Ti<sub>0.2</sub>Fe<sub>0.8</sub>O<sub>3- $\delta$</sub>  (LSTF) membranes were successfully fabricated by electrophoretic deposition (EPD) and dip-coating. It was confirmed that hydrogen production via water splitting is possible using these LSTF microtubular membranes. Oxygen that is produced by water splitting is transported to the sweep side through the LSTF membrane and reacts with methane to produce hydrogen. The oxygen permeability was much higher in 1% CH<sub>4</sub>/Ar than in Ar, which indicates that oxygen permeation can be significantly accelerated by the presence of CH<sub>4</sub> in the sweep side. Under the conditions of 10% H<sub>2</sub>O/Ar (feed side) and 1% CH<sub>4</sub>/Ar (permeate side), hydrogen was produced in both the feed side and in the permeate side. The total hydrogen production rate of the LSTF microtubular membrane was  $0.26\ \text{mL}/\text{min}\cdot\text{cm}^2$  at  $1000^\circ\text{C}$ .

#### Conflict of Interests

The authors declare that there is no conflict of interests regarding the publication of this paper.

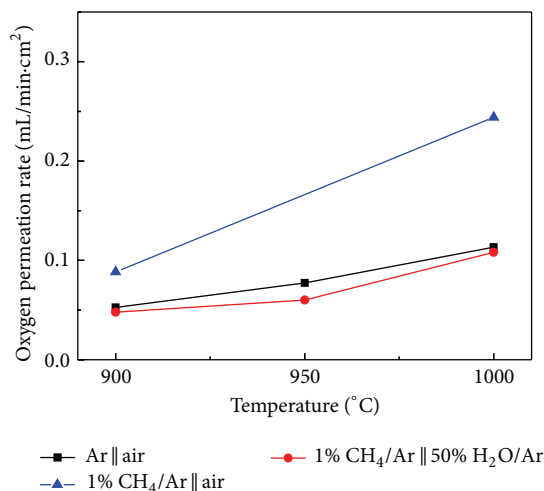


FIGURE 5: The oxygen permeability of the microtubular LSTF membrane as a function of temperature.

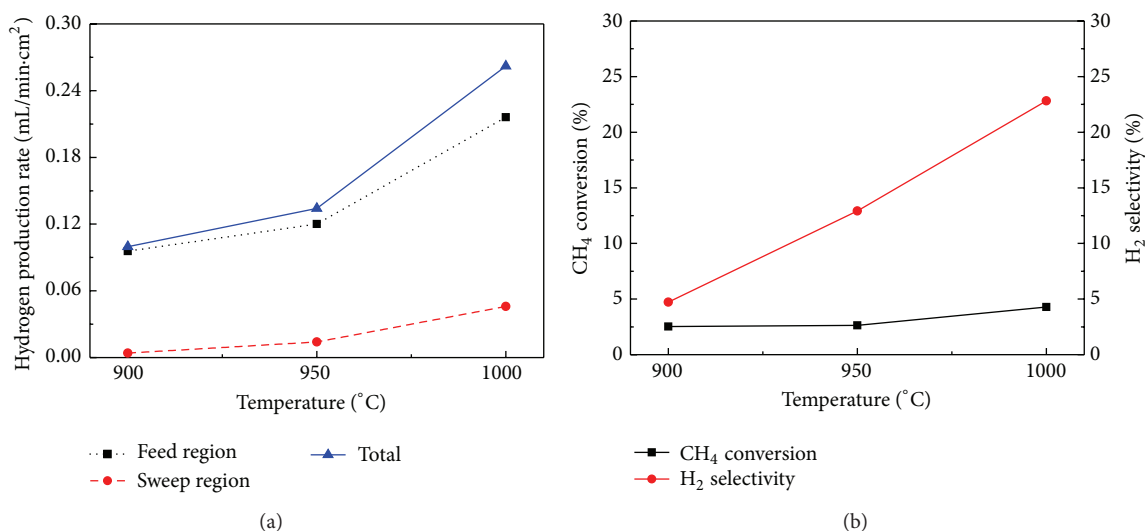


FIGURE 6: The catalytic properties of the microtubular LSTF membrane depending on temperature: (a) hydrogen production rate and (b) CH<sub>4</sub> conversion and H<sub>2</sub> selectivity.

## Acknowledgments

This work was supported by the New & Renewable Energy Core Technology Program of the Korea Institute of Energy Technology Evaluation and Planning (KETEP), granted financial resource from the Ministry of Trade, Industry & Energy, Republic of Korea (no. 20113020030050). This work was supported by INHA UNIVERSITY Research grant.

## References

- [1] M. Momirlan and T. N. Veziroglu, "The properties of hydrogen as fuel tomorrow in sustainable energy system for a cleaner planet," *International Journal of Hydrogen Energy*, vol. 30, no. 7, pp. 795–802, 2005.
- [2] A. Evdou, L. Nalbandian, and V. T. Zaspalis, "Perovskite membrane reactor for continuous and isothermal redox hydrogen production from the dissociation of water," *Journal of Membrane Science*, vol. 325, no. 2, pp. 704–711, 2008.
- [3] U. Balachandran, T. H. Lee, and S. E. Dorris, "Hydrogen production by water dissociation using mixed conducting dense ceramic membranes," *International Journal of Hydrogen Energy*, vol. 32, no. 4, pp. 451–456, 2007.
- [4] T. H. Lee, Y. L. Yang, A. J. Jacobson, B. Abeles, and M. Zhou, "Oxygen permeation in dense SrCo<sub>0.8</sub>Fe<sub>0.2</sub>O<sub>3-δ</sub> membranes: surface exchange kinetics versus bulk diffusion," *Solid State Ionics*, vol. 100, no. 1-2, pp. 77–85, 1997.
- [5] Y. Takahashi, A. Kawahara, T. Suzuki, M. Hirano, and W. Shin, "Perovskite membrane of La<sub>1-x</sub>Sr<sub>x</sub>Ti<sub>1-y</sub>Fe<sub>y</sub>O<sub>3-δ</sub> for partial oxidation of methane to syngas," *Solid State Ionics*, vol. 181, no. 5–7, pp. 300–305, 2010.
- [6] L. Besra and M. Liu, "A review on fundamentals and applications of electrophoretic deposition (EPD)," *Progress in Materials Science*, vol. 52, no. 1, pp. 1–61, 2007.

- [7] E. Bartonickova, K. Wiik, K. Maca, H. L. Lein, and E. A. Rudberg, "Synthesis and oxygen transport properties of  $\text{La}_{0.2}\text{Sr}_{0.8}\text{Fe}_{1-x}\text{Ti}_x\text{O}_{3-\delta}$  ( $x = 0.2, 0.4$ ) intended for syn-gas production," *Journal of the European Ceramic Society*, vol. 30, no. 2, pp. 605–611, 2010.
- [8] J. Maier, "Transport in electroceramics: micro- and nano-structural aspects," *Journal of the European Ceramic Society*, vol. 24, no. 6, pp. 1251–1257, 2004.
- [9] C. Zhang, X. Chang, X. Dong, W. Jin, and N. Xu, "The oxidative stream reforming of methane to syngas in a thin tubular mixed-conducting membrane reactor," *Journal of Membrane Science*, vol. 320, no. 1-2, pp. 401–406, 2008.
- [10] S. Liu, X. Tan, K. Li, and R. Hughes, "Methane coupling using catalytic membrane reactors," *Catalysis Reviews: Science and Engineering*, vol. 43, no. 1-2, pp. 147–198, 2001.

## Research Article

# Improvement of Surface Properties of Inconel718 by HVOF Coating with WC-Metal Powder and by Laser Heat Treatment of the Coating

Hui Gon Chun,<sup>1</sup> Tong Yul Cho,<sup>2</sup> Jae Hong Yoon,<sup>3</sup> and Gun Hwan Lee<sup>4</sup>

<sup>1</sup>School of Materials Science and Engineering, University of Ulsan, Ulsan 680-749, Republic of Korea

<sup>2</sup>Institute of Industrial Technology, Changwon National University, Changwon 641-773, Republic of Korea

<sup>3</sup>School of Nano Advanced Materials Engineering, Changwon National University, Changwon 641-773, Republic of Korea

<sup>4</sup>Surface Technology Department, Korea Institute of Material Science, Changwon 642-010, Republic of Korea

Correspondence should be addressed to Hui Gon Chun; [chunhuigon@gmail.com](mailto:chunhuigon@gmail.com)

Received 22 September 2014; Accepted 9 December 2014

Academic Editor: Kwangho Kim

Copyright © 2015 Hui Gon Chun et al. This is an open access article distributed under the Creative Commons Attribution License, which permits unrestricted use, distribution, and reproduction in any medium, provided the original work is properly cited.

High-velocity oxygen-fuel (HVOF) thermal spray coating with WC-metal powder was carried out by using optimal coating process on an Inconel718 surface for improvement of the surface properties, friction, wear, and corrosion resistance. Binder metals such as Cr and Ni were completely melted and WC was decomposed partially to  $W_2C$  and graphite during the high temperature (up to  $3500^\circ C$ ) thermal spraying. The melted metals were bonded with WC and other carbides and were formed as WC-metal coating. The graphite and excessively sprayed oxygen formed carbon oxide gases, and these gases formed porous coating by evolution of the gases. The surface properties were improved by HVOF coating and were improved further by  $CO_2$  laser heat treatment (LH). Wear resistance of In718 surface was improved by coating and LH at  $25^\circ C$  and an elevated temperature of  $450^\circ C$ , resulting in reduction of wear trace traces, and was further improved by LH of the coating in reducing wear depth. Corrosion resistance due to coating in sea water was improved by LH. HVOF coating of WC-metal powder on a metal surface and a LH of the coating were highly recommended for the improvement of In718 surface properties, the friction behavior, and wear resistance.

## 1. Introduction

Traditionally, electrolytic hard chrome plating (EHC) has been widely used for hard surface coating for over 60 years [1–3]. Recently, EHC has raised health and environmental problems;  $Cr^{+3}$  known as carcinogen is emitted and is forbidden in many developed countries. High-velocity oxygen-fuel (HVOF) thermal spray coating has been investigated as one of the most promising candidates for the replacement of EHC [4–6]. HVOF coatings of WC cermets have been widely used to protect machine components from wear and corrosion, to restore worn components, and to improve the durability of components.

In this work, micron-sized WC-metal powders were coated on In718 (substrate) by HVOF thermal spraying to improve the surface properties, wear resistance, and the durability of the metal components. For further improvement, the

surface was irradiated with a  $CO_2$  laser ( $10.6 \mu m$ , continuous mode, 400 W) on an oval-shaped focal spot ( $5 mm \times 4 mm$ ) for 0.6 s at the scanning speed of 400 mm/min, heating from  $950^\circ C$  to  $1200^\circ C$  from the edge to the center of the spot without heating the whole substrate not to change any structure and properties of substrate. In this experiment, the following were investigated; optimal coating process (OCP) using Taguchi experimental program, laser heat treatment (LH), changes of phases, micro-structures, surface properties, friction, wear and corrosion of HVOF coating and LH coating.

## 2. Experiment

**2.1. Preparation of Coating.** The chemical composition of WC-metal powder (hard cermet WC, bonding metals as Ni and Cr) was coated on the super alloy In718 substrate in Table 1 by using JK3500 HVOF thermal spraying equipment.

TABLE 1: Major chemical compositions of In718 and WC-metal powder.

Elements	W	C	Cr	Ni	Fe	Nb	Mo	Others
In718		0.08	17–20	50–55	11–22	5–6	2–3	Mn, Ti, Si
WC-metal	68	5	21	6				

TABLE 2: Coating processes prepared by Taguchi program and OCP of the highest surface hardness.

Process	Oxygen FR	Hydrogen FR	Feed rate	Spray distance (in)	Hardness (Hv)
1	30	53	25	6	973
2	30	57	30	7	943
3	30	61	35	8	913
4	34	53	35	7	976
5	34	57	25	8	942
6	34	61	30	6	930
7	38	53	30	8	1033
8	38	57	35	6	960
9	38	61	25	7	998
OCP	<b>38</b>	<b>53</b>	<b>25</b>	<b>7</b>	<b>1150</b>

FR: flow rate (FMR = 12 scfh =  $9.44 \times 10^{-5}$  m<sup>3</sup>/s), feed rate: g/min, and OCP: optimal coating process.

The substrates were pre-cleaned in acetone for 5 minutes and then blast cleaned using 60-mesh aluminum oxides to improve adhesion onto In718 substrate. As shown in Table 2, OCP was obtained among the best surface properties of the 9 coatings prepared Taguchi experimental program for 3 levels of 4 spray parameters. Hydrogen flow rate as value was 53 FMR (FMR = 12 scfh =  $9.44 \times 10^{-5}$  m<sup>3</sup>/s), oxygen flow rate as 38 FMR, powder feed rate as 25 g/min, and spray distance as 18 cm. Argon gas of 120–180 psi was used as a powder carrier gas at feed rate of 25–35 g/min. The preparation of coatings was provided by OCP and heat-treated by CO<sub>2</sub> laser.

**2.2. Preparation of LH Coating.** A 5-kW TJ-HL-T 5000-type equipment was used for CO<sub>2</sub> laser heat treatment. The laser beam (10.6 μm, continuous mode, a top-hat laser beam energy distribution in the focal spot) irradiated the substrate from the spot 18.5 mm above in an atmospheric environment. The laser beam with a focal spot of 5 mm × 4 mm (oval shape) moved along the beam direction of the 4 mm at velocity of 400 mm/min, resulting in a LH time of 0.6 s on the spot. Argon gas (10 MPa pressure and 5 L/min flow rate) was used for shrouding the LH region to prevent oxidation during the process.

The laser power was turned off for 5 s at the end of each pass for a new starting position. The laser beam tracks were overlapped by 40% to each other. The optimal laser LH parameters were laser power of 400 W, scanning speed of 400 mm/min, average power density of 20 W/mm<sup>2</sup>, and laser irradiation of 0.6 s on spot. The samples were heat-treated in a furnace at 150°C for 2 hours before and after laser heat treatments. The temperature from edge to center

of the laser spot was in the range from 950°C to 1200°C using a multiwavelength pyrometer.

**2.3. Investigation of Surface Properties, Friction, Wear, and Corrosion in HVOF Coating and LH Coating.** The microstructures of HVOF coating and the LH coating were investigated by using scanning electron microscope (SEM). The phase changes by HVOF powder coating and LH coating were investigated using X-ray diffraction (XRD). Surface hardness was measured by using a Micro Vickers hardness tester with a load of 200 g and a dwelling time of 10 s. Porosity was measured by analyzing the images of optical microscope.

Friction and the wear behaviors were investigated by using a reciprocating slide tester (TE77 AUTO, Plint & Partners). The surfaces were slid by using SUS 304 balls (diameter 9.53 mm and hardness 227 Hv) without lubricants. Before the test, the surfaces were polished to Ra 1–1.4 μm by using silicon carbide abrasive paper and DP-paste. The sliding distance, frequency, speed, load, and sliding time were 16 mm, 2.5 Hz, 0.161 m/s, 10 N, and 10 min, respectively. Sliding wear tests were carried out for the substrate, HVOF coating, and LH coating to study the friction and wear behaviors. Wear traces were investigated using SEM and EDS. The depth profiles of the wear traces were investigated using a surface profiler (Tencor P-11).

The corrosion behavior of HVOF coating and LH coating was investigated in sea water (3.5 wt% NaCl solution).

The sample was mounted in the electrochemical cell with an exposing area of 1.0 cm<sup>2</sup> to the electrolyte. In the electrochemical test, saturated calomel electrode (SCE) and graphite were used as the reference and counter electrode, respectively.

The electrochemical tests included the open-circuit potential (EOC) measurements and potentiodynamic polarization tests. The EOC was measured after 30 min immersion of the coating surface in 3.5 wt% NaCl solution for potential stabilization. The samples were potentiodynamically polarized (anodically) and the tests were performed at a scanning rate of 0.5 mV/s. At least, two sets of measurements were made per sample to ensure reproducibility of the results.

### 3. Results and Discussion

**3.1. HVOF Coating and LH Coating.** Inhomogeneous WC pieces were imbedded in binder metals such as Ni, Cr, Ni-Cr alloy, and WC powders [3, 6, 7]. During the flight of 0.02 s in the HVOF spraying, its velocity and temperature of the flame were reached up to 1000 m/s and 3500°C. The binder metals and some metal carbide were melted, and the metal carbides were decomposed into metals and free carbon. Small portion of WC was found in forms of crystalline compounds

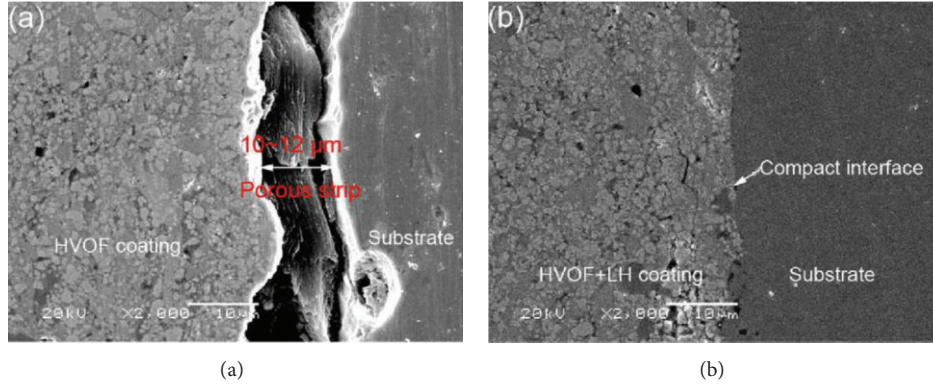


FIGURE 1: (a) Porous coating and interface between coating and substrate; (b) interface compacted by laser heating.

TABLE 3: Improvement of surface properties by coating and LH coating.

Surface	In718	Coating	LH coating
Surface hardness (Hv)	400 ± 10	980 ± 100	1430 ± 90
Porosity (%)	0.00	2.5 ± 0.5	0.35 ± 0.05
Friction coefficient	0.45 ± 0.08	0.32 ± 0.02	0.20 ± 0.03

such as  $W_2C$  [7, 8]. The melts or partially molten splats were impacted on the In718 surface, forming bonds with the surface and subsequently building the porous coating as seen in Figure 1. Although the powder consisted of crystalline carbides such as WC,  $Cr_7C_3$ , and metastable  $Ni_3C$ , the coating showed that only crystalline WC and a new phase  $W_2C$  were observed in Figure 2.

However, the other forms of crystalline carbides disappeared due to the decomposition during heating and rapid cooling processes. According to the phase diagram, WC is decomposed to  $W_2C$  and free carbon above its decomposition temperature of 1250°C [9, 10]. The free carbon and excessively sprayed reagent oxygen formed carbon oxide gases, producing pores and voids inside the porous coating as shown in Table 3 and Figure 1.

During laser heat treatment of the HVOF coating for 0.6 s, the temperature of the irradiated focal area was in the range from 950°C to 1200°C; the porous coating and porous strips at the interface were compacted as seen in Figure 1 and Table 3. The crystalline metal carbides such as  $Ni_3C$  and  $Cr_3C_2$  phases were formed due to the longer heating time (~0.6 s) and proper heating temperature (950°C to 1200°C). This can be compared with spray coating time of about 0.02 s and temperature of up to 3500°C.

**3.2. Improvement of Surface Properties by HVOF Coating and LH Coating.** As seen in Table 3 and Figure 3, the surface hardness and friction coefficient were improved by HVOF coating and LH coating for 0.6 s. These properties of HVOF coating and LH coating were better than the traditional electrolytic hard chrome plating (EHC) as seen in Table 3 according to Fang et al.'s report [6]. The friction coefficient of the coating showed lower value than that of EHC

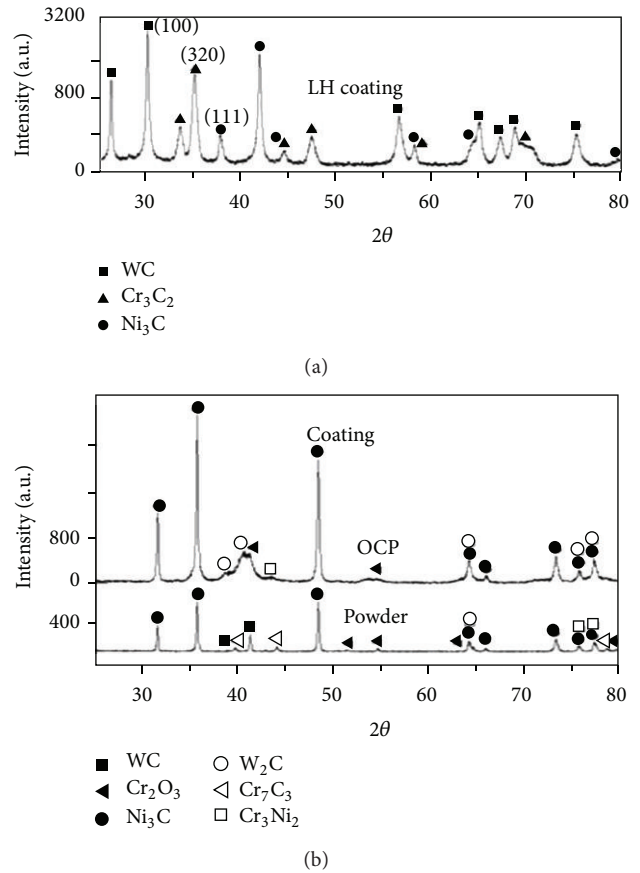


FIGURE 2: Crystalline phases of powder, coating, and LH coating.

(0.52 ± 0.07 Hv), and surface hardness of HVOF coating showed higher value than that of EHC (950 ± 50 Hv). The porous coating was formed by HVOF coating due to formation of carbon oxide gases by the reaction of free carbon (produced by the thermal decompositions of WC and metal carbides) with excessively sprayed oxygen as shown in Table 2. With laser heating, the porosity decreased drastically and HVOF coating was compacted as seen in Table 3 and Figure 1.

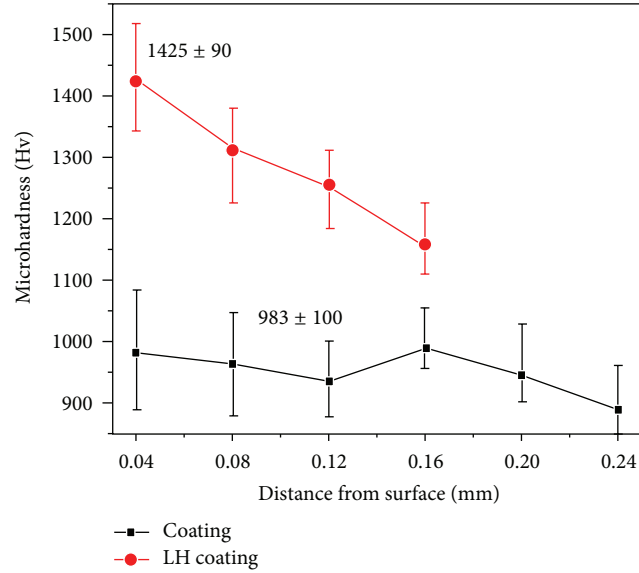


FIGURE 3: Depth profiles of surface hardness of coating and LH coating.

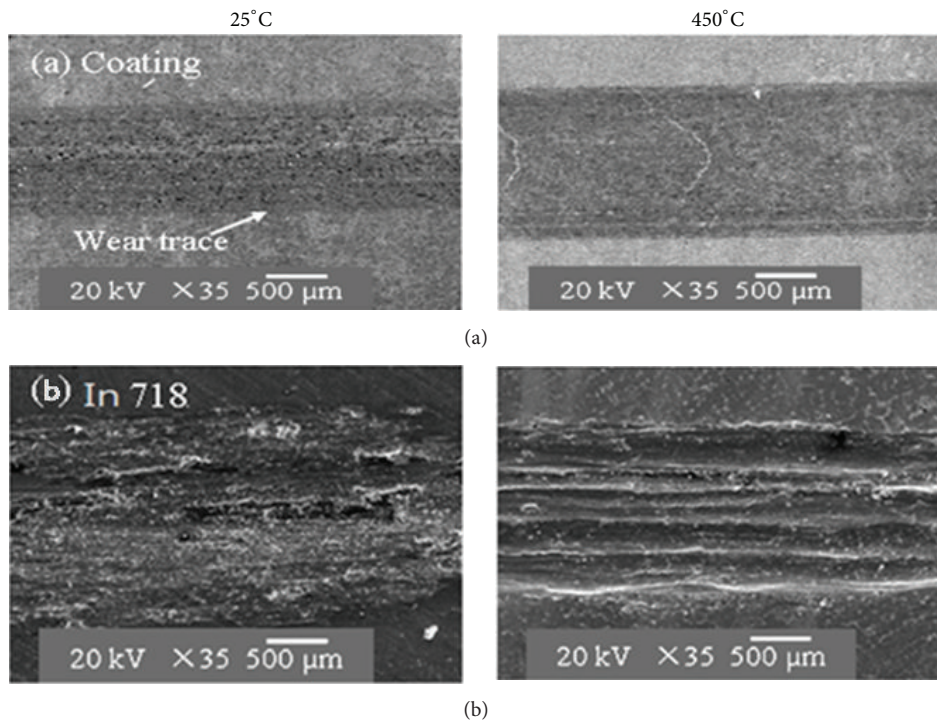


FIGURE 4: Wear traces of (a) coating and (b) In718 at both 25°C and 450°C.

The surface hardness of In718 ( $400 \pm 10$  Hv) increased more than twice to  $980 \pm 100$  Hv due the coating; it was increased 46% to  $1430 \pm 90$  Hv by laser heating for 0.6 s. The porosity of In718 surface (0%) was increased to  $2.5 \pm 0.5\%$  by HVOF coating due to formation of carbon oxide gases inside the coating; it was reduced to  $0.35 \pm 0.05\%$  (to 14%) by laser heating. As seen in Figure 1, laser heating could reduce their porosity by compacting of the coating and the interface of coating/substrate In718. The friction coefficient of In718 was

reduced by 30% from  $0.45 \pm 0.08$  to  $0.32 \pm 0.02$  by coating and 10% to  $0.20 \pm 0.03$  by laser heating. One of the reasons could be the lubrication by the free carbon formed by the decomposition of WC and metal carbides during the spraying and the metal-oxide debris worn during sliding test.

*3.3. Improvement of Surface Wear Resistance by HVOF Coating and by LH Coating.* A reciprocating slide test was carried out for the investigation of wear resistance and

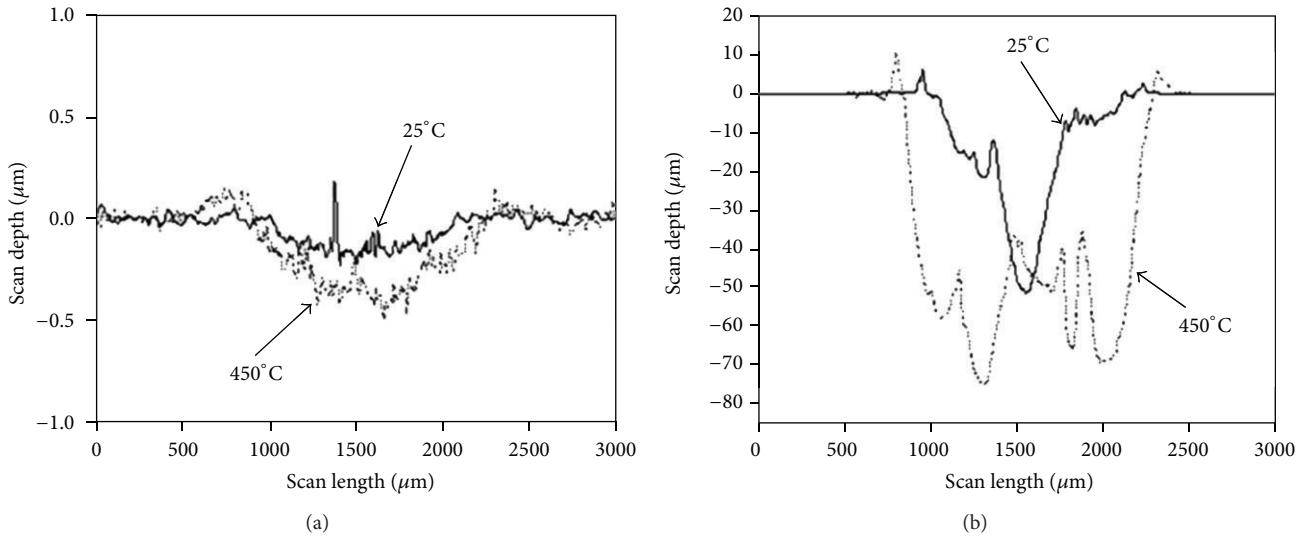


FIGURE 5: Wear depth profiles; (a) coating and (b) In718 at both 25°C and 450°C.

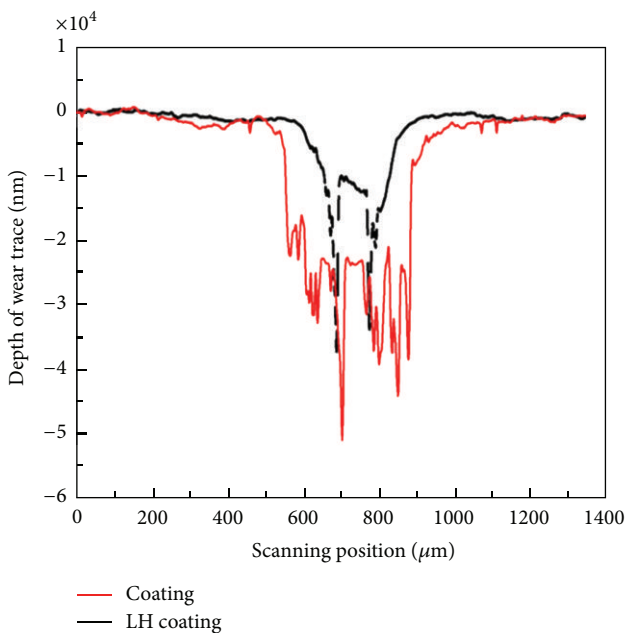


FIGURE 6: Wear depth profiles of coating and LH coating at room temperature.

temperature dependence of wear resistance of In718, coating, and LH coating. As seen in Figures 4~6, the wear resistance was improved by HVOF coating and followed by LH coating, since the surface hardness increased by coating, followed by LH coating in Section 3.2. The temperature dependence of wear resistance of the coating was better than that of In718 which showed a narrower wear trace and shallower wear depth at 25°C and 450°C in Figures 4 and 5. With surface temperature increase from 25°C to 450°C the wear width and depth increased at In718 and the coating. This showed that the wear resistances decreased with surface temperature increase at In718 and the coating because thermal effect

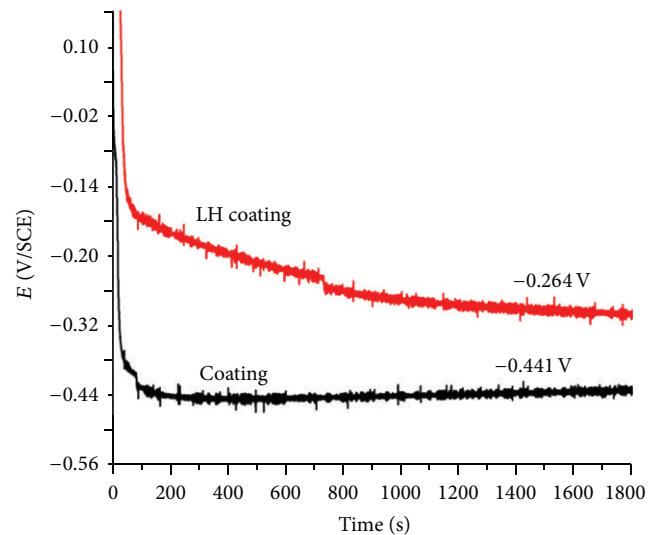


FIGURE 7: Corrosion potential and time of coating and LH coating in sea water (3.5% NaCl).

softens the surface and there was wear debris of metal oxides and free carbon decomposed by thermal effect functioning as solid and liquid lubricants. The lubricating effect was higher at higher temperature. As seen in Figure 6, the wear resistance of the coating increased by laser heating, showing a decrease of wear depth from 5000 nm to 2000 nm due to the increase of surface hardness by laser heating as discussed in Section 3.2.

**3.4. Improvement of Corrosion Resistance by Coating and by LH Coating.** Corrosion behaviors of In718, HVOF coating, and LH coating in 3.5% NaCl solution (sea water) were investigated. As previously reported by S. Y. Park and C. G. Park [4], corrosion resistance of In718 surface was improved by HVOF coating of WC-metal powder in 3.5% NaCl solution and 1 M HCl acid, but it decreased in 1 M NaOH base solution.

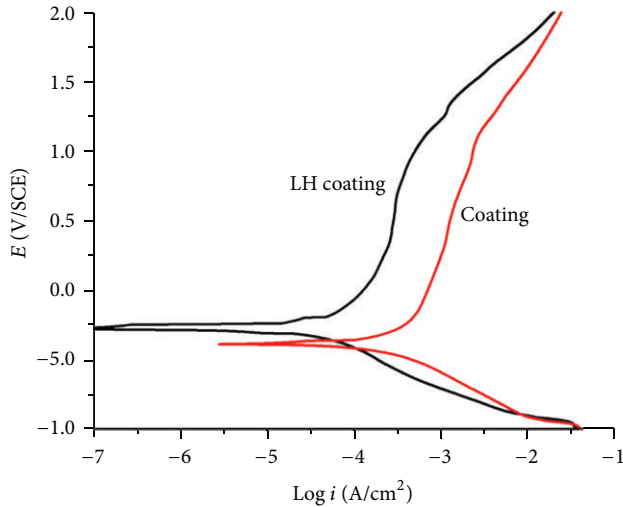


FIGURE 8: Potentiodynamic polarization of coating and LH coating in sea water (3.5% NaCl).

In718 with 100% metals was more corrosive (chemically active) than the coating (WC-metal) with more than 50% inactive cermet of WC. As shown in Figures 7 and 8, the corrosion resistance of coating in 3.5% NaCl solution was improved by laser heating. As seen in Figure 7, corrosion potential decreased and then stayed steady with corrosion time; this suggested the corrosion films on both coating and LH coating were not passive films and did not protect the inner materials of the coating.

The LH coating with lower porosity (dense coating) had higher corrosion potential than the coating. Therefore the LH coating had more corrosion resistance than the coating. As seen in Figure 8, LH coating had a smaller corrosion current density and higher breakdown potential (pitting potential or corroded film breakdown potential), showing LH coating was a better corrosion resistance. The corrosion current density increased rapidly with a small increase of applied potential and there was no significant passive region for both the coating and LH coating. This showed that no protective corrosion films were formed at both coating and LH coating. The very active chlorine ions strongly reacted with the surface atoms but did not form protective passive films on the surface [11].

#### 4. Conclusions

The following conclusions were derived from the investigation of improvement of surface properties of In718 by HVOF coating of WC-metal powder and by laser heating of the coating.

- (1) Metal carbides and WC decomposed during the HVOF coating, forming less hard  $W_2C$  phase and free carbon.
- (2) Porous coating was formed by HVOF coating, but it was compacted from  $2.5 \pm 0.5\%$  to  $0.35 \pm 0.05\%$  (to 14%) by the laser heating.

- (3) The surface hardness of In718 surface improved from  $400 \pm 10$  Hv to  $980 \pm 100$  Hv by the coating; it was further increased to  $1430 \pm 90$  Hv by laser heating.
- (4) Friction coefficient of In718 reduced from  $0.45 \pm 0.08$  to  $0.32 \pm 0.02$  by the coating and to  $0.20 \pm 0.03$  by the laser heating.
- (5) Wear resistance of In718 surface was improved by the coating and further improved by LH coating. And these resistances were decreased with increasing surface temperature in the temperature range from  $25^\circ\text{C}$  to  $450^\circ\text{C}$ .
- (6) Corrosion resistance improved by HVOF coating, followed by LH coating.
- (7) For the improvement of surface properties and durability of materials, HVOF coating of WC-metal powder on the surface and laser heat-treated coating were strongly recommended.

#### Conflict of Interests

The authors declare that there is no conflict of interests regarding the publication of this paper.

#### Acknowledgments

This research was financially supported by R&D fund of the University of Ulsan, Korea. The authors would like to express their sincere thanks for the support. They also would like to thank Dr. Gun Hwan Lee who contributed to investigating of the surface properties of the substrates and the coatings.

#### References

- [1] J. R. Davis, *Handbook of Thermal Spray Technology*, ASM International, 2004.
- [2] B. D. Sartwell, K. O. Legg, J. Schell, J. Sauer, and P. Natishan, "Validation of HVOF WC/Co thermal spray coatings as a replacement for hard chrome plating on aircraft landing gear," DTIC Document, 2004.
- [3] T. Y. Cho, H. G. Chun, Y. K. Joo, and J. H. Yoon, "A study on HVOF coating of WC-metal powder on super alloy In718 of magnetic bearing shaft material of turbo-blower," *International Journal of Precision Engineering and Manufacturing*, vol. 15, no. 7, pp. 1479–1484, 2014.
- [4] S. Y. Park and C. G. Park, "Wear properties of WC-Co nanoparticle coatings fabricated by detonation gun spraying," *Journal of the Korean Institute of Metals and Materials*, vol. 42, p. 582, 2004.
- [5] T. Y. Cho, J. H. Yoon, K. S. Kim et al., "A study on HVOF coatings of micron and nano WC-Co powders," *Surface and Coatings Technology*, vol. 202, no. 22-23, pp. 5556–5559, 2008.
- [6] W. Fang, T. Y. Cho, J. H. Yoon et al., "Processing optimization, surface properties and wear behavior of HVOF spraying WC-CrC-Ni coating," *Journal of Materials Processing Technology*, vol. 209, no. 7, pp. 3561–3567, 2009.
- [7] U. T. Kim, D. W. Park, J. S. Kim, Y. S. Kwon, H. S. Kwon, and B. R. Baek, "Spark plasma sintering behavior of binderless WC powders," *Journal of Korean Powder Metallurgy Institute*, vol. 10, no. 3, pp. 176–180, 2003.

- [8] S.-H. Zhang, T.-Y. Cho, J.-H. Yoon et al., "Characterization of microstructure and surface properties of hybrid coatings of WC-CoCr prepared by laser heat treatment and high velocity oxygen fuel spraying," *Materials Characterization*, vol. 59, no. 10, pp. 1412–1418, 2008.
- [9] P. Chivavibaul, M. Watanabe, S. Kuroda, and K. Shinoda, "Effects of carbide size and Co content on the microstructure and mechanical properties of HVOF-sprayed WC-Co coating," *Surface & Coating Technology*, vol. 202, p. 509, 2004.
- [10] H. H. Ulig and R. W. Revie, *Corrosion and Corrosion Control*, 1985.
- [11] T. Y. Cho, J. H. Yoon, K. S. Kim et al., "Friction behavior of HVOF thermal spray coating of micron size WC-Co powder," *Advanced Materials Research*, vol. 26, pp. 1325–1328, 2007.

## Research Article

# Kinetic Studies of Atom Transfer Radical Polymerisations of Styrene and Chloromethylstyrene with Poly(3-hexyl thiophene) Macroinitiator

Nattawoot Rattanathamwat,<sup>1</sup> Jatuphorn Wootthikanokkhan,<sup>1,2</sup> Nonsee Nimitsiriwat,<sup>2,3</sup> Chanchana Thanachayanont,<sup>4</sup> and Udom Asawapirom<sup>5</sup>

<sup>1</sup>Division of Materials Technology, School of Energy, Environment and Materials, King Mongkut's University of Technology Thonburi (KMUTT), Bangkok 10140, Thailand

<sup>2</sup>Nanotec-KMUTT Center of Excellence on Hybrid Nanomaterials for Alternative Energy (HyNAE), Bangkok 10140, Thailand

<sup>3</sup>Pilot Plant Development and Training Institute, King Mongkut's University of Technology Thonburi, Bangkok 10140, Thailand

<sup>4</sup>National Metal and Materials Technology Center (MTEC), Pathumthani 12120, Thailand

<sup>5</sup>National Nanotechnology Center (NANOTEC), Pathumthani 12120, Thailand

Correspondence should be addressed to Jatuphorn Wootthikanokkhan; [jatuphorn.woo@kmutt.ac.th](mailto:jatuphorn.woo@kmutt.ac.th)

Received 15 October 2014; Revised 9 February 2015; Accepted 10 February 2015

Academic Editor: Doo-In Kim

Copyright © 2015 Nattawoot Rattanathamwat et al. This is an open access article distributed under the Creative Commons Attribution License, which permits unrestricted use, distribution, and reproduction in any medium, provided the original work is properly cited.

Poly(3-hexyl thiophene)-*b*-poly(styrene-*co*-chloromethylstyrene) copolymers, to be used as a prepolymer for preparing donor-acceptor block copolymers for organic solar cells, have been synthesised by reacting P3HT macroinitiators with styrene and chloromethylstyrene via three types of atom transfer radical polymerisation (ATRP) systems, which are (1) a normal ATRP, (2) activators generated by electron transfer (AGET), and (3) a simultaneous reverse and normal initiation (SR&NI). The kinetics of these ATRP systems were studied as a function of monomers to the macroinitiator molar ratio. It was found that all of the three types of ATRP systems led to first order kinetics with respect to monomers. The highest rate constant ( $k$ ) of  $3.4 \times 10^{-3} \text{ s}^{-1}$  was obtained from the SR&NI ATRP system. The molecular weights of the product determined by the GPC were lower than were the theoretical values. The result was discussed in light of the chain transfer reaction to the poly(chloromethylstyrene) repeating units. Morphology of the synthesized block copolymers, examined by an atomic force microscopy (AFM), were also compared and discussed.

## 1. Introduction

Poly(3-hexyl thiophene) (P3HT) is a kind of semiconducting polymer that has been widely used in many electronic devices, including polymer solar cells [1]. In this case, P3HT serves as a donor material in an active layer of the cell, which is sandwiched between two different electrodes. The donor material is always used in combination with an electron acceptor material, such as fullerene ( $C_{60}$ ) and/or a fullerene derivative ([6,6]-phenyl- $C_{61}$ -butyric acid methyl ester, PCBM), to create an interpenetrating structure from the two different conducting materials. This structure, commonly called bulk heterojunction (BHJ), results in a relatively large interfacial area between the two phases. Consequently, more dissociations of an exciton (a tightly bound photo excited

electron-hole pair) into free charges and a greater performance of the polymer solar cell can be expected [2].

However, power conversion efficiency (PCE) values of the BHJ polymer solar cells are still low compared to those of the conventional inorganic based solar cells and dye sensitised solar cells [3, 4]. To enhance PCE of the polymer solar cell, various strategies can be used, including molecular design and synthesis of low band gap polymers to minimise photon loss [5]. In addition, morphology of the BHJ also plays a role. Since the diffusion length of the exciton is normally less than 10 nm. In this regard, the performance of the polymer solar cell is extremely sensitive to the active layer morphology. For example, if the dimensions of the donor and the acceptor phases are larger than the exciton length, then

it is likely that the photo-generated excitons are recombined before splitting into free charges. To suppress the exciton recombination, a nanoscale phase separated morphology of the donor/acceptor blend should be induced. The interfacial area between the donor and acceptor materials should also be as large as possible [6]. In addition, to minimise carrier losses, continuous pathways for both positive and negative charges towards the electrodes have to be ensured.

One possible strategy for inducing a nanostructured polymer solar cell is by using block copolymers as self-organising materials. Block copolymers self-assemble due to the incompatibility of the two blocks that are chemically linked to each other. The type of nanostructuring, taking place at the length scale of the two blocks, depends on their incompatibility, the chain length of the copolymer, and the volume fraction of the two blocks. Alternatively, a block copolymer might be used as a compatibilizer to control morphology of the donor/acceptor polymer blends [7]. By adding a suitable type and amount of a block copolymer into the polymer blend, a better interfacial adhesion and finer dispersed particles of the polymer blends can be expected.

In relation to our research, the block copolymer that is suitable for application in a photovoltaic device should contain a block with electron donating and another block with electron accepting moieties. This study focuses on the synthesis and photovoltaic performance of poly(3-hexyl thiophene)-*b*-fullerene grafted polystyrene (P3HT-*b*-PSFu) block copolymer. It was presumed that the PSFu block should be compatible with an electron acceptor phase (C<sub>60</sub> and/or PCBM) in the active layer. The P3HT-*b*-PSFu molecule was prepared via a prepolymer, which is poly(3-hexyl thiophene)-*b*-poly(styrene-*co*-chloromethylstyrene) [P3HT-*b*-P(S-*co*-CMS)]. This prepolymer, in turn, can be obtained from a controlled radical (co)polymerisation of styrene and chloromethylstyrene (CMS) with the P3HT macroinitiator. It is worth mentioning that the use of CMS monomers containing chlorine atoms will enable the attachment of fullerene groups into the poly(chloromethylstyrene) (PCMS) repeating units.

Atom transfer radical polymerisation (ATRP) is considered to be one of the most robust and widely used controlled radical polymerisation techniques. Wang and Matyjaszewski first reported the ATRP technique in 1995 [8]. Since then, it has been widely used to prepare a variety of well-defined polymers with a PDI value ( $M_w/M_n$ ) of less than 1.5. This technique can also lead to the formation of block copolymer architecture. In principle, this technique relies on the establishment of a dynamic equilibrium between the dormant species (end-capped radical chains) and the propagating radical chains. The polymerisation is initiated by the decomposition of an alkyl halide initiator, catalysed by the transition metal complex. In addition, a variety of modified ATRP techniques have recently been introduced. These include reverse ATRP, activators generated by electron transfer ATRP (AGET-ATRP) [9, 10], and simultaneous reverse and normal initiation ATRP (SR&NI ATRP). It is noteworthy that rather than using low oxidation state metals that require special handling procedures and moisture free storage, AGET-ATRP and SR&NI ATRP techniques employ a high oxidation state

metal complex in combination with a radical initiator and/or a reducing agent, respectively. Consequently, an activator (low oxidation metal compound) is generated *in situ* and the reaction proceeds further in a similar fashion to that of the normal ATRP.

For a good phase separation and a high compatibilizing efficacy, it is important to ensure the preparation of a well-defined block copolymer. This can be achieved by controlling the molecular architecture (block length and block composition) of the donor/acceptor copolymer. In this regard, the kinetics of these ATRP systems are important and deserve consideration, taking into account the fact that monomer conversion, product yield, and molecular weight of the polymerised polymer strongly depend on the kinetics of the polymerisations. Khan et al. [11] studied the kinetics and product characteristics obtained from the polymerisation of MMA by different ATRP systems. It was found that modified ATRP employed a high oxidation state metal complex without any additives (so-called GAMA-ATRP) providing the best controllability and "living polymerisation" characteristics. Matyjaszewski et al. [12] studied the ATRP kinetics of styrene and found that the reaction kinetics exhibited first-order kinetics with respect to both the initiator and copper(I) halide concentration. The polymerisation kinetics were not simple inverse first-order with respect to the initial copper(II) halide concentration. This was ascribed to the persistent radical effect, which resulted in an increase in copper(II) concentration during the initial stages of the polymerisation. Arslan et al. [13] studied ATRP kinetics of styrene and found that the molecular weights of the product determined by GPC were higher than were the theoretical values. This was attributed to the slow deactivation rate of the catalytic system, which causes a rapid increase in the molecular weight at the beginning of polymerisation. Notably, when an initiator used for ATRP was a kind of polymeric molecule, the polymerisation kinetics could have been different from those of the system employing a low molecular weight initiator. For example, Lazzari et al. [14] prepared polyacrylonitrile-block polystyrene (PAN-*b*-PS) copolymers by ATRP, using bromine-terminated PAN macroinitiators. It was found that the first-order kinetic plots of styrene conversion showed a significant curvature. This indicated a progressive decrease in the concentration of active species during the copolymerisation. Results from <sup>1</sup>H-NMR suggested the loss of the bromide end group, which was mainly ascribed to the elimination of HBr.

In relation to this study, poly(3-hexyl thiophene)-*b*-poly(styrene-*co*-chloromethylstyrene) [P3HT-*b*-P(S-*co*-CMS)] were prepared from the ATRP of styrene and chloromethylstyrene (CMS) with the P3HT macroinitiator. In the case of CMS, we hypothesised that the chlorine atoms in the CMS might be eliminated and transferred to a transition metal halide catalyst during the ATRP process. Consequently, the ATRP kinetics for CMS might be different from that of a normal ATRP system. To the best of our knowledge, an ATRP kinetics study of styrene and chloromethylstyrene with the P3HT macroinitiator has not been reported in any open literature. The aim of this work was to investigate the kinetics of three different ATRP systems, namely normal

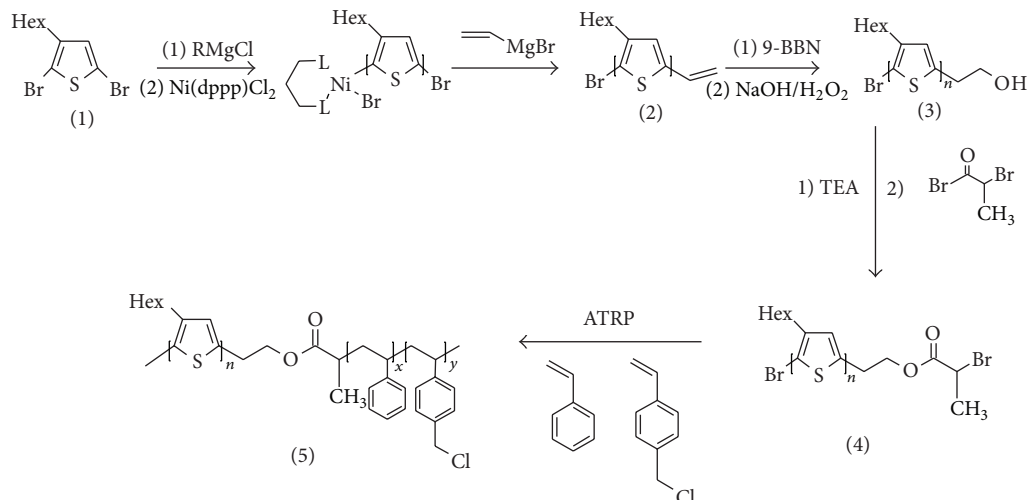


FIGURE 1: Schematic draw illustrating a synthetic route for preparing P3HT-*b*-P(S-*co*-CMS) via atom transfer radical polymerisation (ATRP).

ATRP, AGET-ATRP, and SR&NI ATRP, as a function of the monomers/macromolecule mole ratio. Morphology of the prepared block copolymer was also of our interest.

## 2. Materials and Methods

Styrene (99% from Aldrich) and CMS (90% from Fluka) were purified by passing them through an alumina column in order to remove any inhibitors. 2,5-dibromo-3-hexylthiophene (97%), butyl magnesium chloride (2.0 M in diethyl ether), 1,3-bis(diphenylphosphino) propane dichloronickel (II), vinyl magnesium bromide (1.0 M in THF), 9-BBN, 2-bromopropionyl bromide (97%), Cu(I)Br (98%), Cu(II)Br (99.999%), tin(II) 2-ethylhexanoate (95%), and N,N,N',N'',N'''-pentamethyldiethylenetriamine (PMDETA) (99%) were obtained from Aldrich and were used as received. Triethylamine (purum grade) was purchased from Fluka. Tetrahydrofuran (AR grade from Fisher) was refluxed over calcium hydride (reagent grade from Aldrich) for 24 h and was then distilled before use.

**2.1. Preparation of the P3HT Macroinitiator.** The P3HT macroinitiator was prepared using a multiple step synthetic route, in accordance with procedures described in the literature [15]. After that, the macroinitiator was further reacted with styrene and CMS monomers via three different ATRP systems (Figure 1). All reactions were carried out under nitrogen atmosphere using Schlenk line and cannula techniques.

**2.1.1. Preparation of Vinyl-Terminated Poly(3-hexylthiophene).** First, the vinyl-terminated P3HT was prepared by adding 2,5-dibromo-3-hexylthiophene (2.5 g, 7.5 mmol) to a dry 250 mL Schlenk flask, which was emptied of oxygen by applying a vacuum, followed by nitrogen purging. This process was repeated for three cycles before keeping the solution under a nitrogen atmosphere. Next, anhydrous THF (75 mL) was transferred to the reaction flask via a cannula. A 2 M solution of BuMgCl in diethyl ether (7.5 mL, 15 mmol) was added via

a deoxygenated syringe and the reaction mixture was refluxed for 90 min. After that, the solution was allowed to cool down to room temperature. Ni(dppp)Cl<sub>2</sub> (0.15 g, 0.27 mmol) was then added to the reaction mixture. The polymerization was allowed to proceed for 15 min at room temperature. Next, 1 M solution of vinyl magnesium bromide in THF (3 mL, 3 mmol) was added via a syringe and the reaction mixture was stirred for 15 min. After that, the reaction was terminated via precipitation into a large amount of methanol (1 L), where it was stirred for 1 h. The precipitated product was filtered and purified by sequential soxhlet extractions with methanol, followed by hexane and dichloromethane, respectively. Finally, the product was dried in a vacuum oven at 45°C for 24 h or until it reached a constant weight. The chemical structure of the vinyl-terminated P3HT was confirmed using proton nuclear magnetic resonance (<sup>1</sup>H-NMR) spectroscopy.

**2.1.2. Preparation of Hydroxyl-Terminated Poly(3-hexylthiophene).** Hydroxyethyl-terminated P3HT was prepared by further reacting the vinyl-terminated P3HT with 9-BBN. Vinyl-terminated P3HT (2 g, 0.2 mmol, DP<sub>n</sub> determined by <sup>1</sup>H-NMR = 32.61) was added to a dry 250 mL Schlenk flask. After five cycles of vacuum pumping and nitrogen purging, anhydrous THF (100 mL) was transferred into the reaction flask, under nitrogen atmosphere, via a double tipped needle. To this reaction mixture, a 0.5 M solution of 9-BBN (4 mL, 2.0 mmol) in anhydrous THF was added via a syringe. The reaction mixture was stirred for 24 h at 40°C, and then a 6 M solution of NaOH (2 mL) was added to the reaction flask. The reaction mixture was stirred for another 15 min (at which point, the oil bath was removed). The reaction mixture was allowed to cool down to room temperature, which was followed by the addition of a 33% aqueous solution of hydrogen peroxide (2 mL), wherein the reaction was allowed to proceed for additional 24 h at 40°C. The polymer was isolated by precipitation in a methanol-water mixture. The product was filtered and purified by a soxhlet extraction with

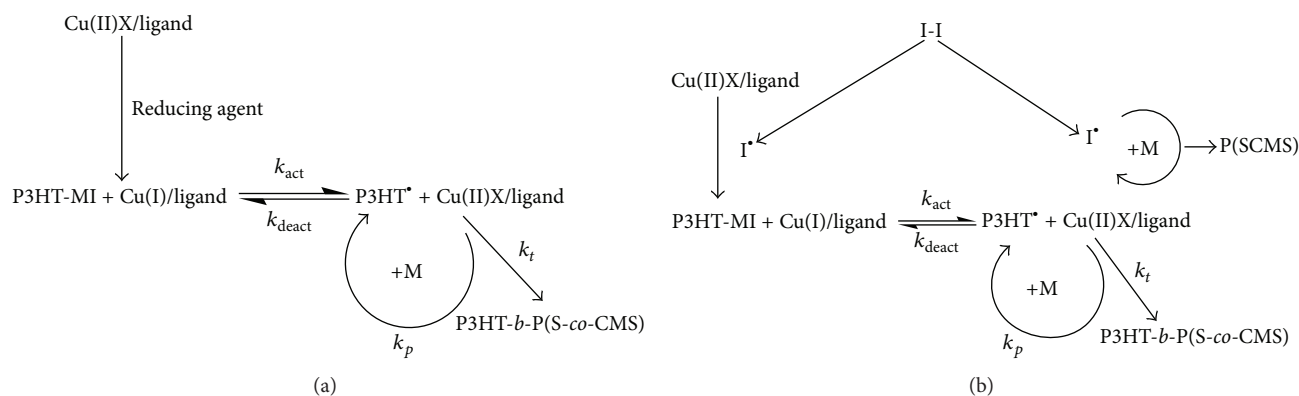


FIGURE 2: Mechanisms of (a) AGET-ATRP and (b) SR&NI ATRP.

methanol. The chemical structure of hydroxyl-terminated P3HT was confirmed by  $^1\text{H}$  NMR analysis.

**2.1.3. Preparation of the P3HT Macroinitiator.** Finally, the P3HT macroinitiator was prepared by dissolving the hydroxyl-terminated P3HT (1 g, 0.1 mmol) in anhydrous THF (100 mL) under nitrogen atmosphere. The reaction mixture was stirred for 15 min at  $40^\circ\text{C}$ , followed by the addition of triethylamine (9 mL, 66 mmol) and a drop-wise addition of 2-bromopropionyl bromide (7.5 mL, 60 mmol). The reaction mixture was stirred for 24 h at  $40^\circ\text{C}$ . The resulting P3HT macroinitiator was precipitated in methanol and refluxed over methanol, followed by drying under vacuum at  $45^\circ\text{C}$  for 24 h. The chemical structure and molecular weight of the synthesised polymer were characterised by  $^1\text{H}$  NMR spectroscopy. Number average molecular weight ( $M_n$ ) and weight average molecular weight ( $M_w$ ) of the polymer, as determined by GPC, were 7,100 g/mol and 9,122 g/mol, respectively.

**2.2. Atom Transfer Radical Polymerisation.** The P3HT macroinitiator (1 g, 0.1 mmol) and CuBr (0.14 g, 0.1 mmol) were added to a dry Schlenk flask. After applying a vacuum, followed by nitrogen purging for five cycles, the reaction mixture was immersed in a thermostat oil bath at  $100^\circ\text{C}$ . Then, a solution of PMDETA (0.02 mL, 0.1 mmol), styrene (1.70 mL, 15 mmol) and CMS (2.13 mL, 15 mmol) in 5 mL of dried THF was transferred into the reaction flask, using a deoxygenated syringe. The polymerisation was allowed to proceed at  $100^\circ\text{C}$  for a given time, ranging from 60 to 240 min. After that, the polymerisation was terminated by precipitation into a large amount of methanol. The residual catalyst was removed from the precipitate product by passing the polymer solution through an alumina column. The product was then washed with methanol. Notably, the product was also extracted with ether, DMSO, and acetone (which are selective solvents for this system) in order to ensure that the synthesised copolymer was free from any possible homopolymer contaminants. Finally, the product was dried in a vacuum oven at  $45^\circ\text{C}$  for 24 h, or until it reached a constant weight.

To determine the monomer conversion and theoretical molecular weight of the polymerised product, the sample

was periodically withdrawn from the reaction mixture with a degassed syringe. Monomer conversion was evaluated from the  $^1\text{H}$ -NMR spectrum of the crude product. In addition, theoretical values of degree of polymerisation ( $DP_n$ ) of the polymerised product with respect to styrene and CMS monomers can also be determined by using

$$DP_{n(i)} = \frac{[M_i]_0}{[\text{initiator}]_0} \times \text{conversion}. \quad (1)$$

**2.3. AGET-ATRP and SR&NI ATRP.** By using  $\text{CuBr}_2$  as a replacement for the CuBr transition metal catalyst, the AGET-ATRP, and SR&NI ATRP were carried out in similar procedures. In these cases,  $\text{Sn}(\text{EH})_2$  and AIBN were used as an activator and initiator, respectively (Figure 2). More specific details concerning the polymerisation recipe for each ATRP system are summarised in Table 1.

**2.4. Preparation of Donor-Acceptor Block Copolymers.** Finally, a kind of electron donor-acceptor block copolymers, namely poly(3-hexyl thiophene)-*b*-fullerene grafted polystyrene (P3HT-*b*-PSFu), to be used as a compatibilizer in bulk heterojunction polymer solar cells were prepared via a fullerenation. The fullerene ( $\text{C}_{60}$ ) groups were attached onto the P3HT-*b*-P(S-co-CMS) molecules via an Atom transfer radical addition (ATRA). Typical experimental procedures are as followed. To a 250 mL three-necked flask, 0.1 g of the P3HT-*b*-P(S-co-CMS) was mixed with the  $\text{C}_{60}$  (0.013 g), bipyridine (0.03 g), and dichlorobenzene (15 mL). The solution was purged with nitrogen gas for 15 min and then sealed with paraffin film and kept for further ATRA reactions. Next, Cu (0.013 g) and CuBr (0.0086 g) were added to a 250 mL three necked round bottom flask. The flask was closed with a rubber septum and sealed before undergoing vacuum and nitrogen purge for 5 cycles. Then, the above prepared polymer solution was introduced into the reaction flask by injection with a syringe through the rubber septum. The mixture was then refluxed at  $100^\circ\text{C}$  in an oil bath for 24 h. After cooling to room temperature, content in the reaction flask was filtrated and precipitated with excess amounts of methanol. The crude precipitated product was re-dissolved in THF and the mixture was passed through

TABLE I: Recipes for carrying out ATRP for styrene and chloromethylstyrene with the use of P3HT macroinitiator.

Polymerization methods	Molar compositions of the chemicals				
	[Cu(I)Br]	[Cu(II)Br <sub>2</sub> ]	[PMDETA]	[AIBN]	[Sn(EH) <sub>2</sub> ]
AGET ATRP	—	1	1	—	0.2
SR&NI ATRP	—	1	1	0.2	—
Normal ATRP	1	—	1	—	—

Styrene = 1.7 mL, chloromethylstyrene = 2.13 mL, P3HT = 1 g, Cu(II)Br<sub>2</sub> = 0.223 g, PMDEA = 0.02 mL,

(i) Sn(EH)<sub>2</sub> = 0.00648 mL for the AGET-ATRP system.

(ii) AIBN = 0.003 mL for the SR&NI-ATRP system.

(iii) Cu(I)Br = 0.14 mL for the normal ATRP system.

an alumina column in order to remove the copper catalyst and then precipitated into a large amount of methanol. The crude precipitated product was re-dissolved in THF, and then precipitated in methanol again. Hexane, which is a selective solvent for C<sub>60</sub> and a nonsolvent for the polymer, was used to remove any residual C<sub>60</sub> from the product. UV-visible spectroscopy was used to examine the presence of a characteristic absorption peak of free C<sub>60</sub> in the leached solvent. The washing process was carried out until the aforementioned UV-visible peak (wavelength 335 nm) was absent. Finally, the purified product was dried in a vacuum oven at 45°C until reaching a constant weight (~24 h). The donor-acceptor block polymer was characterized by UV/Visible spectroscopy and thermal gravimetric analysis (TGA). More details concerning the characterizations can be found elsewhere [16].

**2.5. Characterisations.** The chemical structure of the synthesised polymer was verified using the <sup>1</sup>H-NMR technique. The sample for the <sup>1</sup>H-NMR experiments was prepared by dissolving 5 mg of the polymer in 5 mL of deuterated chloroform (CDCl<sub>3</sub>). The NMR experiment was carried out with a Bruker instrument (500 MHz, ADVANCE DPX 300 model) using tetramethylsilane (TMS) as an external reference at 20°C.

The molecular weight of the purified products was determined by using a gel permeation chromatography (GPC) technique, with the use of a Water (Breeze2 HPLC System) instrument equipped with an RI detector. THF was used as an eluent and 100 μL of the sample solution (3 mg/mL in THF) was prepared and filtered with a nylon 66 membrane before injection. GPC was operated at a flow rate of 1.0 mL/min. The obtained GPC chromatogram was then translated into a molecular weight distribution (MWD) curve via the use of a polystyrene narrow molecular weight calibration curve. The average molecular weight and polydispersity index were determined using standard equations.

Thermal behaviour of the synthesised block copolymer was characterised by thermal gravimetric analysis (TGA), using a Mettler Toledo (TGA/SDTA 851) instrument. The sample (10 mg) was used and then heated over temperatures ranging from 25 to 800°C, at a heating rate of 10°C/min, under nitrogen atmosphere.

Morphology and surface topographical features of the prepared block copolymers were examined by Atomic Force Microscopy (AFM; Seiko Instruments SPA-400). Briefly,

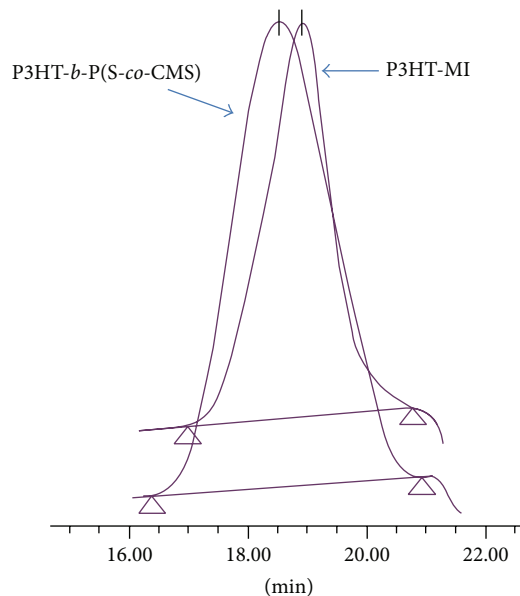


FIGURE 3: Overlaid GPC chromatograms of the P3HT macroinitiator and that of the product obtained from ATRP.

a solution of the sample was spin coated onto a silicon (Si) substrate, at room temperature. Solvent was evaporated by drying at 50°C under reducing pressure in a vacuum oven (10<sup>-2</sup> mbar). The samples then underwent AFM analysis and the corresponding images were examined by using a phase image tapping mode and a topographic mode.

### 3. Results and Discussion

The molecular weight of P3HT-*b*-P(S-*co*-CMS) was determined using the GPC technique, as shown in Figure 3. The GPC peak of the macroinitiator shifted to a shorter retention time, indicating that the molecular weight of the polymer product increased. By using a calibration curve,  $M_n$  of the P3HT macroinitiator and the corresponding product were 7,100 and 9,300 g/mol, respectively. This indicates that further reactions with styrene and CMS extended the chain length of the macroinitiator.

The chain extension of the P3HT macroinitiator was further confirmed by the <sup>1</sup>H-NMR. Figure 4 shows the <sup>1</sup>H-NMR spectrum of the P3HT macroinitiator. Characteristic

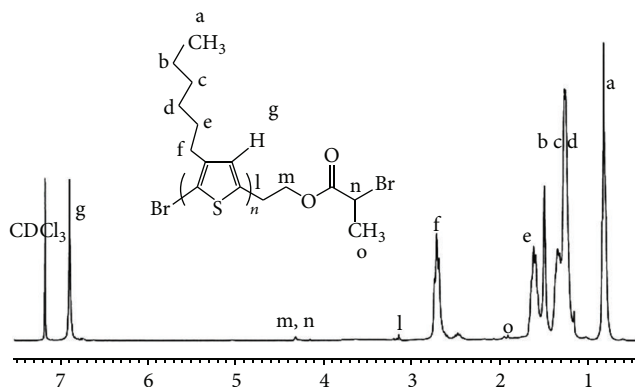


FIGURE 4:  $^1\text{H-NMR}$  spectrum of the P3HT macroinitiator.

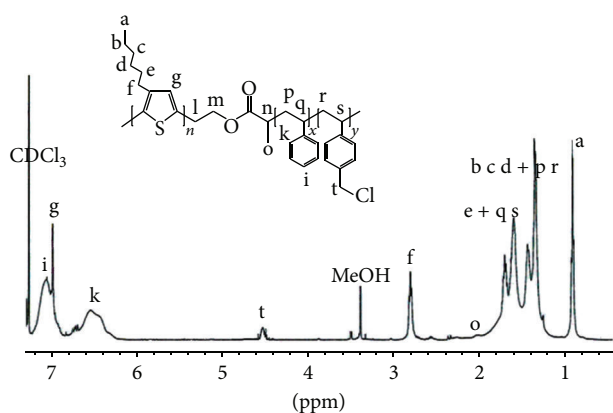


FIGURE 5:  $^1\text{H-NMR}$  spectrum of the P3HT-*b*-P(S-*co*-CMS).

monomer peaks at 1.9, 3.2 and 4.3 ppm that represent the protons in the bromopropionate end groups of the macroinitiator can be seen. The peak at 6.8 ppm can be ascribed to the aromatic protons of the P3HT main chains. After carrying out the ATRP, the peaks at 7.0 and 7.3 ppm emerged (Figure 5). These could be attributed to the aromatic protons in the repeating units of P(CMS) and PS, respectively. On the other hand, the above spectrum lacks peaks at 5.2 and 5.7 ppm of the olefinic proton, indicating that there are no residual monomers in the purified product. The peak at 4.3, representing the protons in the bromopropionate end group of the macroinitiator, also disappears, whereas the peak at 4.6 ppm, belonging to the methylene protons adjacent to the chlorine atom of the P(CMS) repeating units, appears. The above spectral changes are sufficient to confirm that the P3HT-*b*-P(S-*co*-CMS) was obtained. Similar spectral changes were observed from the  $^1\text{H-NMR}$  spectrum of P3HT-*b*-P(S-*co*-CMS), prepared by using different ATRP conditions. In addition, by using the characteristic NMR peaks representing each repeating unit, compositions of the copolymers can be determined. These results are summarised in Table 2.

It is worth noting that a majority of the P(S-*co*-CMS) block contains PS repeating units, regardless of the monomer/macromolecule mole ratio. The composition also changed with the polymerisation time, that is, the longer

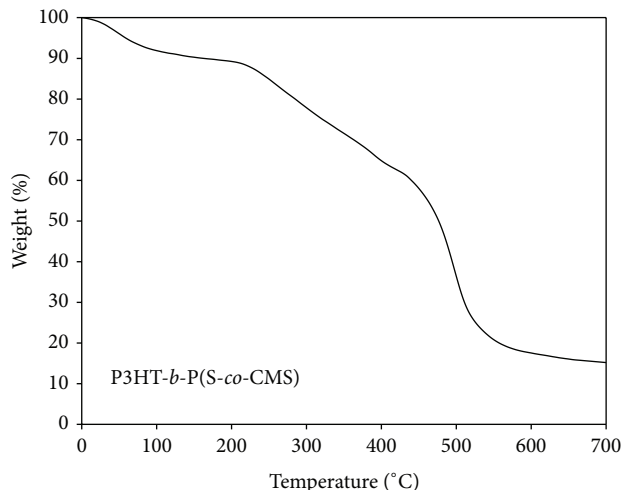


FIGURE 6: TGA thermogram of the P3HT-*b*-P(S-*co*-CMS).

the time, the greater the P(CMS) content. This could be ascribed to the different monomer reactivity ratios and to a composition drift effect [17]. In addition, our earlier work concerning a synthesis of PPV-*g*-P(S-*co*-CMS) via iniferter polymerisation [18] also revealed that the reactivity ratios of CMS and styrene, determined using the Fineman-Ross equation [19], are 0.11 and 0.51, respectively.

In addition, side reactions during ATRP might also be possible. Our control experiments involving free radical copolymerisations of styrene and CMS via the use of either AIBN or iniferter polymerisations revealed that the P(CMS) composition in the P(S-*co*-CMS) chains are 47.57% and 43.82%, respectively. These values are significantly higher than those obtained from the ATRP when the same monomer/feed mole ratio was used (50/50). This discrepancy implies that some side reactions might occur during the ATRP. This includes a chain transfer reaction to the chlorine atoms in the P(CMS) units of the copolymer, leading to some changes and/or deviations in the copolymer composition.

Figure 6 shows a TGA thermogram of the product obtained from copolymerisation of styrene and chloromethylstyrene at 100°C for 180 min via the ATRP technique. A three-step transition can be observed. The first transition occurred over a temperature range of between 50 and 150°C, involving approximately a 10% weight loss, which can be ascribed to the evaporation of absorbed water on the sample's surface. Next, the second weight loss (27 wt%) occurred over a temperature range of 220–390°C. This could be related to the decomposition of P(S-*co*-CMS) units [20, 21]. Finally, the third transition, which accounted for 48% of the weight loss, represents the decomposition of P3HT [22]. Above 700°C, no further weight loss was observed and the remaining weight is attributed to residual solids.

**3.1. ATRP Kinetics.** Figure 7 shows that the monomer conversion increases with the polymerisation time and tends to reach a plateau after 120 min. This can be ascribed to the fact that the ATRP is a type of controlled radical polymerisation.

TABLE 2: Effects of monomer : macroinitiator mole ratios and polymerization times on monomers conversions, molecular weights, and compositions of the P3HT-*b*-P(S-*co*-CMS) copolymers obtained from ATRP of styrene and chloromethylstyrene.

Polymerization time (min)	Conditions		P3HT- <i>b</i> -P(S- <i>co</i> -CMS) compositions			Molecular weight analysis	
	Monomers/P3HT mole ratios	Monomers conversion (%)	P(SCMS) block (% mol)	PS (% mol)	P(CMS) (%mol)	$M_n$ (g/mol)	PDI
60	300 : 1	25.40	14.16	72.73	27.27	9,774	1.09
	200 : 1	19.63	4.84	77.06	22.94	8,249	1.07
90	300 : 1	30.27	16.32	73.85	26.15	9,973	1.09
	200 : 1	26.18	8.41	73.85	26.15	9,321	1.05
120	300 : 1	36.04	18.37	74.67	25.33	11,698	1.06
	200 : 1	29.99	12.79	69.70	30.30	10,112	1.05
180	300 : 1	43.08	20.51	69.70	30.30	13,488	1.13
	200 : 1	35.51	16.53	70.97	29.03	11,190	1.08
240	300 : 1	50.14	28.57	65.61	34.39	15,934	1.12
	200 : 1	38.55	18.57	68.21	31.79	12,079	1.11

Styrene/CMS mole ratio = 50/50.

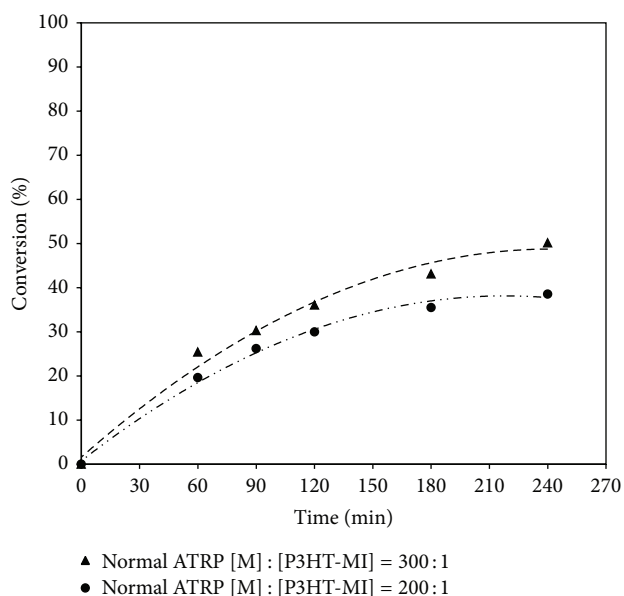


FIGURE 7: Relationships between monomer conversion and reaction time during ATRP of styrene and CMS at 100°C.

The propagating chains are reversibly reacted with bromine atoms, serving as a capping agent. Consequently, the longer the reaction times, the higher the chances for monomers to react with the propagating chains. After a prolonged polymerisation time beyond 120 min, the conversion gradually increased with time, possibly due to changes in monomer composition and depletion of the macroinitiator.

Figure 7 also shows that by increasing the monomers/macroinitiator mole ratio from 200 : 1 to 300 : 1, the monomer conversion and percentage mole of the P(S-*co*-CMS) block increases, regardless of the polymerisation techniques. This is due to the fact that the higher the mole ratio, the greater the polymerisation rate. The above statement is supported by the results from the kinetic plot of  $\ln[M_0]/[M]$  versus time

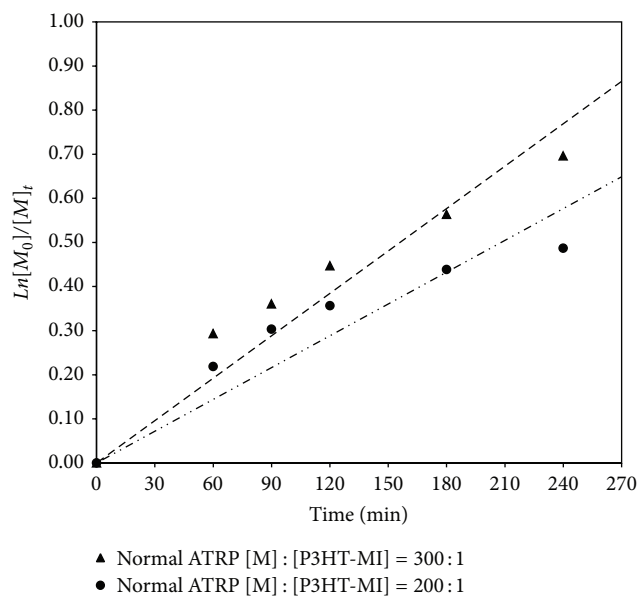


FIGURE 8: Kinetic plots of  $\ln[M_0]/[M]$  versus time for ATRP of styrene and CMS with the P3HT macroinitiator (using different monomers/macroinitiator mole ratios).

for the ATRP of styrene and CMS (Figure 8), which led to the calculated rate constants of  $1.9 \times 10^{-3}$  and  $2.7 \times 10^{-3} \text{ s}^{-1}$  for the ATRP using the mole ratios of 200 : 1 and 300 : 1, respectively.

Figure 9 shows the dependence of the molecular weight and polydispersity index (PDI) on monomer conversion for the ATRP of styrene and CMS with the P3HT macroinitiator. The PDI values of the polymerised products ranged from between 1.05 and 1.13. These values are considerably lower when compared to those obtained from normal free radical polymerisations and/or other controlled radical polymerisation techniques, such as iniferter polymerisation [9]. For example, our control experiments concerning free radical copolymerisation of the styrene and CMS via the use of AIBN

TABLE 3: Monomers conversions, molecular weights, and compositions of the P3HT-*b*-P(S-*co*-CMS) copolymers obtained from various ATRP systems.

Polymerization time (min)	Conditions		P3HT- <i>b</i> -P(S- <i>co</i> -CMS) compositions			Molecular weight analysis	
	ATRP methods	Monomers conversion (%)	P(SCMS) block (% mol)	PS (% mol)	P(CMS) (%mol)	$M_n$ (g/mol)	PDI
60	AGET ATRP	35.75	22.74	75.73	24.27	9,194	1.09
	SR&NI ATRP	16.78	16.45	86.11	13.89	9,671	1.07
	Normal ATRP	25.40	14.16	72.73	27.27	9,774	1.09
90	AGET ATRP	41.34	24.78	75.61	24.39	10,314	1.05
	SR&NI ATRP	25.12	18.51	81.48	18.52	10,067	1.06
	Normal ATRP	30.27	16.32	73.85	26.15	9,973	1.05
120	AGET ATRP	45.03	25.54	72.22	27.78	11,541	1.13
	SR&NI ATRP	38.71	20.25	73.33	26.67	11,572	1.08
	Normal ATRP	36.04	18.37	74.67	25.33	11,698	1.12
180	AGET ATRP	50.71	25.60	70.09	29.91	12,592	1.11
	SR&NI ATRP	45.65	23.78	68.35	31.65	13,646	1.05
	Normal ATRP	43.08	20.51	69.70	30.30	13,488	1.21
180	Iniferter	n/a	n/a	56.18	43.82	8,504	1.84
180	Normal FRP with AIBN	n/a	n/a	52.43	47.57	9,069	2.28
240	AGET ATRP	54.82	29.58	64.29	35.71	16,989	1.12
	SR&NI ATRP	55.54	31.11	60.67	39.33	16,404	1.09
	Normal ATRP	50.14	28.57	65.61	34.39	15,934	1.23

Monomers/P3HT macroinitiator mole ratio = 300/1; styrene/CMS mole ratio = 50/50.

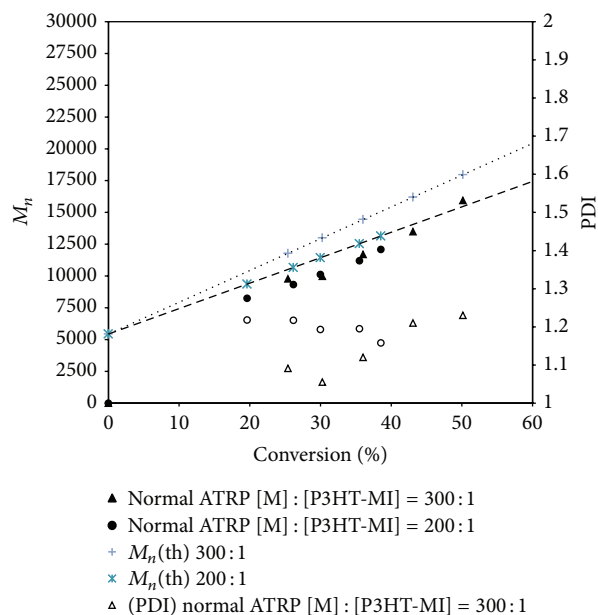


FIGURE 9: Dependence of molecular weight and polydispersity index on monomer conversion for the ATRP of styrene and CMS with the P3HT macroinitiator (using different monomers/macoinitiator mole ratios).

and/or the use of iniferter polymerisation revealed that the obtained PDI values of the products lies between 2.28 and 1.84, respectively (Table 3).

Notably, in all cases, the actual  $M_n$  determined from the GPC technique is lower than that of the theoretical  $M_n$ , regardless of the monomers/macoinitiator mole ratios. In particular, the polymers prepared using the higher mole ratio (300:1) showed this trend at the highest level, that is, the higher the mole ratio, the greater the discrepancy. This result implies that nonnegligible chain transfer reactions occurred during the polymerisation [11].

**3.2. Comparisons of Various ATRP Systems.** Figure 10 shows the relationships between monomer conversion and reaction time during the copolymerisation of styrene and CMS using normal ATRP, AGET-ATRP and SR&NI ATRP, respectively. The monomer conversion linearly increases with time before reaching a plateau. This can be explained in a similar fashion to the above results, as shown in Figure 8. It is worth nothing that at a shorter polymerisation time, the monomer conversion obtained from the AGET-ATRP system is higher than those obtained from the normal ATRP and SR&NI ATRP. This is because  $\text{CuBr}_2$  is more stable than its lower oxidation state analogue ( $\text{CuBr}$ ) that was used in the normal ATRP system. In the case of AGET-ATRP, the reduction of  $\text{CuBr}_2$  with  $\text{Sn}(\text{EH})_2$  leads to a shift toward a dormant species. In this system, homo-polymerisation of the styrene and CMS is less likely to occur due to the fact that there is no radical initiator in this system. This is not the case for the SR&NI-ATRP system where the decomposition of AIBN might induce homo-polymerisation of the monomers, leading to the lower rate of polymerisation. Similar results

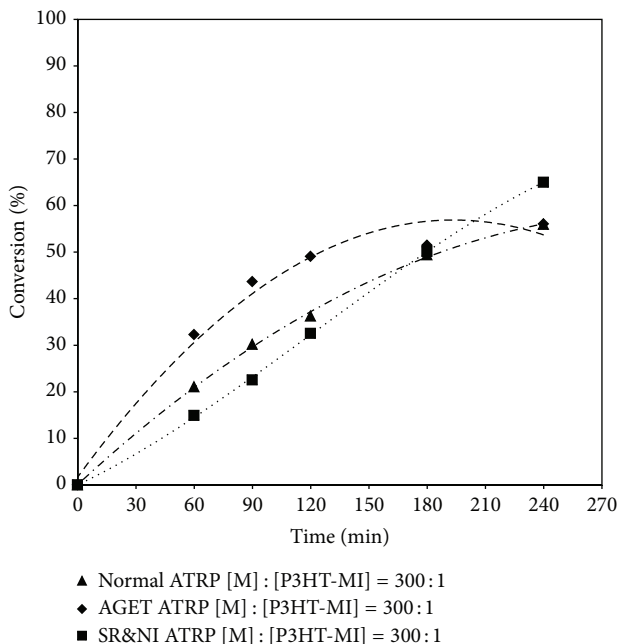


FIGURE 10: Relationships between monomer conversion and reaction time during polymerisations of styrene and chloromethylstyrene via different ATRP systems.

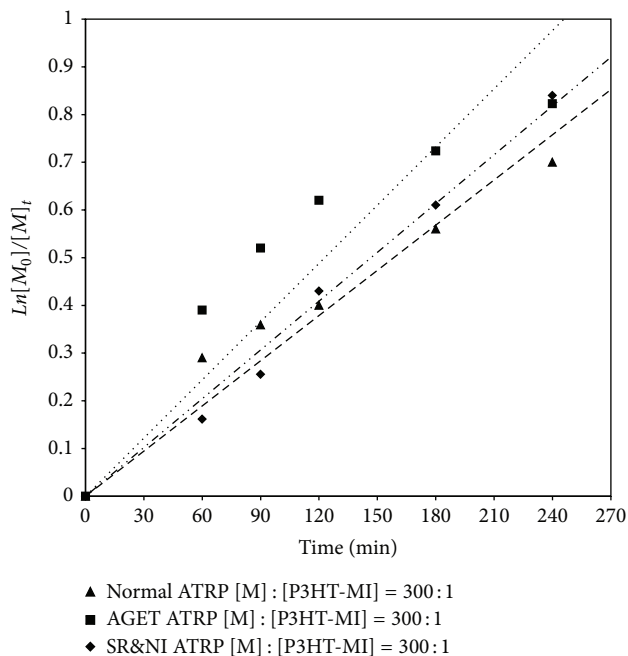


FIGURE 11: Kinetic plots of  $\ln[M_0]/[M]$  versus time for polymerisation of styrene and CMS via different ATRP systems, using the P3HT macroinitiator (monomers/macroinitiator mole ratio = 300 : 1).

were observed by Lacroix-Desmazes et al. [23] in a study on poly(chloromethylstyrene-*b*-styrene) block copolymers.

Kinetic plots of  $\ln[M_0]/[M]$  versus time for the polymerisation of styrene and CMS via different ATRP systems are illustrated in Figure 11. The three types of ATRP systems led to the first order kinetics with respect to the monomers.

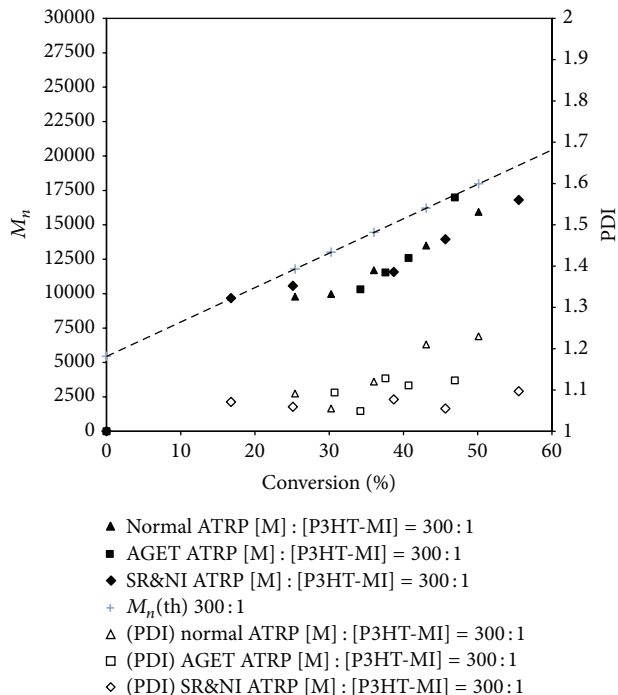


FIGURE 12: Dependence of molecular weight and polydispersity index on monomer conversion for the polymerisation of styrene and CMS via different ATRP systems, using the P3HT macroinitiator (monomers/macroinitiator mole ratio = 300/1).

This behaviour is similar to those behaviours reported in the literature for the homopolymerisation of styrene via ATRP [12, 13]. In this study, we found that the polymerisation rates among the three ATRP systems are slightly different. The rate constant ( $k$ ) for the AGET ATRP system is the highest ( $4.1 \times 10^{-3} \text{ s}^{-1}$ ), followed by that of SR&NI ATRP ( $3.4 \times 10^{-3} \text{ s}^{-1}$ ) and normal ATRP ( $3.2 \times 10^{-3} \text{ s}^{-1}$ ), respectively.

Dependencies of the molecular weight and PDI on the monomer conversion of styrene and CMS from the three ATRP systems are also shown in Figure 12. PDI values of the products ranged from between 1.05 and 1.23. The values are considerably smaller than those generally obtained from a normal free radical polymerisation, as well as the other types of controlled radical polymerisation. Molecular weight values of the synthesised products, determined by GPC technique, are lower than the theoretical values, calculated by assuming a truly *living* polymerisation condition. This indicates that the ATRP polymerisation is not a truly living polymerisation and the reaction is not totally free from any chain transfer reactions. In addition, the chlorine atom of CMS has reactive functionality for ATRP and can act as an initiator and/or a chain transfer agent [24]. Therefore, chain transfer reactions to CMS and/or to the propagating polymer chains can occur. In theory, these side reactions could lead to the formation of various polymer structures, such as P(*S-co*-CMS) linear chains or P(*S-co*-CMS) grafted copolymers (structure No. (3) in Figure 13), in addition to more complex architecture, such as the hyper-grafted copolymer, based on P3HT-*b*-P(*S-co*-CMS) backbone. The latter two by-products cannot be

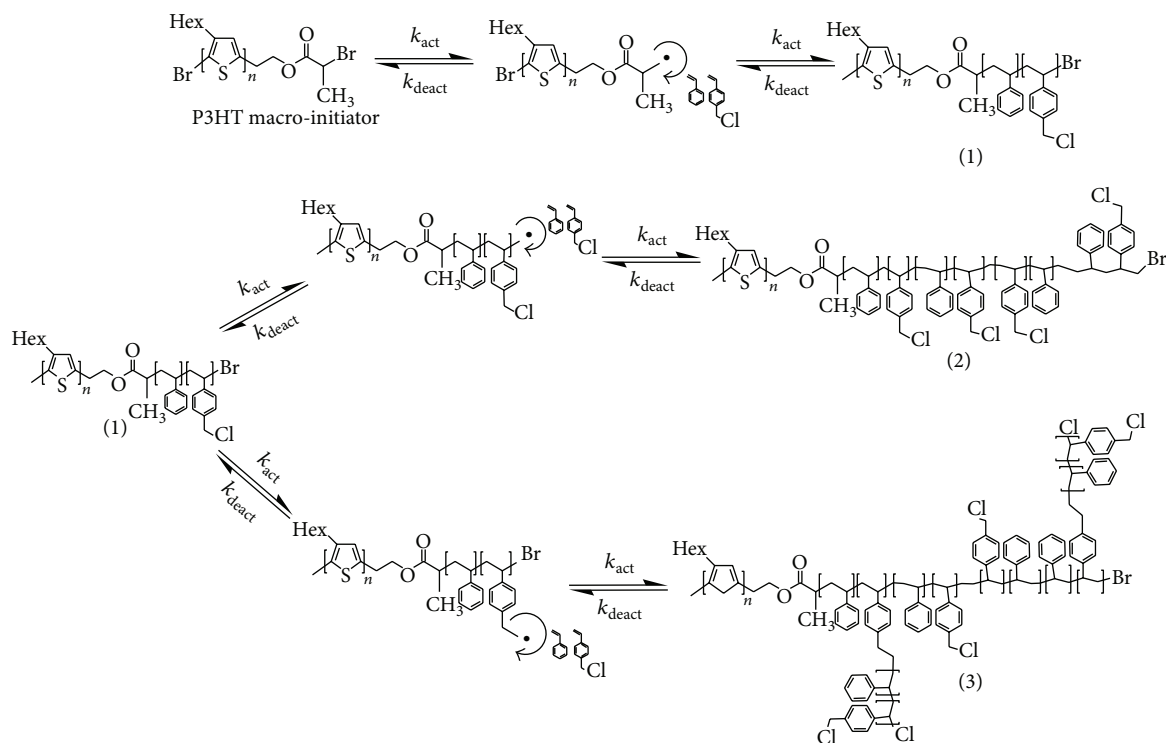


FIGURE 13: A schematic structure of a tentative byproduct attributed to chain transfer reactions occurring during the ATRP of styrene and CMS.

isolated from the main product by multiple extractions with several selective solvents. Due to the different molecular architectures and chain conformations, it might be possible that the presence of these remaining by-products contributed to a deviation of  $M_n$  (determined from GPC technique) of the prepared product from its theoretical  $M_n$  value.

Table 3 shows that by increasing the polymerisation time to 180 min or more, some differences in PDI values between the polymers obtained from the normal ATRP and those from the modified ATRP systems (AGET-ATRP and SR&NI ATRP) were noted. In the latter cases, the PDI values of P3HT-*b*-P(S-*co*-CMS) ranged from 1.05–1.12, which are slightly lower than the values from the normal ATRP (1.21–1.23). This indicates that the AGET-ATRP and SR&NI ATRP systems are the better-controlled polymerisation systems.

Last but not least, morphology of the various block copolymers deserved a consideration. Figure 14 shows AFM micrographs of the P3HT-*b*-P(S-*co*-CMS), experiencing different types of ATRP methods. The micrographs obtained from a phase image tapping mode reveal the presence of two separated phases. The dark area represents the material with a relatively low modulus whereas the brighter area was more rigid. In relation to this study, these two phases corresponded to the P3HT block and the P(S-*co*-CMS) block in the copolymer, respectively. This was due to the fact that glass transition temperature of P(S-*co*-CMS) is about 81°C [24] which is greater than that of the P3HT macroinitiator (67°C). From the above micrographs, a kind of dispersed

particle morphology was noted, regardless of the types of ATRP systems used for the polymerization. The P(S-*co*-CMS) block was a minor phase being dispersed within the continuous P3HT matrix. This is in a good agreement with the results from Table 3, showed that percentage composition of P(S-*co*-CMS) block in the copolymer is lower than that of the P3HT block. In other words, majority of the block copolymer molecule is P3HT. In this study, the effect of polymerization systems on morphology and phase size of the copolymer was not obvious. This was due to the fact that composition of the block copolymers was very similar (Table 3). Nevertheless, the above results indicate that the two blocks were incompatible and the phase separated morphology was induced.

Interestingly, after grafting fullerene groups onto the block copolymer molecules, using the ATRA technique, the AFM micrographs (Figure 15) in a topographic mode revealed that surface roughness of the block copolymers increased significantly. The above change could be attributed to the presence of C<sub>60</sub>. In relation to the bulk heterojunction polymer solar cell application, photovoltaic performance of the BHJ depends on many factors including the morphology of materials in the active layer. Generally speaking, the higher the surface roughness of the donor and acceptor materials, the greater the contact area between the active layer and the metal electrodes. Consequently, more efficient charge collection at the interface and the greater power conversion efficiency can be expected.

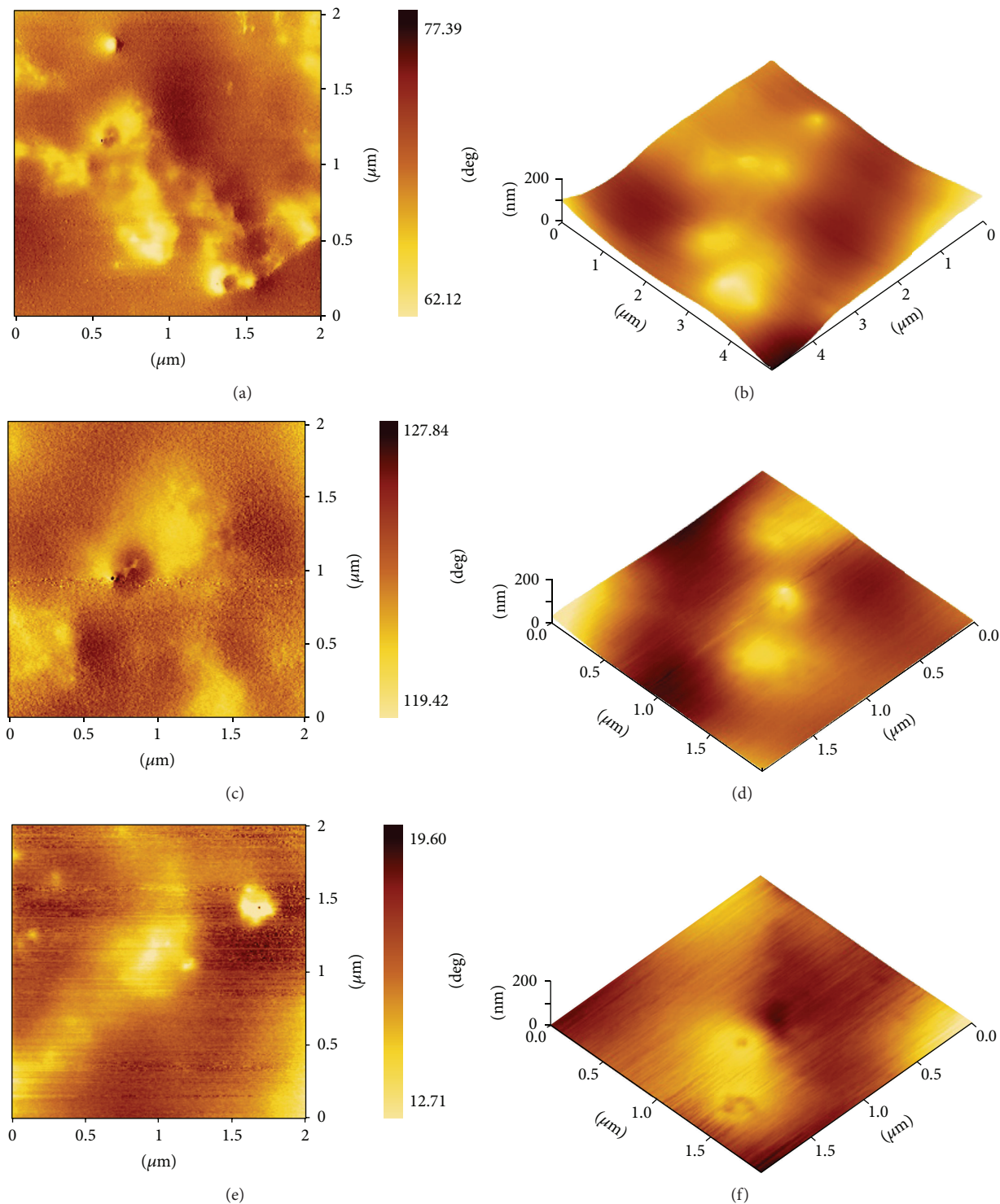


FIGURE 14: AFM micrographs of the P3HT-*b*-P(S-*co*-CMS) prepared by various ATRP systems; normal ATRP (top row), AGET-ATRP (middle row), and SR&NI ATRP (bottom row). The micrographs were recorded in a phase image tapping mode (left column) and a topographic mode (right column).

#### 4. Conclusions

P3HT-*b*-P(S-*co*-CMS) block copolymers were prepared via a chain extension of the P3HT macroinitiator with styrene and CMS comonomers. Kinetics of three different ATRP systems,

normal ATRP, AGET-ATRP, and SR&NI ATRP, were studied. Results from the  $^1\text{H-NMR}$  analysis shows that the copolymer product containing the P(S-*co*-CMS) block (with polystyrene repeating units as a major component) was obtained. The three types of ATRP systems led to the first order kinetics with

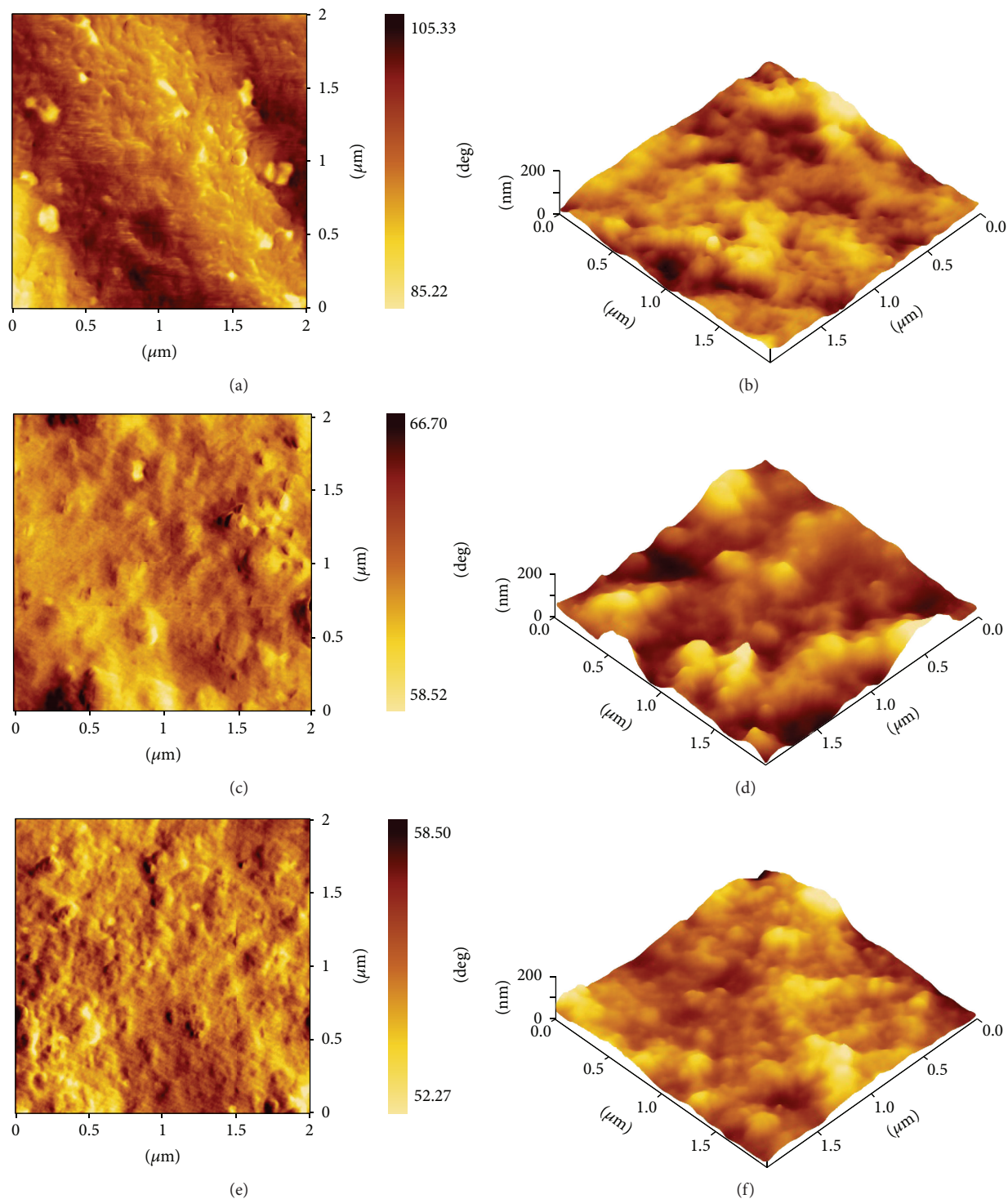


FIGURE 15: AFM micrographs of the donor-acceptor block copolymers (P3HT-*b*-PSFu) prepared by various ATRP systems; normal ATRP (top row), AGET-ATRP (middle row), and SR&NI ATRP (bottom row). The micrographs were recorded in a phase image tapping mode (left column) and a topographic mode (right column).

respect to the monomers. The rate of polymerisation among the three different systems increased in the order of AGET-ATRP > SR&NI-ATRP > normal ATRP. Polydispersity index values of the copolymer products obtained from the modified ATRP systems (AGET-ATRP and SR&NI ATRP) ranged from

1.05–1.12, which are slightly lower than are the values from the normal ATRP system (1.21–1.23). The number average molecular weight ( $M_n$ ) of the block copolymer products is lower than that of the theoretical  $M_n$  values, regardless of the polymerisation conditions. The discrepancies were

discussed in light of the side reactions, including the chain transfer reaction from the propagating chain ends to the chlorine atoms along the P(CMS) repeating units of the copolymer chains. Results from AFM micrographs (phase image) indicated that the synthesized block copolymers are phase separated. Morphology of the block copolymers was also changed significantly after grafting with fullerene.

## Conflict of Interests

There is no conflict of interests in this paper.

## Acknowledgments

Mr. Nattawoot Rattanathamwat would like to thank the National Nanotechnology Center (NANOTEC) for the financial support during this doctoral study (Grant no. P10-10588). This work was also supported by the Nanotechnology Center (NANOTEC), NSTDA, Ministry of Science and Technology, Thailand, through its Center of Excellence Network programme.

## References

- [1] X. Fan, C. Cui, G. Fang et al., "Efficient polymer solar cells based on poly(3-hexylthiophene): indene-C<sub>70</sub> bisadduct with a MoO<sub>3</sub> buffer layer," *Advanced Functional Materials*, vol. 22, no. 3, pp. 585–590, 2012.
- [2] B. C. Thompson and J. M. J. Fréchet, "Polymer-fullerene composite solar cells," *Angewandte Chemie International Edition*, vol. 47, no. 1, pp. 58–77, 2008.
- [3] W. Cai, X. Gong, and Y. Cao, "Polymer solar cells: recent development and possible routes for improvement in the performance," *Solar Energy Materials and Solar Cells*, vol. 94, no. 2, pp. 114–127, 2010.
- [4] S. E. Shaheen, D. S. Ginley, and G. E. Jabbour, "Organic-based photovoltaics: toward low-cost power generation," *MRS Bulletin*, vol. 30, no. 1, pp. 10–15, 2005.
- [5] E. Bundgaard and F. Krebs, "Low band gap polymers for organic photovoltaics," *Solar Energy Materials and Solar Cells*, vol. 91, no. 11, pp. 954–985, 2007.
- [6] D. H. Wang, J. S. Moon, J. Seifert et al., "Sequential processing: control of nanomorphology in bulk heterojunction solar cells," *Nano Letters*, vol. 11, no. 8, pp. 3163–3168, 2011.
- [7] Z. Sun, K. Xiao, J. K. Keum et al., "PS-b-P3HT copolymers as P3HT/PCBM interfacial compatibilizers for high efficiency photovoltaics," *Advanced Materials*, vol. 23, no. 46, pp. 5529–5535, 2011.
- [8] J.-S. Wang and K. Matyjaszewski, "Controlled/living radical polymerization. atom transfer radical polymerization in the presence of transition-metal complexes," *Journal of the American Chemical Society*, vol. 117, no. 20, pp. 5614–5615, 1995.
- [9] W. A. Braunecker and K. Matyjaszewski, "Controlled/living radical polymerization: features, developments, and perspectives," *Progress in Polymer Science*, vol. 32, no. 1, pp. 93–146, 2007.
- [10] J. Chiefari and E. Rizzardo, "Control of free-radical polymerization by chain transfer methods," in *Handbook of Radical Polymerization*, K. Matyjaszewski and T. P. Davis, Eds., chapter 12, pp. 629–690, Wiley, 2003.
- [11] M. Y. Khan, Z. Xue, D. He, S. K. Noh, and W. S. Lyoo, "Comparative study of a variety of ATRP systems with high oxidation state metal catalyst system," *Polymer*, vol. 51, no. 1, pp. 69–74, 2010.
- [12] K. Matyjaszewski, T. E. Patten, and J. Xia, "Controlled/living radical polymerization. Kinetics of the homogeneous atom transfer radical polymerization of styrene," *Journal of the American Chemical Society*, vol. 119, no. 4, pp. 674–680, 1997.
- [13] H. Arslan, Y. Kucuk, A. Mente, and M. H. Acar, "A kinetic study of atom transfer radical polymerization of styrene with bis(2-pyridyl)ethylenedimethanimine derivative ligands," *Turkish Journal of Chemistry*, vol. 37, pp. 824–831, 2013.
- [14] M. Lazzari, O. Chiantore, R. Mendichi, and M. Arturo López-Quintela, "Synthesis of polyacrylonitrile-block-polystyrene copolymers by atom transfer radical polymerization," *Macromolecular Chemistry and Physics*, vol. 206, no. 14, pp. 1382–1388, 2005.
- [15] M. C. Iovu, M. Jeffries-El, E. E. Sheina, J. R. Cooper, and R. D. McCullough, "Regioregular poly(3-alkylthiophene) conducting block copolymers," *Polymer*, vol. 46, no. 19, pp. 8582–8586, 2005.
- [16] N. Rattanathamwat, J. Wootthikanokkhan, N. Nimitsiriwat, C. Thanachayanont, U. Asawapirom, and A. Keawprajak, "Poly(3-hexyl thiophene)-b-fullerene functionalized polystyrene copolymers (P3HT-b-PSFu) as compatibilizer in P3HT/Phenyl-C61-butyric acid methyl ester (PCBM) solar cells," *International Journal of Polymeric Materials and Polymeric Biomaterials*, vol. 63, no. 9, pp. 448–455, 2014.
- [17] X. Chen, B. Gholamkhash, X. Han, G. Vamvounis, and S. Holdcroft, "Polythiophene-graft-styrene and polythiophene-graft-(styrene-graft-C 60) copolymers," *Macromolecular Rapid Communications*, vol. 28, no. 17, pp. 1792–1797, 2007.
- [18] N. Seeponkai, N. Keaitsirisart, J. Wootthikanokkhan, C. Thanachayanont, and S. Chuangchote, "Fullerene functionalized polystyrene: synthesis, characterizations, and application in bulk heterojunction polymer solar cells," *International Journal of Polymeric Materials and Polymeric Biomaterials*, vol. 63, no. 1, pp. 33–40, 2014.
- [19] G. Odian, "Radical chain polymerization," in *Principles of Polymerization*, G. Odian, Ed., chapter 3, pp. 198–349, John Wiley & Sons, New York, NY, USA, 2004.
- [20] J. D. Peterson, S. Vyazovkin, and C. A. K. Wight, "Kinetics of the thermal and thermo-oxidative degradation of polystyrene, polyethylene and poly(propylene)," *Macromolecular Chemistry and Physics*, vol. 202, no. 6, pp. 775–784, 2001.
- [21] C. Kavakli, N. Özvatan, S. A. Tuncel, and B. Salih, "1,4,8,11-Tetraazacyclotetradecane bound to poly(*p*-chloromethylstyrene-ethylene glycol dimethacrylate) microbeads for selective gold uptake," *Analytica Chimica Acta*, vol. 464, no. 2, pp. 313–322, 2002.
- [22] B. K. Kuila, K. Park, and L. Dai, "Soluble P3HT-grafted carbon nanotubes: synthesis and photovoltaic application," *Macromolecules*, vol. 43, no. 16, pp. 6699–6705, 2010.
- [23] P. Lacroix-Desmazes, T. Delair, C. Pichot, and B. Boutevin, "Synthesis of poly(chloromethylstyrene-*b*-styrene) block copolymers by controlled free-radical polymerization," *Journal of Polymer Science Part A: Polymer Chemistry*, vol. 38, no. 21, pp. 3845–3854, 2000.
- [24] H.-J. Paik, S. G. Gaynor, and K. Matyjaszewski, "Synthesis and characterization of graft copolymers of poly(vinyl chloride) with styrene and (meth)acrylates by atom transfer radical polymerization," *Macromolecular Rapid Communications*, vol. 19, no. 1, pp. 47–52, 1998.

## Research Article

# Preparation and Properties of OMMT/PU Composites

Chen Yufei,<sup>1,2</sup> Han Yang,<sup>1</sup> Dai Qiwan,<sup>1</sup> Zhang Xiwan,<sup>1</sup> and Qingyu Zhang<sup>1</sup>

<sup>1</sup>Key Laboratory of Engineering Dielectrics and Its Application, Ministry of Education, Harbin University of Science and Technology, Harbin 150080, China

<sup>2</sup>College of Material Science & Engineering, Harbin University of Science and Technology, Xiangfang District, Harbin, Heilongjiang 150040, China

Correspondence should be addressed to Chen Yufei; [chenyufei@hrbust.edu.cn](mailto:chenyufei@hrbust.edu.cn)

Received 14 August 2014; Revised 2 November 2014; Accepted 7 December 2014

Academic Editor: Kwangho Kim

Copyright © 2015 Chen Yufei et al. This is an open access article distributed under the Creative Commons Attribution License, which permits unrestricted use, distribution, and reproduction in any medium, provided the original work is properly cited.

Prepolymer of polyurethane (PU) was prepared by toluene diisocyanate (TDI) and polyether diol through polymerization, organically modified montmorillonite (OMMT) gained by montmorillonite (MMT) that was modified by octadecyl trimethyl ammonium chloride (OTAC), and the OMMT was used as intercalator; alcohol-based OMMT/PU adhesive was synthesized. The micromorphology of OMMT/PU adhesives was observed by XRD, SEM, and AFM, and the shear strength, elongation at break, peel strength, and water resistance were tested and the relationship between structure and properties of the adhesives was observed and analyzed. XRD suggested that OMMT has been completely peeled in the polyurethane matrix and the spacing of layers has increased. SEM and AFM indicated that the OMMT dispersed evenly in the PU matrix and had a good transition with PU matrix, and the interface effects between two phases were strong. The results of the mechanical properties showed that OMMT could significantly help to improve properties of OMMT/PU adhesive, and the shearing strength, fracture tensile strength, and peel strength of 4 wt% OMMT/PU adhesive were 7.24 MPa, 2.14 MPa, and 451.2 N/m, respectively; the water absorption quantity was 2.82%. Compared with the unmodified PU, the shearing strength, tensile strength, and elongation at break of 4 wt% OMMT/PU adhesive were increased by 36.75%, 134.90%, and 76.80%, respectively. The peel strength decreased by 30.76%, and the water absorption decreased by 17.54%, in the meanwhile.

## 1. Introduction

Nanoparticles have much large surface area and shorter interparticle distance at the same particle content, exist in superior properties, and may have a significant impact on the electrical properties, heat resistance, and mechanical properties of the composites, and the montmorillonite (MMT) is the one of nanoparticles, which is a kind of natural clay mineral and has a layered structure. It consists of stacked, layered silicate about 1 nm thickness including two silica tetrahedral sheets sandwiching an edge-shared octahedral sheet of either aluminum or magnesium hydroxide. There are some hydrophilic cations residing in the gallery, such as Na<sup>+</sup> or K<sup>+</sup> ions, which can be exchanged by other cations [1]. MMT and related layered silicates are the materials of choice for polymer/clay nanocomposites with excellent performances.

Polyurethane (PU) is widely used in engineering thermoplastic material with excellent properties such as good mechanical properties and thermal property; more attention has been given to the PU/filler composites [2, 3]. The curing cycle of water-soluble PU adhesive is long and has a low solid content. The infiltration of solvent-free PU adhesive is bad and the production cost is high; alcohol-based PU adhesive is used widely in the field of fabric, plastic flexible packaging and leather finishing [4, 5], because it has no NCO groups, it is nontoxic, it does not pollute the environment, and it saves energy, and it has excellent flexibility and oil resistance, abrasion resistance [6, 7]. But the drawback of alcohol-based PU adhesive is low bond strength and permeability is not ideal, in some special cases. MMT is lamellar material, having large length thick ratio, but it is difficult to form intercalated or exfoliated structure while MMT is used to modify polymer matrix directly. Polymer chain is difficult to insert between

the MMT layers because the polarity of MMT is strong and the layer thickness is very small, so the MMT should be organically modified (OMMT). On one hand, OMMT has a good compatibility with the PU matrix; on the other hand, due to the presence of nanomaterial, the composite material exhibits high mechanical strength, high modulus, and high thermal stability properties, and nanocomposite modified by OMMT shows excellent performance in these areas [8, 9]. OMMT can improve the mechanical properties of PU adhesive and reduce the permeability effectively [10, 11].

Toluene diisocyanate (TDI) and polyether diol were used to prepare PU and OMMT was used as modifier in this paper, the microstructure and mechanism were studied by XRD, SEM, and AFM, the shear strength, peel strength, and water absorption of OMMT/PU film are tested, and the relationship of structure and properties has been researched and provided experimental data and theoretical basis for the development and application of PU.

## 2. Experimental

**2.1. Materials.** MMT (200 mesh, 90~110 mmol/100 g) was obtained from Henan Yongshun Water Treatment Materials Co., Ltd. (CHN). Polyether diol ( $M_n = 1000$ ) was obtained from Jiangsu Hai'an Petroleum Chemical Plant. Toluene diisocyanate (TDI) was from Shanghai Shengan Chemical Industry Co. (CHN), industrial products. Diethylenetriamine was from Newtop Chemical Material (CHN) Co., Ltd., AR grade. Epoxy resin (E-51) was from Wuxi Guangming Chemical Factory. Octadecyl trimethyl ammonium chloride (OTAC) was from Boxing County Runda chemical Co., Ltd. (CHN).

**2.2. Modification of Na-MMT.** MMT (20 g) was placed in a 500 mL flask, and then distilled water (380 g) and OTAC (7.66 g) were added, where the quality of OTAC could be calculated according to the following formula. The reaction temperature was controlled at 353 K and rapidly stirred for 4 h and filtered. Modified MMT was rinsed with distilled water for 3–5 times and placed in an oven, dried for 6 h at 373 K, grinded and collected OMMT (organically modified montmorillonite) sieved by 200 mesh:

$$m_{\text{OTAC}} = \frac{\text{CEC} \times 10^{-3}}{100} \times m_{\text{Na-MMT}} \times M_{\text{OTAC}}, \quad (1)$$

where  $m_{\text{OTAC}}$  was the mass of OTAC, CEC was the maximum capacity when  $\text{Na}^+$  in Na-MMT would exchange with the outside cations,  $m_{\text{Na-MMT}}$  was the mass of Na-MMT, and  $M_{\text{OTAC}}$  was the molar mass of OTAC.

**2.3. Preparation of Prepolymer.** Polyether diol ( $M_n = 1000$ ) was added into the flask and vacuum dried at 373 K and 2 mmHg for 0.5 h and cooled to 353 K, and TDI, isopropyl alcohol, acetone, and diethylenetriamine were added into above solution, stirred for 1.5 h, heated continuously to 373 K, and kept for 2 h. The mixture was allowed to cool to 318 K and stirred for 3 h before being used.

### 2.4. Preparation of A and B Component

**A Component.** Chain growth agent diethylenetriamine was quickly added into the prepolymer and stirred for 1 h at 313 K~328 K. The temperature was raised to 343 K, and solvent was volatilized for 0.5 h, when the distillate reduced significantly, continued to heat up to 393 K~398 K, and started vacuum, kept for 0.5 h. Lower the temperature to 343 K and added anhydrous ethanol and stirred 0.5 h, got OMMT/PU, finally.

**B Component.** Curing agent was prepared by the epoxy resin E-51 and acetic ether. The B component was mixed with A component in a certain proportion before being used.

**2.5. Preparation of OMMT/PU Adhesive.** B component mixed with A component according to the mass ratio of 1:10, was cured for 24 h at 60°C (333 K), and got OMMT/PU adhesive.

### 2.6. Methods of Testing

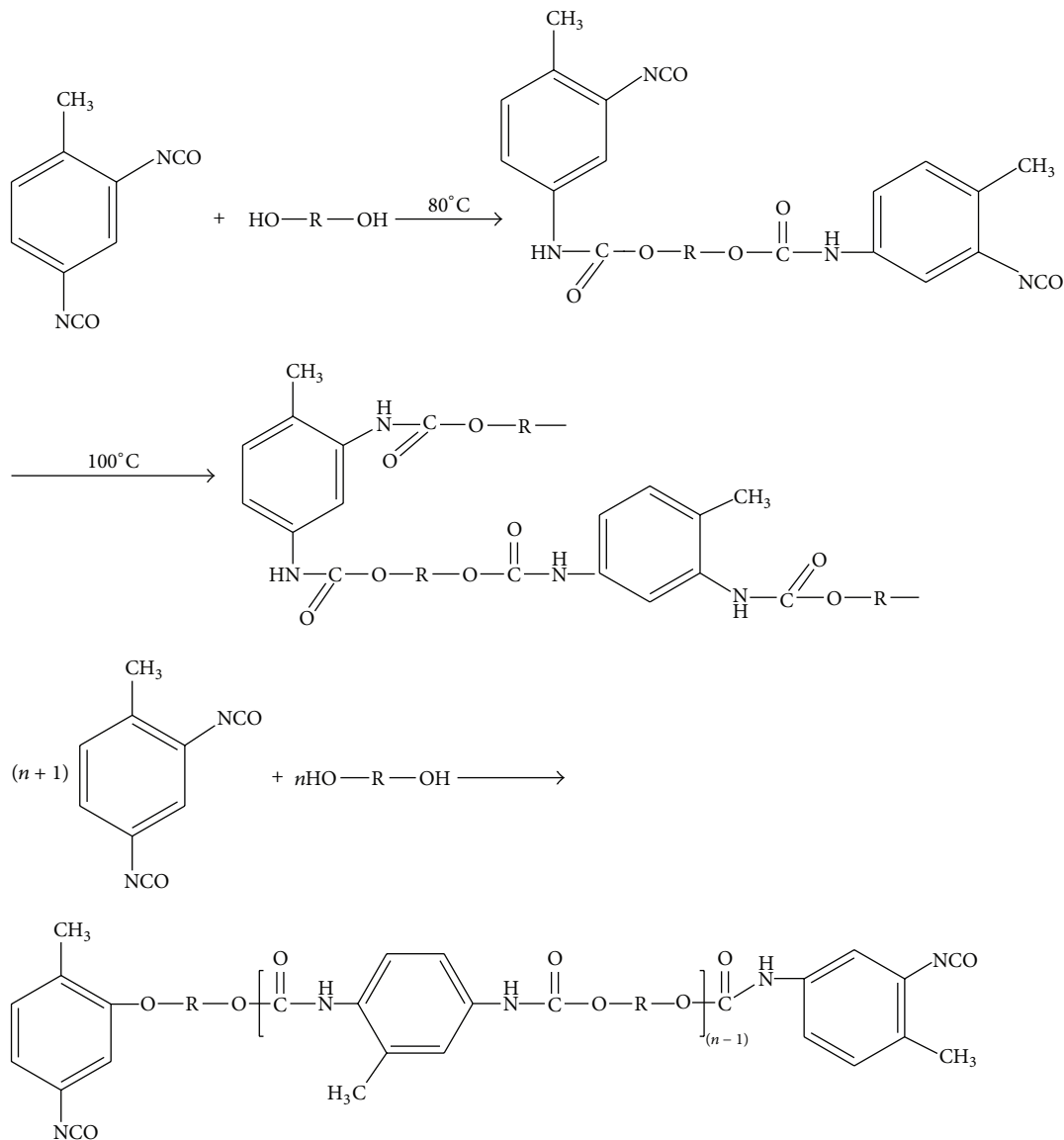
**FT-IR.** The FT-IR spectra, which are used to characterize the chemical structure of the polymer matrix, are performed with EQUINOX-55 Fourier transform spectrometer (GER), in the 400–4000  $\text{cm}^{-1}$  range; 5 scans are averaged for each spectrum. And it could be seen that there exist the characteristic absorption peaks of material.

**XRD.** X-ray diffraction (XRD) patterns are obtained using a Philips (Holland) Y500 diffractometer with a back monochromator and Cu anticathode (scanning rate 1.5°/min, scanning range 2–14°, and step 0.15406 nm). Special attention is paid to the  $2\theta$  region for accurate determination of  $d_{001}$  (i.e., the MMT and OMMT  $d$ -spacing). Spacing of MMT and OMMT are analyzed, and the dispersion effect of OMMT in PU matrix is identified.

**SEM.** The fracture structures of samples were examined on the HITACHI S-4300 scanning electron microscope (SEM, JAPA). Samples were deposited on a sample holder with adhesive carbon foil and were sputtered with gold. The dispersion effect of MMT and the interfacial morphology of OMMT in PU matrix are also observed and analyzed.

**AFM.** Atomic force microscope (Veeco Instruments, USA) is used to observe decentralized state and roughness of OMMT in PU matrix.

**2.6.1. Mechanical Measurements.** Tensile strength, elongation (%), and peel strength are measured using a universal testing machine (model 3000, Shoreatzo Co., Japan) at  $23 \pm 2^\circ$  (276 ± 278 K), with a tensile speed of  $5 \pm 1$  mm/min, according to GB/T7124-1986. The dimensions of the sample are 2 mm in width, 12.5 mm in thickness, and 35 mm in length. The mean value of five measurements for each sample is taken.



SCHEME 1: The reaction equation of performed polymer in the system.

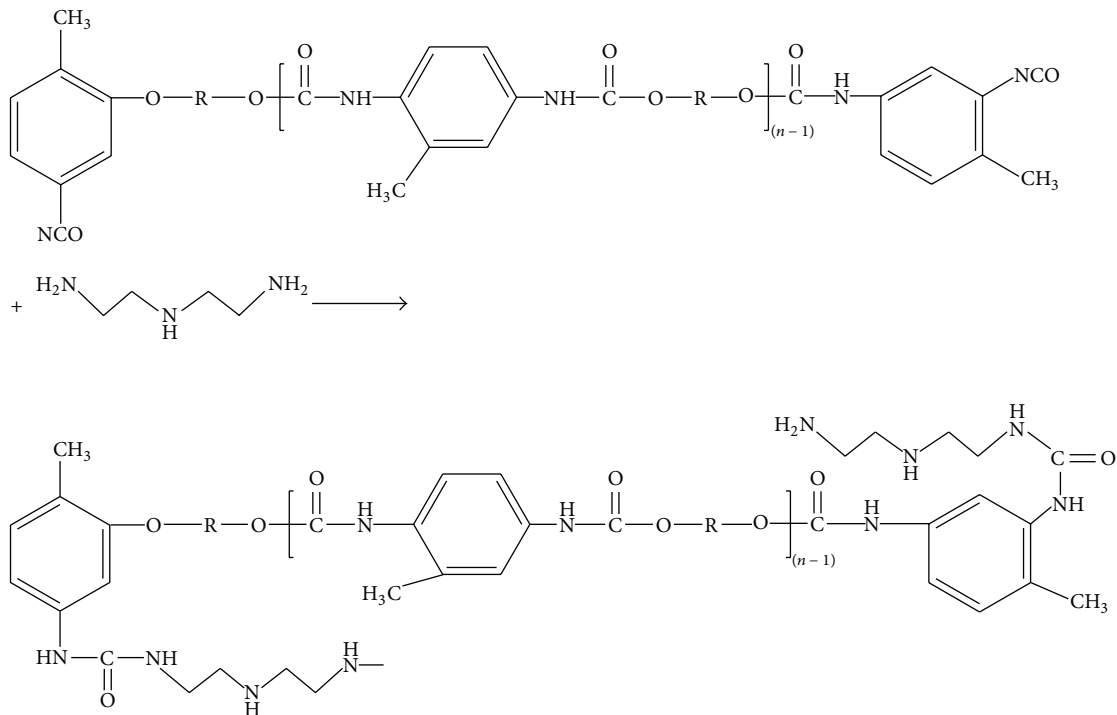
### 3. Results and Discussions

**3.1. FT-IR Spectral Analysis.** FT-IR spectra of composite materials were presented in Figure 1. The curves of (a), (b), and (c) were PU adhesive solution, EP resin, and the film after curing in the FI-IR spectra, respectively. The reaction equation was listed in Schemes 1 and 2. As seen in Figure 1(a) few absorption peaks can be found at  $3297\text{ cm}^{-1}$ ,  $2970\text{ cm}^{-1}$ , and  $1725\text{ cm}^{-1}$  which can be attributed to  $\text{-OH}$  and  $\text{-NH}$  stretching vibration [12, 13], stretching vibration absorption peak of  $\text{-CH}$ , and  $\text{-C=O}$  stretching vibration, respectively, indicating that the organic modifier has been exchanged into the galleries of the silicate layers. This showed that the urethane groups were generated by the reaction of  $\text{-NCO}$  and  $\text{-OH}$  in the system. The absence of the characteristic absorption spectral bands of the  $\text{-NCO}$  at  $2280\text{--}2270\text{ cm}^{-1}$

confirmed that the  $\text{-NCO}$  groups were completely consumed. According to the curve (a), the carbamate was formed due to the reaction between  $\text{-NCO}$  group of TDI and  $\text{-OH}$  of polyether.

Curve (b) was the FT-IR spectrum of curing agent (epoxy resin E-51);  $909\text{ cm}^{-1}$  and  $840\text{ cm}^{-1}$  were the vibration absorption peak of the epoxy ring. The absorption peak at  $1508\text{ cm}^{-1}$  belonged to the *p*-substituted benzene absorption, and a strong absorption peak at  $1242\text{ cm}^{-1}$  was due to the aliphatic aromatic ether bond antisymmetric stretching vibration.

The small peak at  $1100\text{ cm}^{-1}$  in curve (c) was due to  $\text{-O-}$  stretching vibration, which was wider than the curve (a), because of the overlap of the  $\text{-O-}$  in the EP and PU stretching vibration [14, 15]. The absence of the peak of the epoxy groups at  $915\text{ cm}^{-1}$  confirmed the epoxy groups were completely



SCHEME 2: The reaction equation of chain extension agent and performed polymer.

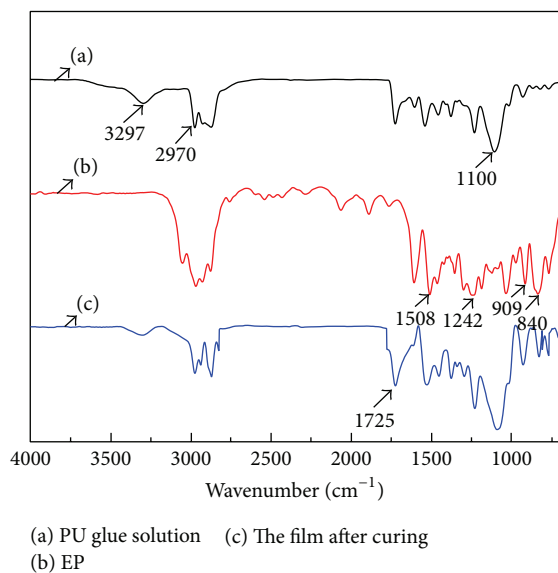


FIGURE 1: FT-IR spectra of the alcohol-based polyurethane adhesives.

consumed. According to the curve of (a), (b), and (c) the target product of alcohol soluble polyurethane adhesive was gained by the reaction between TDI and polyether polyol. The reaction between PU and EP was complete, formed network structure, and achieved the purpose of curing. The reaction mechanism is indicated in Schemes 1 and 2.

**3.2. SEM and AFM Analysis.** The SEM images of MMT and OMMT were shown in Figure 2. Figure 2(a) was SEM of MMT; it indicated that lamellar spacing was fuzzy, layer spacing was not clear, and there were a lot of granular impurities on the surface of layer, and this would influence the performance of MMT as filler material [16, 17]. Figure 2(b) was the SEM image of OMMT (organically modified by OTAC), which showed that the surface of the lamella was with no impurities, clean and clear, and the lamellar spacing was increased. Meanwhile, it was noted that the ratio of length to thickness of OMMT was large, and the thickness was about 1 nm; while the length was about 100 nm, the layer was peeled in the PU matrix and could be further confirmed from the result of XRD.

Figure 3 was the AFM images of OMMT/PU adhesive [18], and Figure 3(a) was the appearance diagram, and Figure 3(b) was three-dimensional phase diagram. The bright part was the higher area, OMMT component, while the dark part was the lower area, PU matrix, in Figures 3(a) and 3(b). OMMT component of the phase diagram was nanoscale dispersion and was uniformly dispersed in PU matrix. The interface between PU matrix and OMMT was fuzzy, which could indicate that the modifier OTAC could play a role of bridge between OMMT and PU matrix, and showed that the surface of OMMT/PU film was jagged, and this could prove the layer of OMMT was peeled completely in matrix, and spatial distribution of layer was random occurrence. The reason was that crossing reaction between PU and OTAC would lead the layer of OMMT to peel completely. On the other hand, there existed electrostatic force between OTAC

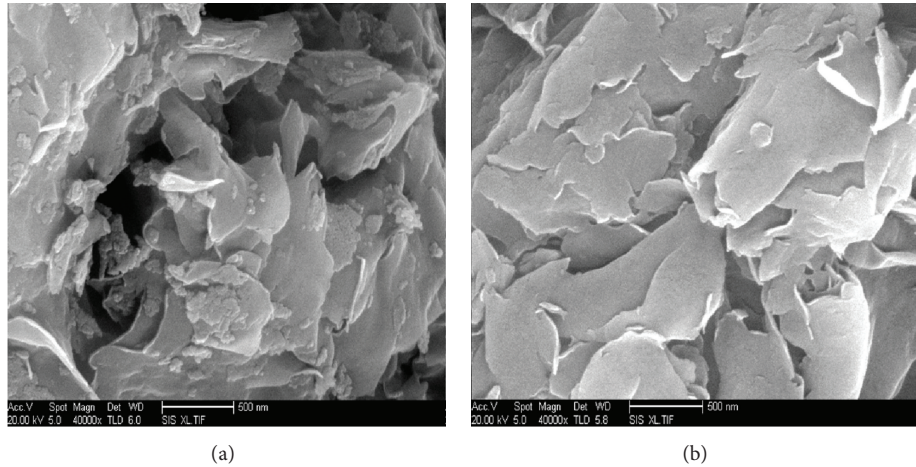


FIGURE 2: The SEM photographs of OMMT.

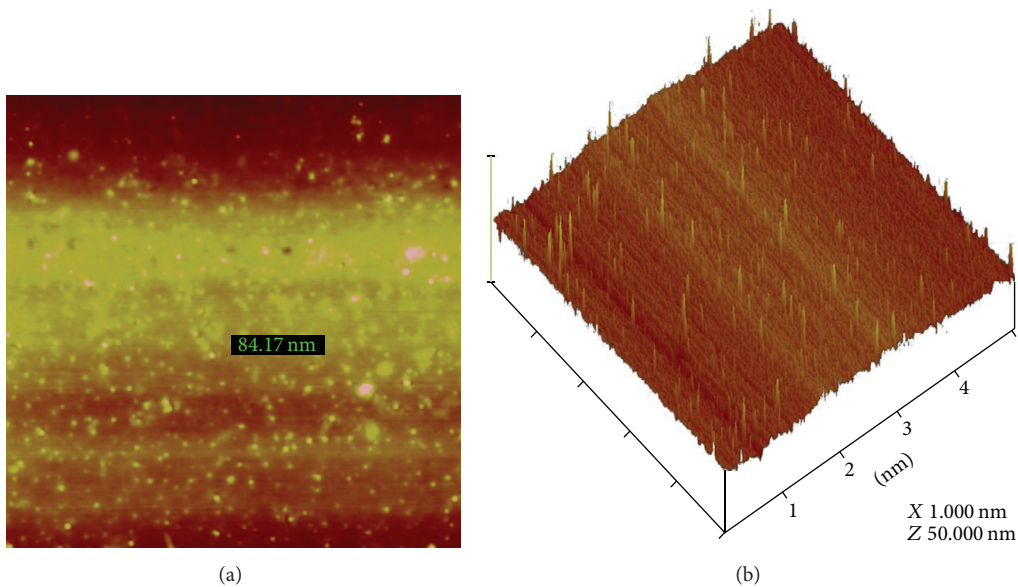


FIGURE 3: The AFM images of OMMT/PU.

and the layer of MMT, so it could play a very good transition connecting role between matrix and inorganic components.

**3.3. XRD Analysis of OMMT/PU.** Figures 4(a) and 4(b) were the XRD [19] patterns of MMT and OMMT;  $2\theta$  angle of them were  $6.4^\circ$  and  $4.3^\circ$ , respectively. According to Bragg's law,  $2d \sin \theta = n\lambda$ , X-ray was a copper target, and the wavelength was  $0.15406 \text{ nm}$ ,  $n = 1$ , and then spacing of MMT and OMMT was  $1.38 \text{ nm}$  and  $2.05 \text{ nm}$ , respectively. The inter-layer spacing was increased 48.6%, which suggested that the interlayer spacing of OMMT was improved.

Figure 5 was XRD patterns of OMMT/PU; it showed that  $2\theta$  angle at the range of  $3^\circ \sim 4^\circ$  gradually appeared as peak with the increase of OMMT content; the peeling effect was fine when the content of OMMT was in the range of 1~4 wt%, and it dispersed disorderly, so no obvious peak appeared. When

the content of OMMT was 5 wt%, weak peak appeared in the range of  $3.8^\circ$  nearby, and it may influence OMMT dispersion in the matrix and there was locally orderly arrangement that was intercalated structure.

#### 3.4. Mechanical Properties Analysis of OMMT/PU Films

**3.4.1. Shear Strength Analysis.** Shear strength was tested according to GB/T 7124-1986; the sample was made with 45 carbons steel, and the size of length was  $100 \pm 0.2 \text{ mm}$ , width was  $25 \pm 0.2 \text{ mm}$ , and thickness was  $2 \pm 0.1 \text{ mm}$ . The length of the bonding part was  $12.5 \pm 0.5 \text{ mm}$ , and stretching rate was  $5 \pm 1 \text{ mm/min}$ .

Figure 6 noted the change of shear strength of PU adhesive with the increase of content OMMT from 1 wt% to 5 wt%. The shear strength increased with the content of

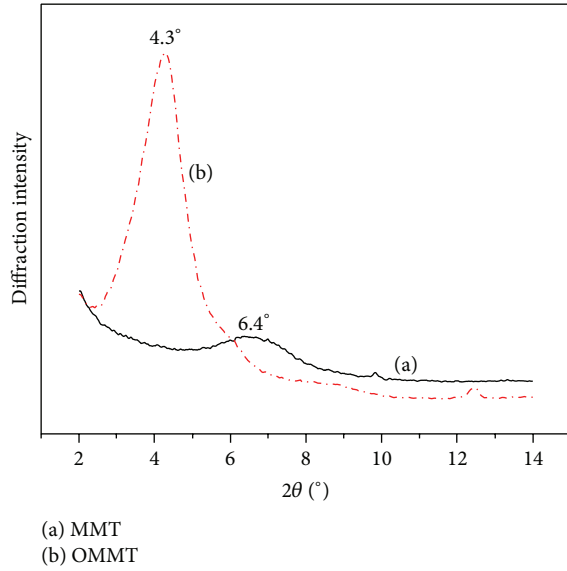


FIGURE 4: XRD patterns of MMT.

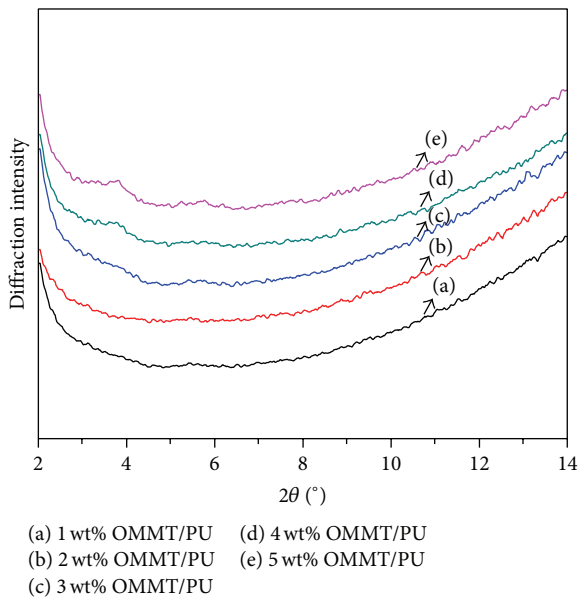


FIGURE 5: XRD patterns of OMMT/PU.

OMMT 1 wt%~4 wt%. The maximum shear strength was 7.24 MPa when the content of OMMT was 4 wt%, which increased by 36.75% than that of pure PU material. But shear strength decreased when the content of OMMT exceeded 5 wt%. The reason was that too many OMMT would result in appearing of the phenomenon of agglomeration. It would help to enhance the interactions of OMMT and weaken the interactions between OMMT and PU. So, it rapidly decreased the shear strength.

**3.4.2. Peel Strength Analysis.** Peel strength [20] was tested according to GB/T 2791-1995, 200 mm in length,  $25 \pm 0.5$  mm

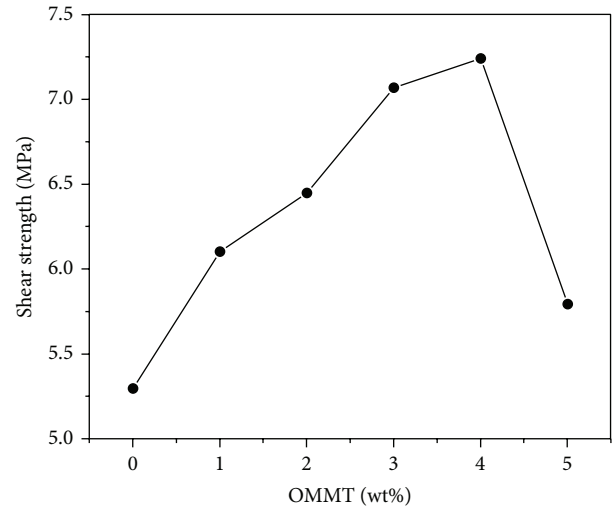


FIGURE 6: The shear strength curve of OMMT/PU.

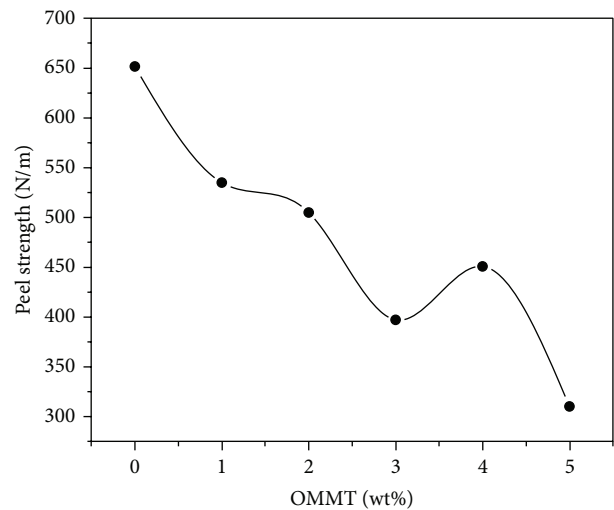


FIGURE 7: The peel strength curve of OMMT/PU.

in width, and 3 mm in thickness. Speed of peeling was  $100 \pm 10$  mm/min, and the length of peeling part was more than 125 mm. The peeling strength was decreased when the content of OMMT was 0%~5 wt% in Figure 7. When the content of OMMT was 4 wt%, there was an inflection point, and it was because the amount of urethane and carbamido which played the role of connection increased, instead of inorganic component OMMT, so the peeling strength of OMMT/PU decreased. The inflection point might be because the dispersion of OMMT in 4 wt% OMMT/PU was better than that of 3 wt% OMMT/PU, OMMT on the surface of 3 wt% OMMT/PU was little, and its peeling strength was lower than that of 4 wt% OMMT/PU, but the overall trend was reduced.

TABLE 1: Tensile strength and elongation at failure of OMMT/PU.

Index sample	Thickness (mm)	Width (mm)	Gauge length (mm)	Tensile force (MPa)	Elongation at break (%)	Tensile strength at break (MPa)
Pure	1.883	6.103	30.10	13.89	20.4	1.21
I	1.786	6.385	32.94	15.87	31.76	1.391
II	1.863	6.075	33.61	16.64	34.44	1.471
III	2.012	6.207	37.45	22.02	49.80	1.761
IV	2.113	6.015	36.98	27.16	47.92	2.14
V	1.996	6.154	36.27	18.44	45.08	1.50

**3.4.3. Tensile Strength Analysis.** The tensile strength of the film was tested according to GB/T 528-1998, the sample size was  $25.0 \pm 0.5$  mm in length,  $2.0 \pm 0.2$  mm in thickness, and 6.0~6.4 mm in width, and stress rate was 500 mm/min  $\pm$  50 mm/min. Table 1 showed that the tensile strength and elongation at break of the film mixed with OMMT increased in some degree, and the mechanical properties of film decreased while the content of OMMT was larger than 4 wt%. The reason was that the intercalation agent molecules reacted with isocyanate groups and then formed a part of PU, and electrostatic interactions existed between the intercalation agent and MMT, so the intercalation agent between MMT and PU matrix sheet played a role as a bridge. The effect of stress concentration would produce around ions and the matrix resin would produce many microcracks, absorbed more fracture energy, and then blocked or inactivated the further expansion of microcracks, while the matrix resin was subjected to external force. So the tensile strength of the composite increased. OMMT could not disperse in the matrix uniformly while the content of OMMT was more than a certain amount. Then made the microcrack develop into macroscopic fracture easily, and then the tensile strength of the composite decreased. The tensile strength at break of 4 wt% OMMT/PU achieves was 2.14 MPa that improved 76.8% than that of unmodified adhesive [21]; elongation at break rose to 47.92% from 20.4% and improved by 134.9%, and it accorded with the front analyzing result.

**3.5. Water Absorption Analysis of OMMT/PU Film.** The size of PU film was 3 cm  $\times$  3 cm, and PU film was immersed in the water (1–5 days) at room temperature and took it out; it absorbed the water on the surface of film by filter paper. We weighed the quality of wet film and dry film, from the formula  $(W2 - W1)/W1$ , ( $W1$ , the quality of dry film,  $W2$ , the quality of wet film) and calculated the water absorption quantity of the film. Figure 8 was the trend of the film water absorption. It reduced the water absorption effectively; with the increase of OMMT content, inflection point appeared when the content of OMMT was 4 wt% and continued to increase OMMT that would increase water absorption quantity. It was because the high content of OMMT could cause local reunion, the resistance of water molecules entering into PU matrix was small, and water absorption quantity was bigger, which was

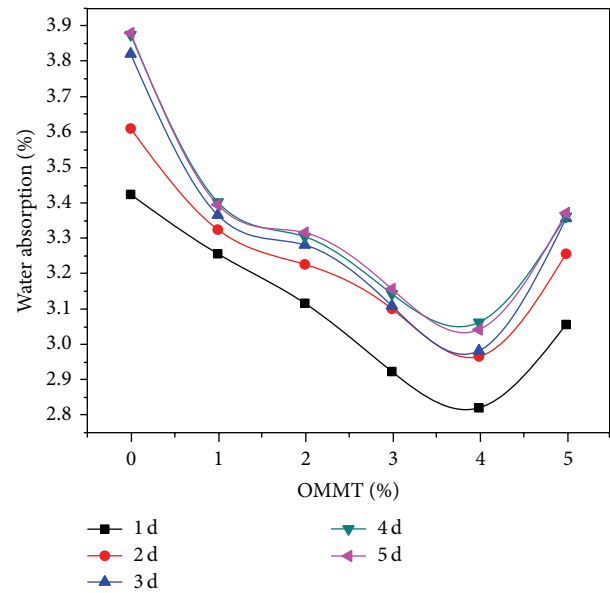


FIGURE 8: Water absorption curves of OMMT/PU.

consistent with the result of XRD. On the other hand, water absorption quantity was increased with the extension of soaking time, achieved a certain values, and tends to be stable. The value of water absorption quantity tended to a certain number when the soaking time was 2 d to 5 d, the reason was that water molecule was quickly infiltrated in shallow film at the beginning and made the water absorption increase. It was difficult to infiltrate deeply; as the lamella of MMT enlarged the path of a water molecule, the water would slowly permeate into the structure of OMMT/PU over time. On the other hand, as the density of OMMT was larger than that of PU matrix, the quality would increase at the same volume; even if it absorbed the same quality of moisture, the water absorption quantity would reduce, too. Soaking time was 1d, water absorption of pure film was 3.42%, and the film of 4 wt% OMMT/PU was lowest, which was 2.82%. Water absorption quantity was reduced by 17.54% after adding OMMT filler and improved the performance of water resistance, effectively.

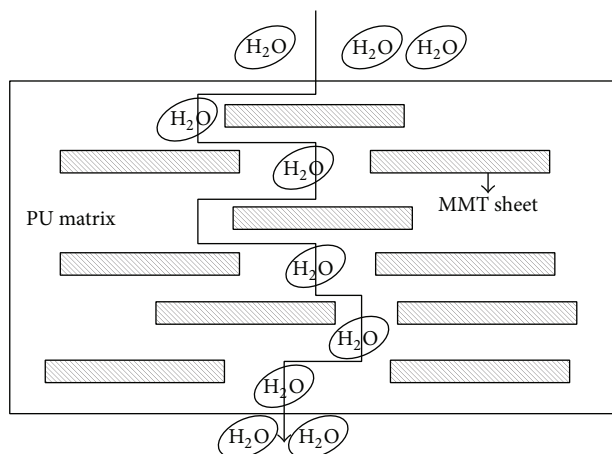


FIGURE 9: The ideal path of water molecules through OMMT/PU film.

Figure 9 showed the process of water molecules through film that mixed with OMMT. The water absorption increased rapidly at the beginning, because the water molecules could rapidly infiltrate into the shallow surface film. But the OMMT formed a barrier; then the path of water molecules crossed PU matrix to increase, so it is difficult to penetrate deeply into the film in limited time. The water absorption quantity rate increased slowly with the increasing of time. On the other hand, because the density of OMMT was much larger than that of the adhesive film, the quality would increase in the same volume. Although it absorbed the same quality of moisture, water absorption rate still decreased.

#### 4. Conclusions

OMMT/PU nanocomposites have synthesized, and the morphologies, mechanical properties, and water absorption property of OMMT/PU nanocomposites have been investigated in this study. The research results lead to the following conclusion. According to the results of FT-IR could determine the reaction product was the target product. SEM and AFM images noted that the morphology of OMMT filler was clear and OMMT dispersed uniformly in OMMT/PU adhesive, and the size of OMMT was nanoscale. Angle  $2\theta$  and spacing of OMMT were  $6.4^\circ$  and  $2.05\text{ nm}$ , which improved by 48.8% and 48.6% than that of MMT in XRD patterns, respectively. When the content of OMMT was 4 wt%, the shear strength was 7.24 MPa, tensile strength was 2.14 MPa, elongation at break was 47.92%, peeling strength was 451.2 N/m, and water absorption decreased by 17.54%. The uniform mixing of OMMT layer and PU matrix could achieve on nanoscale, so mechanical properties of OMMT/PU were improved, and water absorption quantity decreased.

#### Conflict of Interests

The authors declare that there is no conflict of interests regarding the publication of this paper.

#### Acknowledgment

The authors would like to express their appreciation for project supported by Heilongjiang Province Department of Education (12531130).

#### References

- [1] M.-L. Abel and J. F. Watts, "Examination of the interface of a model adhesive joint by surface analysis: a study by XPS and ToF-SIMS," *Surface and Interface Analysis*, vol. 41, no. 6, pp. 508–516, 2009.
- [2] B. C. Chun, M. H. Chong, and Y.-C. Chung, "Effect of glycerol cross-linking and hard segment content on the shape memory property of polyurethane block copolymer," *Journal of Materials Science*, vol. 42, no. 16, pp. 6524–6531, 2007.
- [3] S. Oprea, "Effect of the diisocyanate and chain extenders on the properties of the cross-linked polyetherurethane elastomers," *Journal of Materials Science*, vol. 43, no. 15, pp. 5274–5281, 2008.
- [4] S. Oprea and O. Potolinca, "Synthesis of cross-linked polyurethane elastomers with fluorescein linkages," *Journal of Materials Science*, vol. 44, no. 15, pp. 4181–4187, 2009.
- [5] S. Oprea and O. Potolinca, "Synthesis of polyether urethanes with a pyrimidine ring in the main chain," *Designed Monomers and Polymers*, vol. 13, no. 6, pp. 523–534, 2010.
- [6] S. Oprea, "The effect of chain extenders structure on properties of new polyurethane elastomers," *Polymer Bulletin*, vol. 65, no. 8, pp. 753–766, 2010.
- [7] C. Decker, L. Keller, K. Zahouily, and S. Benfarhi, "Synthesis of nanocomposite polymers by UV-radiation curing," *Polymer*, vol. 46, no. 17, pp. 6640–6648, 2005.
- [8] P. Mondal and D. V. Khakhar, "Rigid polyurethane-clay nanocomposite foams: preparation and properties," *Journal of Applied Polymer Science*, vol. 103, no. 5, pp. 2802–2809, 2007.
- [9] N. Mahmood, J. Kressler, and K. Busse, "Structure analysis in polyurethane foams at interfaces," *Journal of Applied Polymer Science*, vol. 98, no. 3, pp. 1280–1289, 2005.
- [10] S. Gaidukov, R. D. Maksimov, U. Cabulis, E. Plume, and A. Stunda-Zujeva, "Mechanical properties of a rigid polyurethane/montmorillonite composite prepared by using a biopolyol," *Mechanics of Composite Materials*, vol. 49, no. 4, pp. 333–344, 2013.
- [11] M. R. Sanchis, O. Calvo, O. Fenollar, D. Garcia, and R. Balart, "Surface modification of a polyurethane film by low pressure nitrogen plasma for improved adhesion to polyethylene foam for automotive industry laminates," *Plasma Processes and Polymers*, vol. 4, supplement 1, pp. S1091–S1097, 2007.
- [12] H. Javaheriannaghash and M. Arianfar, "Structural, thermal and morphological properties of aqueous hybrid emulsion of silylated poly (urethane)/organic modified montmorillonite nanocomposites based on a new silicone and imide ring containing vinylic macromonomer," *Polymer Science Series B*, vol. 54, no. 1-2, pp. 115–125, 2012.
- [13] R. B. Thompson, V. V. Ginzburg, M. W. Matsen, and A. C. Balazs, "Predicting the mesophases of copolymer-nanoparticle composites," *Science*, vol. 292, no. 5526, pp. 2469–2472, 2001.
- [14] B. F. Schaefer, "When do rocks become oil?" *Science*, vol. 308, no. 5726, pp. 1267–1268, 2005.

- [15] T. Coa, P. Munk, C. Ramireddy, Z. Tuzar, and S. Webber, "Complexation of poly(acrylic acid) and poly(methacrylic acid) with pyrene-end-labeled poly(ethylene glycol): pH and fluorescence measurements," *Macromolecules*, vol. 23, no. 20, pp. 4411–4418, 1990.
- [16] J. H. Kim, M. S. Kim, H. M. Jeong et al., "Acrylic copolymer intercalated in sodium montmorillonite: a modifier of reactive hot melt polyurethane adhesive," *Composite Interfaces*, vol. 15, no. 6, pp. 577–587, 2008.
- [17] J. Pajama, A. Yekta, Y. Hu, and M. Winnik, "Evidence for intramolecular hydrophobic association in aqueous solution for pyrene-end-capped poly(ethylene oxide)," *Macromolecules*, vol. 25, no. 25, pp. 7024–7030, 1992.
- [18] G. N. Mahesh, S. Ramesh, and G. Radhakrishnan, "Segmented polyurethanes using fluorescein," *Journal of Applied Polymer Science*, vol. 60, no. 4, pp. 531–535, 1996.
- [19] M. Pramanik, S. K. Srivastava, B. K. Samantaray, and A. K. Bhowmick, "Synthesis and characterization of organosoluble, thermoplastic elastomer/clay nanocomposites," *Journal of Polymer Science, Part B: Polymer Physics*, vol. 40, no. 18, pp. 2065–2072, 2002.
- [20] P. K. Maji, P. K. Guchhait, and A. K. Bhowmick, "Effect of nanoclays on physico-mechanical properties and adhesion of polyester-based polyurethane nanocomposites: structure-property correlations," *Journal of Materials Science*, vol. 44, no. 21, pp. 5861–5871, 2009.
- [21] S. Oprea and O. Potolinca, "Synthesis of cross-linked polyurethane elastomers with fluorescein linkages," *Journal of Materials Science*, vol. 44, no. 15, pp. 4181–4187, 2009.

## Research Article

# Feasibility Studies on Underwater Laser Surface Hardening Process

**Biao Jin, Min Li, TaeWoo Hwang, and YoungHoon Moon**

*School of Mechanical Engineering, Engineering Research Center for Net Shape and Die Manufacturing, Pusan National University, Busan 609-735, Republic of Korea*

Correspondence should be addressed to YoungHoon Moon; yhmoon@pusan.ac.kr

Received 28 November 2014; Revised 23 March 2015; Accepted 30 March 2015

Academic Editor: Simo-Pekka Hannula

Copyright © 2015 Biao Jin et al. This is an open access article distributed under the Creative Commons Attribution License, which permits unrestricted use, distribution, and reproduction in any medium, provided the original work is properly cited.

Laser surface hardening process is a very promising hardening method for ferrous and nonferrous alloys where transformations occur during cooling after laser melting in the solid state. This study experimentally characterizes laser surface hardening of tool steel in both water and air. For the underwater operation, laser surface scanning is performed over the tool steel surface which is immersed in water. The laser surface hardening tests are performed with a maximum 200 W fiber laser with a Gaussian distribution of energy in the beam. For the surface hardening, single-track melting experiment which sequentially scans elongated path of single line has been performed. As the hardened depth depends on the thermal conductivity of the material, the surface temperature and the penetration depth may be varied by underwater laser processing. The feasibility of underwater laser surface hardening process is discussed on the basis of average hardness level and hardened bead shape.

## 1. Introduction

Lasers have been used in a number of ways to modify the properties of metal surfaces. The most often objective of the laser processing has been to harden the surface in order to provide increased wear resistance [1–4]. The laser beam irradiates the metal surface and causes very rapid heating of a thin layer of material near the surface. When the beam moves along the surface, the local heat deposited in the thin layer will quickly be conducted away, and the heated area cools rapidly. This is basically self-quenching process of the surface region [5, 6]. Certain metals, notably carbon steel, may undergo transformation hardening by heating followed by rapid cooling [7, 8]. This process yields a locally hardened surface. The hardened depth depends on the thermal conductivity of the material. The surface temperature and the penetration depth may be varied by adjusting the laser power, the surface scan speed, and the focusing of the beam. Greater hardening depths may be obtained by slow scan rate and larger laser power. Laser hardening is suitable for applications that require high hardness with relatively shallow case depth on selected surface areas, with no geometrical distortion [9–11].

It can be used for geometries with irregular shapes, grooves, lines, and gear teeth. The automotive industry, in which wear resistance on selected surfaces is desired, has been the most important application area for laser hardening.

As the hardened depth depends on the thermal conductivity of the material, the surface temperature and the penetration depth may be varied by underwater laser processing [12, 13].

This study experimentally characterizes laser surface hardening of tool steel in both water and air. For the underwater operation, single line laser surface scanning is performed over the tool steel surface which is immersion in water. Underwater effects on laser surface hardening process are estimated and discussed on the basis of average hardness level, melted bead shape, and width of heat affected zone in hardened layer.

## 2. Experimental

**2.1. Materials.** Specimen used in this study is AISI D2 cold worked tool steel. AISI D2 is a high-Cr, high-C tool steel alloyed with Mo and V. Chemical compositions of AISI D2 steel are shown in Table 1.

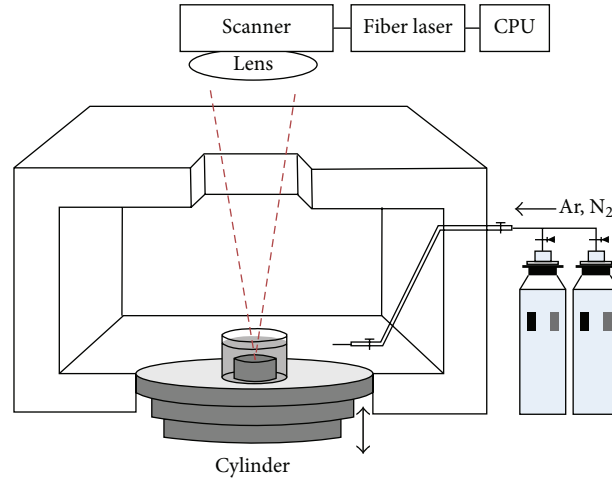


FIGURE 1: Schematic drawing of direct laser hardening system.

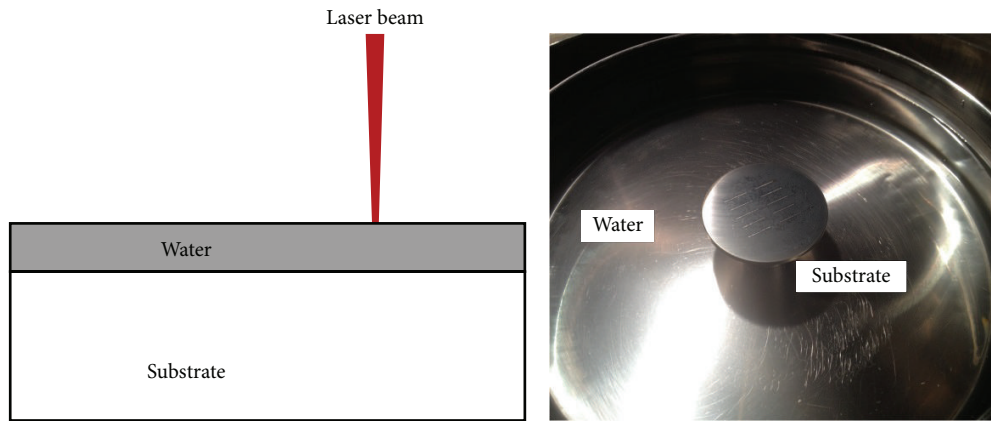


FIGURE 2: Immersed specimen for underwater experiment.

TABLE 1: Chemical compositions of AISI D2 steel.

Element	Fe	Cr	C	Mo	Mn	V	Si
wt.%	Bal.	12.10	1.50	1.00	0.45	0.35	0.25

TABLE 2: Experimental conditions for the direct laser hardening.

Test condition	Laser power (W)	Scan rate (mm/s)
Ar environment, underwater	100, 150, 200	7.32~21.96

**2.2. Equipment.** Figure 1 schematically shows the direct laser hardening system. The source of radiation is a fiber laser (IPG YLR-200) produced by IPG Photonics with a maximum power of 200 W, wave length of  $1.07 \mu\text{m}$ , and a laser beam diameter of 0.08 mm in the focal position. A scanner (SCANLAB hurrySCAN 20) was used to control the laser scanning method. The chamber was filled by argon gas in all experiments. The vertical movement of the cylinder was driven by a motor. The experimental conditions for the laser hardening are shown in Table 2.

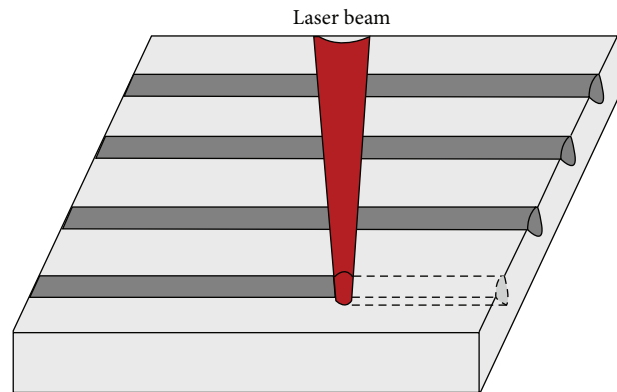


FIGURE 3: Schematic drawing of single-track laser melting experiment.

For the underwater surface hardening experiment, the sample is immersed in distilled water of  $25^\circ\text{C}$  during the laser hardening, as shown in Figure 2. The sample with water was placed in a cylindrical container. Through the series of preliminary tests in a given laser hardening system,

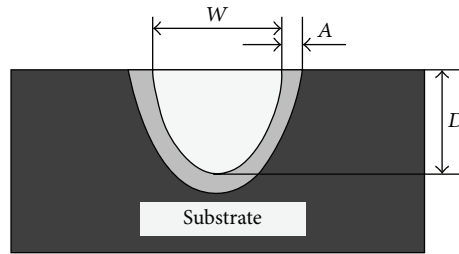


FIGURE 4: Schematic drawings of cross-sectional bead geometry.

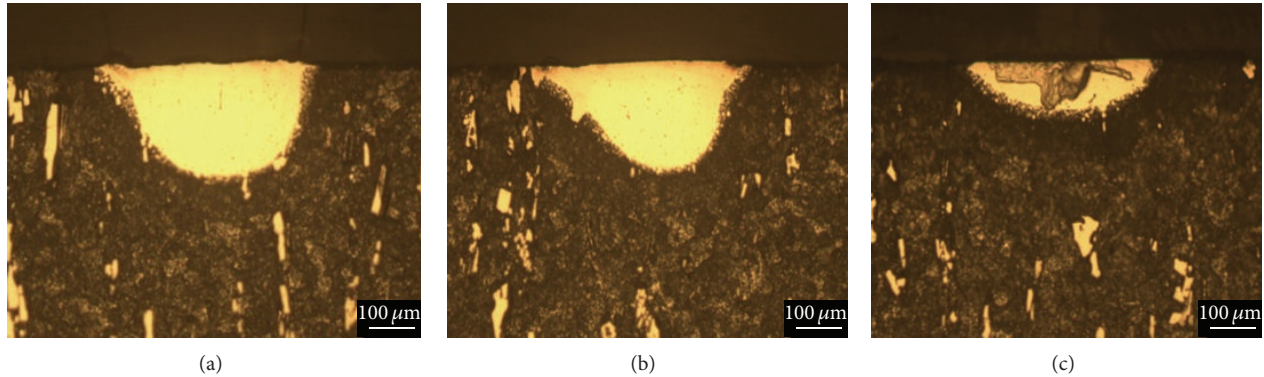


FIGURE 5: Cross-sectional views of a single-line bead hardened at Ar environment. Scanning rates are (a) 7.32 mm/s, (b) 14.64 mm/s, and (c) 21.96 mm/sec. Laser power is constant (150 W).

the water layer above the sample surface is set to be 1 mm. For the comparison purpose, the laser forming in air is also investigated. The distance between the lens and the sample was kept constant during all experiments.

In order to understand the effects of the process parameters such as laser power and scan rate, on the laser hardening behaviors, a series of experiments were conducted. The component properties are strongly influenced by the molten pool size, which is mainly controlled by the laser energy input. For the surface hardening, single-track melting experiment which sequentially scans elongated path of single line has been performed at various laser processing parameters, as shown in Figure 3.

For the analysis of underwater effects on laser surface hardening process, average hardness level, shape of hardened bead, and width of heat affected zone have been analyzed. Hardness values were measured at hardened layer, HAZ, and base metal, respectively, and averaged.

For the analysis of shape of hardened bead and width of heat affected zone, the bead shape in hardened zone was classified by three geometrical variables: penetration depth into the substrate ( $D$ ), deposition width ( $W$ ), and HAZ width ( $A$ ) as shown in Figure 4.

### 3. Results and Discussion

When the beam moves on, the surface will cool extremely rapidly because of thermal conduction of the heat energy from the thin heated layer into the interior of the metal. This leads to transformation hardening of the areas that the laser

beam has traversed. To estimate the underwater effects on laser surface hardening process, shape of hardened bead and average hardness level have been analyzed.

To study the underwater effects on shape of hardened bead, single line beads were produced at different scan rates ranging from 7.32 mm/s, 14.64 mm/s, and 21.96 mm/s, respectively.

Figure 5 shows cross-sectional views of single line beads hardened at Ar environment with different scan rates.

The deposition line width, the penetration depth, and HAZ width have a strong dependence on scan rate. An increase in the scan rate decreases the line width, the penetration depth, and HAZ width, since an increase in speed decreases the melting depth as a consequence of the shorter interaction time. In addition, the thermal gradient does not allow sufficient time for the molten metal to penetrate deeply into the substrate. Figure 6 shows cross-sectional views of single line beads hardened at underwater condition with different scan rates.

The effects of scan rates on shape of hardened bead are somewhat similar, but the penetration depth and HAZ width are significantly smaller than those of Ar environment shown in Figure 7. This is mainly due to the refraction of the beam in water layer, as shown in Figure 8. The laser spot diameter was changed from 430  $\mu\text{m}$  to 380  $\mu\text{m}$  at 1 mm water layer. Furthermore, the accelerated heat dissipation along water layer decreases the melting depth as a consequence of the shorter interaction time.

Figure 9 compares the hardness for underwater condition with those for Ar environment as a function of scan rates.

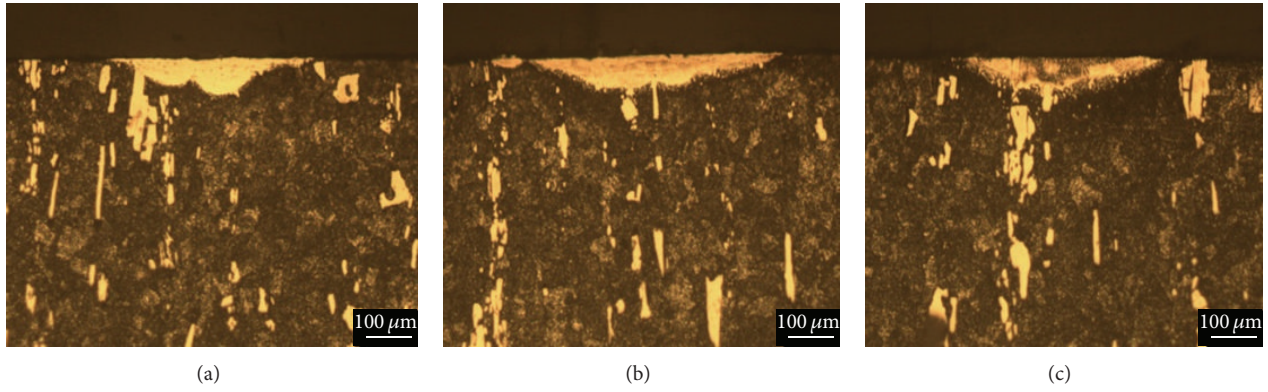


FIGURE 6: Cross-sectional views of a single-line bead hardened at underwater condition. Scanning rates are (a) 7.32 mm/s, (b) 14.64 mm/s, and (c) 21.96 mm/sec. Laser power is constant (150 W).

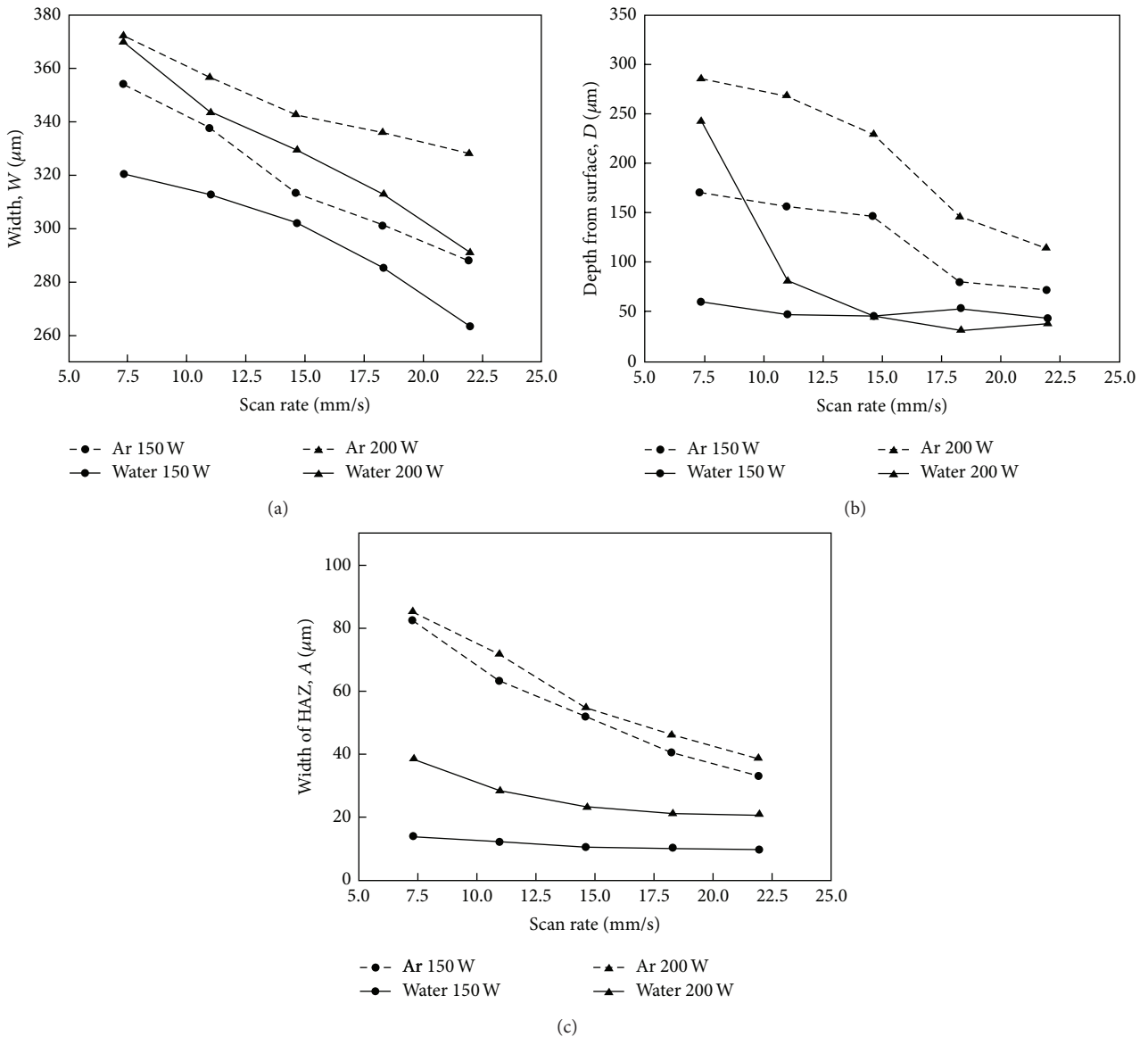


FIGURE 7: Comparisons of laser scan rate effects on (a) deposition width, (b) depth from surface, and (c) HAZ width.

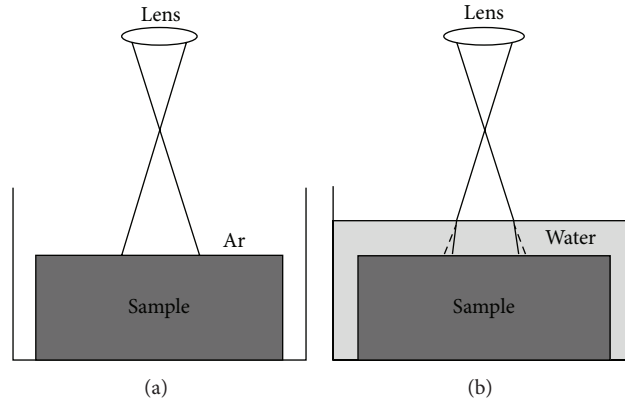


FIGURE 8: Schematic drawings of (a) straight beam at Ar environment and (b) refracted beam in underwater condition.

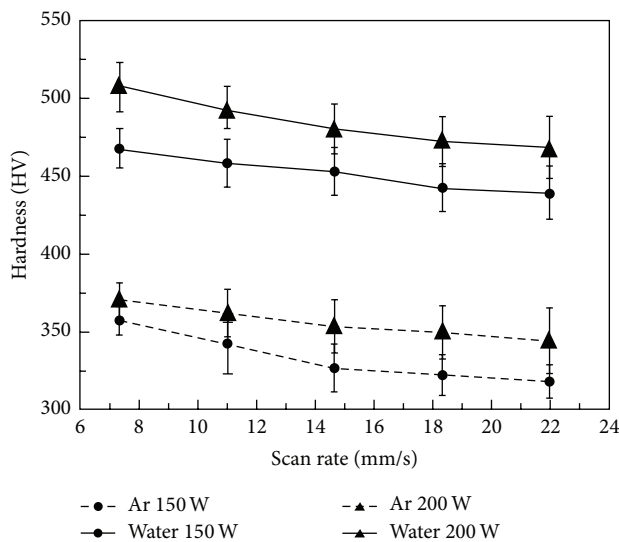


FIGURE 9: Comparisons of laser scan rate effects on microhardness of laser hardened beads.

As the higher heat input (i.e., high laser power and lower scan rate) provides more energy, the temperature of the molten metal increases. High energy input in laser surface hardening has high possibility of increased melting zone. As shown previously, the shape and size of hardened bead generated by laser hardening process are strongly dependent on 3D heat dissipations from molten pool. While, the hardness of hardened layer is mainly determined by microstructure, the cooling rate of molten pool is very crucial for increased hardness. In case of underwater laser hardening, additional heat dissipation effect along water layer accelerates cooling rate. Therefore the hardness of underwater laser hardened layers shows approximately 30% higher hardness than those of laser hardened layers at Ar environment.

#### 4. Conclusions

The feasibility of underwater laser surface hardening process has been discussed on the basis of hardened bead shape

and average hardness level. As the hardened depth depends on the thermal conductivity of the material, the surface temperature and the penetration depth have been varied by underwater laser processing. The shape of hardened bead, such as deposition line width, the penetration depth, and HAZ width are somewhat similar, but the penetration depth and HAZ width are significantly smaller than those of Ar environment due to the refraction of the beam in water layer and the accelerated heat dissipation along water layer. On the viewpoint of hardness, harder layer has been obtained at underwater hardening that is supposed to be caused by faster cooling rate due to accelerated heat dissipation along water layer.

#### Conflict of Interests

The authors declare that there is no conflict of interests regarding the publication of this paper.

#### Acknowledgments

This work was supported by the National Research Foundation of Korea (NRF) grant funded by the Korea government (MSIP) (no. 2012R1A5A1048294).

#### References

- [1] F. Verhaeghe, T. Craeghs, J. Heulens, and L. Pandraers, "A pragmatic model for selective laser melting with evaporation," *Acta Materialia*, vol. 57, no. 20, pp. 6006–6012, 2009.
- [2] A. Simchi and H. Pohl, "Effects of laser sintering processing parameters on the microstructure and densification of iron powder," *Materials Science and Engineering: A*, vol. 359, no. 1-2, pp. 119–128, 2003.
- [3] J.-H. Lee, J.-H. Jang, B.-D. Joo, H.-S. Yim, and Y.-H. Moon, "Application of direct laser metal tooling for AISI H13 tool steel," *Transactions of Nonferrous Metals Society of China*, vol. 19, no. 1, pp. s284–s287, 2009.
- [4] J.-H. Jang and Y.-H. Moon, "Laser processing technology using metal powders," *Journal of Korean Institute of Metals and Materials*, vol. 50, no. 3, pp. 191–200, 2012.

- [5] H. Shin, H. Lee, H. Yoo, K.-S. Lim, and M. Lee, "Laser-direct patterning of nanostructured metal thin films," *Journal of Korean Institute of Metals and Materials*, vol. 48, no. 2, pp. 163–168, 2010.
- [6] S. L. Engel, "Basic of laser heat treating," in *Source Book on Applications of the Laser in Metalworking*, E. A. Metzbower, Ed., p. 149, American Society for Metals, Metals Park, Ohio, USA, 1981.
- [7] J. H. Abboud, K. Y. Benyounis, A. G. Olabi, and M. S. J. Hashmi, "Laser surface treatments of iron-based substrates for automotive application," *Journal of Materials Processing Technology*, vol. 182, no. 1–3, pp. 427–431, 2007.
- [8] R. Komanduri and Z. B. Hou, "Thermal analysis of the laser surface transformation hardening process," *International Journal of Heat and Mass Transfer*, vol. 44, no. 15, pp. 2845–2862, 2001.
- [9] I. Yadroitsev, A. Gusarov, I. Yadroitsava, and I. Smurov, "Single track formation in selective laser melting of metal powders," *Journal of Materials Processing Technology*, vol. 210, no. 12, pp. 1624–1631, 2010.
- [10] S. W. Han, B. D. Joo, and Y. H. Moon, "Selective surface hardening by laser melting of alloying powder," *Materials Research Innovations*, vol. 18, pp. 902–907, 2014.
- [11] J.-H. Jang, B.-D. Joo, C. J. Van Tyne, and Y.-H. Moon, "Characterization of deposited layer fabricated by direct laser melting process," *Metals and Materials International*, vol. 19, no. 3, pp. 497–506, 2013.
- [12] H. Shen, M. Ran, J. Hu, and Z. Yao, "An experimental investigation of underwater pulsed laser forming," *Optics and Lasers in Engineering*, vol. 62, pp. 1–8, 2014.
- [13] S. Mullick, Y. K. Madhukar, S. Roy, S. Kumar, D. K. Shukla, and A. K. Nath, "Development and parametric study of a water-jet assisted underwater laser cutting process," *International Journal of Machine Tools and Manufacture*, vol. 68, pp. 48–55, 2013.